2017

Detection and interpretation of fluorescence signals generated by excitable cells and tissues

Anthony J. Costantino
Binghamton University--SUNY

DETECTION AND INTERPRETATION OF FLUORESCENCE SIGNALS GENERATED BY EXCITABLE CELLS AND TISSUES

BY

ANTHONY J. COSTANTINO

AS, Broome Community College, 2004

BS, Binghamton University, 2006

MS, Binghamton University, 2009

DISSERTATION

Submitted in partial fulfillment of the requirements for
the degree of Doctor of Philosophy in Electrical and Computer Engineering
in the Graduate School of
Binghamton University
State University of New York
2017

Accepted in partial fulfillment of the requirements for
the degree of Doctor of Philosophy in Electrical and Computer Engineering
in the Graduate School of
Binghamton University
State University of New York
2017

October 12, 2017

Dr. Mark L. Fowler, Chair
Department of Electrical and Computer Engineering, Binghamton University.

Dr. Arkady M. Pertsov, Faculty Advisor
Department of Pharmacology, Upstate Medical University.

Dr. David Klotzkin, Member
Department of Electrical and Computer Engineering, Binghamton University.

Dr. Dmitry V Ponomarev, Outside Examiner
Department of Computer Science, Binghamton University

ABSTRACT

Part 1: High-Sensitivity Amplifiers for Detecting Fluorescence

Monitoring electrical activity and Ca_i^{2+}transients in biological tissues and individual cells increasingly utilizes optical sensors based on voltage-dependent and Ca_i^{2+}-dependent fluorescent dyes. However, achieving satisfactory signal-to-noise ratios (SNR) often requires increased illumination intensities and/or dye concentrations, which results in photo-toxicity, photo-bleaching and other adverse effects limiting the utility of optical recordings. The most challenging are the recordings from individual cardiac myocytes and neurons. Here we demonstrate that by optimizing a conventional transimpedance topology one can achieve a 10-20 fold increase of sensitivity with photodiode-based recording systems (dependent on application). We provide a detailed comparative analysis of the dynamic and noise characteristics of different transimpedance amplifier topologies as well as the example(s) of their practical implementation.

Part 2: Light-Scattering Models for Interpretation of Fluorescence Data

Current interest in understanding light transport in cardiac tissue has been motivated in part by increased use of voltage-sensitive and Ca_i^{2+}-sensitive fluorescent probes to map electrical impulse propagation and Ca_i^{2+}-transients in the heart. The fluorescent signals are recorded using such probes represent contributions from different layers of myocardial tissue and are greatly affected by light scattering. The interpretation of these signals thus requires deconvolution which would not be possible without detailed models of light transport in the respective tissue. Which involves the experimental measurements of the absorption, scattering, and anisotropy coefficients, μ_a, μ_s,and g respectively.

The aim of the second part of our thesis was to derive a new method for deriving these parameters from high spatial resolution measurements of forward-directed flux (FDF). To this

end, we carried out high spatial resolution measurements of forward-directed flux (FDF) in intact and homogenized cardiac tissue, as well as in intralipid-based tissue phantoms. We demonstrated that in the vicinity of the illuminated surface, the FDF consistently manifested a fast decaying exponent with a space constant comparable to the decay rate of ballistic photons. Using a Monte Carlo model we obtained a simple empirical formula linking the rate of the fast exponent to the scattering coefficient, the anisotropy parameter *g*, and the numerical aperture of the probe. The estimates of scattering coefficient based on this formula were validated in tissue phantoms. The advantages of the new method are its simplicity and low-cost.

ACKNOWLEDGEMENTS

First and foremost I would like to thank my advisor Dr. Pertsov, without whom this work would not have been possible. After my first advisor left Binghamton University, Dr. Pertsov agreed to take me on as his student and fund my research. He provided very necessary guidance and valuable advice. Even though a large portion of this work was outside his field, he quickly grasped the most important concepts and directed my research toward completion. I would also like to thank my committee members Dr. Fowler and Dr. Klotzkin. Dr. Fowler has always had faith in me and provided a great deal of encouragement since I was an undergraduate student. Dr. Klotzkin has always been a source of useful technical discussions and advice as long as I have known him. I would like to thank Dr. Beaumont who was one of my original committee members. I have always admired his enthusiasm for new ideas, his willingness to work with students to help them grasp new concepts, and his technical prowess in many different areas. I would also like to thank my original advisor Dr. Twigg for getting me to ABD status and teaching me how to effectively present my work. I would like to thank Robert Pulz at the student machine shop for making all the stuff I designed and teaching me about practical considerations for my designs. I would like to thank my friends and family, particularly my parents for all their love and support. Finally, I would like to thank all the students at Binghamton University and Upstate Medical University that have made me feel welcome and encouraged me to persevere even when I thought I might never graduate. And to anyone I may have left out, thank you.

Contents

LIST OF TABLES

LIST OF FIGURES

Part 1 Detection of Low-Intensity Optical Signals from Biological Tissue

During the past two decades there have been dramatic methodological changes in monitoring electrical activity and ion concentrations in biological systems linked to the development of effective intracellular and membrane-bound optical probes. This led to the gradual replacement of conventional intracellular electrical recordings with non-destructive optical recordings, which revolutionized neurophysiology and cardiac electrophysiology.

Instead of impaling individual cells with a conventional or ion-sensitive microelectrode, the cells are stained with a voltage-sensitive or ion-sensitive dye. The dye reacts to changes in membrane potential or ion concentration by changing its fluorescence or absorption spectrum, with changes being recorded optically using photodiode arrays, CCD, or CMOS cameras.

Achieving satisfactory signal-to-noise ratios (SNR) often requires increased illumination intensities and/or dye concentrations, which results in photo-toxicity, photo-bleaching and other adverse effects limiting the utility of optical recordings. The most challenging are the recordings from individual cardiac myocytes and neurons. Thus the goal of our study is to improve the sensitivity of optical recording circuits. While there are many approaches to detecting weak optical signals, here we will focus on transimpedance amplifiers with PIN photodiodes. The reason for this is the low-cost and wide variety of possible applications for these circuits.

Here we demonstrate that by optimizing a conventional transimpedance topology one can achieve a 10-20 fold increase of sensitivity with photodiode-based recording systems (dependent on application). We provide a detailed comparative analysis of the dynamic and noise characteristics of different transimpedance amplifier topologies as well as the example(s) of their practical implementation.

Section 1.1 will describe voltage- and ion-sensitive dyes, their signal characteristics, and systems for excitation and detection of these signals. This will include some variations of the systems, for example how Ca_i^{2+}-sensitive dyes react differently than voltage sensitive dyes, and how absorptive dyes react to changes in voltage and how this change can be recorded. We will also discuss typical $\Delta F/F$ for different fluorescent dyes and $\Delta I/I$ for absorptive dyes and how these may vary with the types of cells under study. We will then discuss sources of noise and where they may appear within the system and how they limit the efficacy of optical recording.

In this work, we will focus primarily on monitoring the transmembrane potential and changes of intracellular calcium ions (Ca_i^{2+}-transients) which play a major role in the regulation of multiple intracellular processes.

One of the major challenges of the optical monitoring of electrical activity is the fact that the voltage-sensitive component represents only a small fraction of the total signal. The ratio for the best fluorescent dyes ($\Delta F/F$) usually does not exceed 5% - 15% [1]. The magnitude of the optical signal is particularly small in measurements of post-synaptic potentials which are usually about an order of magnitude smaller than the amplitude of the action potential.

While Ca_i^{2+}-dependent signals, often called calcium transients, have smaller offset than voltage sensitive signals ($\Delta F/F$ is usually about 50-250%) [2, 3], the use of these Ca-sensitive probes brings up different challenges: they bleach, which requires limiting the light exposure and thus higher gains of the optical signal amplifiers. The need for high-gain low-noise amplifiers is

particularly acute for low-affinity Ca_i^{2+} probes, which interfere less with intracellular processes but produce much weaker signals. This limitation becomes particularly important for optrodes [4], where recordings are taken at low illumination intensities and require high amplification.

In section 1.3 we will conduct an overview of electrical noise. We will discuss the types, the sources, and the models. This will enable us to identify the dominant sources of noise in our amplifier design and limit it as much as possible. In section 1.4 we will discuss the types of photodetectors and their noise models. We will cover light detection with PIN photodiodes, avalanche photodiodes, photomultiplier tubes and CCD/CMOS cameras. This section will also cover light sources as well, such as arc lamps, halogen lamps, LEDs and lasers.

The goal of this work was to develop a photodiode amplifier optimized for detecting voltage and calcium transients in low-light applications, which include optical monitoring of voltage and Ca_i^{2+} transients in heart cell cultures, neuronal cells, and optogenetic applications.

In Chapter 2 we analyze the required bandwidths for different applications. Using a realistic ionic model of cardiac action potential and Ca_i^{2+} transients we demonstrate that for the majority of applications of optical mapping, one can reduce the bandwidth to as low as 250-300Hz and often to 100Hz. Eliminating excess bandwidth lowers the noise level and allows further increase of the gain of the TIA thereby boosting the sensitivity of fluorescence recordings.

In Chapter 3, we will analyze and compare several photodiode amplifier topologies. In section 3.1we will analyze the noise of the single-resistor topology and in section 3.2 we will analyze the noise of the amplifier with the T-bridge feedback network. We will also look at a variety of AC-coupled amplifiers in 3.3 with the intention of removing the background fluorescence in the 1st stage. One may think that removing the offset in the 1st stage will allow for higher-gain in that stage and therefore higher SNR. We will show, however, that this is not true for TIAs because whatever circuit element is used to draw away the offset current will add noise

of its own. Thus no matter how the offset is removed, the SNR of AC- and DC-coupled topologies is essentially the same.

In Chapter 5 we determine the maximum possible SNR that can be achieved with current technology. The estimates were obtained based on modeling the inherent noise of operational amplifiers, resistors, and photodiodes. We also model the parasitic capacitances in each circuit to determine the limitations on bandwidth, which becomes critical at high gains.

3.4 will contain a fairly extensive survey of photodiode amplifier components. Specifically, an extensive survey of photodiodes and their noise model parameters and various types of low-noise op-amps and their noise model parameters.

In Chapter 6, we describe a physical implementation of a TIA with a gain as high as 10GΩ, which is more than 100 times higher of the conventional TIAs utilized for biological applications [2, 5, 6, 7, 8, 9, 10, 11, 12, 13]. To achieve a required bandwidth we use a field-shunting ground trace, a technique borrowed from high-frequency circuit design.

The prototype amplifier allows the detection of photocurrents as low as 1pA peak (500fA RMS for an action potential). The SNR of the recordings is 10-20 times higher (depending on application) than the SNR achievable with a conventional 100MΩ gain TIAs.

We describe a custom-built device form emulating biological fluorescence which is used not only to generate artificial optical action potentials, but is also used to measure the frequency response of our circuits to ensure that the bandwidth specification is met. In this chapter, we show that the major obstacle to increasing gain is losing bandwidth. We discuss some of the traditional methods for increasing bandwidth by reducing stray capacitance. We then suggest the use of a technique adapted from high-frequency design called field shunting. This technique proves to considerably extend the TIA bandwidth which allows us to achieve even more than the minimum bandwidth required for our application (see Chapter 2).

Chapter 1 Background and Significance

1.1 Optical Monitoring of Voltage and Calcium Transients in Biological Tissues

The procedure optically monitoring voltage and ion transients in tissue involves staining perfused tissue with a voltage-sensitive or ion-sensitive dye, and exciting that dye with a light source. In response to electrophysiological changes, the dye changes its fluorescence and/or absorbance proportionally.

A diagram of a system for recording changes in fluorescence produced by voltage-sensitive dyes and some of the relevant waveforms are shown in Figure 1-1. Here we see that exciting the dye with a light source with narrow spectral width and centered at wavelength λ_{Ex} produces a fluorescence spectrum of longer wavelengths centered at λ_{Em}. The dichroic mirror is used to separate the excitation and emission light while allowing them to travel on the same path. Notice how it reflects the shorter excitation wavelength while passing the longer fluorescent wavelength. In order to do this, its cutoff wavelength is usually chosen to be about half way between λ_{Ex} and λ_{Em} [14, p. 240]. The fluorescence spectrum will shift by an amount proportional to the change in V_m depending on the dye. This spectral shift is then effectively converted to a changing amplitude by an emission filter which is centered at either the positive or negative (shown in figure) slope of the fluorescence spectra. The light is then captured with a photodetector array, usually some type of high-speed camera. The detected signal consists of changes in fluorescence proportional to V_m labeled in the figure as ΔF and a large offset caused by background fluorescence.

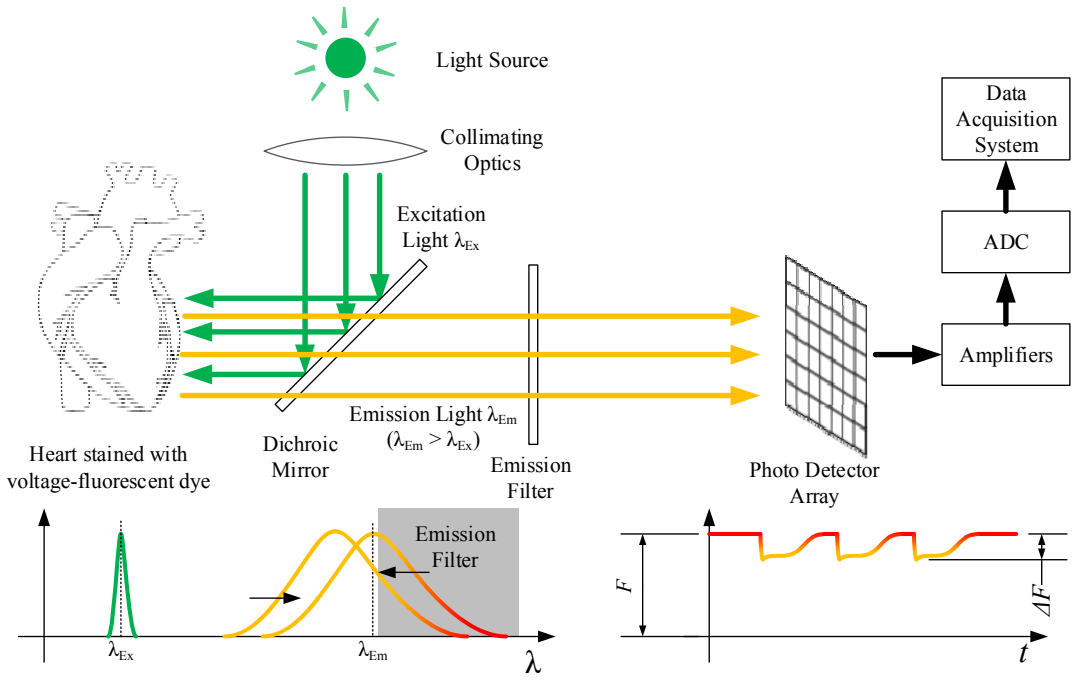

Figure 1-1: Diagram depicting a typical system for detecting voltage-fluorescence signals (top). The spectra of the excitation light source and the corresponding fluorescence are shown in the bottom left corner and the signal after the light has passed through the emission filter is shown in the bottom right corner.

A diagram of a system for monitoring transmittance is shown in Figure 1-2. Similar to fluorescent dyes, absorptive dyes produce a small change in light intensity by shifting spectral absorbance $\mu_a(\lambda)$. The difference is that with an absorptive dye, the light passes through the preparation, usually a cell culture, and changing transmembrane potential causes the dye to absorb more or less light. Thus the excitation wavelength is the same as the wavelength detected by the sensor. The change in detected light intensity corresponding to a change in V_m is termed ΔI and the ratio of changing intensity to total intensity is $\Delta I/I$.

Absorptive dyes are an older technology, so there use began to decrease when fluorescent dyes became available. The problem with these dyes is that $\Delta I/I$ for absorptive dyes tends to be much less than $\Delta F/F$ for voltage-fluorescent dye (see Table 1-1). There is an advantage to absorptive dyes, however, which is that the light collected will undergo less scattering, thus allowing for clearer images.

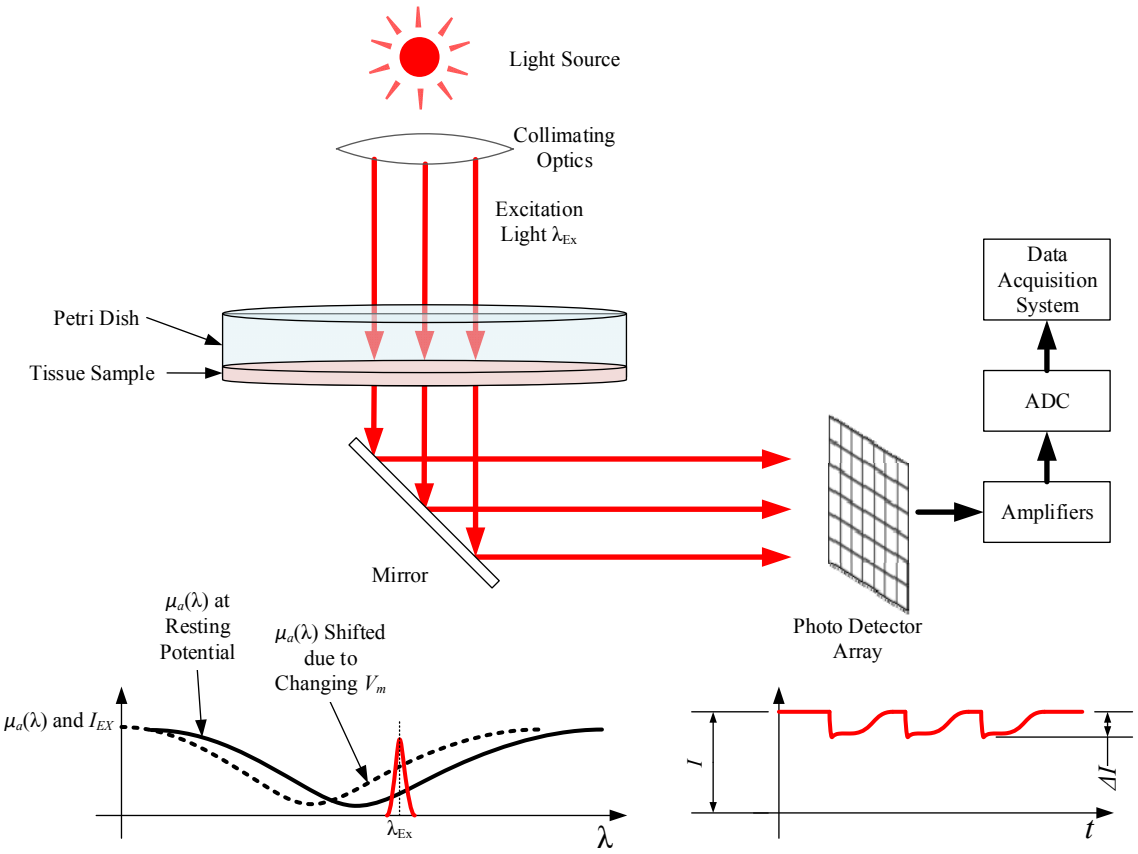

Figure 1-2: Example of a system for monitoring changes in absorbance (top). The changing absorbance spectra is shown in the bottom left corner and the detected signal is shown in the bottom right corner.

Figure 1-3 shows a diagram of a setup for monitoring calcium transients. The difference is that rather than shifting the fluorescence spectrum, Ca_i^{2+}-sensitive dyes change the spectral peak amplitude with changing calcium concentration. An emission filter is now center at the peak which experiences the most fluctuation.

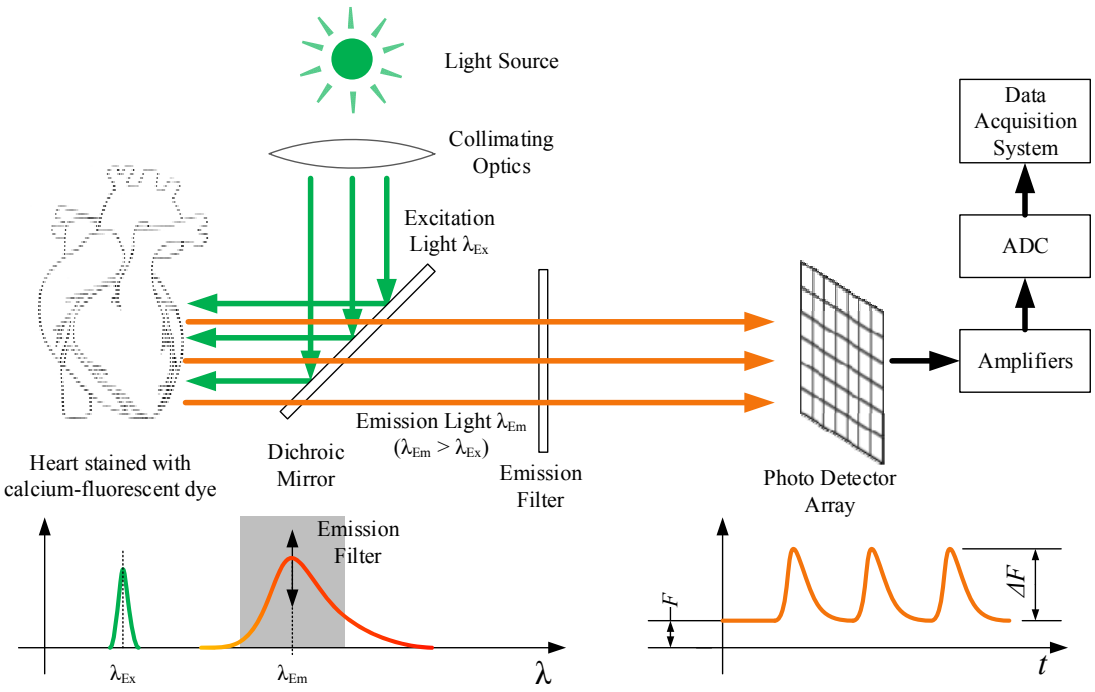

Figure 1-3: Diagram depicting a typical system detecting calcium-fluorescence signals (top). The spectra of the excitation light source and the corresponding fluorescence are shown in the bottom left corner and the signal after the light has passed through the emission filter is shown in the bottom right corner.

Looking at the signal chain of the above 3 systems we can see that the detection limit is set primarily by the noise of the light source, light detection circuit, and acquisition system. As we will show in the following chapters, the noise of the light source and the detection system is small compared to the detection circuit. Hence we will focus our efforts on optimizing that part of the system.

The signals collected by the above 3 systems are characterized by $\Delta F/F$ which is the ratio of changing fluorescence to total fluorescence. The best $\Delta F/F$ for voltage-sensitive dyes is around 15% while the best for calcium-sensitive dyes is around 200%. Table 1-1 shows $\Delta F/F$ for several applications of voltage-fluorescent and calcium-fluorescent dyes.

Table 1-1: $\Delta F/F$ and $\Delta I/I$ for voltage- and calcium-sensitive dyes in different applications.

Dye Type	$\Delta F/F$ or $\Delta I/I$	Tissue Type	Species	Dye Name	λ_{Ex} (nm)	λ_{Em} (nm)	Source
Voltage-Fluorescent	15.0%	Heart Cells	Rat	RH437	550	800	[14]
	1.90%	Brain	Turtle	Di-4-ANEPPS	-	-	[1]
	1%	SCG Neuron Cells	Rat	RH423	520-550	>610nm	[15]
	15.2%	Whole Heart	Pig	Di-4-ANBDQPQ	630-670	>720	[16]
	11.1%		Rat				
	9.10%		Mouse				
	15.0%		Pig	Di-4-ANBDQBS			
	13.9%		Rat				
	10.5%		Mouse				
	8.90%		Pig	Di-4-ANEPPS	480-560	590-690	
	6.80%		Rat				
	2-8.3%	Heart Cells	Rat	DI-8-ANEPPS	>600	<500	[11]
	4.5%	Heart Cells	Rat	RH237	488-513	>650	[2]
Calcium-Fluorescent	2.50%	Brain	Turtle	Ca-Crimson Dextran	-	-	[1]
	26.0%	Whole Heart	Rabbit	Rhod-2 AM	532	>600	[17]
	205%	Heart Cells	Rat	FLUO-3AM	488-513	533-588	[2]
Absorptive	0.10%	Axon	Squid	Merocyanine Dye	-	N/A	[1]
	~0.1%	Brain Stem	Chick	NK2761	688-718		[18]
	~0.01%	Hippocampus Neuron Cells	Rat	RH482	670-730		[19]

Notice that $\Delta F/F$ is heavily dependent on the type of tissue and the type of dye. It is also important to note that for a given application, calcium-fluorescent dye will have a larger $\Delta F/F$ than voltage-sensitive dye. For any type of fluorescence imaging, the $\Delta F/F$ also depends on the emission filter. The cut-off wavelength of which must be carefully chosen to achieve the maximum possible $\Delta F/F$.

1.2 Devices and Circuits for Monitoring Fluorescence

1.2.1 *Devices for Photon Detection*

As of the writing of this work, there are 4 types of devices commonly used for optical monitoring of fluorescent signals. These are PIN (p-type-intrinsic-n-type) photodiodes, avalanche photodiodes, photomultiplier tubes, and CCD/CMOS cameras. In this section we will discuss some aspects of each and select the one that is best for optical monitoring of voltage and calcium transients.

PIN photodiodes are the simplest, most robust, and most cost-effective way to detect photons. Their name derives from their structure which consists of a layer of positive-doped semiconductor (p-type), a layer of intrinsic semiconductor, and a layer of negative-doped semiconductor (n-type). They have been used extensively for fluorescence detection applications both in single-chip arrays and individual photodiode and amplifier combinations [2, 5, 6, 7, 8, 9, 10, 11, 12, 13].

Avalanche photodiodes (APDs) have been used for fluorescence detection, though not as frequently as PIN photodiodes [3]. These devices have an internal gain that is dependent upon their bias voltage. The bias voltage required to produce high gain in the APDs is on the order of 100V, near the edge of where reverse breakdown will occur. Because of this, the APD's temperature and/or bias voltage must be carefully controlled to prevent component failure. The avalanche gain enables APDs to produce higher photocurrents and thus have higher SNR than PIN photodiodes, at least theoretically. However, we will show in section 4.1.2 that in practice it may be difficult to create an APD and amplifier circuit that will offer significant advantages over PIN photodiodes.

The photomultiplier tube (PMT) is one of the oldest electronic photodetectors. It is also one of the few types of vacuum tubes to survive the rapid proliferation of solid state devices. This is likely due to its unparalleled speed and photon-counting capabilities. At the time of the writing of this work, the photomultiplier tube is still in wide use and available in a wide variety of types optimized for different applications. In the study of electrophysiology by means of fluorescent dye, the PMT has been used with various optrodes to detect the weak fluorescent signal produced by calcium-sensitive dyes [20, 21].

Unlike PIN or avalanche photodiodes, the PMT is rather delicate and difficult to work with. Since the gain of photomultiplier tubes is extremely high, they are very susceptible to variations in the high-voltage power supply. If the output stability of a photomultiplier must be maintained within 1%, the power supply stability must be held within 0.1% [22, p. 24]. If exposed to sunlight or extremely intense light (10,000 lux or higher), this may cause unrecoverable damage and must therefore be avoided [22, p. 68]. They are also sensitive to magnetic fields and exhibit some hysteresis under certain operating conditions.

By far the most convenient way to detect small changes in either fluorescence or transmittance in biological applications is by using a scientific camera. These cameras are typically designed to output a high frame rate (~1kHz), sample with high resolution (12-16 bits) and are very sensitive to low light levels. The cameras most commonly used for recording absorbance or fluorescence can be divided into 2 types: CCD and CMOS. The CCD (charge-coupled device) cameras are very sensitive to low light levels and have very good spatial resolution. The CMOS (complementary metal-oxide-semiconductor) cameras use simple amplifiers, usually a single transistor, to amplify the signal before it is sent to the A/D converter.

1.2.2 *Amplifiers for Light Detection*

There exist in the current body of knowledge many different topologies of transimpedance amplifier. When detecting weak optical signals, these topologies must be designed with very high gain. In this section we will give a brief overview of the different amplifier topologies we intend to analyze in this work.

Figure 1-4 shows 2 different TIA topologies, the single-resistor topology (A) and the T-bridge topology (B). While the single-resistor photodiode amplifier topology is the most widely used for detecting low-intensity optical signals from stained tissue [7, 2, 11, 12, 6, 18], it is worth analyzing the performance of the T-bridge topology. Both topologies can achieve high-gain, but because the topology in panel (A) must do so with 1 resistor, its gain is limited to commercially available resistor sizes, which for resistances $> 100\text{M}\Omega$ are seldom available in the standard E96, E24 or even E12 series. The T-bridge offers a possible solution to this problem by using 3 resistors, each with a value less than the total gain, to determine its gain. It also has the advantage of distributing the resistor's parasitic capacitance.

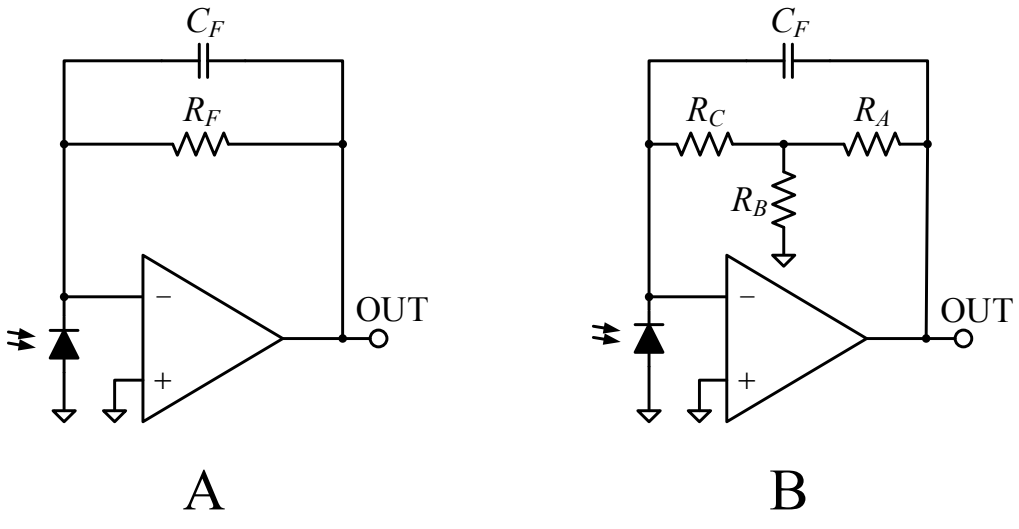

Figure 1-4: TIA with 1 feedback resistor (A) and TIA with T-bridge feedback network (B).

Due to the fact that optical markers used in electrophysiological monitoring applications typically have a large offset, we investigated several topologies designed for offset removal. Figure 1-5 shows 4 such topologies, each with its own method for removing the offset.

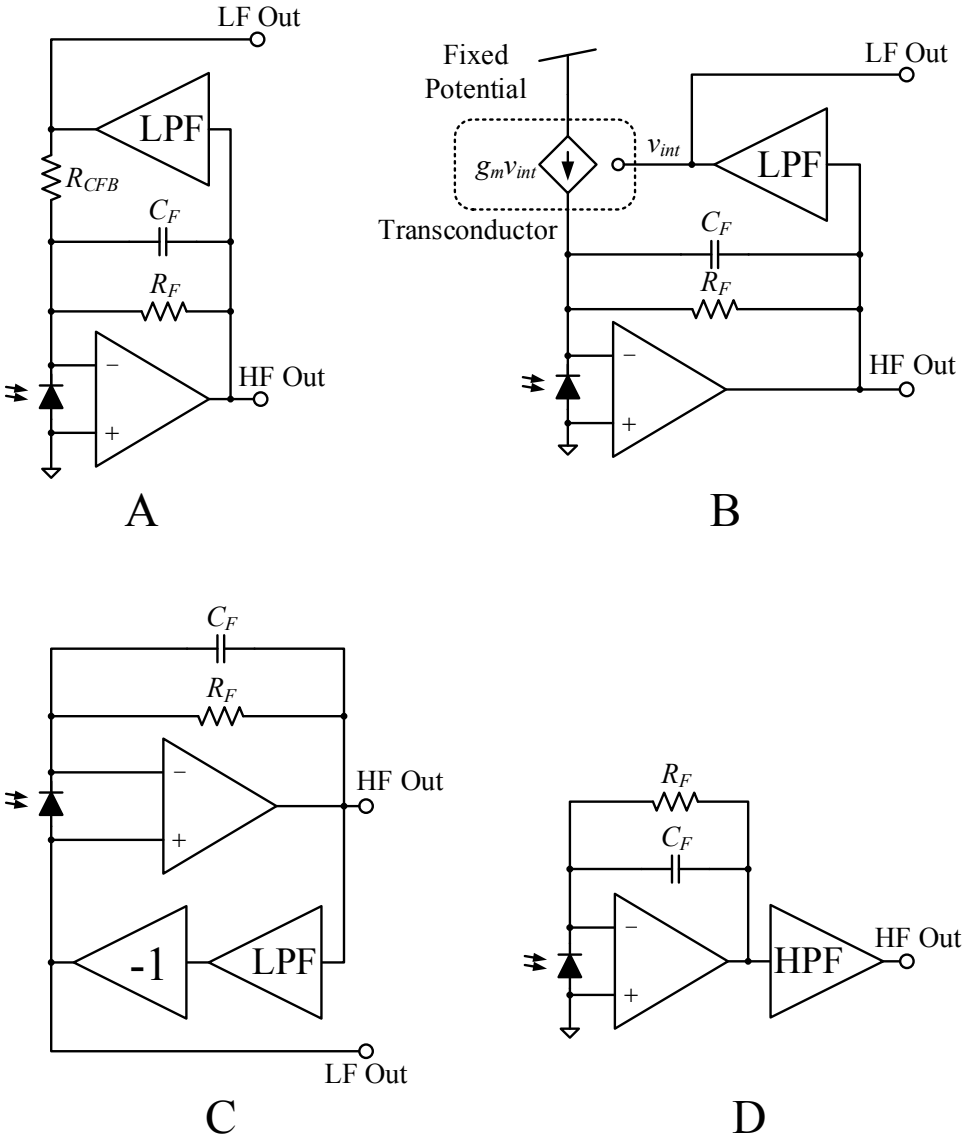

Figure 1-5: AC-coupled transimpedance amplifier topologies. Active current feedback topology for offset cancellation with a resistor (A) and a transconductor (B), offset voltage subtraction topology (C) and 2nd stage offset removal (D). The nodes labeled "HF Out" (high-frequency out) are where the output voltage will be measured after removal of the offset and the nodes labeled "LF Out" (low-frequency out) are where the portion of the removed signal can be measured. Thus no component of the signal is lost (ideally) and the entire collected signal can be reconstructed.

Panels (A) and (B) use a method called active current feedback. This involves isolating the low-frequency component of the signal, converting it to a current, and injecting that current back into the input which causes it to cancel the low-frequency component of the input signal. The topology in panel (A) uses a resistor to convert the voltage output of the low-pass filter (LPF) to a current. Panel (B) uses a transconductor, e.g. a transistor, to accomplish the same thing. Both of these topologies have the advantage of being able to remove an offset of any size independent of supply voltage (within reason). However, the additional circuit elements will add additional noise.

Panel (C) uses a method called offset voltage subtraction. This involves feeding the low-frequency component of the signal back to the noninverting input of an op-amp, which subtracts it from the input signal. The advantage of this topology is that it can remove the offset without adding a significant amount of additional noise (see section 3.3.3); however the size of the offset that it can remove is dependent on the op-amp supply voltage.

Panel (D) is the simplest AC-coupled topology. Unlike the others, the offset is removed in the 2nd stage instead of in the 1st stage using a feedback loop, which makes it unconditionally stable. This topology is also commonly cited in the literature [8, 11, 13].

The topology in Figure 1-6 is called a charge amplifier. It is a type of transimpedance amplifier like the others discussed thus far, except a capacitor rather than a resistor is responsible for the current-to-voltage conversion. The capacitive element in the feedback path is used to accumulate charge. The gain of the circuit is inversely proportional to the feedback capacitance C_F. The particular configuration of the charge amplifier shown here is essentially a continuous-time CCD cell. The forward path contains an integrator and the feedback path provides a continuous current that prevents it from reaching saturation. The 2nd stage is a differentiator to produce a “flat” frequency response in the pass-band.

The charge amp is more commonly used in integrated circuits because it does not require a large feedback resistor ($> 100\text{M}\Omega$), but rather a small feedback capacitor ($< 100\text{pF}$) which makes it more area-efficient. The removal of the feedback resistor may provide an improvement in noise performance and thus sensitivity, so we will investigate this topology to find out.

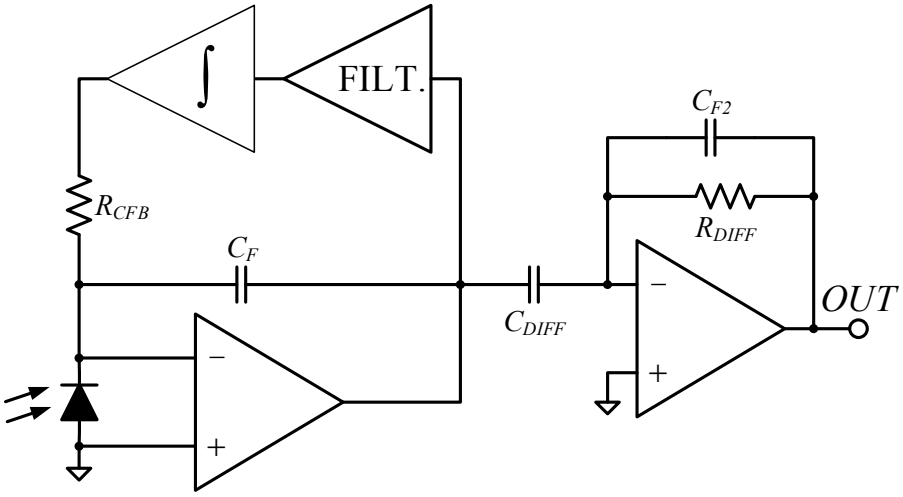

Figure 1-6: Charge amplifier. The forward path of the circuit is an integrator and the feedback path provides offset removal to prevent the integrator from saturating.

The topology shown in Figure 1-7 is an avalanche photodiode amplifier circuit. The topology is the same as the one in Figure 1-4A, but a different photosensitive element is used and it is biased at a high voltage. Though we could also connect APDs to any of the circuit topologies discussed thus far, we will only consider the single-resistor topology because as the analysis in Chapter 3 will show, this topology produces the least amount of circuit noise.

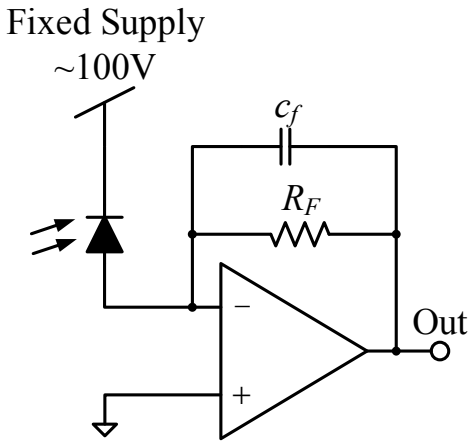

Figure 1-7: Avalanche photodiode amplifier.

1.3 Modeling of Inherent Noise in Devices for optical recordings of voltage and Ca transients

Electrical noise can be subdivided into 2 categories: ***external noise*** or as ***inherent noise***. External noise is generated by an outside source and then somehow couples into the circuit of interest. This coupling may take the form of capacitive coupling which occurs when two circuits are in close proximity of each other, or of electromagnetic interference (EMI) where magnetic fields generated in one circuit induce current in another. Inherent noise results from the random movement of electrons within a conductor [23, p. 213]. Noise of this type can be subdivided into categories such as flicker noise, thermal noise, shot noise, etc. based on its specific cause, frequency content, and statistical nature.

Noise is a purely random signal, the instantaneous value and/or phase cannot be predicted at any time. Because of this, it can only be described in terms of a probability density function. The most common probability density function is Gaussian [24, p. 123]. Figure 1-8 below shows an example of Gaussian noise [25]. Here, the average value of the noise signal corresponds to the center of the bell curve. The root-mean-square (RMS) value of the noise signal corresponds to 1 standard deviation σ from the mean value. The instantaneous noise amplitude is within $\pm 1\sigma$ 68% of the time and within $\pm 3\sigma$ 99.7% of the time [24, p. 124].

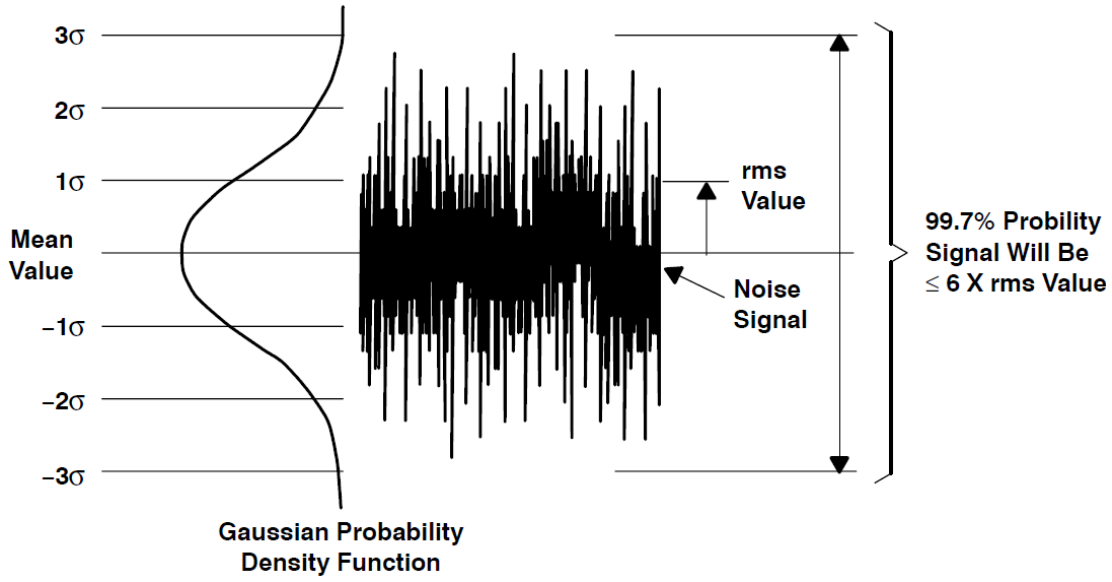

Figure 1-8: Example of white Gaussian noise.

When all inputs are turned off (voltage sources replaced by short circuits and current sources replaced by open circuits), the level of noise in the circuit is called the ***noise floor***, which determines the smallest signal for which the circuit is useful [24, p. 125].

The signal-to-noise ratio SNR is the ratio of the RMS signal to the RMS noise [24, p. 125]:

$$SNR = \frac{RMS\ signal\ voltage}{RMS\ noise\ voltage} \qquad (1-1)$$

If there are multiple sources of noise in a circuit, then the total RMS noise signal is the square root of the sum of the average mean-square values of the individual sources [24, p. 125].

$$v_{n,Total,RMS} = \sqrt{v_{n,1,RMS}^2 + v_{n,2,RMS}^2 + \cdots + v_{n,N,RMS}^2} \qquad (1-2)$$

This relationship means that the worst noise source in the system will tend to dominate the total noise [24, p. 125]. Note that while we regularly sum mean-squared voltages while performing noise analysis, we never sum RMS voltages [23, p. 215].

Noise is typically specified as ***amplitude spectral density*** (ASD), also called ***voltage*** or ***current spectral density*** or ***noise spectral density*** having units of $\mathrm{V}/\sqrt{\mathrm{Hz}}$ or $\mathrm{A}/\sqrt{\mathrm{Hz}}$ or as ***power spectral density*** (PSD) having units of V^2/Hz or A^2/Hz [23, p. 217] [24, p. 126] [26, p. 1] [27, p. 17]. To convert PSD to RMS noise voltage or current, we need to integrate over the part of the spectrum where the noise is present [23, p. 219]:

$$v_{n,RMS} = \sqrt{\int_0^\infty |\psi(f)|^2 df} \qquad (1-3)$$

$$i_{n,RMS} = \sqrt{\int_0^\infty |\xi(f)|^2 df} \qquad (1-4)$$

where $|\psi(f)|^2$ is the PSD of a band-limited voltage noise source and $|\xi(f)|^2$ is the PSD of a band-limited current noise source.

1.3.1 *Noise Equivalent Bandwidth*

When performing noise analysis in the later sections of this work, we will frequently need to calculate integrals like those in equations $(1-3)$ and $(1-4)$. In order to make this task more efficient, we will first calculate the ***noise equivalent bandwidth*** (NEB) [23, pp. 220-222]. This simply means that we will calculate in advance the integrals for commonly encountered transfer function and noise spectra combinations.

For the NEB calculations in this section, we will use either flat spectra or spectra inversely proportional to frequency $(1/f)$ like that of flicker noise. Shown below are 3 examples of the integration.

$$v_n^2 = \int_0^\infty \psi_o^2 |G(f)|^2 df = \psi_o^2 f_{eq} \qquad (1-5)$$

$$i_n^2 = \int_0^\infty \xi_o^2 |G(f)|^2 df = \xi_o^2 f_{eq} \qquad (1-6)$$

$$v_n^2 = \int_0^\infty \frac{FNN^2}{f} |G(f)|^2 df = FNN^2 f_{eq} \qquad (1-7)$$

Where $|G(f)|$ is the magnitude of the system frequency response, ψ_o and ξ_o are the voltage and current noise densities of flat spectra, and FNN is the flicker noise numerator (see section 1.3.3.3 for more detail). In order to avoid having to repeat our equations for voltage and current, the coefficients ψ_o and ξ_o will be set to 1 for this analysis as will FNN.

We will begin with a simple 1st-order low-pass system, the transfer function of which is shown below.

$$G_{LP1}(f) = \frac{1}{1 + jf/f_L} \qquad (1-8)$$

Integration of the magnitude square of the above transfer function yields

$$f_{eq,LP1}^2 = \int_0^\infty |G_{LP1}(f)|^2 df = \int_0^\infty \frac{1}{1 + (f/f_L)^2} df = \frac{\pi}{2} f_L \qquad (1-9)$$

Figure 1-9 (modified from [23]) shows the noise density seen at the output of the 1st –order system for an input that is spectrally flat. From the figure, we can see that the 2 shaded areas are the same. Equation $(1-9)$ shows that total area under the curve is $\frac{\pi}{2} f_L$. Thus the result of the integral would be the same if the curve were simply a

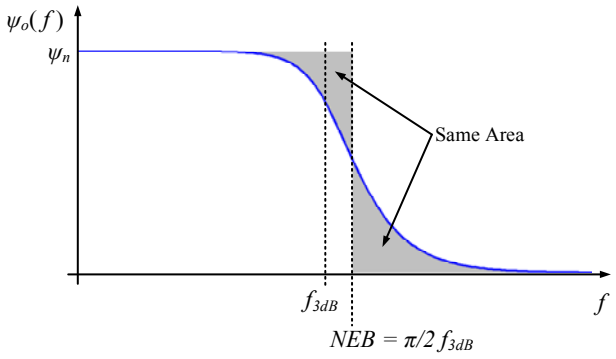

Figure 1-9: NEB for first-order filter frequency response. Notice that the 2 shaded areas are equal. Therefore integrating a flat spectrum up to NEB is equivalent to integrating the transfer function from 0 to ∞.

rectangle from 0 to $\frac{\pi}{2}f_L$.

The equation below is for a band-pass circuit. The parameter f_L is the low-pass cut-off frequency and the parameter f_H is the high-pass cut-off frequency.

$$f_{eq,BP}^2 = \int_0^\infty \frac{(f/f_H)^2}{\left(1 - f^2/(f_H f_L)\right)^2 + f^2(1/f_H + 1/f_L)^2} df = \frac{\pi}{2}\frac{f_L^2}{f_L + f_H} \qquad (1-10)$$

The integral of a 1st-order high-pass transfer function is

$$f_{eq,HP}^2 = \int_0^{f_{co}} \frac{f^2/f_H^2}{1 + f^2/f_H^2} df = \left(1 - \frac{\pi}{4}\right) f_{co} \qquad (1-11)$$

where f_{co} is the cutoff frequency. Obviously, we cannot integrate to $f = \infty$ with a high-pass filter because the result would be infinite.

In many cases, the circuit under analysis may be followed by a 2nd stage consisting of a high-order low-pass filter. If the order of the filter is sufficiently high, it can be approximated by a unit step function in the frequency domain, as shown below.

$$G_{LPF}(f) = u\left(f - \frac{\pi}{2}f_L\right) \qquad (1-12)$$

Here we have chosen the cutoff of this filter to be $\frac{\pi}{2}f_L$ because it will simplify the final NEB expression. For example, if we repeat the integral for the first order low-pass filter with $G_{LPF}(f)$ in the 2nd stage, we get

$$f_{eq,LP1,LPF} = \int_0^\infty |G_{LPF}(f)|^2 |G_{1LP}(f)|^2 df = \int_0^\infty u^2\left(f - \frac{\pi}{2}f_L\right)\frac{1}{1 + (f/f_L)^2} df$$

$$f_{eq,LP1,LPF} = \int_0^{\frac{\pi}{2}f_L} \frac{1}{1 + (f/f_L)^2} df = f_L \qquad (1-13)$$

For a high-pass filter with zero in the transfer function not located at $f = 0$Hz, a sort of modified high-pass filter, the transfer function is defined below. This type of transfer function is commonly associated with noise gain as we will show later on.

$$G_{ng}^2(f) = \frac{1 + f^2/f_z^2}{1 + f^2/f_p^2} \tag{1-14}$$

where f_z is the frequency of the zero and f_p is the frequency of the pole.

Multiplying $(1-14)$ by the high-order low-pass filter $G_{LPF}(f)$ yields

$$f_{eq,ng}^2 = \int_0^\infty |G_{LPF}(f)|^2 |G_{NG}(f)|^2 df = \int_0^\infty u^2\left(f - \frac{\pi}{2} f_{co}\right) \frac{1 + f^2/f_z^2}{1 + f^2/f_p^2} df = \int_0^{\frac{\pi}{2} f_L} \frac{1 + f^2/f_z^2}{1 + f^2/f_p^2} df$$

$$f_{eq,ng}^2 = \frac{f_p}{f_z^2}\left(\frac{\pi}{2} f_L f_p + \tan^{-1}\left(\frac{\pi}{2}\frac{f_L}{f_p}\right)\left(f_z^2 - f_p^2\right)\right) \tag{1-15}$$

If $f_p = f_L$, then

$$f_{eq,ng}^2 = f_L\left(\left(\frac{\pi}{2} - 1\right)\frac{f_L^2}{f_z^2} + 1\right) \tag{1-16}$$

Considering the transfer function in equation $(1-14)$ with a frequency-dependent noise signal, such as flicker noise

$$f_{eq,ng,1/f}^2 = \int_{f_0}^\infty |G_{LPF}(f)||G_{NG}(f)| \frac{1}{f} df = \int_{f_0}^\infty u^2\left(f - \frac{\pi}{2} f_L\right) \frac{1 + f^2/f_z^2}{1 + f^2/f_p^2} \frac{1}{f} df$$

$$= \int_{f_0}^{\frac{\pi}{2} f_L} \frac{1 + f^2/f_z^2}{1 + f^2/f_p^2} \frac{1}{f} df$$

$$f_{eq,ng,1/f}^2 = \ln\left(\frac{\pi}{2}\frac{f_L}{f_0}\right) + \frac{1}{2}\left(\frac{f_p^2}{f_z^2} - 1\right) \ln\left(\frac{\left(\frac{\pi}{2} f_L\right)^2 + f_p^2}{f_0^2 + f_p^2}\right) \tag{1-17}$$

where f_0 is the lower limit of the integral and not 0Hz. This is because of the 1/f term, hence we must choose f_0 to be a very small number such as 10^{-10}Hz as was done in [23].

If $f_p^2 \gg f_0^2$

$$f_{eq,ng,1/f}^2 = \ln\left(\frac{\pi}{2}\frac{f_L}{f_0}\right) + \frac{1}{2}\left(\frac{f_p^2}{f_z^2} - 1\right)\ln\left(1 + \frac{\left(\frac{\pi}{2}f_L\right)^2}{f_p^2}\right) \qquad (1-18)$$

If $f_L = f_p$

$$f_{eq,ng,1/f}^2 = \ln\left(\frac{\pi}{2}\frac{f_L}{f_0}\right) + \frac{\ln\left(1 + \frac{\pi^2}{4}\right)}{2}\left(\frac{f_L^2}{f_z^2} - 1\right) \qquad (1-19)$$

1.3.2 *Types of Noise and Their Sources*

Electrical noise comes in a variety of shapes and colors. This may seem like a strange thing to say, but as we will show in this section, this statement is completely true. Noise sources can have different "shapes" or spectral content in the frequency domain. Most are flat, but some, such as flicker noise, are mostly concentrated at lower frequencies. Physicists and engineers studying electrical noise have also assigned noise sources different "colors." For example, noise that is spectrally flat is called white noise, and noise concentrated at lower frequencies is called pink or red noise depending on the function which best models its spectral content.

The main types of noise are shot noise, thermal noise, flicker noise, burst noise, and avalanche noise. In this section we will briefly discuss the different types, where the come from, and other important characteristics.

1.3.2.1 Shot Noise

When an electron encounters a barrier, such as a pn junction, potential energy begins to build up until it has enough energy to cross that barrier. When an electron has enough potential energy, it is abruptly transformed into kinetic energy as the electron crosses the barrier. As each electron randomly crosses a potential barrier, energy is stored and released as the electrons encounter and then shoot across the barriers. Each electron contributes a little *pop* as its stored energy is released when it crosses the barrier [24, p. 127]. Here are some important facts about shot noise.

- Alternate Names: Schottky Noise or Quantum Noise [24, p. 127]
- Spectral Distribution: Flat [24, p. 128]
- Probability Distribution: Gaussian [24, p. 124]
- Temperature Dependence: None [24, p. 127]
- Current Flow Dependence: $\sqrt{I}$. When current goes to zero, so does shot noise [24, p. 127].
- Color: White [24, p. 133]

The RMS shot noise current and voltage are

$$i_{n,shot} = \sqrt{2qf_{eq}(I_{DC} + 2I_0)} \qquad (1-20)$$

$$v_{n,shot} = kT\sqrt{\frac{2f_{eq}}{qI_{DC}}} \qquad (1-21)$$

Where q is the charge of an electron (1.6×10^{-19} C), f_{eq} is the noise-equivalent bandwidth of the circuit under consideration (Hz), k is Boltzmann's constant (1.38×10^{-23} J/K), I_{DC} is the average forward current (A), and I_0 is the reverse saturation current (A). Note that if the junction is forward biased then $I_0 = 0$.

1.3.2.2 Thermal Noise

Thermal noise is caused by thermal agitation of electrons in a conductor [24, p. 129]. It is present in all electronic devices both passive and active. Here are some important facts about thermal noise:

- Alternate Names: Johnson Noise [24, p. 129]
- Spectral Distribution: Flat [24, p. 128]
- Probability Distribution: Gaussian [24, p. 124]
- Temperature Dependence: $\sqrt{T}$
- Current Flow Dependence: None
- Color: White

The RMS thermal noise voltage and current (below 100MHz) are defined below [24, p. 129].

$$v_{n,T} = \sqrt{4kTRf_{eq}} \qquad (1-22)$$

$$i_{n,T} = \sqrt{\frac{4kT}{R} f_{eq}} \qquad (1-23)$$

Where R is the resistance of the device (Ω).

1.3.2.3 Flicker Noise

Flicker noise is not as well understood as some of the other types of noise. It may be related to imperfections in crystalline structure of semiconductors as better processing can reduce it [24,

p. 130]. It is concentrated at low frequencies. Unlike thermal and shot noise, its probability distribution is not Gaussian [24]. Some important facts about flicker noise are listed below.

- Alternate Names: $1/f$ noise, excess noise [24, pp. 130-131]
- Spectral Distribution: $\propto 1/f$ [24, p. 130]
- Current Flow Dependence: Proportional to current [24, p. 131] [28, p. 7]
- Color: Pink

The RMS voltage and current flicker noise are defined below.

$$v_{n,1/f} = K_v \sqrt{\mathrm{Ln}\left(\frac{f_{max}}{f_{min}}\right)} \qquad (1-24)$$

$$i_{n,1/f} = K_i \sqrt{\mathrm{Ln}\left(\frac{f_{max}}{f_{min}}\right)} \qquad (1-25)$$

Where K_v and K_i are proportionality constants equal to $\psi_{1/f}(f = 1\mathrm{Hz})$ and $\xi_{1/f}(f = 1\mathrm{Hz})$ respectively, f_{max} is the maximum frequency (Hz) which is the upper limit of the integral and f_{min} us the minimum frequency (Hz) which is the lower limit of the integral (see section 1.3.1).

1.3.2.4 Burst Noise

Burst noise is related to imperfections in semiconductor material and heavy ion implants. Modern processing techniques at Texas Instruments has all but eliminated its occurrence [24, p.

131]. It is characterized by high-frequency pulses several times greater than the thermal noise amplitude [24, p. 131]. Below is a list of facts about burst noise.

- Alternate Names: Popcorn noise [24, p. 131] or random telegraph signal (RTS) noise [23, p. 252]
- Spectral Distribution: $\propto 1/f^2$ [24, p. 133]
- Color: Red/Brown [24, p. 133] at high frequencies but white at low frequencies [23, p. 252]

Power spectral density of burst noise current $\mathrm{A}/\sqrt{\mathrm{Hz}}$ is defined below [23, p. 252].

$$i_{n,burst} = \sqrt{\frac{K_{burst} I_{DC}}{1 + \left(\frac{f}{f_{3dB}}\right)^2}} \qquad (1-26)$$

Where K_{burst} is a scaling factor (A/Hz), and f_{3dB} is the point where the noise starts to roll off and is related to the number of pops per second (typically 100Hz).

1.3.2.5 Avalanche Noise

Avalanche noise is created when a pn junction is operated in the reverse breakdown mode. Under the influence of a strong reverse electric field within the junction's depletion region, electrons have enough kinetic energy that, when they collide with atoms of the crystal lattice, additional electron-hole pairs are formed. These collisions produce random current pulses similar to shot noise, but much more intense [24, p. 131]. The magnitude of noise spikes caused by the avalanche effect is difficult to predict due to its dependence on the materials. Zener diodes operating in reverse breakdown exhibit avalanche noise [24, p. 132]. The spectral distribution of avalanche noise is proportional to $1/f^2$ and its color is Red/Brown.

1.3.3 *Device Noise Models*

1.3.3.1 Resistor Noise Models

The dominant noise source in most resistors is thermal noise, though some types do exhibit flicker noise as well. The amount of flicker noise that a resistor generates is dependent upon its construction. Wire wound resistors have the least amount of flicker noise [24, p. 131].

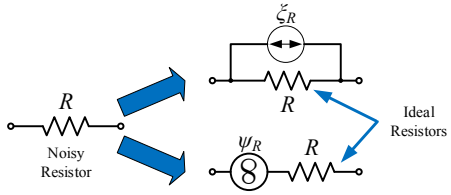

Figure 1-10: Resistor noise models. The noise from a resistor can be modeled as either a current noise source in parallel with an ideal resistor (top) or a voltage noise source in series with an ideal resistor (bottom).

Figure 1-10 shows the most commonly used type of resistor noise model. Here a noisy resistor can be modeled as either a current noise source in parallel with an ideal resistor or a voltage noise source in series with an ideal resistor. The equations for resistor thermal noise density are defined below.

$$\psi_R = \sqrt{4kTR} \qquad (1-27)$$

$$\xi_R = \sqrt{\frac{4kT}{R}} \qquad (1-28)$$

1.3.3.2 Op-Amp Noise Model

Though the noise spectral density of an op-amp is formed by the contribution of many smaller devices, it can be modeled with reasonable accuracy using 2 sources of noise voltage and 2 sources of noise current as shown in Figure 1-11 (modified from [24, p. 137]). Input voltage

noise is *always* represented by a voltage source in series with the non-inverting input [24, p. 137]. It is usually comprised of a thermal noise component and a flicker noise component. Here we have drawn the flicker and thermal noise as 2 separate sources, but they could just as easily be made into 1. The input current noise is *always* represented by current sources from each input to ground [24, p. 137].

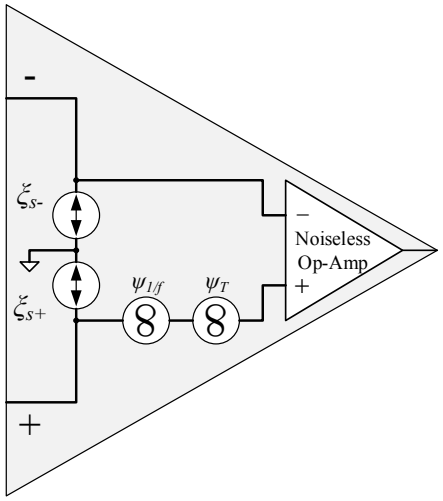

Figure 1-11: Circuit model of noisy op-amp. The model contains 2 current noise sources and 2 voltage noise sources. The sources represent the input-referred noise density.

In order to create a noise model of a particular op-amp, one must first extract certain parameters from the device's datasheet. The specific parameters for modeling op-amp noise are seldom stated in the datasheet, though it is possible to extract the required information from a plot of input voltage noise which usually *is* included.

1.3.3.3 Extracting Op-Amp Noise Model Parameters from a Datasheet

The plot in Figure 1-12 was taken from the OPA140 datasheet. As we can see from Figure 1-12, at lower frequencies flicker noise is dominant and the higher frequencies thermal noise is dominant. The ***noise corner frequency*** f_{nc} is defined as the frequency where thermal noise and flicker noise are equal [24, p. 135]. We can determine this f_{nc} using a graphical technique like the one described in [24, pp. 134-136]. This technique involves tracing a line over the flat portion of the curve where thermal noise is dominant and continuing the line back to the lowest frequency shown (horizontal, red, dashed line shown in Figure 1-12). Then then tracing a line over the slope of the curve where flicker noise is dominant and continuing the line to

estimate the flicker noise at higher frequencies (sloping, red, dashed line shown in Figure 1-12). The intersection of these 2 lines indicates f_{nc}. Now, 2 data points must be read from the plot, one where the flicker noise is dominant (low frequency) and one where the thermal noise is dominant (high frequency). Therefore, the 2 points chosen should meet the following criteria:

$$\text{Low Frequency Point: } |\psi_o(f_{flick})| \text{ where } f_{flick} \ll f_{nc}$$

$$\text{High Frequency Point: } |\psi_o(f_{therm})| \text{ where } f_{therm} \gg f_{nc}$$

By reading the values at the indicated points we can determine the flicker and thermal noise of the device. The general equation for the flicker noise numerator is

$$FNN = \sqrt{\left(|\psi_o(f_{flick})|^2 - |\psi_o(f_{therm})|^2\right) f_{flick}} \qquad (1-29)$$

For our example, this equation becomes

$$FNN = \sqrt{[|\psi_o(0.1)|^2 - |\psi_o(1000)|^2](0.1)} = 14.5\text{nV}$$

The thermal noise is simply

$$\psi_T \approx |\psi_o(f_{therm})| \qquad (1-30)$$

$$\psi_T = 5.1\text{nV}$$

Here we $f_{therm} = 1\text{kHz}$, simply because the value of noise density was specified in the datasheet at 1kHz. In practice, any part of the noise density plot that is spectrally flat will work just as well. The noise voltage $|\psi_o(f = 0.1\text{Hz})|$ could also have been read at a different frequency, so long as it was significantly lower than the noise corner frequency f_{nc}.

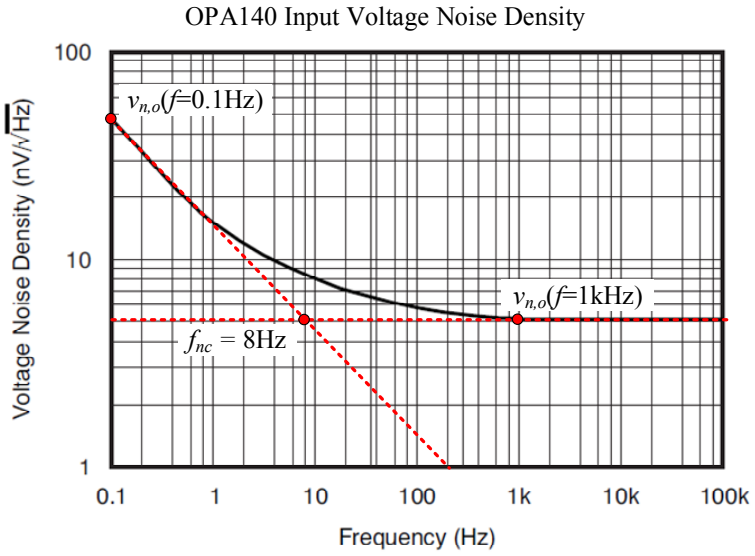

Figure 1-12: Plot of voltage noise density vs. frequency from OPA140 datasheet.

Now we can define our total op-amp noise voltage as

$$|\psi_o(f)| = \sqrt{\frac{FNN^2}{f} + \psi_T^2} \qquad (1-31)$$

Current noise in op-amps can vary much more widely than voltage noise, depending on the input stage. It ranges from around $0.1\text{fA}/\sqrt{\text{Hz}}$ (in JFET electrometer op-amps) to several $\text{pA}/\sqrt{\text{Hz}}$ (in high-speed bipolar op-amps) [26, p. 2]. Though the current noise is not always specified in datasheets, it can be calculated for op-amps with simple BJT or JFET input stages as the shot noise generated by the input bias current [26, pp. 2-3]. The current noise spectral density can therefore be estimated to be

$$\xi_s = \sqrt{2qI_B} \qquad (1-32)$$

Note that this approximation will not work for bias-compensated or current-feedback op-amps [26, pp. 2-3]. It should also be mentioned that the noise corner frequency f_{nc} may be different for an op-amp's voltage noise and current noise [25, p. 5].

A comparison between equation $(1-32)$, the PSPICE model provided by Texas Instruments, and the measured noise density given in the datasheet (digitized using PlotDigitizer software) is shown in Figure 1-13A. The OPA140 PSPICE model was downloaded from http://www.ti.com/product/OPA140/toolssoftware. The circuit used to extract the noise density curve is shown in Figure 1-13B.

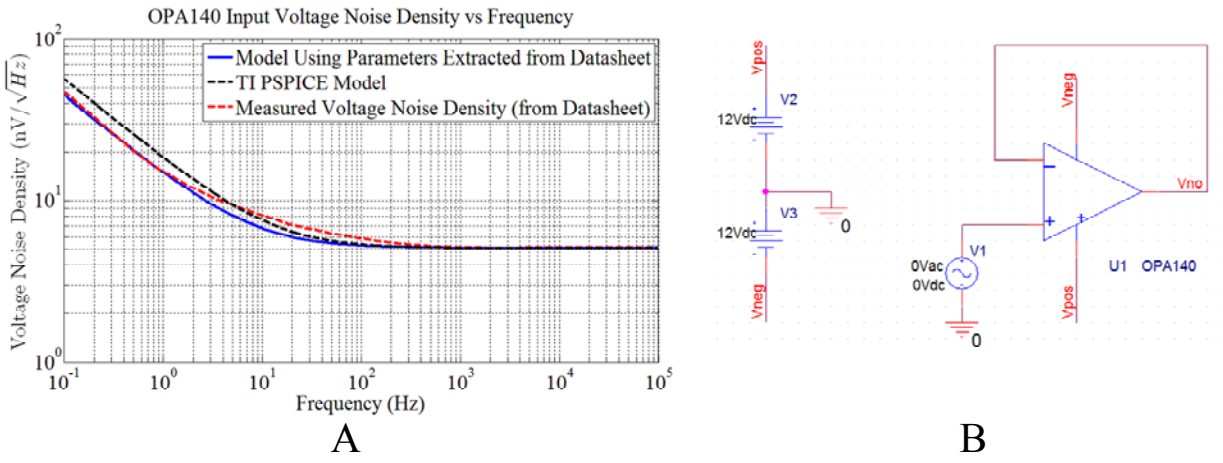

Figure 1-13: Comparison of noise models (A) and schematic of test circuit for the OPA140 PSPICE model (B).

From Figure 1-13A we can see that all of the models are in close agreement. It should be noted that the only difference between the TI PSPICE model and the model based on the parameters from the datasheet is that the TI PSPICE model uses $FNN = 17.7\text{nV}$.

If a PSPICE model is not available for download from the manufacturer, one can be created using simple building blocks. Figure 1-14B shows a schematic of a noisy op-amp created with PSPICE that can be used to simulate op-amp flicker, thermal, and input current shot noise. The flicker noise source consists of a resistor and a frequency response table, the latter produces the -10dB/dec (-3dB/octave) slope that corresponds to the spectral content of flicker noise. The thermal noise source is simply a resistor, the noise from which is added to the flicker noise. The

total noise is then added to the non-inverting input of a noiseless op-amp. The resistances required to produce the desired effect can be calculated as

$$R_{1/f} = \frac{FNN^2}{4kT} \qquad (1-33)$$

$$R_T = \frac{\psi_T^2}{4kT} \qquad (1-34)$$

$$R_{s+} = \frac{\xi_{s+}^2}{4kT} \qquad (1-35)$$

$$R_{s-} = \frac{\xi_{s-}^2}{4kT} \qquad (1-36)$$

Figure 1-14A shows a comparison of the calculated noise using equation $(1-32)$ and the noise from the simulation done in PSPICE.

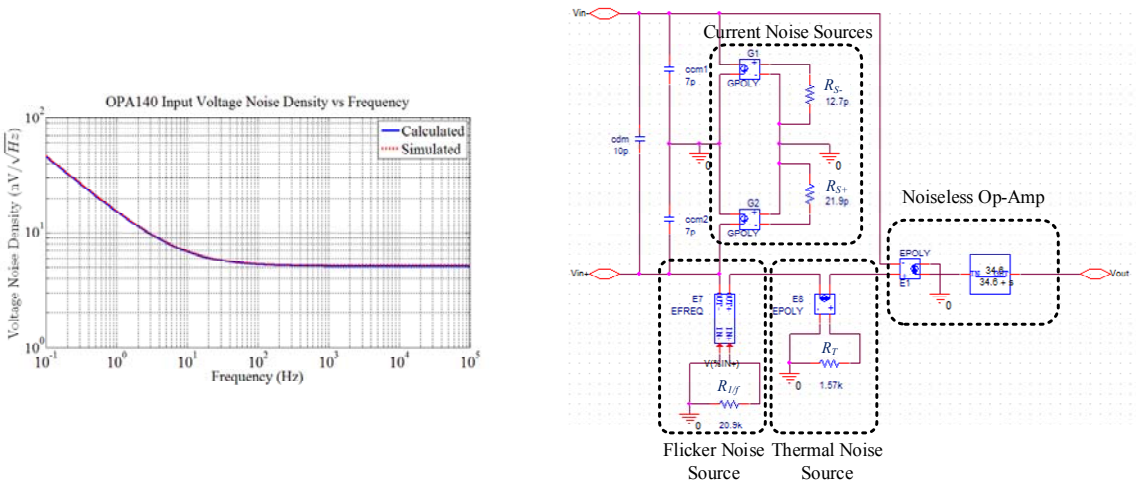

Figure 1-14: Comparison of simulated and calculated op-amp noise (A) and schematic of noisy op-amp (B).

1.4 Noise of Photodetectors and Light-Sources

1.4.1 *Noise Considerations for Biasing Photodiodes*

There are two ways to bias a photodiode: photovoltaic mode and photoconductive mode. When the bias voltage is 0V, the photodiode is said to be in photovoltaic mode. When there is a non-zero bias voltage, it is in photoconductive mode. Figure 1-15 shows an example a photodiode biased in photovoltaic mode (left) and one biased in photoconductive mode (right).

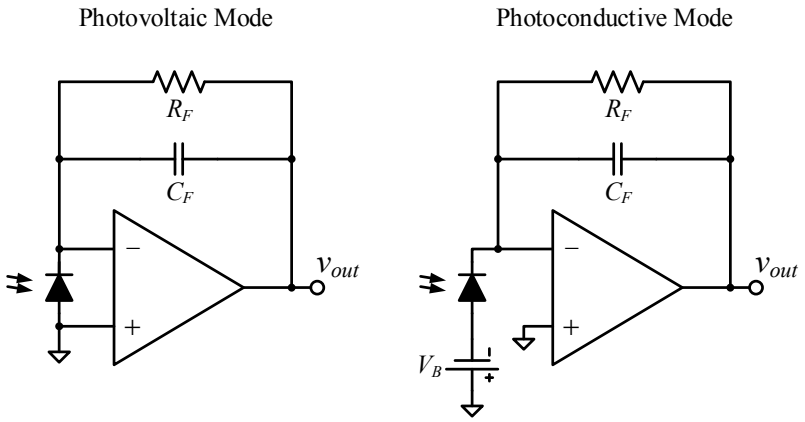

Figure 1-15: Simple op-amp-based photodiode amplifiers with photodiodes biased in photovoltaic mode (left) and photoconductive mode (right).

Which biasing scheme is chosen for a design is determined by the applications. Typically, photovoltaic mode is used when low noise is more important than speed and photoconductive mode is chosen when speed is more important [28]. The reasons for this are discussed in the next section.

1.4.2 *Photodiode Models*

Photodiodes are in general non-linear devices. They can, however, be modeled as linear over a small range of signals. This is the so-called small signal model also used to model transistors and other nonlinear devices as linear circuit models valid over a small range of currents and/or voltages. Figure 1-16 shows a commonly used photodiode model [29, 28, 30]. The dependent current source i_p represents photocurrent and is proportional to the amount of incident light. D_1 is an ideal diode, r_{sh} is the shunt resistance of the diode and c_j is its junction capacitance. The series resistance R_s arises from the resistance of the contacts and the resistance of the undepleted silicon and is typically and is typically on the order of 10 to 1kΩ [29].

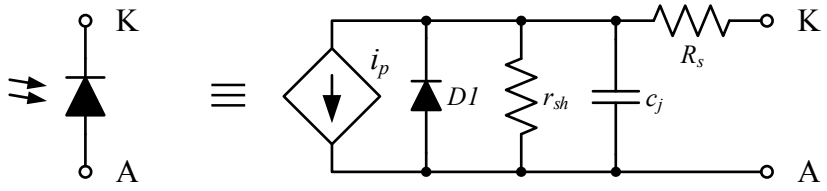

Figure 1-16: Photodiode (left) and equivalent circuit model (right).

The shunt resistance is of critical importance because it is used to calculate the photodiode's thermal noise. It is defined as the slope of the current-voltage curve of the photodiode at the origin, i.e. $V = 0$ in darkness. Experimentally it is measured by applying $\pm 10\text{mV}$, measuring the current and calculating the resistance [29]. This range is chosen because the dark current is approximately linear from -10mV to $+10\text{mV}$ [30]. The equation for shunt resistance is shown below.

$$r_{sh} = \frac{10\text{mV}}{I_D} \qquad (1-37)$$

where I_D is the dark current at 10mV. The value of r_{sh} is reported to range from $\sim 10\text{M}\Omega$ to $\sim 1\text{G}\Omega$ [29], but as we will show in 3.4, the upper limit is closer to $100\text{G}\Omega$.

The junction capacitance c_j is also a nonlinear function of voltage. It will decrease exponentially with increasing bias voltage. The bias voltage is typically high for applications where speed is more important than SNR.

1.4.3 *Photodiode Spectral Response*

Photodiodes respond to incident light differently depending on their composition. Silicon (Si) photodiodes are optimal over the range of visible light and near infrared. Diodes made from Indium Gallium Arsenide (InGaAs) and those made from Germanium are better suited for longer wavelengths, i.e. above 1000nm. The photodiode's response to incident light as a function of wavelength is called the responsivity $R(\lambda)$ and is typically given in units of A/W. It is related to the quantum efficiency η of the device by the equation shown below.

$$\eta = 10^9 \frac{hcR(\lambda)}{q\lambda} = \frac{1240\, R(\lambda)}{\lambda} \qquad (1-38)$$

where $h = 6.63 \times 10^{-34}\text{Js}$ is Planck's constant, $c = 3 \times 10^8 \text{m/s}$ is the speed of light, $R(\lambda)$ is given in A/W and λ is in nm [29].

1.4.4 *PIN Photodiode Noise Sources and Performance Metrics*

The dominant noise source in a photodiode depends on the method of biasing. In photovoltaic mode, the thermal noise generated by the shunt resistance is the dominant source. In

photoconductive mode, the shot noise from dark current is the dominant source. The noise current generated by the shunt resistance is defined below in $\mathrm{A}/\sqrt{\mathrm{Hz}}$.

$$\xi_{rsh} = \sqrt{\frac{4kT}{r_{sh}}} \qquad (1-39)$$

Notice that this is the same equation to determine thermal noise generated by a resistor. To determine the noise at the output of a transimpedance amplifier, this current is multiplied by the feedback resistance.

It is important to note that the approximation of shunt resistance only holds if the photodiode amplifier is biased in photovoltaic mode, where the bias voltage across the diode is 0V. Increasing the bias voltage will cause the resistance of the diode to change as a nonlinear function of voltage. In the case of non-zero bias voltage, the shot noise from the leakage current will typically become dominant over the thermal noise of the device. The shot noise is defined below in units of $A/\sqrt{Hz}$.

$$\xi_{leak} = \sqrt{2qI_D} \qquad (1-40)$$

The lower limit of light detection for a photodiode is expressed as the intensity of incident light required to generate a current equal to the noise current, ξ_{eq}. Essentially this is the amount of input power for which the noise-to-signal ratio is 1. This limit is referred to as ***noise equivalent power***, and is defined as [28, p. 7] [29, p. 2]

$$NEP = \xi_{eq}/R(\lambda_{peak}) \qquad (1-41)$$

where $R(\lambda_{peak})$ is the peak responsivity. Values of NEP range from $\sim 1\mathrm{fW}/\sqrt{\mathrm{Hz}}$ for small-area, low-noise silicon photodiodes to $\sim 1\mathrm{pW}/\sqrt{\mathrm{Hz}}$ for large area photodiodes. The *NEP* is commonly provided in photodiode datasheets, usually at some bias voltage, and can be used to calculate the

noise current simply by rearranging the above equation. This is very useful when the shunt resistance is not specified or when the photodiode is to be operated in photoconductive mode. Occasionally the *NEP* is specified at 0V bias, in which case the corresponding current noise should be about the same as the thermal noise current generated by the shunt resistance. Such is the case for the S2281 series and the S2386 series photodiodes from Hamamatsu. Any difference in the two noise currents (only when the bias voltage is 0) is likely due to the presence of flicker noise or shot noise from leakage current.

Another metric of photodiode noise performance is the detection capability or ***detectivity***, D. Detectivity is the inverse of the NEP, or

$$D = \frac{1}{NEP} = \frac{R(\lambda_{peak})}{\xi_{eq}} \qquad (1-42)$$

where the resulting units of D are $\sqrt{\text{Hz}}/\text{W}$ [28]. This is essentially the amount of input power for which the signal-to-noise ratio is 1. Since noise is proportional to the square root of the photosensitive area, the smaller the photosensitive area A_D, the better the apparent NEP and detectivity. The ***specific detectivity*** D^* takes account of this factor and produces a figure of merit which is area-independent. By definition:

$$D^* = D\sqrt{A_D} \qquad (1-43)$$

where D^* has units of $\text{cm}\sqrt{\text{Hz}}/\text{W}$. Values of D^* range from $10^{11}\text{cm}\sqrt{\text{Hz}}/\text{W}$ to $10^{13}\text{cm}\sqrt{\text{Hz}}/\text{W}$.

1.4.5 *Avalanche Photodiodes*

Avalanche photodiodes APDs have an internal gain that multiplies the inherent photocurrent. This is achieved by biasing the diode near its breakdown voltage. It can be described by the equation below.

$$i_{p,APD} = Mi_{p0} \qquad (1-44)$$

where i_{p0} is the inherent photocurrent with no bias, M is the avalanche gain, and $i_{p,APD}$ is the resulting photocurrent produced by the avalanche photodiode. Internally, the multiplication of photocurrent occurs by way of a chain reaction. When a photon strikes the diode surface and generates an electron-hole pair, the freed carriers are accelerated by the high bias voltage and collide with atoms in the lattice. This collision frees more carriers which are also accelerated by the bias voltage, and so on. The value of M ranges from 50 to 1000 for silicon APDS and is limited to 10 to 40 for germanium and InGaAs APDs [31].

The noise in an APD is typically dominated by shot noise, either from dark leakage current or photocurrent. The leakage current in an APD has 2 components: the ***surface leakage current*** I_{DS} and the ***bulk leakage current*** I_{DB} which is multiplied by the avalanche gain. Thus the total leakage current can be defined as [32]

$$I_D = I_{DS} + MI_{DB} \qquad (1-45)$$

The total dark current shot noise density is then

$$\xi_{dcs} = \sqrt{2q(I_{DS} + M^2 F I_{DB})} \qquad (1-46)$$

where F is the ***excess noise factor***. In many cases I_{DS} and I_{DB} are not specified separately in the APD's datasheet. In these situations, the total dark current I_D at a particular gain M is given instead. The above equation then becomes

$$\xi_{dcs} = \sqrt{2qI_DF} \tag{1-47}$$

The noise density in illuminated conditions is

$$\xi_{shot} = \sqrt{2q\left(I_{DS} + M^2F\left(I_{DB} + \overline{\iota_{p,APD}}\right)\right)} \tag{1-48}$$

or alternatively,

$$\xi_{shot} = \sqrt{2q\left(I_D + M^2\overline{\iota_{p,APD}}\right)F} \tag{1-49}$$

where $\overline{\iota_{p,APD}}$ is the average photocurrent. All avalanche photodiodes generate excess noise due to the statistical nature of the avalanche process. It can be defined as

$$F = M^x \tag{1-50}$$

where x is an empirically derived parameter often given in datasheets [32].

1.4.6 *Photomultiplier Tubes*

Like the avalanche photodiode, the photomultiplier tube has an internal amplification. The gain of PMTs is typically higher than that of APDs ($\sim 10^6$) though the quantum efficiency is typically lower (<50%) [22]. Light enters the PMT through the ***photocathode*** where the incident photons are converted to electrons. Then the number of electrons is multiplied by internal secondary emission electrodes called ***dynodes***. Finally, the increased flow of electrons strikes the ***anode*** where it exits the device as an output current.

Figure 1-17 shows a quasi-schematic view of a PMT with N dynode stages (d_1 through d_N). When an electron strikes the first dynode stage d_1 multiple electrons are released through secondary emission. The ratio of secondary electrons to incident electrons is the ***secondary emission ratio*** δ [22, p. 17]. Each interdynode space characterized by a collection efficiency α. The secondary emission coefficient δ_i of the i^{th} dynode and the collection coefficient α_{i-1} of the space that precedes it are both increasing functions of the voltage $V_{i-1} - V_i$ between the dynodes d_i and d_{i-1} (the rate increase being faster for δ_i than for α_{i-1} [33, pp. 1-12]. The product of α_{i-1} and δ_i varies as a power of the applied voltage:

$$\alpha_{i-1}\delta_i = a_i(V_{i-1} - V_i)^k$$

Where a is a constant and k is determined by the structure and material of the dynode and has a value of 0.65-0.75 [33, pp. 1-12].

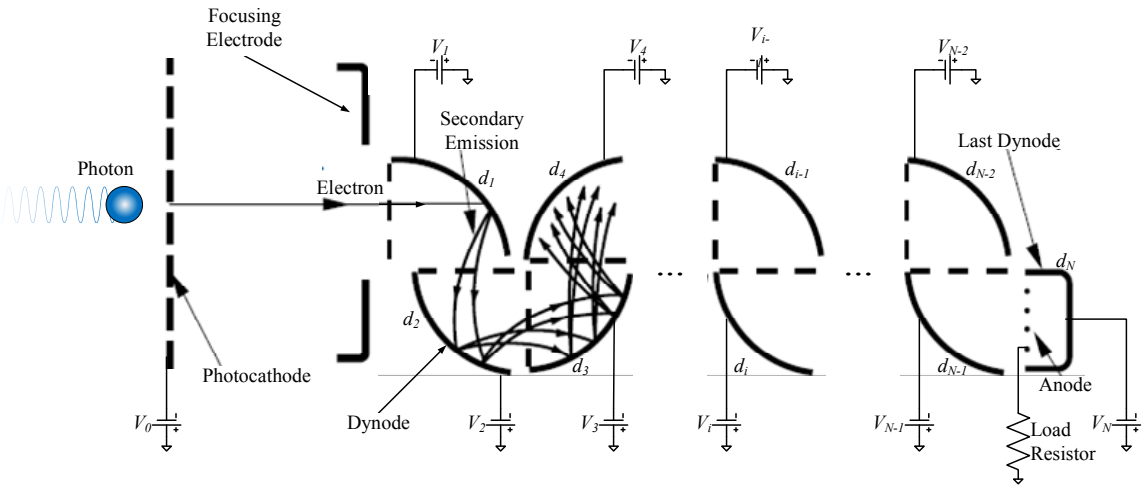

Figure 1-17: Quasi-schematic view of a photomultiplier tube containing *N* dynode stages.

The gain of each stage is then

$$g_i = \alpha_i\delta_i$$

Making the total gain μ of the multiplier

$$\mu = \prod_{i=1}^{N} g_i$$

Where *N* is the total number of stages [33, pp. 1-12].

The ***noise figure*** *F* is the noise that is produced in the multiplication process. The *F* indicates how much SNR degrades from input to output [22, p. 73]. The *F* is defined as

$$F = \frac{(S/N)_{in}^2}{(S/N)_{out}^2}$$

Where $(S/N)_{in}$ is the SNR of the input and $(S/N)_{out}$ is the SNR at the output. For a photomultiplier tube having N dynode stages, *F* from the cascade multiplication process is given by [22, p. 73]

$$F = 1 + \frac{1}{\delta_1} + \frac{1}{\delta_1 \delta_2} + \cdots + \frac{1}{\delta_1 \delta_2 \ldots \delta_N}$$

Where $\delta_1, \delta_2, \ldots, \delta_N$ are the secondary emission ratios of each dynode stage. If the secondary emission ratio of each stage is the same, i.e. $\delta_1, \delta_2, \ldots, \delta_N = \delta$, then

$$F \approx \frac{\delta}{\delta - 1}$$

The shot noise produced by signal current is then

$$\xi_{\ell s} = \mu \sqrt{2q\overline{\iota_{p,K}}\alpha F}$$

Where μ is the gain, q is the charge of an electron, $\overline{\iota_{p,K}}$ is the cathode current, and α is the ***collection efficiency***. The signal current is defined as

$$i_{p,A} = \mu\alpha i_{p,K}$$

The shot noise produced by dark current can be described in terms of the anode current or the cathode current. The shot noise produced by the ***cathode-equivalent dark current*** I_{KD} is

$$\xi_{KD} = \mu\sqrt{2qI_{KD}\alpha F}$$

and ***anode-equivalent dark current*** I_{AD} is

$$\xi_{AD} = \sqrt{2qI_{AD}\alpha F}$$

In terms of cathode-equivalent dark current, the SNR is

$$SNR = \frac{\alpha\widetilde{i_{p,K}}}{\sqrt{2q\left(\overline{i_{p,K}} + I_{KD}\right)\alpha F f_{eq}}}$$

and in terms of the anode-equivalent dark current it is

$$SNR = \frac{\mu\alpha\widetilde{i_{p,K}}}{\sqrt{2q\left(\mu^2\overline{i_{p,K}} + I_{AD}\right)\alpha F f_{eq}}}$$

where f_{eq} is the noise equivalent bandwidth (Hz). To make the above equations a little easier to manage, certain assumptions can be made. For example, in most cases it can be assumed that $\alpha = 1$. It may also be assumed that $\delta = 6$ which is a typical secondary emission ratio, making $F \approx 1.2$ [22, p. 74].

Even though their quantum efficiency is low, PMTs are actually pretty good at detecting weak optical signals. Parasitic capacitance around the feedback resistor is a major limiting factor for the bandwidth of photodiode amplifiers. Yet there is no alternative because the photodiode cannot drive a significant load on its own. The PMT, however, produces so much current that it can drive low-resistance loads without an amplifier.

1.4.7 *Cameras for Fluorescence Detection*

As stated in section 1.2.1, cameras used for detecting fluorescence can be divided into 2 types: CCD and CMOS. To illustrate the difference between CMOS and CCD cameras a simplified schematic of the pixels and read circuitry is shown in Figure 1-18, taken from [34, p. 91]. Here we can see that the chief difference is that CMOS cameras have an in-pixel amplifier whereas CCD cameras do not. Thus CMOS sensors are also called ***active pixel sensors*** (APS) and CCD sensors are called ***passive pixel sensors*** (PPS).

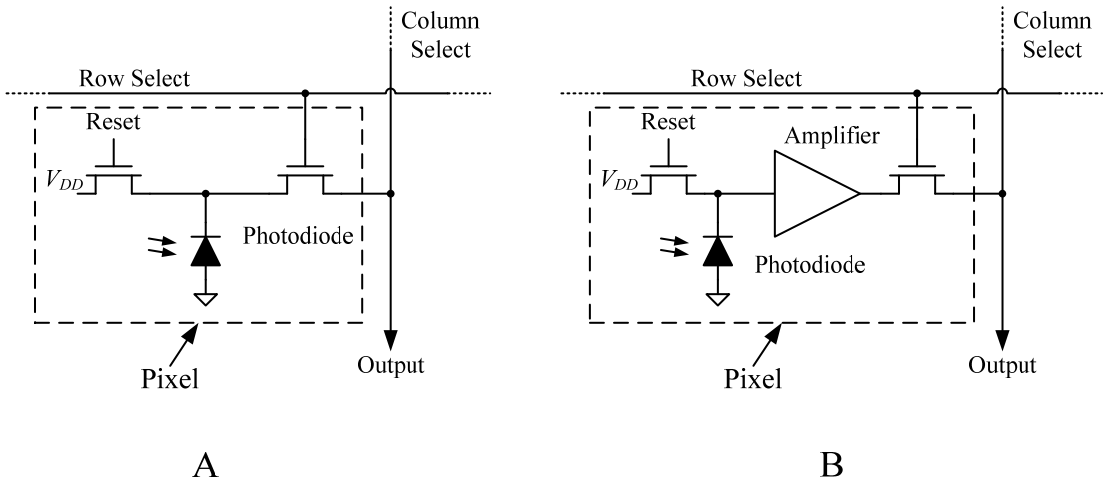

Figure 1-18: Simplified schematic of a CCD pixel (A) and a CMOS pixel (B).

In recent decades the CCD camera has become efficient enough to capture fluorescent signals tissues stained with voltage- or calcium-fluorescent dye [16, 17, 35]. This is due to improvements in both speed and sensitivity. As with all electronic devices, however, there are several sources of noise in CCD cameras that limit their performance. These sources include the shot noise from the photocurrent, the shot noise from the dark current, and the read noise. A commonly used equation for the SNR of a CCD camera incorporates these as shown below [36].

$$SNR_{CCD} = \frac{P\eta t_{int}}{\sqrt{(P+B)\eta t_{int} + Dt_{int} + N_r^2}}$$

where P is the optical power in photons/pixel/s, η is the quantum efficiency of the pixel, t_{int} is the integration time, B is the background light in photons/pixel/s, D is the dark noise in electrons/pixel/s or e^-/pixel/s, and N_r is the read noise in e^-/pixel/s. Note that aside from the read noise, all other sources of noise or signal must be multiplied by t_{int}. This is because the current generated from the photoelectric effect initiated by light hitting the pixel, charges a capacitor thus integrating the input signal over time t_{int}. The amount of charge that this capacitor can hold is called the ***well size*** and is typically given in electrons.

1.4.8 *Light Source Noise*

The light source used to illuminate the tissue under study may prove a significant factor in determining the lower limit of signal detection. Some of the most commonly used light sources for optical mapping are tungsten-halogen lamps, arc lamps such as xenon lamps, mercury lamps, or mercury/xenon lamps, LEDs, and lasers.

Tungsten-halogen lamps have been very popular in the past because they are cheap, produce little noise, and are spectrally flat over the visible range. This spectral flatness allows the user to change the excitation wavelength by simply changing the excitation filter [14]. The noise produced by a tungsten halogen lamp relative to the total output intensity, $\Delta I/I$, is in the range of 0.01-0.04% [37].

Arc lamps are typically used when higher light intensity is required. The price of the increased light intensity is increased noise. Part of this comes from arc wander, where the path of current through the medium may change. Mercury arc lamps have been reported to fluctuate by

anywhere from 0.1% to 3% during arc wander. Arc lamps are known to go through so called quiet and noisy periods. The noisy periods (periods of significant arc wander) can last for several minutes and tend to increase in frequency of occurrence with age. Optical feedback can help to minimize the fluctuation of light intensity. This is achieved by using the signal from an optical sensor such as a photodiode to regulate the current through the lamp. Feedback has been shown to reduce the fluctuation in intensity to around 0.02% [15].

LEDs have gained popularity in recent years as an efficient, low cost alternative to tungsten-halogen and arc lamps [38, 39, 5]. Their higher efficiency and narrow spectrum allow more of the input power to be converted to light of the wavelength needed. Whereas with tungsten-halogen lamps most of the input power is turned into heat, then most of the light that is generated will be blocked by the excitation filter which will allow only a small range of wavelengths to pass through to the prep. The noise of LEDs is also significantly lower than that of tungsten-halogen lamps, specifically $\Delta I/I$ is around 0.002% [37].

Lasers are capable of producing a great amount of light output with a very narrow spectrum. Like LEDs, lasers too have gained popularity in recent years [35, 17] but are less common because of the associated increase in cost. Lasers tend to be very stable and there are currently many companies offering lasers with less than 1% variation in output power, typically measured over 4 hours or more and with output power of up to 20W. This is typically the way the spec is given by the manufacturer, but one must keep in mind that for optical mapping experiments, recording time will be much shorter and therefore the amount of variation captured as noise should be considerably less.

Chapter 2 Estimation of Bandwidth Requirements for Voltage and Calcium Transient Optical Signals

In optical mapping applications the bandwidth range is usually between 300Hz and 3KHz [2, 3, 15, 11]. Although using a broader bandwidth would cause less signal distortion, for low light applications were SNR is relatively small, one may prefer to choose the narrowest bandwidth that application allows. Considering that the noise floor of a circuit is proportional to the square root of its bandwidth $\left(v_n \propto \sqrt{B}\right)$, removing the excess bandwidth could be highly beneficial.

2.1 Computational Modeling of Voltage and Calcium Transients

The model used for the purkinje fiber simulation was taken from [40] . The equations were not modified and the specified initial conditions and parameters were used. The simulation was for a single cell and the equations were solved using a finite difference approximation with a time-step of 1μs. No external stimulus was applied and the cell was allowed to beat on its own.

The simulated action potentials and Ca_i^{2+}-transients were passed through a simulated 1st–order low-pass filter using PSPICE circuit simulation software. The effects of filtering on the output were characterized in the range of cut-off frequencies from 100Hz to 10kHz for the action potential and 1Hz to 100Hz for the calcium transients. The changes in action potential duration (APD_{50}) and the upstroke delay were evaluated at 50% of the maximum voltage level. The rise time was measured as the time for the upstroke to go from 10% of its maximum to 90% of its

maximum. The error of the peak amplitude of the calcium transient was evaluated as the difference between the input peak and the output peak amplitude.

2.2 Quantifying Linear Distortion as a Function of Cutoff Frequency

To determine what the real requirements are for recordings of cardiac action potentials and Ca_i^{2+} transients we used a realistic computer model of the action potential in cardiac Purkinje fiber. The selection was motivated by the fact that the action potential of the purkinje fiber has the fastest upstroke and broadest plateau thus giving it the broadest frequency content. Using this model we estimated how much the action potential and intracellular Ca_i^{2+} transients are distorted after passing through a 1st–order low-pass filter.

Figure 2-1 shows the effect of linear distortion on different action potential characteristics. The effects of filtering on the output were characterized from cut-off frequencies from 100Hz to 10kHz. Panel A shows a comparison of the input and filtered output (Top) and the residual or difference between input and output (Bottom) for a cutoff frequency of 300Hz. One can see that the shape of the action potential is well preserved except for the upstroke which shows a noticeable residual.

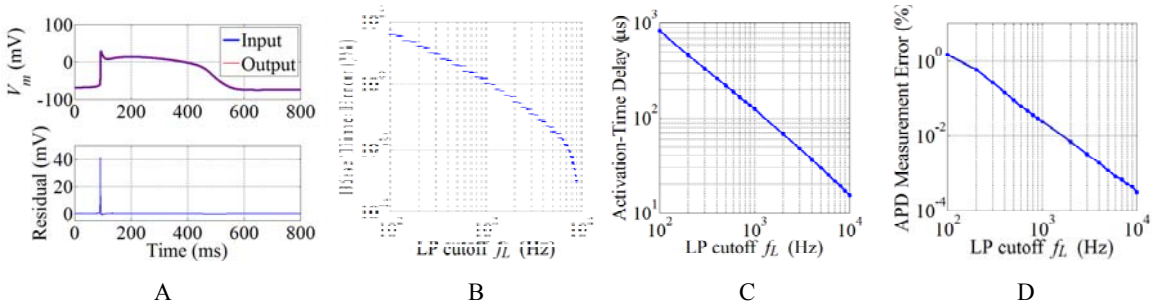

Figure 2-1: Plots showing the effects of linear distortion from a 1st-order low-pass filter on action potentials from a purkinje fiber. The action potential and the filter output at 300Hz cut-off (Top A) and the residual (Bottom A). The percent error of the rise-time (B), the percent error in the APD measurement (C), and the activation- time delay (D).

Figure 2-1B shows the error for rise time as a function of cutoff frequency. As f_L increases the error becomes smaller. At 300Hz the error is less than 10%. The error in APD (Figure 2-1C) shows a similar trend, but the errors are much smaller. At cutoff frequencies as low as 100Hz the error is only about 1.5% and at 300Hz it is about 0.28%. Figure 2-1D shows the activation time error (the parameter used for construction of so-called activation maps). At 300Hz, the error is about 340μs.

It is worth noting the error in the rise time and the activation time have practically no impact on the measurements of conduction velocity and isochronal maps. Indeed, the conduction velocity as well as the distance between isochrones in isochronal maps is determined not by the absolute value of the activation time but by the difference between activation times in different locations. Upon subtraction, the systematic error in activation times cancels out even when the latter is not particularly small.

The results presented above suggest that for most applications, excluding measurements of upstroke, a bandwidth of 300Hz is perfectly adequate, causing negligible error in APD measurements and activation time (delay). Measurements of conduction velocity are of course unaffected at any bandwidth, because each amplifier will create the same delay.

Using the same model and same filter, we applied our analysis to calcium transients. Figure 2-2 shows the results of our analysis. The Ca_i^{2+} transients are much slower which significantly reduces the error and allows using lower cutoff frequencies. Panel A shows the input Ca_i^{2+} transient and the output of the filter at 100Hz cutoff (Top) and the residual of the output compared to the input (Bottom). Despite a very narrow bandwidth the filter does not cause significant distortion and fully preserves the peak. A noticeable residual (5% of the peak) is observed.

Panel B shows the error in rise time. At a bandwidth as low as 100Hz the rise time can be measured with only 0.6% distortion. The peak error (panel C) is only 0.5%, and the error in the duration (Ca_iD) measurement, shown in part D, is also small, showing an error of only about 1% at 100Hz. Thus for measurement Ca_i^{2+} transients the bandwidth of 100Hz is more than sufficient.

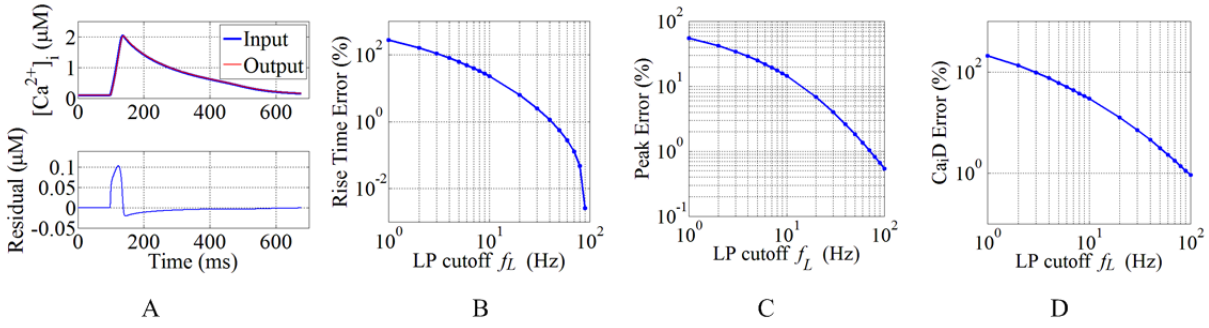

Figure 2-2: Plots showing the effects of linear distortion from a 1st-order low-pass filter on calcium transients from a purkinje fiber. The calcium transient and the filter output at 100Hz cutoff (Top A) and the residual (Bottom A). The percent error of the rise-time (B), the percent error in the peak measurement (C), and the percent error of the duration measurement (D).

Chapter 3 Evaluation of the SNR and Frequency Response for Different Transimpedance Amplifier Topologies

3.1 Single-Feedback Resistor Amplifier

The basic photodiode amplifier topology is the most widely used for detecting low-intensity optical signals from stained tissue [7, 2, 11, 12, 6, 18]. Though it is a simple topology, this analysis and the analysis of other topologies in the next chapter will show that it produces the least amount of noise.

3.1.1 *Noise Analysis*

Figure 3-1 shows the basic amplifier topology (left) and the corresponding noise model (right). For this analysis, we will consider each noise source individually and then use superposition to determine the total noise.

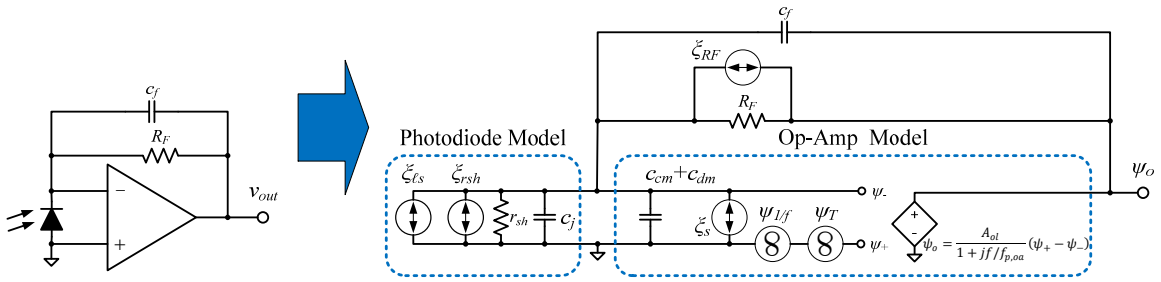

Figure 3-1: Basic photodiode amplifier topology (left) and corresponding noise model (right).

The op-amp in this circuit will be modeled as having common-mode and differential-mode input capacitances c_{cm} and c_{dm} respectively. It will have input-current shot noise ξ_s, thermal noise ψ_T and flicker noise $\psi_{1/f}$. It will be modeled as having finite gain A_{ol} and one internal pole located at $f_{p,oa}$. Its transfer function is shown below.

$$\psi_o = \frac{A_{ol}}{1 + jf/f_{p,oa}}(\psi_+ - \psi_-) \tag{3-1}$$

The photodiode is modeled as having shunt-resistance-related thermal noise and photocurrent shot noise. It has junction capacitance c_j. The photodiode junction capacitance and op-amp input capacitance combine in parallel to produce c_{in} which is defined as

$$c_{in} = c_{cm} + c_{dm} + c_j \tag{3-2}$$

For all calculations of RMS noise in this section, we will assume that the TIA is followed by a high-order low-pass filter like the one described in section 1.3.1 which can be approximated by equation $(1-12)$. Thus the upper limit of the integrals will not be ∞ but instead $\frac{\pi}{2} f_L$.

The transfer function seen by the op-amp thermal noise is defined by the equation shown below.

$$\frac{\psi_{o,T}}{\psi_T} = \frac{G_{DC}\left(1 + j2\pi f R_F \parallel r_{sh}(c_f + c_{in})\right)}{1 + j(2\pi f)x_1 - (2\pi f)^2 x_2} \tag{3-3}$$

where

$$G_{DC} = \frac{A_{ol}}{1 + A_{ol}\dfrac{r_{sh}}{R_F + r_{sh}}} \tag{3-4}$$

$$x_1 = \frac{R_F \parallel r_{sh}\left((1 + A_{ol})c_f + c_{in}\right) + 1/(2\pi f_{p,oa})}{1 + A_{ol}\dfrac{r_{sh}}{R_F + r_{sh}}}$$

$$x_2 = \frac{R_F \parallel r_{sh}(c_f + c_{in})/f_{p,oa}}{1 + A_{ol}\frac{r_{sh}}{R_F + r_{sh}}}$$

The magnitude of this expression gives us the noise density.

$$|\psi_{o,T}| = \frac{G_{DC}\sqrt{1 + f^2\left(2\pi R_F \parallel r_{sh}(c_f + c_{in})\right)^2}}{\sqrt{(1 - (2\pi f)^2 x_2)^2 + (2\pi f)^2 x_1^2}}\psi_T \qquad (3-5)$$

In order to more easily extract information from $(3-3)$, we can eliminate the high-frequency pole created by the op-amp by assuming $A_{ol} = \infty$. Equation $(3-3)$ then reduces to

$$\frac{\psi_{o,T}}{\psi_T} = \left(1 + \frac{R_F}{r_{sh}}\right)\frac{1 + j2\pi f R_F \parallel r_{sh}(c_f + c_{in})}{1 + j2\pi f R_F c_f} \qquad (3-6)$$

Now we can clearly see that there is a pole at

$$f_p = \frac{1}{2\pi R_F c_f} \qquad (3-7)$$

and a zero at

$$f_z = \frac{1}{2\pi R_F \parallel r_{sh}\,(c_f + c_{in})} \qquad (3-8)$$

and that the pass-band gain is

$$G_{PB} = 1 + \frac{c_{in}}{c_f} \qquad (3-9)$$

Take the magnitude of $(3-6)$

$$|\psi_{o,T}| = \left(1 + \frac{R_F}{r_{sh}}\right)\frac{\sqrt{1 + f^2\left(2\pi R_F \parallel r_{sh}\,(c_f + c_{in})\right)^2}}{\sqrt{1 + f\left(2\pi R_F c_f\right)^2}}\psi_T \qquad (3-10)$$

Because the transfer function in $(3-6)$ has the form of the filter described in section 1.3.1 equation $(1-14)$, we can use equation $(1-16)$.

$$v_{n,T} = \sqrt{\int_0^{\frac{\pi}{2}f_L} \left|\psi_{o,T}\right|^2 df} = \left(1 + \frac{R_F}{r_{sh}}\right)\psi_T \sqrt{f_L\left(\left(\frac{\pi}{2}-1\right)\frac{f_L^2}{f_z^2}+1\right)} \qquad (3-11)$$

If $\left(\frac{\pi}{2}-1\right)\frac{f_L^2}{f_z^2} \gg 1$, then

$$v_{n,T} = \left(1 + \frac{R_F}{r_{sh}}\right)\psi_T \frac{f_L}{f_z}\sqrt{\left(\frac{\pi}{2}-1\right)f_L} \qquad (3-12)$$

Substitute $(3-8)$ into $(3-12)$

$$v_{n,T} = 2\pi R_F\left(c_{in}+c_f\right)f_L\psi_T\sqrt{\left(\frac{\pi}{2}-1\right)f_L} \qquad (3-13)$$

For high-gain applications, we can assume that $c_{in} \gg c_f$. Therefore

$$v_{n,T} = 2\pi R_F c_{in} f_L \psi_T \sqrt{\left(\frac{\pi}{2}-1\right)f_L} \qquad (3-14)$$

The flicker noise of this circuit sees the same transfer function.

$$\frac{\psi_{o,1/f}}{\psi_{1/f}} = G_{DC}\frac{1 + j2\pi f R_F \parallel r_{sh}\left(c_f + c_{in}\right)}{1 + j(2\pi f)x_1 - (2\pi f)^2 x_2} \qquad (3-15)$$

Take the magnitude of $(3-15)$ to get the noise density

$$\left|\psi_{o,1/f}\right| = \frac{G_{DC}\sqrt{1 + f^2\left(2\pi R_F \parallel r_{sh}\left(c_f + c_{in}\right)\right)^2}}{\sqrt{(1-(2\pi f)^2 x_2)^2 + (2\pi f)^2 x_1^2}}\frac{FNN}{\sqrt{f}} \qquad (3-16)$$

If $A_{ol} = \infty$ in $(3-15)$

$$\frac{\psi_{o,1/f}}{\psi_{1/f}} = \left(1 + \frac{R_F}{r_{sh}}\right)\frac{1 + j2\pi f R_F \parallel r_{sh}(c_f + c_{in})}{1 + j2\pi f R_F c_f} \qquad (3-17)$$

Take the magnitude of $(3-17)$ to get the noise density.

$$\left|\psi_{o,1/f}\right| = \left(1 + \frac{R_F}{r_{sh}}\right)\frac{\sqrt{1 + f^2\left(2\pi R_F \parallel r_{sh}(c_f + c_{in})\right)^2}}{\sqrt{1 + f^2(2\pi R_F c_f)^2}}\frac{FNN}{\sqrt{f}} \qquad (3-18)$$

Squaring $(3-18)$, integrating over f, and taking the square root yields the RMS noise voltage. Because the transfer function in $(3-17)$ has the same form as that in $(1-14)$, we can use equation $(1-19)$ as the result of the integration.

$$v_{n,1/f} = \sqrt{\int_0^{\frac{\pi}{2}f_L}\left|\psi_{o,1/f}\right|^2 df} = \left(1 + \frac{R_F}{r_{sh}}\right)FNN\sqrt{\ln\left(\frac{\pi}{2}\frac{f_L}{f_0}\right) + \frac{\ln\left(1 + \frac{\pi^2}{4}\right)}{2}\left(\frac{f_L^2}{f_z^2} - 1\right)} \qquad (3-19)$$

It is safe to say that $f_L^2/f_z^2 \gg 1$, hence the above expression reduces to

$$v_{n,1/f} = \left(1 + \frac{R_F}{r_{sh}}\right)FNN\sqrt{\ln\left(\frac{\pi}{2}\frac{f_L}{f_0}\right) + \frac{\ln\left(1 + \frac{\pi^2}{4}\right)}{2}\frac{f_L^2}{f_z^2}} \qquad (3-20)$$

The frequency f_0 is typically chosen to be a very small number. If $f_0 = 1\text{mHz}$, then for high-gain applications we can assume that $\frac{\ln\left(1+\frac{\pi^2}{4}\right)}{2}\frac{f_L^2}{f_z^2} \gg \ln\left(\frac{\pi}{2}\frac{f_L}{f_0}\right)$. Therefore the above expression becomes

$$v_{n,1/f} = \left(1 + \frac{R_F}{r_{sh}}\right)FNN\frac{f_L}{f_z}\sqrt{\frac{\ln\left(1 + \frac{\pi^2}{4}\right)}{2}} \qquad (3-21)$$

Substitute $(3-8)$ into $(3-21)$

$$v_{n,1/f} = 2\pi R_F(c_{in} + c_f) f_L FNN \sqrt{\frac{\ln\left(1 + \frac{\pi^2}{4}\right)}{2}} \qquad (3-22)$$

For high-gain applications we can assume that $c_{in} \gg c_f$. Therefore equation $(3-22)$ reduces to

$$v_{n,1/f} = 2\pi R_F c_{in} f_L FNN \sqrt{\frac{\ln\left(1 + \frac{\pi^2}{4}\right)}{2}} \qquad (3-23)$$

The resistor thermal noise transfer function is defined as

$$\frac{\psi_{o,RF}}{\xi_{RF}} = -G_{DC} \frac{(R_F \parallel r_{sh})}{1 + j(2\pi f)x_1 - (2\pi f)^2 x_2} \qquad (3-24)$$

Taking the magnitude of $(3-24)$ gives us the noise density as a function of frequency

$$\left|\psi_{o,RF}\right| = \frac{G_{DC}(R_F \parallel r_{sh})\sqrt{4kT/R_F}}{\sqrt{(1-(2\pi f)^2 x_2)^2 + (2\pi f)^2 x_1^2}} \qquad (3-25)$$

If $A_{ol} = \infty$, $(3-24)$ becomes

$$\frac{\psi_{o,RF}}{\xi_{RF}} = -\frac{R_F}{1 + j2\pi f R_F c_f} \qquad (3-26)$$

The magnitude of $(3-26)$ is

$$\left|\psi_{o,RF}\right| = \frac{\sqrt{4kTR_F}}{\sqrt{1 + f^2\left(2\pi R_F c_f\right)^2}} \qquad (3-27)$$

The RMS voltage noise at the circuit's output contributed by R_F can be found by taking the square root of the integral of the noise density as shown below. Because the transfer function in $(3-26)$ is the same form as that in $(1-8)$, we can use equation $(1-13)$ as the result of the integral. We then have

$$v_{n,RF} = \sqrt{\int_0^{\frac{\pi}{2}f_L} \left|\psi_{o,RF}\right|^2 df} = \sqrt{4kTR_F f_L} \qquad (3-28)$$

The op-amp current noise density has the transfer function shown below

$$\frac{\psi_{o,s}}{\xi_s} = \frac{-G_{DC}(R_F \parallel r_{sh})}{1 + j(2\pi f)x_1 - (2\pi f)^2 x_2} \qquad (3-29)$$

The magnitude of $(3-29)$ to get the noise density as a function of frequency

$$\left|\psi_{o,s}\right| = \frac{G_{DC}(R_F \parallel r_{sh})\xi_s}{\sqrt{(1-(2\pi f)^2 x_2)^2 + (2\pi f)^2 x_1^2}} \qquad (3-30)$$

If $A_{ol} = \infty$ in $(3-29)$ then

$$\frac{\psi_{o,s}}{\xi_s} = \frac{R_F}{1 + j2\pi f R_F c_f} \qquad (3-31)$$

Take the magnitude of $(3-31)$ to get the voltage noise density as a function of frequency

$$\left|\psi_{o,s}\right| = \frac{R_F \xi_s}{\sqrt{1 + f^2\left(2\pi R_F c_f\right)^2}} \qquad (3-32)$$

The RMS voltage noise at the circuit's output contributed by ξ_s can be found by taking the square root of the integral of the noise density as shown below. Because the transfer function in $(3-31)$ is the same form as that in $(1-8)$, we can use equation $(1-13)$ as the result of the integral. We then have

$$v_{n,s} = \sqrt{\int_0^{\frac{\pi}{2}f_L} \left|\psi_{o,s}\right|^2 df} = R_F \xi_s \sqrt{f_L} \qquad (3-33)$$

The photodiode thermal noise sees the same transfer function as the op-amp current noise

$$\frac{\psi_{o,rsh}}{\xi_{rsh}} = \frac{-G_{DC}(R_F \parallel r_{sh})}{1 + j(2\pi f)x_1 - (2\pi f)^2 x_2} \qquad (3-34)$$

The magnitude of $(3-34)$ gives the noise density

$$\left|\psi_{o,rsh}\right| = \frac{G_{DC}(R_F \parallel r_{sh})}{\sqrt{(1-(2\pi f)^2 x_2)^2 + (2\pi f)^2 x_1^2}} \sqrt{\frac{4kT}{r_{sh}}} \qquad (3-35)$$

If $A_{ol} = \infty$ in $(3-34)$ then

$$\frac{\psi_{o,rsh}}{\xi_{rsh}} = \frac{R_F}{1 + j2\pi f R_F c_f} \qquad (3-36)$$

Take the magnitude of $(3-36)$ to get the voltage noise density as a function of frequency

$$\left|\psi_{o,rsh}\right| = \frac{R_F \sqrt{\frac{4kT}{r_{sh}}}}{\sqrt{1 + f^2\left(2\pi R_F c_f\right)^2}} \qquad (3-37)$$

The RMS voltage noise at the circuit's output contributed by ξ_s can be found by taking the square root of the integral of the noise density as shown below. Because the transfer function in $(3-37)$ is the same form as that in $(1-8)$, we can use equation $(1-13)$ as the result of the integral. We then have

$$v_{n,rsh} = \sqrt{\int_0^{\frac{\pi}{2} f_L} \left|\psi_{o,rsh}\right|^2 df} = R_F \sqrt{\frac{4kT}{r_{sh}} f_L} \qquad (3-38)$$

The photocurrent shot noise sees the same transfer function as the op-amp current noise

$$\frac{\psi_{o,\ell s}}{\xi_{\ell s}} = \frac{-G_{DC}(R_F \parallel r_{sh})}{1 + j(2\pi f)x_1 - (2\pi f)^2 x_2} \qquad (3-39)$$

The magnitude of $(3-39)$ to get the noise density.

$$\left|\psi_{o,\ell s}\right| = \frac{G_{DC}(R_F \parallel r_{sh})\sqrt{2q\bar{\imath}_p}}{\sqrt{(1-(2\pi f)^2 x_2)^2 + (2\pi f)^2 x_1^2}} \qquad (3-40)$$

If $A_{ol} = \infty$ in $(3-39)$ then

$$\frac{\psi_{o,\ell s}}{\xi_{\ell s}} = \frac{R_F}{1 + j2\pi f R_F c_f} \qquad (3-41)$$

Take the magnitude of $(3-41)$ to get the voltage noise density as a function of frequency

$$\left|\psi_{o,\ell s}\right| = \frac{R_F\sqrt{2q\bar{\imath}_p}}{\sqrt{1 + f^2\left(2\pi R_F c_f\right)^2}} \qquad (3-42)$$

The RMS voltage noise at the circuit's output contributed by ξ_s can be found by taking the square root of the integral of the magnitude of the noise density squared as shown below. Because the transfer function in $(3-37)$ is the same form as that in $(1-8)$, we can use equation $(1-13)$ as the result of the integral. We then have

$$v_{n,light} = \sqrt{\int_0^{\frac{\pi}{2}f_L} \left|\psi_{o,\ell s}\right|^2 df} = R_F\sqrt{2q\bar{\imath}_p f_L} \qquad (3-43)$$

The total dark noise is then the quadratic sum of all the noise sources inherent to the amplifier

$$v_{n,dark} = \sqrt{v_{n,T}^2 + v_{n,1/f}^2 + v_{n,RF}^2 + v_{n,s}^2 + v_{n,rsh}^2} \qquad (3-44)$$

The total noise is then the quadratic sum of the dark and light noise

$$v_{n,total} = \sqrt{v_{n,dark}^2 + v_{n,light}^2} \qquad (3-45)$$

Substituting equations $(3-14)$, $(3-23)$, $(3-28)$, $(3-33)$, $(3-38)$ into $(3-44)$

$$v_{n,dark} = \sqrt{(\xi_s^2 + 4kT/r_{sh} + (2\pi c_{in})^2 \gamma f_L) f_L R_F^2 + \beta f_L R_F} \qquad (3-46)$$

$$\beta = 4kT \qquad (3-47)$$

$$\gamma = \psi_T^2 \left(\frac{\pi}{2} - 1\right) f_L + FNN^2 \frac{\ln\left(1 + \frac{\pi^2}{4}\right)}{2} \qquad (3-48)$$

Substitute $(3-43)$ and $(3-46)$ into $(3-45)$

$$v_{n,total} = \sqrt{\alpha f_L R_F^2 + \beta f_L R_F} \qquad (3-49)$$

$$\alpha = \xi_s^2 + 4kT/r_{sh} + 2q\bar{\imath_p} + (2\pi c_{in})^2 \gamma f_L \qquad (3-50)$$

The total noise density, using the equations with the finite-gain single-pole op-amp model, specifically equations $(3-5)$, $(3-16)$, $(3-30)$, $(3-25)$, and $(3-35)$ $(3-35)$, is defined below.

$$|\psi_{o,dark}| = \sqrt{\psi_{o,T}^2 + \psi_{o,1/f}^2 + \psi_{o,s}^2 + \psi_{o,RF}^2 + \psi_{o,rsh}^2} \qquad (3-51)$$

The above equation will be compared with experimental noise density data.

3.1.2 *Noise Density*

To test the theory of the previous section and to show the advantage of increasing the gain of the TIA from the commonly used $100\text{M}\Omega$ to $10\text{G}\Omega$, we built 2 transimpedance amplifiers and measured their noise density.

The TIA output was connected to the E5061B network analyzer. The resolution bandwidth was set to 1Hz and frequencies from 5Hz to 100kHz were captured. The result was averaged 10 times. To eliminate interference from external noise or power supply coupling, the PCB with was placed in a closed metal box and powered by four 9V batteries for $\pm$18V supply.

According to the theory, using a single-stage, 10GΩ-TIA versus a conventional two-stage amplifier with 100MΩ first-stage gain and the same total gain should reduce the noise by an order of magnitude. Our experiments show that this is the case (see Figure 3-2). Indeed, at low frequencies the noise density of a 10GΩ is about 16.5 $\mu V/\sqrt{Hz}$ versus 128 $\mu V/\sqrt{Hz}$ at 100MΩ.

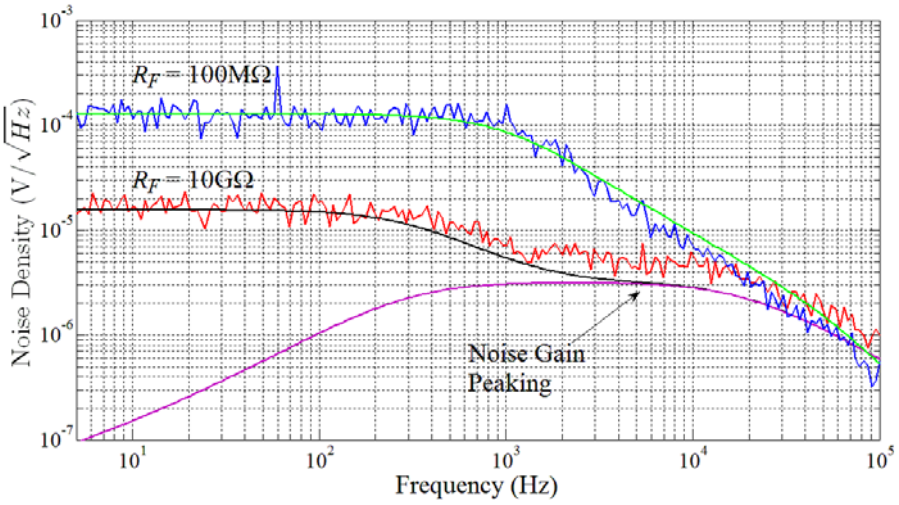

Figure 3-2: Noise density spectra for amplifier with single 100MΩ resistor, second stage with voltage gain of 100, and no photodiode (blue), its theoretical noise density (green) and single 10GΩ feedback resistor with field-shunting ground trace and SFH229 photodiode (red) along with its theoretical noise density (black), both amplifiers use the OPA140 in an SOT-23-5 package both with a 300Hz low-pass cutoff frequency. The purple line shows the theoretical model of the amplification of the op-amp voltage noise by noise gain peaking.

The experimentally measured noise spectra are consistent with the theoretically derived spectra (black and green solid lines). The theoretical spectra were obtained by using the parameters from the OPA140 datasheet and in the case of the TIA with 10GΩ in the 1st stage, the

c_j given in the SFH229 datasheet and the assumption that the diode has $r_{sh} = 100\text{G}\Omega$. These parameters were then plugged into formula $(3-51)$, which is derived in the previous section.

Note that the noise density roll off of the $10\text{G}\Omega$-TIA slows down at frequencies beyond 2kHz. This is the result of noise gain peaking, the amplification of flicker and thermal noise of the op-amp. The purple line shows the theoretical op-amp voltage noise density calculated using only the op-amp thermal and flicker noise components of equations $(3-5)$ and $(3-16)$.

3.1.3 *Signal-to-Noise Ratio*

The signal to noise ratio is defined as the RMS value of the signal to be detected to the RMS value of the noise in the detector circuit. In our case, this is

$$SNR = \frac{R_F \tilde{\imath_p}}{v_{n,total}} \qquad (3-52)$$

where $\tilde{\imath_p}$ is the RMS photocurrent corresponding to the detected signal. We then substitute $(3-45)$ into $(3-52)$ to get the equation below.

$$SNR = \frac{R_F \tilde{\imath_p}}{\sqrt{\alpha f_L R_F^2 + \beta f_L R_F}} \qquad (3-53)$$

Recall that the term α in equation contains the shot noise which is proportional to $\sqrt{\bar{\imath_p}}$, the average photocurrent. If we choose the input signal to be a sinusoid with peak-to-peak amplitude $\hat{\imath_p}$, then the RMS and DC current are defined as

$$\tilde{\imath_p} = \frac{\sqrt{6}}{4}\hat{\imath_p} \qquad (3-54)$$

and

$$\overline{\iota_p} = \frac{1}{2}\widehat{\iota_p} \qquad (3-55)$$

Taking the limit of equation $(3-53)$ as R_F approaches infinity gives us the maximum possible SNR for a given op-amp and photodiode.

$$SNR_\infty = \lim_{R_F \to \infty} SNR = \frac{\widetilde{\iota_p}}{\sqrt{\alpha f_L}} \qquad (3-56)$$

While the SNR_∞ represents the theoretical ceiling, a "practical" target for R_F can be $R_{F,90}$, the feedback resistance corresponding to 90% of SNR_∞. Increasing R_F beyond $R_{F,90}$ would no longer result in significant improvement of SNR. The value of $R_{F,90}$ can be approximated using the following simple formula:

$$R_{F,90} = 4.26\frac{\beta}{\alpha} \qquad (3-57)$$

We can see from equation $(3-57)$ that $R_{F,90}$ is inversely proportional to α which is dependent on the average photocurrent $\overline{\iota_p}$. Thus $R_{F,90}$ will reach its maximum when $\overline{\iota_p}$ goes to 0. We will call this condition $\hat{R}_{F,90}$ and define it as

$$\hat{R}_{F,90} = \lim_{\overline{\iota_p} \to 0} R_{F,90} = 4.26\frac{\beta}{\alpha'} \qquad (3-58)$$

where

$$\alpha' = \xi_s^2 + 4kT/r_{sh} + (2\pi c_{in})^2 \gamma f_L$$

In later sections we will use equation $(3-56)$ and $(3-58)$ to show the optimal performance that can be obtained for this topology with the current technology.

3.2 T-Bridge Feedback Network Topology

The T-bridge network is an alternative to the single feedback resistor with the aim of achieving very high transimpedance gain. The 3 feedback resistors combine to produce a gain of

$$R_{F,eq} = R_A + R_C + \frac{R_A R_C}{R_B} \qquad (3-59)$$

In this chapter, we will first analyze the noise produced by the T-bridge. Then, we will model the bandwidth to determine if there is any advantage to be gained over the single-resistor amplifier.

3.2.1 *Noise Analysis*

The figure below shows the T-bridge TIA and the corresponding noise model that we will be using. Note that for this portion of the analysis we will be neglecting the resistor parasitic capacitance because these will only take effect beyond the cutoff frequency and thus not have a large impact on the noise. For this analysis we will consider each noise source independently and then use superposition to determine the total noise.

The op-amp in this circuit will be modeled as having common-mode and differential-mode input capacitances, c_{cm} and c_{dm} respectively. It will have input-current shot noise ξ_s, thermal noise ψ_T and flicker noise $\psi_{1/f}$. It will be modeled as having infinite gain.

The photodiode is modeled as having shunt-resistance-related thermal noise and photocurrent shot noise. It has junction capacitance c_j. The photodiode junction capacitance and op-amp input capacitance combine in parallel to produce c_{in} which is defined in the previous section in equation $(3-2)$.

For all calculations of RMS noise in this section, we will assume that the TIA is followed by a high-order low-pass filter like the one described in section 1.3.1 which can be approximated by equation $(1-12)$. Thus the upper limit of the integrals will not be ∞ but instead $\frac{\pi}{2} f_L$.

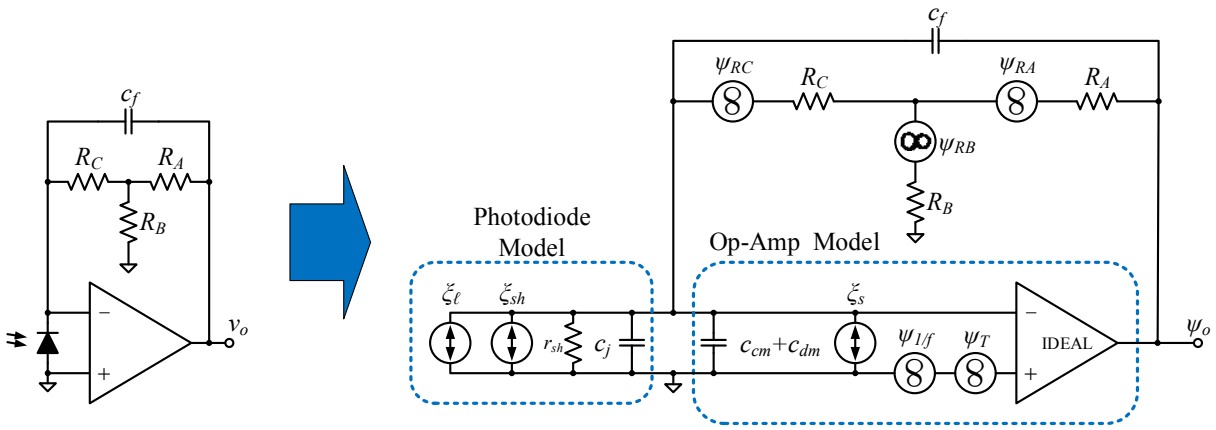

Figure 3-3: Transimpedance amplifier with T-bridge feedback network (left) and corresponding noise model (right).

The transfer function seen by the op-amp thermal noise is

$$G_{n,T} = \frac{\psi_{o,T}}{\psi_T} = \frac{1 + j2\pi f R_{F,eq}(c_f + c_{in})\beta_T}{\beta_T(1 + j2\pi f R_{F,eq} c_f)} \qquad (3-60)$$

where

$$\beta_T = \frac{1}{1 + \frac{R_A}{R_B} + \frac{R_{F,eq}}{r_{sh}}} \qquad (3-61)$$

and where the zero and pole frequencies are

$$f_z = \frac{1}{2\pi R_{F,eq}(c_f + c_{in})\beta_T} \qquad (3-62)$$

$$f_p = \frac{1}{2\pi R_{F,eq} c_f} \tag{3-63}$$

and the mid-band gain is

$$G_{MB} = \frac{f_p}{f_z} = \frac{1 + \frac{c_{in}}{c_f}}{1 + \frac{R_A}{R_B} + \frac{R_{F,eq}}{r_{sh}}} \tag{3-64}$$

The contribution of op amp thermal noise density ψ_T to the output noise density can be found by taking the magnitude of the transfer function $(3-60)$ and multiplying it by the op-amp thermal noise. Taking the magnitude of $(3-60)$ yields the noise density as a function of frequency without high-frequency poles

$$\left|\psi_{o,T}\right| = \left(1 + \frac{R_A}{R_B} + \frac{R_{F,eq}}{r_{sh}}\right) \frac{\sqrt{1 + f^2 \left(2\pi \frac{R_{F,eq}(c_f + c_{in})}{1 + \frac{R_A}{R_B} + \frac{R_{F,eq}}{r_{sh}}} \right)^2}}{\sqrt{1 + f^2 \left(2\pi R_{F,eq} c_f\right)^2}} \psi_T \tag{3-65}$$

The total noise can then be found by squaring $(3-65)$, integrating over f and taking the square root

$$v_{n,T} = \sqrt{\int_0^{\frac{\pi}{2} f_L} \left|G_{n,T}\right|^2 \psi_T^2 df} = \sqrt{\int_0^{\frac{\pi}{2} f_L} \frac{1}{\beta_T^2} \frac{1 + f^2/f_z^2}{1 + f^2/f_L^2} \psi_T^2 df} \tag{3-66}$$

Because the transfer function in $(3-60)$ has the form of the filter described in section 1.3.1 equation $(1-14)$, we can use equation $(1-16)$. The above integral becomes

$$v_{n,T} = \frac{\psi_T}{\beta_T} \sqrt{f_L \left(\left(\frac{\pi}{2} - 1\right) \frac{f_L^2}{f_z^2} + 1 \right)} \tag{3-67}$$

If $\left(\frac{\pi}{2}-1\right)\frac{f_L^2}{f_z^2} \gg 1$, equation $(3-67)$ reduces to

$$v_{n,T} = \frac{\psi_T}{\beta_T}\frac{f_L}{f_z}\sqrt{\left(\frac{\pi}{2}-1\right)f_L} \qquad (3-68)$$

Substitute $(3-62)$ into $(3-68)$

$$v_{n,T} = 2\pi R_{F,eq}(c_f + c_{in})f_L\psi_T\sqrt{\left(\frac{\pi}{2}-1\right)f_L} \qquad (3-69)$$

For high-gain applications $c_{in} \gg c_f$, therefore equation $(3-69)$ becomes

$$v_{n,T} = 2\pi R_{F,eq}c_{in}f_L\psi_T\sqrt{\left(\frac{\pi}{2}-1\right)f_L} \qquad (3-70)$$

The flicker noise transfer function is the same as the thermal noise transfer function given in $(3-60)$, thus

$$G_{n,1/f} = \frac{\psi_{o,1/f}}{\psi_{1/f}} = \frac{1 + j2\pi f R_{F,eq}(c_f + c_{in})\beta_T}{\beta_T(1 + j2\pi f R_{F,eq}c_f)} \qquad (3-71)$$

Similarly, the noise density is defined as

$$\left|\psi_{o,1/f}\right| = \left(1 + \frac{R_A}{R_B} + \frac{R_{F,eq}}{r_{sh}}\right)\frac{\sqrt{1 + f^2\left(2\pi\dfrac{R_{F,eq}(c_f + c_{in})}{1 + \dfrac{R_A}{R_B} + \dfrac{R_{F,eq}}{r_{sh}}}\right)^2}}{\sqrt{1 + f^2(2\pi R_{F,eq}c_f)^2}}\frac{FNN}{\sqrt{f}} \qquad (3-72)$$

The RMS flicker noise voltage at the circuit output is then

$$v_{n,1/f} = \sqrt{\int_{f_0}^{\frac{\pi}{2}f_L}\frac{1}{\beta_T^2}\frac{1 + f^2/f_z^2}{1 + f^2/f_L^2}\frac{FNN^2}{f}df} \qquad (3-73)$$

Because the transfer function in $(3-71)$ has the form of the filter described in section 1.3.1 equation $(1-14)$, we can use equation $(1-19)$ as long as we choose f_0 such that $f_L \gg f_0$. The above integral becomes

$$v_{n,1/f} = \frac{FNN}{\beta_T}\sqrt{\ln\left(\frac{\pi}{2}\frac{f_L}{f_0}\right) + \frac{\ln\left(1+\frac{\pi^2}{4}\right)}{2}\left(\frac{f_L^2}{f_z^2}-1\right)} \qquad (3-74)$$

If $f_L^2/f_z^2 \gg 1$, then $(3-74)$ becomes

$$v_{n,1/f} = \frac{FNN}{\beta_T}\sqrt{\ln\left(\frac{\pi}{2}\frac{f_L}{f_0}\right) + \frac{\ln\left(1+\frac{\pi^2}{4}\right)}{2}\frac{f_L^2}{f_z^2}} \qquad (3-75)$$

The frequency f_0 is typically chosen to be a very small number. If $f_0 = 1\text{mHz}$, then for high-gain applications we can assume that $\frac{\ln\left(1+\frac{\pi^2}{4}\right)}{2}\frac{f_L^2}{f_z^2} \gg \ln\left(\frac{\pi}{2}\frac{f_L}{f_0}\right)$. Therefore the above expression becomes

$$v_{n,1/f} = \frac{FNN}{\beta_T}\frac{f_L}{f_z}\sqrt{\frac{\ln\left(1+\frac{\pi^2}{4}\right)}{2}} \qquad (3-76)$$

Substitute $(3-62)$ into $(3-76)$

$$v_{n,1/f} = 2\pi R_{F,eq}\left(c_f + c_{in}\right)f_L FNN\sqrt{\frac{\ln\left(1+\frac{\pi^2}{4}\right)}{2}} \qquad (3-77)$$

For high gain applications $c_{in} \gg c_f$, therefore equation $(3-77)$ becomes

$$v_{n,1/f} = 2\pi R_{F,eq} c_{in} f_L FNN\sqrt{\frac{\ln\left(1+\frac{\pi^2}{4}\right)}{2}} \qquad (3-78)$$

The transfer function for the op-amp current noise source is

$$G_{n,s} = \frac{\psi_{o,s}}{\xi_s} = \frac{R_{F,eq}}{1 + j2\pi f R_{F,eq} c_f} \tag{3-79}$$

where ξ_s can be extracted from the op-amp's datasheet. The noise density due to op-amp current noise observed at the output is then

$$\left|\psi_{o,s}\right| = \frac{R_{F,eq}\xi_s}{\sqrt{1 + f^2\left(2\pi R_{F,eq} c_f\right)^2}} \tag{3-80}$$

The RMS noise at the output is then

$$v_{n,s} = \sqrt{\int_0^{\frac{\pi}{2}f_L} \left|\psi_{o,s}\right|^2 df} = R_{F,eq}\xi_s\sqrt{f_L} \tag{3-81}$$

The transfer function for the R_A noise source is

$$G_{n,RA} = \frac{\psi_{o,RA}}{\psi_{RA}} = \frac{1}{1 + j2\pi f R_{F,eq} c_f} \tag{3-82}$$

Where

$$\psi_{RA} = \sqrt{4kTR_A} \tag{3-83}$$

The noise density due to R_A observed at the output is then

$$\left|\psi_{o,RA}\right| = \frac{\sqrt{4kTR_A}}{\sqrt{1 + f^2\left(2\pi R_{F,eq} c_f\right)^2}} \tag{3-84}$$

The RMS noise at the output is then

$$v_{n,RA} = \sqrt{\int_0^{\frac{\pi}{2}f_L} \left|\psi_{o,RA}\right|^2 df} = \sqrt{4kTR_A f_L} \qquad (3-85)$$

The transfer function for the R_B noise source is

$$G_{n,RB} = \frac{R_A/R_B}{1 + j2\pi f R_{F,eq} c_f} \qquad (3-86)$$

Where

$$\psi_{RB} = \sqrt{4kTR_B} \qquad (3-87)$$

The noise density due to R_B observed at the output is then

$$\left|\psi_{o,RB}\right| = \frac{R_A/R_B\sqrt{4kTR_B}}{\sqrt{1 + f^2\left(2\pi R_{F,eq} c_f\right)^2}} \qquad (3-88)$$

The RMS noise at the output is then

$$v_{n,RB} = \sqrt{\int_0^{\frac{\pi}{2}f_L} \left|\psi_{o,RB}\right|^2 df} = \frac{R_A}{R_B}\sqrt{4kTR_B f_L} \qquad (3-89)$$

The transfer function for the R_C noise source is

$$G_{n,RC} = \left(1 + \frac{R_A}{R_B}\right) \frac{1}{1 + j2\pi f R_{F,eq} c_f} \qquad (3-90)$$

Where

$$\psi_{RC} = \sqrt{4kTR_C} \qquad (3-91)$$

The noise density corresponding to R_C observed at the circuit's output is

$$\left|\psi_{o,RC}\right| = \frac{\left(1+\frac{R_A}{R_B}\right)\sqrt{4kTR_C}}{\sqrt{1+f^2\left(2\pi R_{F,eq}c_f\right)^2}} \qquad (3-92)$$

The RMS noise corresponding to R_C observed at the output is

$$v_{n,RC} = \sqrt{\int_0^{\frac{\pi}{2}f_L}\left|\psi_{o,RC}\right|^2 df} = \sqrt{4kTR_Cf_L} \qquad (3-93)$$

We can combine the 3 expressions for resistor noise to produce a single equation for RMS noise and noise density observed at the output. For the noise density, we will combine equations $(3-84)$, $(3-88)$, and $(3-92)$ by summing them in quadrature. The result is shown below.

$$\left|\psi_{o,RFeq}\right| = \frac{\sqrt{4kT\left(1+\frac{R_A}{R_B}\right)R_{F,eq}}}{\sqrt{1+f^2\left(2\pi R_{F,eq}c_f\right)^2}} \qquad (3-94)$$

We can then determine the total noise contribution of all resistors.

$$v_{n,RFeq} = \sqrt{\int_0^{\frac{\pi}{2}f_L}\left|\psi_{o,RFeq}\right|^2 df} = \sqrt{4kT\left(1+\frac{R_A}{R_B}\right)R_{F,eq}f_L} \qquad (3-95)$$

The photodiode thermal noise (shunt resistance r_{sh} thermal noise) has the same transfer function as the op-amp current noise defined in $(3-79)$.

$$G_{n,sh} = \frac{\psi_{o,rsh}}{\xi_{rsh}} = \frac{R_{F,eq}}{1+j2\pi fR_{F,eq}c_f} \qquad (3-96)$$

The noise density due to photocurrent shot noise is then

$$\left|\psi_{o,sh}\right| = \frac{R_{F,eq}\sqrt{4kT/r_{sh}}}{\sqrt{1+f^2\left(2\pi R_{F,eq}c_f\right)^2}} \qquad (3-97)$$

The RMS noise at the output is then

$$v_{n,sh} = \sqrt{\int_0^{\frac{\pi}{2}f_L} \left|\psi_{o,rsh}\right|^2 df} = R_{F,eq}\sqrt{\frac{4kT}{r_{sh}} f_L} \qquad (3-98)$$

The photocurrent shot noise has the same transfer function as the op-amp current noise defined in $(3-79)$.

$$G_{n,\ell s} = \frac{\psi_{o,\ell s}}{\xi_{\ell s}} = \frac{R_{F,eq}}{1 + j2\pi f R_{F,eq} c_f} \qquad (3-99)$$

where $\psi_{\ell s} = \sqrt{2q\bar{\imath_p}}$. The noise density due to photocurrent shot noise is then

$$\left|\psi_{o,\ell s}\right| = \frac{R_{F,eq}\sqrt{2q\bar{\imath_p}}}{\sqrt{1 + f^2\left(2\pi R_{F,eq} c_f\right)^2}} \qquad (3-100)$$

The RMS noise at the output is then

$$v_{n,light} = \sqrt{\int_0^{\frac{\pi}{2}f_L} \left|\psi_{o,\ell s}\right|^2 df} = R_{F,eq}\sqrt{2q\bar{\imath_p} f_L} \qquad (3-101)$$

Now we will assess the noise density of our amplifier without illumination. For this we must combine equations $(3-65)$, $(3-72)$, $(3-80)$, $(3-94)$, and $(3-97)$ in quadrature. The general form is

$$\psi_{o,dark} = \sqrt{\psi_{o,T}^2 + \psi_{o,1/f}^2 + \psi_{o,s}^2 + \psi_{o,RFeq}^2 + \psi_{o,sh}^2} \qquad (3-102)$$

The total RMS dark noise observed at the output is then the quadrature sum of $(3-70)$, $(3-78)$, $(3-81)$, $(3-95)(3-81)$, and $(3-98)$.

$$v_{n,dark} = \sqrt{v_{n,T}^2 + v_{n,1/f}^2 + v_{n,s}^2 + v_{n,RFeq}^2 + v_{n,sh}^2} \qquad (3-103)$$

The total noise is the combination of light and dark noise.

$$v_{n,total} = \sqrt{v_{n,dark}^2 + v_{n,light}^2} \qquad (3-104)$$

Substitute equations $(3-103)$ and $(3-101)$ into $(3-104)$.

$$v_{n,total} = \sqrt{\alpha f_L R_{F,eq}^2 + \beta f_L R_{F,eq}} \qquad (3-105)$$

where

$$\alpha = \xi_s^2 + 4kT/r_{sh} + 2q\bar{\imath_p} + (2\pi c_{in})^2 f_L \gamma \qquad (3-106)$$

$$\beta = 4kT\left(1 + \frac{R_A}{R_B}\right) \qquad (3-107)$$

and

$$\gamma = \psi_T^2\left(\frac{\pi}{2} - 1\right) f_L + FNN^2 \ln\left(\frac{\pi^2}{4} + 1\right) \qquad (3-108)$$

3.2.2 *Signal-to-Noise Ratio*

From section 3.1.3 we know that the SNR is define by equation $(3-52)$. The same applies to the amplifier with the T-bridge network. If we substitute equation $(3-104)$ into $(3-52)$, we get

$$SNR = \frac{R_{F,eq}\tilde{\imath_p}}{\sqrt{\alpha f_L R_{F,eq}^2 + \beta f_L R_{F,eq}}} \qquad (3-109)$$

Equation $(3-109)$ and equation $(3-52)$ may look similar, but keep in mind that the β in $(3-109)$ will always be greater than that in $(3-53)$ by a factor of $1 + R_A/R_B$.

3.2.3 *Frequency Response*

In this section we will analyze the frequency response of a TIA with a T-bridge feedback network. The model used in this section is shown below. Note that in this section we did not include the photodiode shunt resistance r_{sh} because it does not have a significant impact on the bandwidth. We will be using the single-pole op-amp model and include the op-amp common mode and differential mode input capacitance . As in the previous section, c_{cm} and c_{dm} combine in parallel with the photodiode's junction capacitance c_j (see equation $(3-2)$).

The op-amp is modeled as having finite gain of A_{ol} and an internal pole at $f_{p,oa}$. The op-amp's transfer function is shown below.

$$v_{out} = \frac{A_{ol}}{1 + jf/f_{p,oa}}(v_+ - v_-)$$

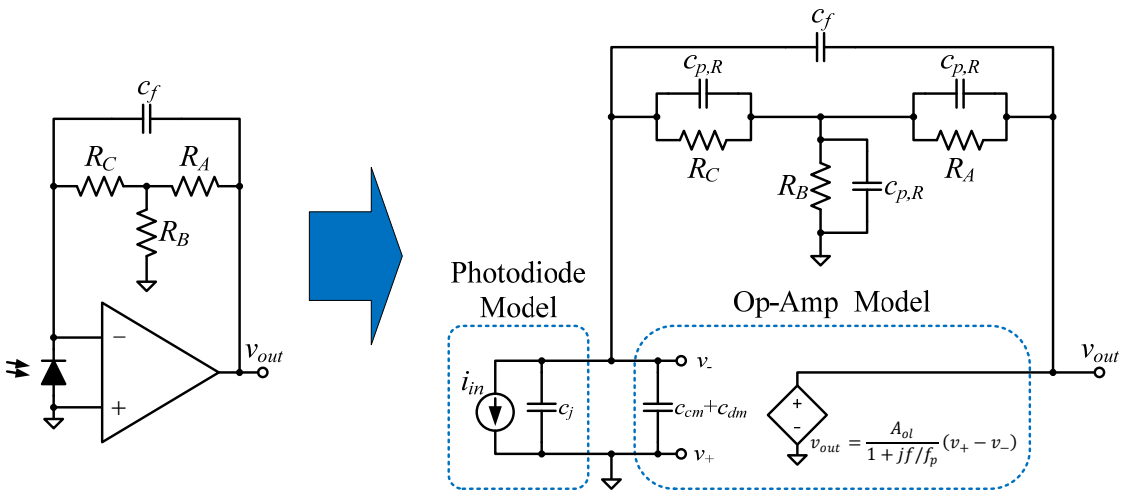

Figure 3-4: T-bridge circuit (left) and corresponding circuit model (right)

Circuit analysis yields the amplifier's frequency response

$$G_T = \frac{v_{out}}{i_{in}} = \frac{G_{DC}\left(1 + jfk_{n,im}\right)}{1 - f^2 k_{d,re} + jfk_{d,im1} - jf^3 k_{d,im2}} \quad (3-110)$$

Where

$$G_{DC} = \frac{A_{ol} R_{F,eq}}{A_{ol} + \left(1 + \frac{R_A}{R_B}\right)} \quad (3-111)$$

$$k_{n,im} = 2\pi \frac{3R_A R_C c_{p,R}}{R_{F,eq}} \quad (3-112)$$

$$k_{d,re} = \frac{\begin{array}{c} 4\pi^2 R_A R_C c_{p,R}\left(\left(c_{p,R} + 3c_f\right)A_{ol} + 3\left(c_{in} + c_{p,R}\right)\right) \\ +2\pi\left(R_{F,eq}\left(c_{in} + c_f + c_{p,R}\right) + R_A c_{p,R}\right)/f_{p,oa} \end{array}}{A_{ol} + \left(1 + \frac{R_A}{R_B}\right)} \quad (3-113)$$

$$k_{d,im1} = \frac{\begin{array}{c} 2\pi(A_{ol}(R_A + R_C) + R_A)c_{p,R} \\ +2\pi R_{F,eq}\left((A_{ol} + 1)c_f + c_{in} + c_{p,R}\right) + \left(1 + \frac{R_A}{R_B}\right)/f_{p,oa} \end{array}}{A_{ol} + \left(1 + \frac{R_A}{R_B}\right)} \quad (3-114)$$

$$k_{d,im2} = 4\pi^2 \frac{3R_A R_C c_p\left(c_{in} + c_{p,R}\right)/f_{p,oa}}{A_{ol} + \left(1 + \frac{R_A}{R_B}\right)} \quad (3-115)$$

The magnitude of the frequency response is then

$$|G_T| = \frac{G_{DC}\sqrt{1 + f^2 k_{n,im}^2}}{\sqrt{\left(1 - f^2 k_{d,re}\right)^2 + \left(fk_{d,im1} - jf^3 k_{d,im2}\right)^2}} \quad (3-116)$$

One can solve for the cutoff frequency by substituting f_L for f and G_{3dB}, the gain in the pass band reduced by 3dB, for $|G_T|$. Rearranging the above equation then results in the 6th-order polynomial shown below.

$$k_6 f_L^6 + k_4 f_L^4 + k_2 f_L^2 + k_0 = 0 \tag{3-117}$$

$$k_0 = \frac{G_{3\text{dB}}^2}{G_{DC}^2} - 1 \tag{3-118}$$

$$k_2 = \frac{G_{3\text{dB}}^2}{G_{DC}^2}\left(k_{d,im1}^2 - 2k_{d,re}\right) - k_{n,im}^2 \tag{3-119}$$

$$k_4 = \frac{G_{3\text{dB}}^2}{G_{DC}^2}\left(k_{d,re}^2 - 2k_{d,im1}k_{d,im2}\right) \tag{3-120}$$

$$k_6 = \frac{G_{3\text{dB}}^2}{G_{DC}^2} k_{d,im2}^2 \tag{3-121}$$

The cutoff frequency can be approximated however using a simpler method. In equation $(3-110)$ set $A_{ol} = \infty$ and $c_f = 0$. This leaves only the poles corresponding to the parasitic capacitance of the resistors. The resulting equation is written below.

$$G_T = \frac{R_{F,eq}\left(1 + j\omega\frac{3R_A R_C c_{p,R}}{R_{F,eq}}\right)}{\left(1 + j\omega R_A c_{p,R}\right)\left(1 + j\omega R_C c_{p,R}\right)} \tag{3-122}$$

From the above equation we can see that there are 2 poles and 1 zero. These are

$$f_{p1} = \frac{1}{2\pi R_A c_{p,R}}$$

$$f_{p2} = \frac{1}{2\pi R_C c_{p,R}}$$

$$f_z = \frac{R_{F,eq}}{6\pi R_A R_C c_{p,R}}$$

If $A_{ol} = \infty$ and $c_{p,R} = 0$ in equation $(3-110)$, then the transfer function reduces to

$$G_T = \frac{R_{F,eq}}{1 + j2\pi f R_{F,eq} c_f}$$

From the above expression we can see there is one pole at

$$f_{p3} = \frac{1}{2\pi R_{F,eq} c_f}$$

There is another pole, though its derivation is not as simple as those described above [31]. This one is related to the op-amp's gain-bandwidth product, the transimpedance gain, and the input capacitance. It is defined as

$$f_{p4} = \sqrt{\frac{GBW}{2\pi R_{F,eq} c_{in}}}$$

Of poles f_{p1}, f_{p2}, f_{p3}, and f_{p4}, the one which is the smallest will be the best approximation of the amplifier's cutoff frequency.

3.3 AC-Coupled Amplifier Topologies

To determine if there is any advantage to AC-coupling in the first stage, we will analyze the inherent noise produced by each topology to create an equation for its SNR. Then compare the SNR of each of the topologies in Figure 3-5. It seems logical that if the offset is removed in the first stage, the gain can be increased and therefore circuits with AC-coupling in the 1st stage should have a higher SNR than those with DC-coupling in the 1st stage. The following sections will show, however, that this is not the case.

For the analysis, we will model all op-amps as having infinite gain. The reason for this being that the op-amp's internal poles will only have an effect at higher frequencies beyond the low-pass cutoff f_L. These effects will be further attenuated by a 2nd stage high-order filter (not shown in the figure) described in section 1.3.1 equation $(1-12)$. The op-amp in the forward path of the circuits will be modeled as having common mode and differential mode input capacitance, c_{cm} and c_{dm} respectively, which will combine in parallel with the photodiode's junction capacitance c_j to produce c_{in} (see equation $(3-2)$). The op-amp in the forward path of each circuit will be modeled as having input current shot noise, thermal noise, and flicker noise whereas the op-amp in the feedback path will be modeled as having only thermal and flicker noise. This is because the input current noise for the feedback op-amps will not be connected to a high impedance like those in the forward path.

The figure below shows a generic low-pass filter in the feedback path to cancel the low-frequency input. It is possible to implement these circuits with a variety of different low-pass filters so long as the feedback loop is properly stabilized. Our analysis, however, will replace the LPF with an integrator for simplicity.

In most bio-signal detection applications, the high-pass cutoff frequency f_H is typically very low ~50mHz [14], while the low-pass cutoff frequency can be anywhere from 300-2kHz [15, 7, 3, 11, 2]. Thus it is safe to say that $f_L \gg f_H$ which will greatly simplify the integration of the noise density.

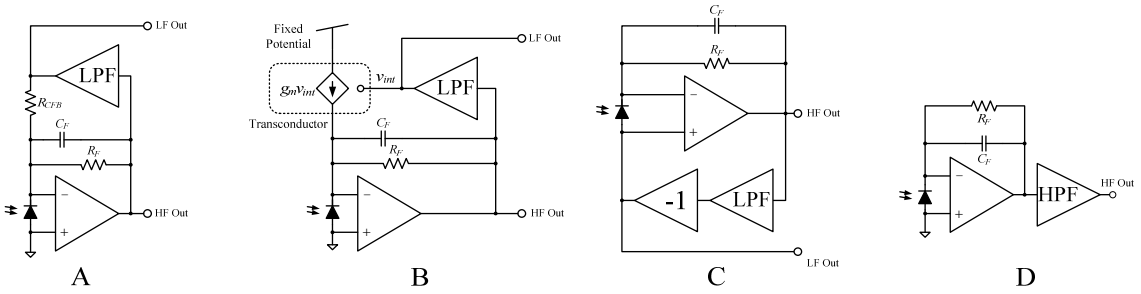

Figure 3-5: AC-coupled photodiode amplifier topologies.

3.3.1 *Active Current Feedback Using a Resistor*

The topology in Figure 3-5A uses active current feedback to remove the DC component of the signal. The low-pass filter isolates the DC component of the output and then subtracts it by injecting a current back into the input. The voltage output of the LPF is converted to a current by the resistor R_{CFB}. This sets the high-pass cutoff frequency at

$$f_H = \frac{R_F}{R_{CFB}} f_L \qquad (3-123)$$

where f_L is the cutoff frequency of the low-pass filter. The low-pass cutoff of the amplifier is then determined by

$$f_L = \frac{1}{2\pi R_F C_F} \qquad (3-124)$$

The resistor R_{CFB} also determines the maximum amount of current offset that can be removed. This limit is defined as

$$\bar{\iota_p} \leq \frac{V_{CC}}{R_{CFB}} \qquad (3-125)$$

Where V_{CC} is the supply rail voltage.

Figure 3-6 shows the noise model for the amplifier and photodiode. For this analysis we will use an op-amp model with infinite gain for the forward-path and feedback-path op-amps.

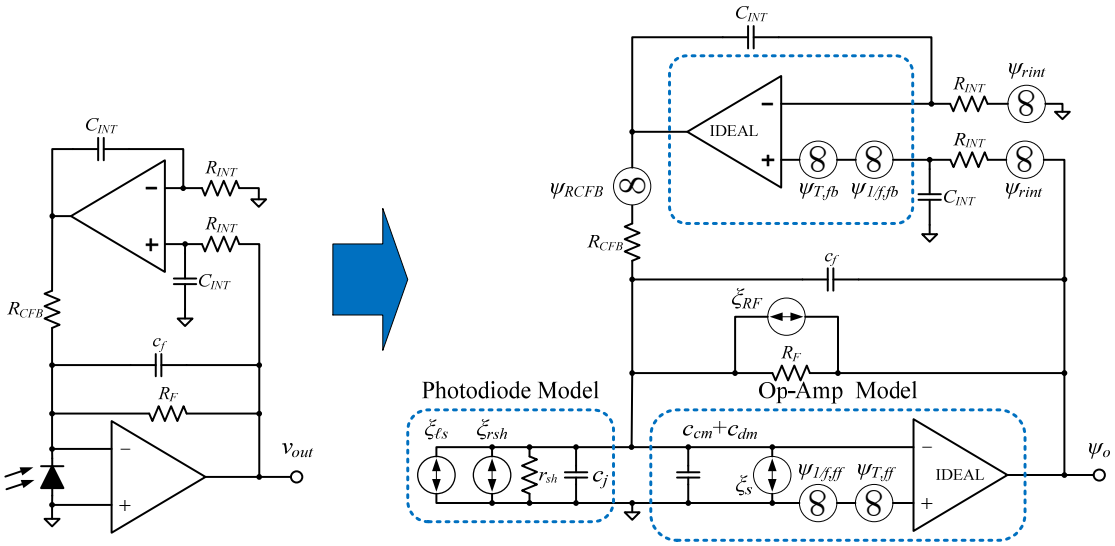

Figure 3-6: Photodiode amplifier with active current feedback (left) and corresponding noise model (right).

Performing circuit analysis for each individual noise source yields an expression for each. The feedback resistor thermal noise transfer function is shown below.

$$\frac{\psi_{o,RF}}{\xi_{RF}} = R_F \frac{j2\pi f R_{INT} C_{INT} \frac{R_{CFB}}{R_F}}{1 + j2\pi f R_{INT} C_{INT} \frac{R_{CFB}}{R_F}\left(1 + j2\pi f R_F c_f\right)} \qquad (3-126)$$

The noise density is then

$$\left|\psi_{o,RF}\right| = \frac{\left|2\pi f R_{INT} C_{INT} \frac{R_{CFB}}{R_F}\right| \sqrt{4kTR_F}}{\sqrt{\left(1-(2\pi f)^2 R_{INT} C_{INT} R_{CFB} c_f\right)^2 + f^2 \left(2\pi R_{INT} C_{INT} \frac{R_{CFB}}{R_F}\right)^2}} \quad (3-127)$$

Assuming that $f_L \gg f_H$, the transfer function in $(3-126)$ is the same form as that in $(1-8)$, we can use equation $(1-13)$ as the result of the integral. We then have

$$v_{n,RF} = \sqrt{\int_0^\infty |G_{LPF}|^2 \left|\psi_{o,RF}\right|^2 df} = \sqrt{\int_0^{\frac{\pi}{2} f_L} \left|\psi_{o,RF}\right|^2 df} = \sqrt{4kTR_F f_L} \quad (3-128)$$

The transfer function seen by the R_{CFB} thermal noise is

$$\frac{\psi_{o,RCFB}}{\psi_{RCFB}} = -\frac{R_F}{R_{CFB}} \frac{j2\pi f R_{INT} C_{INT} \frac{R_{CFB}}{R_F}}{1 + j2\pi f R_{INT} C_{INT} \frac{R_{CFB}}{R_F}\left(1 + j2\pi f R_F c_f\right)} \quad (3-129)$$

The noise density is then

$$\left|\psi_{o,RCFB}\right| = \frac{R_F}{R_{CFB}} \frac{\left|2\pi f R_{INT} C_{INT} \frac{R_{CFB}}{R_F}\right| \sqrt{4kTR_{CFB}}}{\sqrt{(1-(2\pi f)^2 C_{INT} R_{INT} R_{CFB} C_F)^2 + f^2 \left(2\pi C_{INT} R_{INT} \frac{R_{CFB}}{R_F}\right)^2}} \quad (3-130)$$

Assuming that $f_L \gg f_H$, the RMS noise voltage is

$$v_{n,RCFB} = \sqrt{\int_0^\infty |G_{LPF}|^2 \left|\psi_{o,RCFB}\right|^2 df} = \sqrt{\int_0^{\frac{\pi}{2} f_L} \left|\psi_{o,RCFB}\right|^2 df}$$

$$= \frac{R_F}{R_{CFB}} \sqrt{4kTR_{CFB} f_L} \quad (3-131)$$

The forward-path op-amp thermal noise sees the transfer function shown below

$$\frac{\psi_{o,T,ff}}{\psi_{T,ff}} = \left(1 + \frac{R_F}{R_{CFB} \parallel r_{sh}}\right) \frac{jf/f_H(1 + jf/f_z)}{1 + jf/f_H(1 + jf/f_L)} \qquad (3-132)$$

where

$$f_H = \frac{R_F}{2\pi R_{INT} C_{INT} R_{CFB}} \qquad (3-133)$$

$$f_z = \frac{1}{2\pi R_F \parallel r_{sh} \parallel R_{CFB}(c_f + c_{in})} \qquad (3-134)$$

$$f_p = f_L = \frac{1}{2\pi R_F c_f} \qquad (3-135)$$

The noise density is then

$$\left|\psi_{o,T,ff}\right| = \left(1 + \frac{R_F}{R_{CFB} \parallel r_{sh}}\right) \frac{|f/f_H|\sqrt{1 + f^2/f_z^2}}{\sqrt{\left(1 - f^2/(f_H f_L)\right)^2 + f^2/f_H^2}} \psi_{T,ff} \qquad (3-136)$$

Assuming that $f_L \gg f_H$, the RMS noise at the output is then

$$v_{n,T,ff} = \sqrt{\int_0^\infty |G_{LPF}|^2 \left|\psi_{o,T,ff}\right|^2 df} = \sqrt{\int_0^{\frac{\pi}{2}f_L} \left|\psi_{o,T,fb}\right|^2 df}$$

$$= \left(1 + \frac{R_F}{R_{CFB} \parallel r_{sh}}\right) \psi_{T,ff} \sqrt{\int_0^{\frac{\pi}{2}f_L} \frac{1 + f^2/f_z^2}{1 + f^2/f_L} df}$$

$$v_{n,T,ff} = \left(1 + \frac{R_F}{R_{CFB} \parallel r_{sh}}\right) \psi_{T,ff} \sqrt{\left(\left(\frac{\pi}{2} - 1\right)\frac{f_L^2}{f_z^2} + 1\right) f_L} \qquad (3-137)$$

Assuming that $(\pi/2 - 1)(f_L/f_z)^2 \gg 1$

$$v_{n,T,ff} = \left(1 + \frac{R_F}{R_{CFB} \parallel r_{sh}}\right) \psi_{T,ff} \frac{f_L}{f_z} \sqrt{\left(\frac{\pi}{2} - 1\right) f_L} \qquad (3-138)$$

Substitute $(3-134)$ into $(3-138)$

$$v_{n,T,ff} = 2\pi R_F(c_f + c_{in})f_L\psi_{T,ff}\sqrt{\left(\frac{\pi}{2}-1\right)f_L} \qquad (3-139)$$

For high-gain applications $c_{in} \gg c_f$, the above equation then becomes

$$v_{n,T,ff} = 2\pi R_F c_{in} f_L \psi_{T,ff}\sqrt{\left(\frac{\pi}{2}-1\right)f_L} \qquad (3-140)$$

The forward-path op-amp flicker noise sees the same transfer function as the thermal noise. Using equation $(3-132)$, we get

$$\frac{\psi_{o,1/f,ff}}{\psi_{1/f,ff}} = \left(1+\frac{R_F}{R_{CFB} \parallel r_{sh}}\right)\frac{jf/f_H(1+jf/f_z)}{1+jf/f_H(1+jf/f_L)} \qquad (3-141)$$

The noise density is then

$$\left|\psi_{o,1/f,ff}\right| = \left(1+\frac{R_F}{R_{CFB} \parallel r_{sh}}\right)\frac{|f/f_H|\sqrt{1+f^2/f_z^2}}{\sqrt{\left(1-f^2/(f_H f_L)\right)^2 + f^2/f_H^2}}\frac{FNN_{ff}}{\sqrt{f}} \qquad (3-142)$$

The RMS noise voltage is then

$$v_{n,1/f,ff} = \sqrt{\int_0^\infty |G_{LPF}|^2 \left|\psi_{o,1/f,ff}\right|^2 df} = \sqrt{\int_0^{\frac{\pi}{2}f_L} \left|\psi_{o,1/f,ff}\right|^2 df}$$

$$= \left(1+\frac{R_F}{R_{CFB} \parallel r_{sh}}\right) FNN_{ff}\sqrt{\int_{f_0}^{\frac{\pi}{2}f_L} \frac{1+f^2/f_z^2}{1+f^2/f_L}\frac{1}{f}df}$$

$$v_{n,1/f,ff} = \left(1+\frac{R_F}{R_{CFB} \parallel r_{sh}}\right), FNN_{ff}\sqrt{\ln\left(\frac{\pi}{2}\frac{f_L}{f_0}\right) + \frac{1}{2}\left(\frac{f_L^2}{f_z^2}-1\right)\ln\left(\frac{\left(\frac{\pi}{2}f_L\right)^2 + f_L^2}{f_0^2+f_L^2}\right)} \qquad (3-143)$$

If $f_L^2 \gg f_0^2$

$$v_{n,1/f,ff} = \left(1 + \frac{R_F}{R_{CFB} \parallel r_{sh}}\right) FNN_{ff} \sqrt{\ln\left(\frac{\pi}{2}\frac{f_L}{f_0}\right) + \frac{\ln\left(1+\frac{\pi^2}{4}\right)}{2}\left(\frac{f_L^2}{f_z^2} - 1\right)} \qquad (3-144)$$

If $f_0 = 1\text{mHz}$, $f_L \gg f_z$ and $f_L \gg 1\text{Hz}$

$$v_{n,1/f,ff} = \left(1 + \frac{R_F}{R_{CFB} \parallel r_{sh}}\right) FNN_{ff} \frac{f_L}{f_z} \sqrt{\frac{\ln\left(1+\frac{\pi^2}{4}\right)}{2}} \qquad (3-145)$$

Substitute $(3-134)$ into $(3-145)$

$$v_{n,1/f,ff} = 2\pi R_F (c_f + c_{in}) f_L FNN_{ff} \sqrt{\frac{\ln\left(1+\frac{\pi^2}{4}\right)}{2}} \qquad (3-146)$$

For high-gain applications $c_{in} \gg c_f$

$$v_{n,1/f,ff} = 2\pi R_F c_{in} f_L FNN_{ff} \sqrt{\frac{\ln\left(1+\frac{\pi^2}{4}\right)}{2}} \qquad (3-147)$$

The transfer function of the forward-path op-amp current noise is

$$\frac{\psi_{o,s,ff}}{\xi_{s,ff}} = R_F \frac{j2\pi f R_{INT} C_{INT} \frac{R_{CFB}}{R_F}}{1 + j2\pi f R_{INT} C_{INT} \frac{R_{CFB}}{R_F}\left(1 + j2\pi f R_F c_f\right)} \qquad (3-148)$$

The noise density is then

$$\left|\psi_{o,s,ff}\right| = \frac{R_F \xi_s \left|2\pi f R_{INT} C_{INT} \frac{R_{CFB}}{R_F}\right|}{\sqrt{\left(1 - (2\pi f)^2 R_{INT} C_{INT} R_{CFB} c_f\right)^2 + f^2 \left(2\pi R_{INT} C_{INT} \frac{R_{CFB}}{R_F}\right)^2}} \qquad (3-149)$$

Assuming that $f_L \gg f_H$, the RMS noise voltage is

$$v_{n,s,ff} = \sqrt{\int_0^\infty |G_{LPF}|^2 \left|\psi_{o,s,ff}\right|^2 df} = \sqrt{\int_0^{\frac{\pi}{2}f_L} \left|\psi_{o,s,ff}\right|^2 df} = R_F \xi_s \sqrt{f_L} \qquad (3-150)$$

The photodiode thermal noise current sees the same transfer function as the op-amp input current shot noise. Using equation $(3-148)$ we have

$$\frac{\psi_{o,rsh}}{\xi_{rsh}} = R_F \frac{j2\pi f R_{INT} C_{INT} \frac{R_{CFB}}{R_F}}{1 + j2\pi f R_{INT} C_{INT} \frac{R_{CFB}}{R_F}\left(1 + j2\pi f R_F c_f\right)} \qquad (3-151)$$

The noise density is then

$$\left|\psi_{o,rsh}\right| = \frac{R_F \left|2\pi f R_{INT} C_{INT} \frac{R_{CFB}}{R_F}\right| \sqrt{\frac{4kT}{r_{sh}}}}{\sqrt{\left(1 - (2\pi f)^2 R_{INT} C_{INT} R_{CFB} c_f\right)^2 + f^2 \left(2\pi R_{INT} C_{INT} \frac{R_{CFB}}{R_F}\right)^2}} \qquad (3-152)$$

Assuming that $f_L \gg f_H$, the RMS noise voltage is

$$v_{n,rsh} = \sqrt{\int_0^\infty |G_{LPF}|^2 \left|\psi_{o,rsh}\right|^2 df} = \sqrt{\int_0^{\frac{\pi}{2}f_L} \left|\psi_{o,rsh}\right|^2 df} = R_F \sqrt{\frac{4kT}{rsh} f_L} \qquad (3-153)$$

The transfer function seen by thermal noise from the op-amp in the feedback path is

$$\frac{\psi_{o,T,fb}}{\psi_{T,fb}} = -\frac{1 + j2\pi f R_{INT} C_{INT}}{1 + j2\pi f R_{INT} C_{INT} \frac{R_{CFB}}{R_F}\left(1 + j2\pi f R_F c_f\right)} \qquad (3-154)$$

From the above transfer function we can see that there is one zero

$$f_z = \frac{1}{2\pi R_{INT} C_{INT}} \qquad (3-155)$$

and 2 poles

$$f_{p1} = f_H = \frac{R_F}{2\pi R_{INT} C_{INT} R_{CFB}} \tag{3-156}$$

$$f_{p2} = f_L = \frac{1}{2\pi R_F c_f} \tag{3-157}$$

The noise density is then

$$\left|\psi_{o,T,fb}\right| = \frac{\sqrt{1 + f^2(2\pi C_{INT} R_{INT})^2}}{\sqrt{\left(1 - (2\pi f)^2 C_{INT} R_{INT} R_{CFB} c_f\right)^2 + f^2\left(2\pi R_{INT} C_{INT} \frac{R_{CFB}}{R_F}\right)^2}} \psi_{T,fb} \tag{3-158}$$

The RMS noise at the output is then

$$v_{n,T,fb} = \sqrt{\int_0^\infty |G_{LPF}|^2 \left|\psi_{o,T,fb}\right|^2 df} = \sqrt{\int_0^{\frac{\pi}{2} f_L} \left|\psi_{o,T,fb}\right|^2 df} \tag{3-159}$$

$$v_{n,T,fb} = \psi_{T,fb} \sqrt{\int_0^{\frac{\pi}{2} f_L} \frac{1 + f^2/f_z^2}{1 + f^2/f_{p1}} df} \tag{3-160}$$

$$v_{n,T,fb} = \psi_{T,fb} \sqrt{\frac{f_{p1}}{f_z^2}\left(\frac{\pi}{2} f_L f_{p1} + \tan^{-1}\left(\frac{\frac{\pi}{2} f_L}{f_{p1}}\right)\left(f_z^2 - f_{p1}^2\right)\right)} \tag{3-161}$$

If $f_L \gg f_{p1}$

$$v_{n,T,fb} = \psi_{T,fb} \sqrt{\frac{\pi}{2}\left(\frac{f_{p1}^2}{f_z^2}(f_L - 1) + f_{p1}\right)} \tag{3-162}$$

If $f_L \gg 1$ and $\frac{f_{p1}^2}{f_z^2} f_L \gg f_{p1}$

$$v_{n,T,fb} = \psi_{T,fb}\frac{f_{p1}}{f_z}\sqrt{\frac{\pi}{2}f_L} \qquad (3-163)$$

Substitute $(3-155)$ and $(3-156)$ into $(3-163)$

$$v_{n,T,fb} = \psi_{T,fb}\frac{R_F}{R_{CFB}}\sqrt{\frac{\pi}{2}f_L} \qquad (3-164)$$

The feedback op-amp flicker noise sees the same transfer function as the thermal noise. Hence we can use equation $(3-154)$ to write

$$\frac{\psi_{o,1/f,fb}}{\psi_{1/f,fb}} = -\frac{1+j2\pi f R_{INT}C_{INT}}{1+j2\pi f R_{INT}C_{INT}\frac{R_{CFB}}{R_F}\left(1+j2\pi f R_F c_f\right)} \qquad (3-165)$$

Similarly, the noise density at the output due to op-amp flicker noise is

$$\left|\psi_{o,1/f,fb}\right| = \frac{\sqrt{1+f^2(2\pi C_{INT}R_{INT})^2}}{\sqrt{\left(1-(2\pi f)^2 C_{INT}R_{INT}R_{CFB}c_f\right)^2 + f^2\left(2\pi R_{INT}C_{INT}\frac{R_{CFB}}{R_F}\right)^2}}\frac{FNN_{fb}}{\sqrt{f}} \qquad (3-166)$$

The RMS noise at the output is then

$$v_{n,1/f,fb} = \sqrt{\int_0^\infty |G_{LPF}|^2\left|\psi_{o,1/f,fb}\right|^2 df} = \sqrt{\int_0^{\frac{\pi}{2}f_L}\left|\psi_{o,1/f,fb}\right|^2 df} \qquad (3-167)$$

$$v_{n,1/f,fb} = FNN_{fb}\sqrt{\int_0^{\frac{\pi}{2}f_L}\frac{1+f^2/f_z^2}{1+f^2/f_{p1}}\frac{1}{f}df} \qquad (3-168)$$

$$v_{n,1/f,fb} = FNN_{fb}\sqrt{\ln\left(\frac{\pi}{2}\frac{f_L}{f_0}\right)+\frac{1}{2}\left(\frac{f_{p1}^2}{f_z^2}-1\right)\ln\left(\frac{\left(\frac{\pi}{2}f_L\right)^2+f_{p1}^2}{f_0^2+f_{p1}^2}\right)} \qquad (3-169)$$

If $f_{p1}^2 \gg f_0^2$

$$v_{n,1/f,fb} = FNN_{fb}\sqrt{\ln\left(\frac{\pi}{2}\frac{f_L}{f_0}\right) + \frac{1}{2}\left(\frac{f_{p1}^2}{f_z^2} - 1\right)\ln\left(1 + \frac{\left(\frac{\pi}{2}f_L\right)^2}{f_{p1}^2}\right)} \qquad (3-170)$$

Insert $(3-155)$ and $(3-156)$ into $(3-170)$

$$v_{n,1/f,fb} = FNN_{fb}\sqrt{\ln\left(\frac{\pi}{2}\frac{f_L}{f_0}\right) + \frac{1}{2}\left(\left(\frac{R_F}{R_{CFB}}\right)^2 - 1\right)\ln\left(1 + \left(\frac{\pi}{2}\frac{f_L}{f_H}\right)^2\right)} \qquad (3-171)$$

If $\left(\frac{\pi}{2}\frac{f_L}{f_H}\right)^2 \gg 1$, then

$$v_{n,1/f,fb} = FNN_{fb}\sqrt{\ln\left(\frac{\pi}{2}\frac{f_L}{f_0}\right) + \left(\left(\frac{R_F}{R_{CFB}}\right)^2 - 1\right)\ln\left(\frac{\pi}{2}\frac{f_L}{f_H}\right)} \qquad (3-172)$$

If $R_F^2/R_{CFB}^2 \gg 1$, then

$$v_{no,1/f,fb} = FNN_{fb}\sqrt{\ln\left(\frac{\pi}{2}\frac{f_L}{f_0}\right) + \left(\frac{R_F}{R_{CFB}}\right)^2\ln\left(\frac{\pi}{2}\frac{f_L}{f_H}\right)} \qquad (3-173)$$

If $\left(\frac{R_F}{R_{CFB}}\right)^2\ln\left(\frac{\pi}{2}\frac{f_L}{f_H}\right) \gg \ln\left(\frac{\pi}{2}\frac{f_L}{f_0}\right)$, then

$$v_{n,1/f,fb} = \frac{R_F}{R_{CFB}}FNN_{fb}\sqrt{\ln\left(\frac{\pi}{2}\frac{f_L}{f_H}\right)} \qquad (3-174)$$

The transfer function seen by the integrator resistor thermal noise is shown below.

$$\frac{\psi_{o,RINT}}{\psi_{RINT}} = -\frac{1}{1 + j2\pi f R_{INT}C_{INT}\frac{R_{CFB}}{R_F}\left(1 + j2\pi f R_F c_f\right)} \qquad (3-175)$$

From the above transfer function we can see 2 poles

$$f_{p1} = f_H = \frac{R_F}{2\pi R_{INT}C_{INT}R_{CFB}}$$

$$f_{p2} = f_L = \frac{1}{2\pi R_F c_f}$$

$$\left|\psi_{o,RINT}\right| = \frac{\sqrt{4kTR_{INT}}}{\sqrt{\left(1-(2\pi f)^2 C_{INT} R_{INT} R_{CFB} c_f\right)^2 + f^2\left(2\pi R_{INT} C_{INT}\frac{R_{CFB}}{R_F}\right)^2}} \quad (3-176)$$

The RMS noise at the output is then

$$v_{n,RINT} = \sqrt{\int_0^\infty |G_{LPF}|^2 \left|\psi_{o,RINT}\right|^2 df} = \sqrt{\int_0^{\frac{\pi}{2}f_L} \left|\psi_{o,RINT}\right|^2 df}$$

If $f_L \gg f_H$, we can use the noise equivalent bandwidth of a first order low-pass system with cutoff frequency f_H

$$v_{n,RINT} = \sqrt{2\pi kTR_{INT} f_H} \quad (3-177)$$

The noise transfer function, noise density and RMS noise voltage is the same for both resistors.

The photocurrent shot noise sees the same transfer function as the photodiode thermal noise current. Using equation $(3-151)$, we can write

$$\frac{\psi_{o,\ell s}}{\xi_{\ell s}} = R_F \frac{j2\pi f R_{INT} C_{INT}\frac{R_{CFB}}{R_F}}{1 + j2\pi f R_{INT} C_{INT}\frac{R_{CFB}}{R_F}\left(1 + j2\pi f R_F c_f\right)} \quad (3-178)$$

The noise density is then

$$\left|\psi_{o,\ell s}\right| = \frac{R_F\left|2\pi f R_{INT} C_{INT}\frac{R_{CFB}}{R_F}\right|\sqrt{2q\bar{\imath}_p}}{\sqrt{\left(1-(2\pi f)^2 R_{INT} C_{INT} R_{CFB} c_f\right)^2 + f^2\left(2\pi R_{INT} C_{INT}\frac{R_{CFB}}{R_F}\right)^2}} \quad (3-179)$$

Assuming that $f_L \gg f_H$, the RMS noise voltage is

$$v_{no,light} = \sqrt{\int_0^{\infty} |G_{LPF}|^2 \left|\psi_{o,\ell s}\right|^2 df} = \sqrt{\int_0^{\frac{\pi}{2} f_L} \left|\psi_{o,\ell s}\right|^2 df} = R_F \sqrt{2q\bar{\imath_p} f_L} \quad (3-180)$$

The total dark noise is the quadratic sum of all the noise sources inherent to the amplifier when no illumination is present.

$$v_{n,dark} = \sqrt{\begin{matrix} v_{n,T,ff}^2 + v_{n,1/f,ff}^2 + v_{n,s,ff}^2 + v_{n,RF}^2 \\ +v_{n,RCFB}^2 + v_{n,rsh}^2 + v_{n,T,fb}^2 + v_{n,1/f,fb}^2 + 2v_{n,RINT}^2 \end{matrix}} \quad (3-181)$$

Substitute $(3-140)$, $(3-147)$, $(3-150)$, $(3-128)$, $(3-131)$, $(3-153)$, $(3-164)$, $(3-174)$ and $(3-177)$ into $(3-181)$

$$v_{n,dark} = \sqrt{R_F^2 \left(\xi_s^2 + \frac{4kT}{rsh} + \frac{4kT}{R_{CFB}} + (2\pi c_{in})^2 \gamma f_L\right) f_L + R_F \beta f_L + \kappa_{INT}} \quad (3-182)$$

$$\beta = 4kT \quad (3-183)$$

$$\gamma = \psi_{T,ff}^2 \left(\frac{\pi}{2} - 1\right) f_L + FNN_{ff}^2 \frac{\ln\left(1 + \frac{\pi^2}{4}\right)}{2} \quad (3-184)$$

$$\kappa_{INT} = \left(\frac{R_F}{R_{CFB}}\right)^2 \left(\psi_{T,fb}^2 \frac{\pi}{2} f_L + FNN_{fb}^2 \ln\left(\frac{\pi}{2} \frac{f_L}{f_H}\right)\right) + 4\pi kT R_{INT} f_H \quad (3-185)$$

The total noise is the quadratic sum of the light and dark noise components.

$$v_{n,total} = \sqrt{v_{n,dark}^2 + v_{n,light}^2} \quad (3-186)$$

$$v_{n,total} = \sqrt{R_F^2 \alpha' f_L + R_F^2 \left(\frac{4kT}{R_{CFB}} + 2q\bar{\imath_p}\right) f_L + R_F \beta f_L + \kappa_{INT}} \quad (3-187)$$

$$\alpha' = \xi_s^2 + \frac{4kT}{rsh} + (2\pi c_{in})^2 \gamma f_L \qquad (3-188)$$

The input signal is

$$i_p = i_{p,sig} + \bar{i_p}$$

Where $i_{p,sig}$ represents the signal current amplitude and is related to the RMS signal current by a scaling factor. The SNR is then

$$SNR = \frac{R_F \tilde{i_p}}{\sqrt{R_F^2 \alpha' f_L + R_F^2 \left(\frac{4kT}{R_{CFB}} + 2q\bar{i_p}\right) f_L + R_F \beta f_L + \kappa_{INT}}} \qquad (3-189)$$

$$SNR = \frac{R_F \tilde{i_p}}{\sqrt{R_F^2 \alpha' f_L + 4kTR_F \left(\left(\frac{1}{R_{CFB}} + \frac{1}{2}\frac{q}{kT}\bar{i_p}\right) R_F + 1\right) f_L + \kappa_{INT}}} \qquad (3-190)$$

The noise produced by R_{CFB} is inversely proportional to the size of the resistor, R_{CFB} should therefore be made as large as possible. Hence

$$R_{CFB} = \frac{V_{CC}}{\bar{i_p}} \qquad (3-191)$$

Substitute $(3-191)$ into $(3-190)$

$$SNR = \frac{R_F \tilde{i_p}}{\sqrt{R_F^2 \alpha' f_L + 4kTR_F \left(1 + \left(1 + \frac{1}{2}\frac{q}{kT}V_{CC}\right)\frac{\bar{i_p}}{V_{CC}} R_F\right) f_L + \kappa_{INT}}} \qquad (3-192)$$

The maximum value of R_F is

$$R_F = \frac{V_{CC}}{i_{p,sig}} \qquad (3-193)$$

Substitute $(3-193)$ into $(3-192)$

$$SNR = \frac{V_{CC}\,\frac{\widetilde{\imath_p}}{i_{p,sig}}}{\sqrt{\left(\frac{V_{CC}}{i_{p,sig}}\right)^2 \alpha' f_L + 4kT\left(\frac{V_{CC}}{i_{p,sig}}\right)\left(1+\left(1+\frac{1}{2}\frac{q}{kT}V_{CC}\right)\frac{\overline{\imath_p}}{i_{p,sig}}\right) f_L + \kappa_{INT}}} \qquad (3-194)$$

3.3.2 *Active Current Feedback Using a Transconductor*

The topology in Figure 3-5B also uses active current feedback. However, in this case it is implemented with a transconductor instead of a resistor. This circuit has theoretically no limit on the current offset that it can remove. Though in practice, it is limited by the parameters of the transconductor and the supply voltage. For this analysis, however, we will assume that no such limit exists.

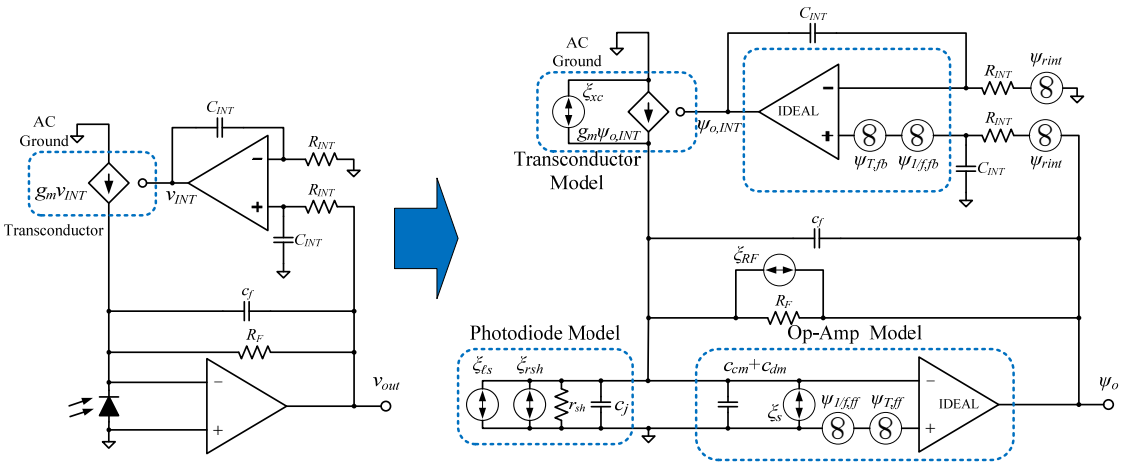

Figure 3-7: Schematic of amplifier using a transconductor for offset removal (left) and the corresponding noise model (right).

The transfer function seen by the feedback resistor current noise is

$$\frac{\psi_{o,RF}}{\xi_{RF}} = R_F \frac{j2\pi f \frac{R_{INT}C_{INT}}{R_F g_m}}{1 + j2\pi f \frac{R_{INT}C_{INT}}{R_F g_m}\left(1 + j2\pi f R_F c_f\right)} \qquad (3-195)$$

The noise density is then

$$\left|\psi_{o,RF}\right| = \frac{\left|2\pi f \frac{R_{INT}C_{INT}}{R_F g_m}\right| \sqrt{4kTR_F}}{\sqrt{\left(1 - (2\pi f)^2 \frac{R_{INT}C_{INT}c_f}{g_m}\right)^2 + f^2\left(2\pi \frac{R_{INT}C_{INT}}{R_F g_m}\right)^2}} \qquad (3-196)$$

Assuming that $f_L \gg f_H$, the RMS noise at the output is then

$$v_{no,RF} = \sqrt{\int_0^\infty |G_{LPF}|^2 \left|\psi_{o,RF}\right|^2 df}$$

$$= \sqrt{\int_0^{\frac{\pi}{2}f_L} \left|\psi_{o,RF}\right|^2 df} = \sqrt{4kTR_F f_L} \qquad (3-197)$$

The shot noise produced by the transconductor sees the transfer function shown below.

$$\frac{\psi_{o,xc}}{\xi_{xc}} = R_F \frac{j2\pi f \frac{R_{INT}C_{INT}}{R_F g_m}}{1 + j2\pi f \frac{R_{INT}C_{INT}}{R_F g_m}\left(1 + j2\pi f R_F c_f\right)} \qquad (3-198)$$

The noise density is then

$$\left|\psi_{o,xc}\right| = R_F \frac{\left|2\pi f \frac{R_{INT}C_{INT}}{R_F g_m}\right| \sqrt{2q\bar{i}_p}}{\sqrt{\left(1 - (2\pi f)^2 \frac{R_{INT}C_{INT}c_f}{g_m}\right)^2 + f^2\left(2\pi \frac{R_{INT}C_{INT}}{R_F g_m}\right)^2}} \qquad (3-199)$$

Assuming that $f_L \gg f_H$, the RMS noise at the output is then

$$v_{n,xc} = \sqrt{\int_0^\infty |G_{LPF}|^2 \left|\psi_{o,xc}\right|^2 df}$$

$$= \sqrt{\int_0^{\frac{\pi}{2}f_L} \left|\psi_{o,xc}\right|^2 df} = R_F\sqrt{2q\bar{\imath_p}f_L} \qquad (3-200)$$

The forward-path op-amp thermal noise sees the transfer function below.

$$\frac{\psi_{o,T,ff}}{\psi_{T,ff}} = \left(1+\frac{R_F}{r_{sh}}\right)\frac{j2\pi f\frac{R_{INT}C_{INT}}{R_F g_m}\left(1+j2\pi f R_F \parallel r_{sh}\left(c_{in}+c_f\right)\right)}{1+j2\pi f\frac{R_{INT}C_{INT}}{R_F g_m}\left(1+j2\pi f R_F c_f\right)} \qquad (3-201)$$

From the above transfer function we can see that there are 2 zeros

$$f_{z1} = f_H = \frac{R_F g_m}{2\pi R_{INT}C_{INT}} \qquad (3-202)$$

and

$$f_{z2} = \frac{1}{2\pi R_F \parallel r_{sh}\left(c_{in}+c_f\right)} \qquad (3-203)$$

and 2 poles

$$f_{p1} = f_H = \frac{R_F g_m}{2\pi R_{INT}C_{INT}} \qquad (3-204)$$

and

$$f_{p2} = \frac{1}{2\pi R_F c_f} \qquad (3-205)$$

The noise density is then

$$\left|\psi_{o,T,ff}\right| = \left(1+\frac{R_F}{r_{sh}}\right)\frac{\left|2\pi f\frac{R_{INT}C_{INT}}{R_F g_m}\right|\sqrt{1+f^2\left(2\pi R_F \parallel r_{sh}\left(c_{in}+c_f\right)\right)^2}}{\sqrt{\left(1-(2\pi f)^2\frac{R_{INT}C_{INT}c_f}{g_m}\right)^2+f^2\left(2\pi\frac{R_{INT}C_{INT}}{R_F g_m}\right)^2}}\psi_{T,ff} \qquad (3-206)$$

Assuming that $f_L \gg f_H$, the RMS noise at the output is then

$$v_{n,T,ff} = \sqrt{\int_0^\infty |G_{LPF}|^2\left|\psi_{o,T,ff}\right|^2 df} = \sqrt{\int_0^{\frac{\pi}{2}f_L}\left|\psi_{o,T,ff}\right|^2 df}$$

$$= \left(1+\frac{R_F}{r_{sh}}\right)\psi_{T,ff}\sqrt{\int_0^{\frac{\pi}{2}f_L}\frac{1+f^2/f_{z2}^2}{1+f^2/f_L}df}$$

$$v_{n,T,ff} = \left(1+\frac{R_F}{r_{sh}}\right)\psi_{T,ff}\sqrt{\left(\left(\frac{\pi}{2}-1\right)\frac{f_L^2}{f_{z2}^2}+1\right)f_L} \qquad (3-207)$$

Assuming that $(\pi/2-1)(f_L/f_{z2})^2 \gg 1$

$$v_{n,T,ff} = \left(1+\frac{R_F}{r_{sh}}\right)\psi_{T,ff}\frac{f_L}{f_{z2}}\sqrt{\left(\frac{\pi}{2}-1\right)f_L} \qquad (3-208)$$

Substitute $(3-203)$ into $(3-208)$

$$v_{n,T,ff} = 2\pi R_F\left(c_{in}+c_f\right)f_L\psi_{T,ff}\sqrt{\left(\frac{\pi}{2}-1\right)f_L} \qquad (3-209)$$

For high-gain applications $c_{in} \gg c_f$, therefore the above expression becomes

$$v_{n,T,ff} = 2\pi R_F c_{in} f_L\psi_{T,ff}\sqrt{\left(\frac{\pi}{2}-1\right)f_L} \qquad (3-210)$$

The op-amp flicker noise sees the same transfer function as the op-amp thermal noise. Using equation $(3-201)$ we have

$$\frac{\psi_{o,1/f,ff}}{\psi_{1/f,ff}} = \left(1+\frac{R_F}{r_{sh}}\right)\frac{j2\pi f\frac{R_{INT}C_{INT}}{R_F g_m}\left(1+j2\pi f R_F \parallel r_{sh}(c_{in}+c_f)\right)}{1+j2\pi f\frac{R_{INT}C_{INT}}{R_F g_m}\left(1+j2\pi f R_F c_f\right)} \quad (3-211)$$

The noise density is then

$$\left|\psi_{o,1/f,ff}\right| = \left(1+\frac{R_F}{r_{sh}}\right)\frac{\left|2\pi f\frac{R_{INT}C_{INT}}{R_F g_m}\right|\sqrt{1+f^2\left(2\pi R_F \parallel r_{sh}(c_{in}+c_f)\right)^2}}{\sqrt{\left(1-(2\pi f)^2\frac{R_{INT}C_{INT}c_f}{g_m}\right)^2+f^2\left(2\pi\frac{R_{INT}C_{INT}}{R_F g_m}\right)^2}}\frac{FNN_{ff}}{\sqrt{f}} \quad (3-212)$$

Assuming that $f_L \gg f_H$, the RMS noise at the output is then

$$v_{n,1/f,ff} = \sqrt{\int_{f_0}^{\infty}|G_{LPF}|^2\left|\psi_{o,1/f,ff}\right|^2 df} = \sqrt{\int_{f_0}^{\frac{\pi}{2}f_L}\left|\psi_{o,1/f,ff}\right|^2 df}$$

$$v_{n,1/f,ff} = \left(1+\frac{R_F}{r_{sh}}\right)FNN_{ff}\sqrt{\int_{f_0}^{\frac{\pi}{2}f_L}\frac{1+f^2/f_{z2}^2}{1+f^2/f_L}\frac{1}{f}df} \quad (3-213)$$

$$v_{n,1/f,ff} = \left(1+\frac{R_F}{r_{sh}}\right)FNN_{ff}\sqrt{\ln\left(\frac{\pi}{2}\frac{f_L}{f_0}\right)+\frac{1}{2}\left(\frac{f_L^2}{f_{z2}^2}-1\right)\ln\left(\frac{\left(\frac{\pi}{2}f_L\right)^2+f_L^2}{f_0^2+f_L^2}\right)} \quad (3-214)$$

If $f_L^2 \gg f_0^2$

$$v_{n,1/f,ff} = \left(1+\frac{R_F}{r_{sh}}\right)FNN_{ff}\sqrt{\ln\left(\frac{\pi}{2}\frac{f_L}{f_0}\right)+\frac{\ln\left(1+\frac{\pi^2}{4}\right)}{2}\left(\frac{f_L^2}{f_{z2}^2}-1\right)} \quad (3-215)$$

If $f_0 = 1\text{mHz}$, $f_L \gg f_z$ and $f_L \gg 1\text{Hz}$

$$v_{n,1/f,ff} = \left(1+\frac{R_F}{r_{sh}}\right)FNN_{ff}\frac{f_L}{f_{z2}}\sqrt{\frac{\ln\left(1+\frac{\pi^2}{4}\right)}{2}} \quad (3-216)$$

Substitute $(3-203)$ into $(3-216)$

$$v_{n,1/f,ff} = 2\pi R_F\left(c_{in}+c_f\right)f_L FNN_{ff}\sqrt{\frac{\ln\left(1+\frac{\pi^2}{4}\right)}{2}} \qquad (3-217)$$

For high-gain applications $c_{in} \gg c_f$, therefore the above expression becomes

$$v_{n,1/f,ff} = 2\pi R_F c_{in} f_L FNN_{ff}\sqrt{\frac{\ln\left(1+\frac{\pi^2}{4}\right)}{2}} \qquad (3-218)$$

The op-amp input current shot noise density sees the transfer function

$$\frac{\psi_{o,s,ff}}{\xi_{s,ff}} = R_F\frac{j2\pi f\frac{R_{INT}C_{INT}}{R_F g_m}}{1+j2\pi f\frac{R_{INT}C_{INT}}{R_F g_m}\left(1+j2\pi f R_F c_f\right)} \qquad (3-219)$$

The noise density is then

$$\left|\psi_{o,s,ff}\right| = \frac{R_F\xi_{s,ff}\left|2\pi f\frac{R_{INT}C_{INT}}{R_F g_m}\right|}{\sqrt{\left(1-(2\pi f)^2\frac{R_{INT}C_{INT}c_f}{g_m}\right)^2+f^2\left(2\pi\frac{R_{INT}C_{INT}}{R_F g_m}\right)^2}} \qquad (3-220)$$

Assuming that $f_L \gg f_H$, the RMS noise at the output is then

$$v_{no,s,ff} = \sqrt{\int_0^\infty |G_{LPF}|^2\left|\psi_{o,s,ff}\right|^2 df}$$

$$= \sqrt{\int_0^{\frac{\pi}{2}f_L}\left|\psi_{o,s,ff}\right|^2 df} = R_F\xi_{s,ff}\sqrt{f_L} \qquad (3-221)$$

The photodiode thermal noise sees the same transfer function as the op-amp input current shot noise. Using equation $(3-219)$ we have

$$\frac{\psi_{o,rsh}}{\xi_{rsh}} = R_F \frac{j2\pi f \frac{R_{INT}C_{INT}}{R_F g_m}}{1 + j2\pi f \frac{R_{INT}C_{INT}}{R_F g_m}\left(1 + j2\pi f R_F c_f\right)} \qquad (3-222)$$

The noise density is then

$$\left|\psi_{o,rsh}\right| = R_F \frac{\left|2\pi f \frac{R_{INT}C_{INT}}{R_F g_m}\right| \sqrt{\frac{4kT}{r_{sh}}}}{\sqrt{\left(1 - (2\pi f)^2 \frac{R_{INT}C_{INT}c_f}{g_m}\right)^2 + f^2\left(2\pi \frac{R_{INT}C_{INT}}{R_F g_m}\right)^2}} \qquad (3-223)$$

Assuming that $f_L \gg f_H$, the RMS noise at the output is then

$$v_{n,rsh} = \sqrt{\int_0^\infty |G_{LPF}|^2 \left|\psi_{o,rsh}\right|^2 df}$$

$$= \sqrt{\int_0^{\frac{\pi}{2}f_L} \left|\psi_{o,rsh}\right|^2 df} = R_F \sqrt{\frac{4kT}{r_{sh}} f_L} \qquad (3-224)$$

The feedback op-amp thermal noise sees the transfer function below.

$$\frac{\psi_{o,T,fb}}{\psi_{T,fb}} = -\frac{1 + j2\pi f R_{INT}C_{INT}}{1 + j2\pi f \frac{R_{INT}C_{INT}}{R_F g_m}\left(1 + j2\pi f R_F c_f\right)} \qquad (3-225)$$

From the transfer function above, we can see that the system has 1 zero

$$f_z = \frac{1}{2\pi R_{INT}C_{INT}} \qquad (3-226)$$

and 2 poles

$$f_{p1} = f_H = \frac{R_F g_m}{2\pi R_{INT} C_{INT}} \tag{3-227}$$

and

$$f_{p2} = f_L = \frac{1}{2\pi R_F c_f} \tag{3-228}$$

The noise density is then

$$\left|\psi_{o,T,fb}\right| = \frac{\sqrt{1 + f^2(2\pi R_{INT} C_{INT})^2}}{\sqrt{\left(1 - (2\pi f)^2 \frac{R_{INT} C_{INT} c_f}{g_m}\right)^2 + f^2 \left(2\pi \frac{R_{INT} C_{INT}}{R_F g_m}\right)^2}} \psi_{T,fb} \tag{3-229}$$

The RMS noise at the output is then

$$v_{n,T,fb} = \sqrt{\int_0^\infty |G_{LPF}|^2 \left|\psi_{o,T,fb}\right|^2 df} = \sqrt{\int_0^{\frac{\pi}{2} f_L} \left|\psi_{o,T,fb}\right|^2 df} \tag{3-230}$$

$$v_{n,T,fb} = \psi_{T,fb} \sqrt{\int_0^{\frac{\pi}{2} f_L} \frac{1 + f^2/f_z^2}{1 + f^2/f_{p1}} df} \tag{3-231}$$

$$v_{n,T,fb} = \psi_{T,fb} \sqrt{\frac{f_{p1}}{f_z^2}\left(\frac{\pi}{2} f_L f_{p1} - \tan^{-1}\left(-\frac{\frac{\pi}{2} f_L}{f_{p1}}\right)\left(f_z^2 - f_{p1}^2\right)\right)} \tag{3-232}$$

If $f_L \gg f_{p1}$

$$v_{n,T,fb} = \psi_{T,fb} \sqrt{\frac{\pi}{2}\left(\frac{f_{p1}^2}{f_z^2}(f_L - 1) + f_{p1}\right)} \tag{3-233}$$

If $f_L \gg 1$ and $\frac{f_{p1}^2}{f_z^2} f_L \gg f_{p1}$

$$v_{n,T,fb} = \psi_{T,fb}\frac{f_{p1}}{f_z}\sqrt{\frac{\pi}{2}f_L} \qquad (3-234)$$

Substitute $(3-226)$ and $(3-227)$ into $(3-234)$

$$v_{n,T,fb} = \psi_{T,fb}R_F g_m\sqrt{\frac{\pi}{2}f_L} \qquad (3-235)$$

The feedback op-amp flicker noise sees the same transfer function as the op-amp thermal noise.

Using equation $(3-225)$ we can write

$$\frac{\psi_{o,1/f,fb}}{\psi_{1/f,fb}} = -\frac{1+j2\pi f R_{INT}C_{INT}}{1+j2\pi f\frac{R_{INT}C_{INT}}{R_F g_m}\left(1+j2\pi f R_F c_f\right)} \qquad (3-236)$$

The noise density is then

$$\left|\psi_{o,T,fb}\right| = \frac{\sqrt{1+f^2(2\pi R_{INT}C_{INT})^2}}{\sqrt{\left(1-(2\pi f)^2\frac{R_{INT}C_{INT}c_f}{g_m}\right)^2+f^2\left(2\pi\frac{R_{INT}C_{INT}}{R_F g_m}\right)^2}}\frac{FNN_{fb}}{\sqrt{f}} \qquad (3-237)$$

The RMS noise at the output is then

$$v_{n,1/f,fb} = \sqrt{\int_0^\infty |G_{LPF}|^2\left|\psi_{o,1/f,fb}\right|^2 df} = \sqrt{\int_0^{\frac{\pi}{2}f_L}\left|\psi_{o,1/f,fb}\right|^2 df} \qquad (3-238)$$

$$v_{n,1/f,fb} = FNN_{fb}\sqrt{\int_0^{\frac{\pi}{2}f_L}\frac{1+f^2/f_z^2}{1+f^2/f_{p1}}\frac{1}{f}df} \qquad (3-239)$$

$$v_{n,1/f,fb} = FNN_{fb}\sqrt{\ln\left(\frac{\pi}{2}\frac{f_L}{f_0}\right)+\frac{1}{2}\left(\frac{f_{p1}^2}{f_z^2}-1\right)\ln\left(\frac{\left(\frac{\pi}{2}f_L\right)^2+f_{p1}^2}{f_0^2+f_{p1}^2}\right)} \qquad (3-240)$$

If $f_{p1}^2 \gg f_0^2$

$$v_{no,1/f,fb} = FNN_{fb}\sqrt{\ln\left(\frac{\pi}{2}\frac{f_L}{f_0}\right) + \frac{1}{2}\left(\frac{f_{p1}^2}{f_z^2} - 1\right)\ln\left(1 + \frac{\left(\frac{\pi}{2}f_L\right)^2}{f_{p1}^2}\right)} \qquad (3-241)$$

Insert $(3-226)$ and $(3-227)$ into $(3-241)$

$$v_{n,1/f,fb} = FNN_{fb}\sqrt{\ln\left(\frac{\pi}{2}\frac{f_L}{f_0}\right) + \frac{1}{2}((R_F g_m)^2 - 1)\ln\left(1 + \left(\frac{\pi}{2}\frac{f_L}{f_H}\right)^2\right)} \qquad (3-242)$$

If $\left(\frac{\pi}{2}\frac{f_L}{f_H}\right)^2 \gg 1$, then

$$v_{n,1/f,fb} = FNN_{fb}\sqrt{\ln\left(\frac{\pi}{2}\frac{f_L}{f_0}\right) + ((R_F g_m)^2 - 1)\ln\left(\frac{\pi}{2}\frac{f_L}{f_H}\right)} \qquad (3-243)$$

If $(R_F g_m)^2 \gg 1$, then

$$v_{n,1/f,fb} = FNN_{fb}\sqrt{\ln\left(\frac{\pi}{2}\frac{f_L}{f_0}\right) + (R_F g_m)^2\ln\left(\frac{\pi}{2}\frac{f_L}{f_H}\right)} \qquad (3-244)$$

If $(R_F g_m)^2 \ln\left(\frac{\pi}{2}\frac{f_L}{f_H}\right) \gg \ln\left(\frac{\pi}{2}\frac{f_L}{f_0}\right)$, then

$$v_{n,1/f,fb} = R_F g_m FNN_{fb}\sqrt{\ln\left(\frac{\pi}{2}\frac{f_L}{f_H}\right)} \qquad (3-245)$$

The integrator resistor thermal noise ψ_{RINT} sees the transfer function below.

$$\frac{\psi_{o,RINT}}{\psi_{RINT}} = -\frac{1}{1 + j2\pi f\frac{R_{INT}C_{INT}}{R_F g_m}\left(1 + j2\pi f R_F c_f\right)} \qquad (3-246)$$

The noise density is then

$$\left|\psi_{o,RINT}\right| = \frac{\sqrt{4kTR_{INT}}}{\sqrt{\left(1-(2\pi f)^2\frac{R_{INT}C_{INT}c_f}{g_m}\right)^2 + f^2\left(2\pi\frac{R_{INT}C_{INT}}{R_F g_m}\right)^2}} \qquad (3-247)$$

The RMS noise at the output is then

$$v_{n,RINT} = \sqrt{\int_0^\infty |G_{LPF}|^2\left|\psi_{o,RINT}\right|^2 df} = \sqrt{\int_0^{\frac{\pi}{2}f_L}\left|\psi_{o,RINT}\right|^2 df} \qquad (3-248)$$

If $f_L \gg f_H$, we can use the noise equivalent bandwidth of a first order system with cutoff frequency f_H

$$v_{n,RINT} = \sqrt{2\pi kTR_{INT}f_H} \qquad (3-249)$$

Both of the integrator's resistors see the same transfer function and therefore produce the same RMS noise voltage.

The photocurrent shot noise sees the same transfer function as the photodiode thermal noise current. Using equation $(3-222)$, we can write

$$\frac{\psi_{o,\ell s}}{\xi_{\ell s}} = R_F\frac{j2\pi f\frac{R_{INT}C_{INT}}{R_F g_m}}{1+j2\pi f\frac{R_{INT}C_{INT}}{R_F g_m}\left(1+j2\pi f R_F c_f\right)} \qquad (3-250)$$

The noise density is then

$$\left|\psi_{o,\ell s}\right| = R_F\frac{\left|2\pi f\frac{R_{INT}C_{INT}}{R_F g_m}\right|\sqrt{2q\overline{\iota_p}}}{\sqrt{\left(1-(2\pi f)^2\frac{R_{INT}C_{INT}c_f}{g_m}\right)^2 + f^2\left(2\pi\frac{R_{INT}C_{INT}}{R_F g_m}\right)^2}} \qquad (3-251)$$

Assuming that $f_L \gg f_H$, the RMS noise at the output is then

$$v_{n,light} = \sqrt{\int_0^\infty |G_{LPF}|^2 \left|\psi_{o,\ell s}\right|^2 df}$$

$$= \sqrt{\int_0^{\frac{\pi}{2} f_L} \left|\psi_{o,\ell s}\right|^2 df} = R_F \sqrt{2q\bar{\imath_p} f_L} \qquad (3-252)$$

The RMS dark noise is

$$v_{n,dark} = \sqrt{\begin{matrix} v_{n,T,ff}^2 + v_{n,1/f,ff}^2 + v_{n,s,ff}^2 + v_{n,RF}^2 \\ +v_{n,xc}^2 + v_{n,rsh}^2 + v_{n,T,fb}^2 + v_{n,1/f,fb}^2 + 2v_{n,RINT}^2 \end{matrix}} \qquad (3-253)$$

Insert $(3-210)$, $(3-218)$, $(3-221)$, $(3-197)$, $(3-200)$, $(3-224)$, $(3-235)$, $(3-245)$, and $(3-249)$ into $(3-253)$

$$v_{n,dark} = \sqrt{R_F^2 \left(\xi_{S,ff}^2 + 2q\bar{\imath_p} + \frac{4kT}{r_{sh}} + (2\pi c_{in})^2 \gamma f_L\right) f_L + 4kTR_F f_L + \kappa_{INT}} \qquad (3-254)$$

$$\gamma = \psi_{T,ff}^2 \left(\frac{\pi}{2} - 1\right) f_L + FNN_{ff}^2 \frac{\ln\left(1 + \frac{\pi^2}{4}\right)}{2} \qquad (3-255)$$

$$\kappa_{INT} = (R_F g_m)^2 \left(\psi_{T,fb}^2 \frac{\pi}{2} f_L + FNN_{fb}^2 \ln\left(\frac{\pi}{2}\frac{f_L}{f_H}\right)\right) + 4\pi kTR_{INT} f_H \qquad (3-256)$$

The total noise is

$$v_{n,total} = \sqrt{v_{n,dark}^2 + v_{n,light}^2} \qquad (3-257)$$

$$v_{n,total} = \sqrt{R_F^2 \left(\xi_{S,ff}^2 + \frac{4kT}{r_{sh}} + (2\pi c_{in})^2 \gamma f_L\right) f_L + R_F^2 \left(4q\bar{\imath_p}\right) f_L + 4kTR_F f_L + \kappa_{INT}}$$

$$v_{n,total} = \sqrt{R_F^2 \alpha' f_L + R_F^2 \left(4q\bar{\imath_p}\right) f_L + 4kTR_F f_L + \kappa_{INT}} \qquad (3-258)$$

$$\alpha' = \xi_{S,ff}^2 + \frac{4kT}{r_{sh}} + (2\pi c_{in})^2 \gamma f_L \qquad (3-259)$$

The SNR is then

$$SNR = \frac{R_F \widetilde{\imath_p}}{v_{n,total}} = \frac{R_F \widetilde{\imath_p}}{\sqrt{R_F^2 \alpha' f_L + R_F \left(\left(4q\overline{\imath_p} \right) R_F + 4kT \right) f_L + \kappa_{INT}}} \qquad (3-260)$$

$$SNR = \frac{R_F \widetilde{\imath_p}}{\sqrt{R_F^2 \alpha' f_L + 4kTR_F \left(1 + \frac{q}{kT} \overline{\imath_p} R_F \right) f_L + \kappa_{INT}}} \qquad (3-261)$$

The input signal is

$$i_p = i_{p,sig} + \overline{\imath_p}$$

Where $i_{p,sig}$ represents the signal current amplitude.

The maximum value of R_F is

$$R_F = \frac{V_{CC}}{i_{p,sig}} \qquad (3-262)$$

Substitute $(3-262)$ into $(3-261)$

$$SNR = \frac{V_{CC} \frac{\widetilde{\imath_p}}{i_{p,sig}}}{\sqrt{\left(\frac{V_{CC}}{i_{p,sig}} \right)^2 \alpha' f_L + 4kT \frac{V_{CC}}{i_{p,sig}} \left(1 + \frac{q}{kT} V_{CC} \frac{\overline{\imath_p}}{i_{p,sig}} \right) f_L + \kappa_{INT}}} \qquad (3-263)$$

3.3.3 *Offset Voltage Subtraction*

The topology in Figure 3-5C uses feedback to subtract the offset voltage at the non-inverting input of the op-amp in the forward path. While this method avoids the additional noise caused by the resistor or semiconductor element in the active current feedback circuits, it cannot remove very large offsets. Indeed, the maximum DC offset current that can be removed is defined as

$$\bar{\iota_p} \leq \frac{V_{CC}}{R_F} \qquad (3-264)$$

In this section, we will analyze the noise inherent to this topology. The schematic of which is shown in Figure 3-8 on the left and the corresponding noise model on the right. Here we will implement an integrator for the low-pass filter circuit.

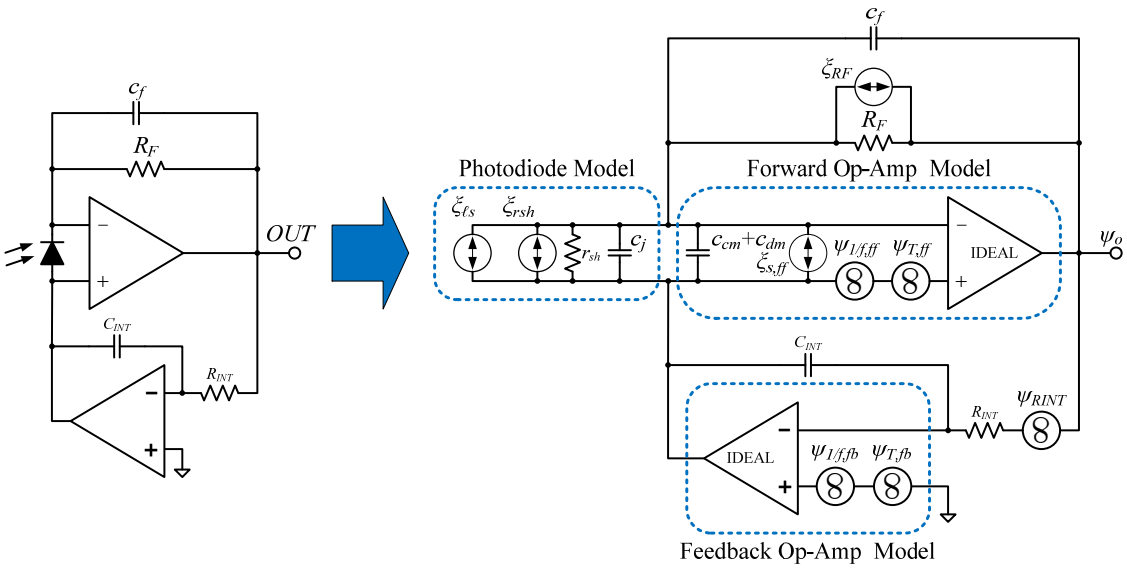

Figure 3-8: Circuit with voltage-offset subtraction (left) and corresponding noise model (right).

Transfer function seen by the feedback resistor thermal noise

$$\frac{\psi_{o,RF}}{\xi_{RF}} = R_F \frac{jf/f_H}{(1+jf/f_H)(1+jf/f_L)} \quad (3-265)$$

Where the thermal noise current from the feedback resistor is

$$\xi_{RF} = \sqrt{\frac{4kT}{R_F}} \quad (3-266)$$

the high-pass cutoff frequency is

$$f_H = \frac{1}{2\pi R_{INT} C_{INT}} \quad (3-267)$$

and the low-pass cutoff frequency is

$$f_L = f_p = \frac{1}{2\pi R_F c_f} \quad (3-268)$$

The noise density in $\mathrm{V}/\sqrt{\mathrm{Hz}}$ is then

$$\left|\psi_{o,RF}\right| = R_F \frac{|f/f_H|\sqrt{4kT/R_F}}{\sqrt{\left(1-f^2/(f_H f_L)\right)^2 + (f/f_H + f/f_L)^2}} \quad (3-269)$$

Assuming that $f_L \gg f_H$, the RMS noise at the output is then

$$v_{n,RF} = \sqrt{\int_0^\infty |G_{LPF}|^2 \left|\psi_{o,RF}\right|^2 df} = \sqrt{\int_0^{\frac{\pi}{2}f_L} \left|\psi_{o,RF}\right|^2 df} = \sqrt{4kTR_F f_L} \quad (3-270)$$

The transfer function seen by the forward path op-amp's thermal noise is

$$\frac{\psi_{o,T,ff}}{\psi_{T,ff}} = G_{LF} \frac{jf/f_H(1+jf/f_z)}{(1+jf/f_L)(1+jf/f_H)} \quad (3-271)$$

Where the zero frequency is

$$f_z = \frac{1}{2\pi R_F \parallel r_{sh}(c_f + c_{in})} \tag{3-272}$$

the low-frequency gain is

$$G_{LF} = 1 + \frac{R_F}{r_{sh}} \tag{3-273}$$

and the mid-band gain is

$$G_{MB} = \frac{f_z}{f_L} = 1 + \frac{c_{in}}{c_f} \tag{3-274}$$

The noise density in $\mathrm{V}/\sqrt{\mathrm{Hz}}$ at the output is then

$$\left|\psi_{o,T,ff}\right| = \left(1 + \frac{R_F}{r_{sh}}\right) \frac{|f/f_H|\sqrt{1 + f^2/f_z^2}}{\sqrt{\left(1 - f^2/(f_H f_L)\right)^2 + (f/f_L + f/f_H)^2}} \psi_{T,ff} \tag{3-275}$$

Assuming that $f_L \gg f_H$ and that $f_p = f_L$, the RMS noise at the output is then

$$v_{n,T,ff} = \sqrt{\int_0^\infty |G_{LPF}|^2 \left|\psi_{o,T,ff}\right|^2 df} = \sqrt{\int_0^{\frac{\pi}{2}f_L} \left|\psi_{o,T,ff}\right|^2 df} \tag{3-276}$$

$$v_{n,T,ff} = \left(1 + \frac{R_F}{r_{sh}}\right) \psi_{T,ff} \sqrt{\int_0^{\frac{\pi}{2}f_L} \frac{1 + f^2/f_z^2}{1 + f^2/f_L^2} df} \tag{3-277}$$

$$v_{n,T,ff} = \left(1 + \frac{R_F}{r_{sh}}\right) \psi_{T,ff} \sqrt{\left(\left(\frac{\pi}{2} - 1\right)\frac{f_L^2}{f_z^2} + 1\right) f_L} \tag{3-278}$$

Assuming that $(\pi/2 - 1)(f_L/f_z)^2 \gg 1$

$$v_{n,T,ff} = \left(1 + \frac{R_F}{r_{sh}}\right)\psi_{T,ff}\frac{f_L}{f_z}\sqrt{\left(\frac{\pi}{2} - 1\right)f_L} \qquad (3-279)$$

Substitute $(3-272)$ into $(3-279)$

$$v_{n,T,ff} = \psi_{T,ff}2\pi R_F\left(c_f + c_{in}\right)f_L\sqrt{\left(\frac{\pi}{2} - 1\right)f_L} \qquad (3-280)$$

For high-gain applications we can assume that $c_{in} \gg c_f$. Equation $(3-280)$ then becomes

$$v_{n,T,ff} = \psi_{T,ff}2\pi R_F c_{in} f_L\sqrt{\left(\frac{\pi}{2} - 1\right)f_L} \qquad (3-281)$$

The op-amp flicker noise sees the same transfer function as the op-amp thermal noise. Using $(3-271)$ we have

$$\frac{\psi_{o,1/f,ff}}{\psi_{1/f,ff}} = G_{LF}\frac{jf/f_H(1 + jf/f_z)}{(1 + jf/f_L)(1 + jf/f_H)} \qquad (3-282)$$

The noise density is then

$$\left|\psi_{o,1/f,ff}\right| = G_{LF}\frac{|f/f_H|\sqrt{1 + f^2/f_z^2}}{\sqrt{\left(1 - f^2/(f_H f_L)\right)^2 + (f/f_L + f/f_H)^2}}\frac{FNN_{ff}}{\sqrt{f}} \qquad (3-283)$$

Assuming that $f_L \gg f_H$ the RMS noise at the output is then

$$v_{n,1/f,ff} = \sqrt{\int_{f_0}^{\infty}|G_{LPF}|^2\left|\psi_{o,1/f,ff}\right|^2 df} = \sqrt{\int_{f_0}^{\frac{\pi}{2}f_L}\left|\psi_{o,1/f,ff}\right|^2 df} \qquad (3-284)$$

$$v_{n,1/f,ff} = \left(1 + \frac{R_F}{r_{sh}}\right)\sqrt{\int_{f_0}^{\frac{\pi}{2}f_L}\frac{1 + f^2/f_z^2}{1 + f^2/f_L^2}\frac{FNN_{ff}}{f}df} \qquad (3-285)$$

$$v_{n,1/f,ff} = \left(1 + \frac{R_F}{r_{sh}}\right) FNN_{ff} \sqrt{\ln\left(\frac{\pi}{2}\frac{f_L}{f_0}\right) + \frac{1}{2}\left(\frac{f_L^2}{f_z^2} - 1\right)\ln\left(\frac{\left(\frac{\pi}{2}f_L\right)^2 + f_L^2}{f_0^2 + f_L^2}\right)} \qquad (3-286)$$

If $f_L^2 \gg f_0^2$

$$v_{n,1/f,ff} = \left(1 + \frac{R_F}{r_{sh}}\right) FNN \sqrt{\ln\left(\frac{\pi}{2}\frac{f_L}{f_0}\right) + \frac{\ln\left(1 + \frac{\pi^2}{4}\right)}{2}\left(\frac{f_L^2}{f_z^2} - 1\right)} \qquad (3-287)$$

If $f_0 = 1\text{mHz}$, $f_L \gg f_z$ and $f_p \gg 1\text{Hz}$

$$v_{n,1/f,ff} = \left(1 + \frac{R_F}{r_{sh}}\right) FNN_{ff} \frac{f_L}{f_z} \sqrt{\frac{\ln\left(1 + \frac{\pi^2}{4}\right)}{2}} \qquad (3-288)$$

Substitute $(3-272)$ into $(3-288)$

$$v_{n,1/f,ff} = FNN_{ff} 2\pi R_F (c_f + c_{in}) f_L \sqrt{\frac{\ln\left(1 + \frac{\pi^2}{4}\right)}{2}} \qquad (3-289)$$

For high-gain applications we can assume that $c_{in} \gg c_f$. Equation $(3-289)$ then becomes

$$v_{n,1/f,ff} = FNN_{ff} 2\pi R_F c_{in} f_L \sqrt{\frac{\ln\left(1 + \frac{\pi^2}{4}\right)}{2}} \qquad (3-290)$$

The transfer function seen by the forward-path op-amp current noise is

$$\frac{\psi_{o,s,ff}}{\xi_s} = R_F \frac{jf/f_H}{(1 + jf/f_H)(1 + jf/f_L)} \qquad (3-291)$$

From the transfer function $(3-291)$, we can get the equation for the noise density

$$\left|\psi_{o,s,ff}\right| = R_F \frac{|f/f_H|}{\sqrt{\left(1-f^2/(f_H f_L)\right)^2 + (f/f_H + f/f_L)^2}} \xi_s \qquad (3-292)$$

Assuming that $f_L \gg f_H$, the RMS noise at the output is then

$$v_{n,s,ff} = \sqrt{\int_0^\infty |G_{LPF}|^2 \left|\psi_{o,s,ff}\right|^2 df} = \sqrt{\int_0^{\frac{\pi}{2}f_L} \left|\psi_{o,s,ff}\right|^2 df} = R_F \xi_s \sqrt{f_L} \qquad (3-293)$$

The thermal noise from the photodiode sees the same transfer function as the op-amp input current shot noise. Using $(3-291)$ we have

$$\frac{\psi_{o,rsh}}{\xi_{rsh}} = R_F \frac{jf/f_H}{(1+jf/f_H)(1+jf/f_L)} \qquad (3-294)$$

The noise density is then

$$\left|\psi_{o,rsh}\right| = \frac{R_F|f/f_H|}{\sqrt{\left(1-f^2/(f_H f_L)\right)^2 + (f/f_H + f/f_L)^2}} \sqrt{\frac{4kT}{r_{sh}}} \qquad (3-295)$$

Assuming that $f_L \gg f_H$, the RMS noise at the output is then

$$v_{n,rsh} = \sqrt{\int_0^\infty |G_{LPF}|^2 \left|\psi_{o,rsh}\right|^2 df} = \sqrt{\int_0^{\frac{\pi}{2}f_L} \left|\psi_{o,rsh}\right|^2 df} = R_F \sqrt{\frac{4kT}{r_{sh}} f_L} \qquad (3-296)$$

Now we will analyze the elements of the feedback integrator. The integrator op-amp noise sees a gain of unity, hence the transfer function is

$$\frac{\psi_{o,T,fb}}{\psi_{T,fb}} = 1 \qquad (3-297)$$

The noise density in $\mathrm{V}/\sqrt{\mathrm{Hz}}$ is then

$$\left|\psi_{o,T,fb}\right| = \psi_{T,fb} \tag{3-298}$$

The RMS noise at the output is then

$$v_{n,T,fb} = \sqrt{\int_0^\infty |G_{LPF}|^2 \left|\psi_{o,T,fb}\right|^2 df} = \sqrt{\int_0^{\frac{\pi}{2}f_L} \left|\psi_{o,T,fb}\right|^2 df} = \psi_{T,fb}\sqrt{f_L} \tag{3-299}$$

The integrator flicker noise sees the same transfer function as the integrator thermal noise.

Therefore

$$\frac{\psi_{o,T,fb}}{\psi_{1/f,fb}} = 1 \tag{3-300}$$

The noise density in $\mathrm{V}/\sqrt{\mathrm{Hz}}$ is then

$$\left|\psi_{o,1/f,fb}\right| = \frac{FNN_{fb}}{\sqrt{f}} \tag{3-301}$$

The RMS noise at the output is then

$$v_{n,1/f,fb} = \sqrt{\int_{f_0}^\infty |G_{LPF}|^2 \left|\psi_{o,1/f,fb}\right|^2 df}$$

$$= \sqrt{\int_{f_0}^{\frac{\pi}{2}f_L} \left|\psi_{o,1/f,fb}\right|^2 df} \approx 7FNN_{fb} \tag{3-302}$$

The integrator resistor thermal noise sees the transfer function

$$\frac{\psi_{o,RINT}}{\psi_{RINT}} = -\frac{1}{1 + j2\pi f R_{INT} C_{INT}} \tag{3-303}$$

The noise density in $\mathrm{V}/\sqrt{\mathrm{Hz}}$ is then

$$\left|\psi_{o,RINT}\right| = \frac{\sqrt{4kTR_{INT}}}{\sqrt{1+f^2(2\pi R_{INT}C_{INT})^2}} \qquad (3-304)$$

The RMS noise voltage is then

$$v_{noRINT} = \sqrt{\int_0^\infty |G_{LPF}|^2 \left|\psi_{o,RINT}\right|^2 df} = \sqrt{\int_0^{\frac{\pi}{2}f_L} \left|\psi_{o,RINT}\right|^2 df} = \sqrt{4kTR_{INT}f_H} \qquad (3-305)$$

The photocurrent shot noise from the photodiode sees the same transfer function as the op-amp input current shot noise. Using $(3-291)$ we have

$$\frac{\psi_{o,\ell s}}{\xi_{\ell s}} = R_F \frac{jf/f_H}{(1+jf/f_H)(1+jf/f_L)} \qquad (3-306)$$

The noise density is then

$$\left|\psi_{o,\ell s}\right| = R_F \frac{|f/f_H|\sqrt{2q\bar{\imath_p}}}{\sqrt{\left(1-f^2/(f_Hf_L)\right)^2 + (f/f_H + f/f_L)^2}} \qquad (3-307)$$

The RMS noise voltage is

$$v_{n,light} = \sqrt{\int_0^\infty |G_{LPF}|^2 \left|\psi_{o,\ell s}\right|^2 df} = \sqrt{\int_0^{\frac{\pi}{2}f_L} \left|\psi_{o,\ell s}\right|^2 df} = R_F\sqrt{2q\bar{\imath_p}f_L} \qquad (3-308)$$

The dark noise is the quadratic sum of all the noise sources in the system except the photocurrent-related noise.

$$v_{n,dark} = \sqrt{\begin{matrix} v_{n,T,ff}^2 + v_{n,1/f,ff}^2 + v_{n,s,ff}^2 + v_{n,RF}^2 \\ +v_{n,rsh}^2 + v_{n,T,fb}^2 + v_{n,1/f,fb}^2 + v_{n,RINT}^2 \end{matrix}} \qquad (3-309)$$

Substituting equations $(3-281)$, $(3-290)$, $(3-293)$, $(3-270)$, $(3-296)$, $(3-299)$, $(3-302)$, and $(3-305)$ into $(3-309)$.

$$v_{n,dark} = \sqrt{\begin{matrix} R_F^2\left(\xi_s^2 + \frac{4kT}{r_{sh}} + (2\pi c_{in})^2 f_L \gamma\right) f_L + 4kTR_F f_L \\ +\psi_{T,fb}^2 f_L + \left(7FNN_{fb}\right)^2 + 4kTR_{INT} f_H \end{matrix}} \quad (3-310)$$

$$\gamma = \psi_{T,ff}^2 \left(\frac{\pi}{2} - 1\right) f_L + FNN_{ff}^2 \frac{\ln\left(1 + \frac{\pi^2}{4}\right)}{2} \quad (3-311)$$

The total noise is then

$$v_{n,total} = \sqrt{v_{n,dark}^2 + v_{n,light}^2} \quad (3-312)$$

Substitute $(3-308)$ and $(3-310)$ into $(3-312)$

$$v_{n,total} = \sqrt{\begin{matrix} R_F^2\left(\xi_s^2 + \frac{4kT}{r_{sh}} + 2q\bar{\imath_p} + (2\pi c_{in})^2 f_L \gamma\right) f_L + 4kTR_F f_L \\ +\psi_{T,fb}^2 f_L + \left(7FNN_{fb}\right)^2 + 4kTR_{INT} f_H \end{matrix}}$$

$$v_{n,total} = \sqrt{R_F^2 \alpha' f_L + R_F^2\left(2q\bar{\imath_p}\right) f_L + \beta R_F f_L + \kappa_{INT}} \quad (3-313)$$

$$\alpha' = \xi_s^2 + \frac{4kT}{r_{sh}} + (2\pi c_{in})^2 f_L \gamma \quad (3-314)$$

$$\beta = 4kT \quad (3-315)$$

$$\kappa_{INT} = \psi_{T,fb}^2 f_L + \left(7FNN_{fb}\right)^2 + 4kTR_{INT} f_H \quad (3-316)$$

The SNR is then

$$SNR = \frac{R_F \widetilde{\imath_p}}{\sqrt{R_F^2 \alpha' f_L + R_F^2\left(2q\bar{\imath_p}\right) f_L + \beta R_F f_L + \kappa_{INT}}} \quad (3-317)$$

Rearrange $(3-317)$

$$SNR = \frac{R_F \widetilde{i_p}}{\sqrt{\alpha' R_F^2 f_L + R_F 4kT\left(1 + \frac{1}{2}\frac{q}{kT}\overline{i_p}R_F\right) f_L + \kappa_{INT}}} \qquad (3-318)$$

The maximum possible signal is $i_{p,sig} + \overline{i_p} = \frac{V_{CC}}{R_F}$

$$R_F = \frac{V_{CC}}{i_{p,sig} + \overline{i_p}} \qquad (3-319)$$

Substitute $(3-319)$ into $(3-318)$

$$SNR = \frac{V_{CC}\dfrac{\widetilde{i_p}}{i_{p,sig}}}{\sqrt{\alpha' f_L\left(\dfrac{V_{CC}}{i_{p,sig}}\right)^2 + \beta f_L\left(1 + \left(1 + \dfrac{1}{2}\dfrac{q}{kT}V_{CC}\right)\dfrac{\overline{i_p}}{i_{p,sig}}\right)\dfrac{V_{CC}}{i_{p,sig}} + \left(1 + \dfrac{\overline{i_p}}{i_{p,sig}}\right)^2 \kappa_{INT}}} \qquad (3-320)$$

Where

$$\beta = 4kT$$

3.3.4 *Removing Offset in the 2nd Stage*

The topology in Figure 3-5D removes the offset in the 2nd stage. This circuit will serve as a sort of control when we compare the topologies in the next section. This topology is essentially the same as that in section 3.1 with the exception that a small portion of the bandwidth is removed at low frequencies. That said, there is no need to repeat the noise analysis of section 3.1. We will however modify the equation for the SNR, we will start by stating that the maximum current that this topology can amplify without clipping is

$$\overline{i_p} + i_{p,sig} \leq \frac{V_{CC}}{R_F} \qquad (3-321)$$

We can re-write equation $(3-53)$ which describes the SNR of the single-resistor topology in terms of its maximum dynamic range. Begin by pulling the shot noise term out of α.

$$SNR = \frac{R_F \widetilde{i_p}}{\sqrt{\alpha' f_L R_F^2 + 4kT\left(1 + \frac{1}{2}\frac{q}{kT}\overline{i_p}R_F\right)R_F f_L}} \qquad (3-322)$$

Rearranging equation $(3-321)$, we find that the maximum value of R_F is

$$R_F = \frac{V_{CC}}{i_{p,sig} + \overline{i_p}} \qquad (3-323)$$

Substitute $(3-323)$ into $(3-322)$

$$SNR = \frac{V_{CC}\dfrac{\widetilde{i_p}}{i_{p,sig}}}{\sqrt{\alpha' f_L\left(\dfrac{V_{CC}}{i_{p,sig}}\right)^2 + \beta f_L\left(1 + \left(1 + \frac{1}{2}\frac{q}{kT}V_{CC}\right)\dfrac{\overline{i_p}}{i_{p,sig}}\right)\dfrac{V_{CC}}{i_{p,sig}}}} \qquad (3-324)$$

Where

$$\alpha' = \xi_s^2 + \frac{4kT}{rsh} + (2\pi c_{in})^2 \gamma f_L$$

$$\beta = 4kT$$

and

$$\gamma = \psi_T^2\left(\frac{\pi}{2} - 1\right)f_L + FNN^2\frac{\ln\left(1 + \frac{\pi^2}{4}\right)}{2}$$

3.3.5 *Comparison of AC-Coupled Topologies' SNR*

From the analysis of the previous sections we can see that there is no significant advantage to AC-coupling. Comparison of equations $(3-194)$, $(3-263)$, $(3-320)$, and $(3-322)$ shows that no matter how the offset is removed the resulting SNR is about the same. The only discrepancy is the term κ_{INT} which is the feedback integrator noise. While κ_{INT} is the same for the two active-current-feedback topologies, it is different for the offset-voltage-subtraction topology and not present for the topology which removes the offset in the 2nd stage. In any case, κ_{INT} can be made very small with proper component selection and careful design. It is therefore reasonable to neglect this term when comparing the SNR of the different AC-coupled topologies.

3.4 Charge Amplifier Topology

A charge amplifier uses a capacitive element to accumulate charge. The gain of the circuit is inversely proportional to the feedback capacitance C_F. The particular configuration of the charge amplifier that we will present in this section is essentially a continuous-time CCD cell. The forward path contains an integrator and the feedback path provides a continuous current that prevents it from reaching saturation. The 2nd stage is a differentiator used to produce a "flat" frequency response in the pass-band.

3.4.1 *Noise Analysis*

In this section we will analyze the noise produced by the charge amplifier. The schematic of the charge amplifier and the corresponding noise model is shown in Figure 3-9. For simplicity, we will analyze the noise above the high-pass cutoff. Notice that the feedback structure in the noise model has been replaced with an AC ground. This is because at high frequencies this node will be at a fixed potential. We have also shown in previous sections that a well-designed feedback structure will produce a negligible amount of noise. Our choice is further justified by the fact that the high-pass cutoff for systems designed to detect biological signals is typically very low ~50mHz [14].

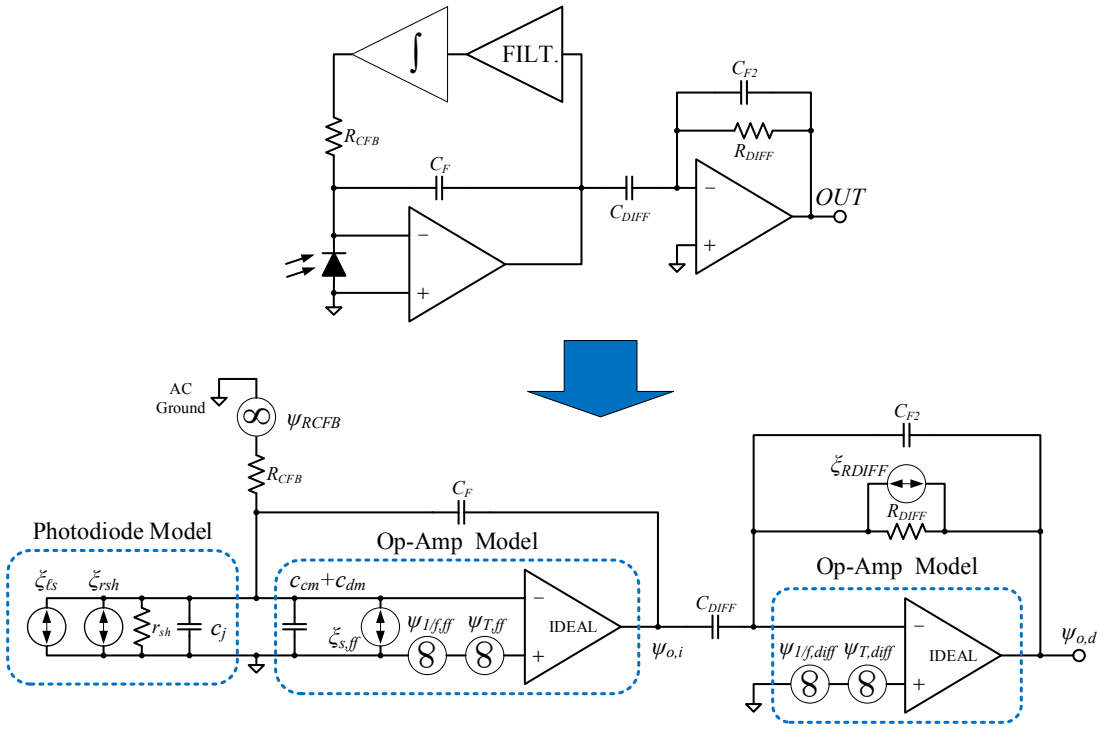

Figure 3-9: Charge amplifier schematic (top) and corresponding high-frequency noise model (bottom).

We will conduct the analysis the same as we did in previous sections. Each noise source shall be analyzed independently and then the total noise will be the vector magnitude of the individual sources. The transfer functions of all the noise sources in the first stage will be multiplied by that of the differentiator before reaching the final output . The transfer function of the differentiator is shown below.

$$\frac{\psi_{o,d}}{\psi_{o,i}} = -\frac{j2\pi f R_{DIFF} C_{DIFF}}{1 + j2\pi f R_{DIFF} C_{F2}} \qquad (3-325)$$

Notice that the above transfer function has 1 pole and 1 zero:

$$f_{p,diff} = \frac{1}{2\pi R_{DIFF} C_{F2}} \qquad (3-326)$$

$$f_{z,diff} = \frac{1}{2\pi R_{DIFF} C_{DIFF}} \qquad (3-327)$$

The zero obviously produces the differentiator action, the pole is there to roll off the differentiator action at higher frequencies where it is no longer needed. This helps reduce high-frequency noise. For this analysis, we will choose $f_{p,diff}$ to be the same as the cutoff frequency f_L since there will be no need to differentiate signals beyond the cutoff frequency.

The input capacitance of the 1st –stage amplifier is the same as that defined in $(3-2)$. For all calculations of RMS noise in this section, we will assume that the TIA is followed by a high-order low-pass filter like the one described in section 1.3.1 which can be approximated by equation $(1-12)$. Thus the upper limit of the integrals will not be ∞ but instead $\frac{\pi}{2}f_L$.

We will begin the noise analysis with the transfer function seen by the thermal noise from the current feedback resistor R_{CFB}.

$$\frac{\psi_{o,i,RCFB}}{\psi_{RCFB}} = -\frac{1}{j2\pi f R_{CFB} C_F} \qquad (3-328)$$

Using equation $(3-325)$, the transfer function after the differentiator is

$$\frac{\psi_{o,d,RCFB}}{\psi_{RCFB}} = \frac{R_{DIFF}C_{DIFF}}{R_{CFB}C_F}\frac{1}{1+j2\pi f R_{DIFF}C_{F2}} \qquad (3-329)$$

The noise density is then

$$\left|\psi_{o,d,RCFB}\right| = \frac{R_{DIFF}C_{DIFF}}{R_{CFB}C_F}\frac{\sqrt{4kTR_{CFB}}}{\sqrt{1+f^2(2\pi R_{DIFF}C_{F2})^2}} \qquad (3-330)$$

The RMS noise is then

$$v_{n,RCFB} = \sqrt{\int_0^{\infty} |G_{LPF}(f)|^2 \left|\psi_{o,d,RCFB}\right|^2 df} = \sqrt{\int_0^{\frac{\pi}{2}f_L} \left|\psi_{o,d,RCFB}\right|^2 df} \qquad (3-331)$$

$$v_{n,RCFB} = \frac{R_{DIFF}C_{DIFF}}{R_{CFB}C_F}\sqrt{4kTR_{CFB}}\sqrt{\int_0^{\frac{\pi}{2}f_L}\frac{1}{1+f^2/f_{p,diff}^2}df} \qquad (3-332)$$

Using equation $(1-13)$ the result of the integral is

$$v_{n,RCFB} = R_{DIFF}\frac{C_{DIFF}}{C_F}\sqrt{\frac{4kT}{R_{CFB}}f_L} \qquad (3-333)$$

The transfer function seen by the integrator op-amp thermal noise is

$$\frac{\psi_{o,i,T,ff}}{\psi_{T,ff}} = \frac{1+j2\pi f(C_F+c_{in})\,r_{sh} \parallel R_{CFB}}{j2\pi f C_F\,r_{sh} \parallel R_{CFB}} \qquad (3-334)$$

The using equation $(3-325)$ transfer function at the output of the differentiator is

$$\frac{\psi_{o,d,T,ff}}{\psi_{T,ff}} = -\frac{R_{DIFF}C_{DIFF}}{r_{sh} \parallel R_{CFB}\,C_F}\frac{(1+j2\pi f(C_F+c_{in})\,r_{sh} \parallel R_{CFB})}{1+j2\pi f R_{DIFF}C_{F2}} \qquad (3-335)$$

The above transfer function has one pole $f_{p,diff}$ and one zero:

$$f_{z,int} = \frac{1}{2\pi r_{sh} \parallel R_{CFB}(C_F+c_{in})} \qquad (3-336)$$

The noise density is

$$\left|\psi_{o,d,T,ff}\right| = \frac{R_{DIFF}C_{DIFF}}{r_{sh} \parallel R_{CFB}\,C_F}\frac{\sqrt{1+f^2(2\pi(C_F+c_{in})\,r_{sh} \parallel R_{CFB})^2}}{\sqrt{1+f^2(2\pi R_{DIFF}C_{F2})^2}}\psi_{T,ff} \qquad (3-337)$$

The RMS noise is then

$$v_{n,T,ff} = \sqrt{\int_0^{\infty}|G_{LPF}(f)|^2\left|\psi_{o,d,T,ff}\right|^2 df} = \sqrt{\int_0^{\frac{\pi}{2}f_L}\left|\psi_{o,d,T,ff}\right|^2 df} \qquad (3-338)$$

$$v_{n,T,ff} = \frac{R_{DIFF}C_{DIFF}}{r_{sh} \parallel R_{CFB}\, C_F}\psi_{T,ff}\sqrt{\int_0^{\frac{\pi}{2}f_L} \frac{1 + f/f_{z,int}}{1 + f/f_{p,diff}}\,df} \qquad (3-339)$$

The result of the above integral, using equation $(1-16)$ and recalling that $f_{p,diff} = f_L$ is then

$$v_{n,T,ff} = \frac{R_{DIFF}C_{DIFF}}{r_{sh} \parallel R_{CFB}\, C_F}\psi_{T,ff}\sqrt{\left(\left(\frac{\pi}{2}-1\right)\frac{f_L^2}{f_z^2}+1\right)f_L} \qquad (3-340)$$

If $\left(\frac{\pi}{2}-1\right)\frac{f_L^2}{f_z^2} \gg 1$

$$v_{n,T,ff} = \frac{R_{DIFF}C_{DIFF}}{r_{sh} \parallel R_{CFB}\, C_F}\frac{f_L}{f_z}\psi_{T,ff}\sqrt{\left(\frac{\pi}{2}-1\right)f_L} \qquad (3-341)$$

Substitute $(3-336)$ into $(3-341)$

$$v_{n,T,ff} = 2\pi R_{DIFF}C_{DIFF}\left(1+\frac{c_{in}}{C_F}\right)f_L\psi_{T,ff}\sqrt{\left(\frac{\pi}{2}-1\right)f_L} \qquad (3-342)$$

The integrator op-amp flicker noise sees the same transfer function as the thermal noise. Using equation $(3-334)$ we can write

$$\frac{\psi_{o,i,1/f,ff}}{\psi_{1/f,ff}} = \frac{1 + j2\pi f(C_F + c_{in})\, r_{sh} \parallel R_{CFB}}{j2\pi f C_F\, r_{sh} \parallel R_{CFB}} \qquad (3-343)$$

With the differentiator, the transfer function is

$$\frac{\psi_{o,d,1/f,ff}}{\psi_{1/f,ff}} = -\frac{R_{DIFF}C_{DIFF}}{C_F\, r_{sh} \parallel R_{CFB}}\frac{1 + j2\pi f(C_F + c_{in})\, r_{sh} \parallel R_{CFB}}{1 + j2\pi f R_{DIFF}C_{F2}} \qquad (3-344)$$

The noise density is then

$$\left|\psi_{o,d,1/f,ff}\right| = \frac{R_{DIFF}C_{DIFF}}{r_{sh} \parallel R_{CFB}\, C_F}\frac{\sqrt{1 + f^2(2\pi(C_F + c_{in})\, r_{sh} \parallel R_{CFB})^2}}{\sqrt{1 + f^2(2\pi R_{DIFF}C_{F2})^2}}\frac{FNN_{ff}}{\sqrt{f}} \qquad (3-345)$$

The RMS noise voltage is

$$v_{n,1/f,ff} = \sqrt{\int_{f_0}^{\infty} |G_{LPF}(f)|^2 \left|\psi_{o,d,T,ff}\right|^2 df} = \sqrt{\int_{f_0}^{\frac{\pi}{2}f_L} \left|\psi_{o,d,1/f,ff}\right|^2 df} \qquad (3-346)$$

$$v_{n,1/f,ff} = \frac{R_{DIFF}C_{DIFF}}{r_{sh} \parallel R_{CFB}\, C_F} FNN_{ff} \sqrt{\int_{f_0}^{\frac{\pi}{2}f_L} \frac{1 + f^2/f_{z,int}^2}{1 + f^2/f_{p,diff}^2} \frac{1}{f} df} \qquad (3-347)$$

Knowing that $f_{p,diff}=f_L$ and using equation $(1-17)$ the result of the above integral is

$$v_{n,1/f,ff} = \frac{R_{DIFF}C_{DIFF}}{r_{sh} \parallel R_{CFB}\, C_F} FNN_{ff} \sqrt{\ln\left(\frac{\pi}{2}\frac{f_L}{f_0}\right) + \frac{1}{2}\left(\frac{f_L^2}{f_z^2} - 1\right)\ln\left(\frac{\left(\frac{\pi^2}{4}+1\right)f_L^2}{f_0^2 + f_L^2}\right)} \qquad (3-348)$$

If $f_L \gg f_0$

$$v_{n,1/f,ff} = \frac{R_{DIFF}C_{DIFF}}{r_{sh} \parallel R_{CFB}\, C_F} FNN_{ff} \sqrt{\ln\left(\frac{\pi}{2}\frac{f_L}{f_0}\right) + \frac{1}{2}\left(\frac{f_L^2}{f_z^2} - 1\right)\ln\left(\frac{\pi^2}{4}+1\right)} \qquad (3-349)$$

If $f_L^2/f_z^2 \gg 1$

$$v_{n,1/f,ff} = \frac{R_{DIFF}C_{DIFF}}{r_{sh} \parallel R_{CFB}\, C_F} FNN \sqrt{\ln\left(\frac{\pi}{2}\frac{f_L}{f_0}\right) + \frac{1}{2}\frac{f_L^2}{f_z^2}\ln\left(\frac{\pi^2}{4}+1\right)} \qquad (3-350)$$

If we choose $f_0 = 1\text{mHz}$, and $\frac{1}{2}\frac{f_L^2}{f_z^2}\ln\left(\frac{\pi^2}{4}+1\right) \gg \ln\left(\frac{\pi}{2}\frac{f_L}{f_0}\right)$ then

$$v_{n,1/f,ff} = \frac{R_{DIFF}C_{DIFF}}{r_{sh} \parallel R_{CFB}\, C_F} \frac{f_L}{f_z} FNN \sqrt{\frac{1}{2}\ln\left(\frac{\pi^2}{4}+1\right)} \qquad (3-351)$$

Substitute $(3-336)$ into $(3-351)$

$$v_{n,1/f,ff} = 2\pi R_{DIFF} C_{DIFF} \left(1 + \frac{c_{in}}{C_F}\right) f_L FNN \sqrt{\frac{1}{2} \ln\left(\frac{\pi^2}{4} + 1\right)} \qquad (3-352)$$

The transfer function seen by the forward-path integrator op-amp input current shot noise at the output of the integrator is

$$\frac{\psi_{o,i,s,ff}}{\xi_{s,ff}} = \frac{1}{j2\pi f C_F} \qquad (3-353)$$

At the output of the differentiator, the transfer function becomes

$$\frac{\psi_{o,d,s,ff}}{\xi_{s,ff}} = -\frac{R_{DIFF} C_{DIFF}}{C_F} \frac{1}{1 + j2\pi f R_{DIFF} C_{F2}} \qquad (3-354)$$

The noise density is then

$$\left|\psi_{o,d,s,ff}\right| = \frac{R_{DIFF} C_{DIFF}}{C_F} \frac{\xi_{s,ff}}{\sqrt{1 + f^2 (2\pi R_{DIFF} C_{F2})^2}} \qquad (3-355)$$

The RMS noise is then

$$v_{n,s,ff} = \sqrt{\int_0^\infty |G_{LPF}(f)|^2 \left|\psi_{o,d,s,ff}\right|^2 df} = \sqrt{\int_0^{\frac{\pi}{2} f_L} \left|\psi_{o,d,s,ff}\right|^2 df} \qquad (3-356)$$

$$v_{n,s,ff} = \frac{R_{DIFF} C_{DIFF}}{C_F} \xi_{s,ff} \sqrt{\int_0^{\frac{\pi}{2} f_L} \frac{1}{1 + f^2 / f_{p,diff}^2} df} \qquad (3-357)$$

Using equation $(1-13)$ the result of the above integral is

$$v_{n,s,ff} = \frac{R_{DIFF} C_{DIFF}}{C_F} \xi_{s,ff} \sqrt{f_L} \qquad (3-358)$$

The photodiode thermal noise sees the same transfer function as the input current shot noise. Using equation $(3-353)$ we can write

$$\frac{\psi_{o,i,rsh}}{\xi_{rsh}} = \frac{1}{j2\pi f C_F} \tag{3-359}$$

With the differentiator, the transfer function is

$$\frac{\psi_{o,d,rsh}}{\psi_{rsh}} = -\frac{R_{DIFF}C_{DIFF}}{C_F}\frac{1}{1+j2\pi f R_{DIFF}C_{F2}} \tag{3-360}$$

The noise density is then

$$\left|\psi_{o,d,rsh}\right| = \frac{R_{DIFF}C_{DIFF}}{C_F}\frac{\sqrt{\frac{4kT}{r_{sh}}}}{\sqrt{1+f^2(2\pi R_{DIFF}C_{F2})^2}} \tag{3-361}$$

The RMS voltage noise

$$v_{n,rsh} = \sqrt{\int_0^\infty |G_{LPF}(f)|^2 \left|\psi_{o,d,rsh}\right|^2 df} = \sqrt{\int_0^{\frac{\pi}{2}f_L} \left|\psi_{o,d,rsh}\right|^2 df} \tag{3-362}$$

$$v_{n,rsh} = \frac{R_{DIFF}C_{DIFF}}{C_F}\sqrt{\frac{4kT}{r_{sh}}}\sqrt{\int_0^{\frac{\pi}{2}f_L} \frac{1}{1+f^2/f_{p,diff}^2} df} \tag{3-363}$$

Using equation $(1-13)$ the result of the above integral is

$$v_{n,rsh} = \frac{R_{DIFF}C_{DIFF}}{C_F}\sqrt{\frac{4kT}{r_{sh}} f_L} \tag{3-364}$$

The transfer function seen by the resistor thermal noise is

$$\frac{\psi_{o,d,RDIFF}}{\xi_{RDIFF}} = \frac{R_{DIFF}}{1+j2\pi f R_{DIFF}C_{F2}} \tag{3-365}$$

The noise density is then

$$\psi_{o,d,RDIFF} = \frac{\sqrt{4kTR_{DIFF}}}{\sqrt{1+f^2(2\pi R_{DIFF}C_{F2})^2}} \quad (3-366)$$

The RMS voltage noise

$$v_{n,RDIFF} = \sqrt{\int_0^\infty |G_{LPF}(f)|^2 \left|\psi_{o,d,RDIFF}\right|^2 df} = \sqrt{\int_0^{\frac{\pi}{2}f_L} \left|\psi_{o,d,RDIFF}\right|^2 df} \quad (3-367)$$

$$v_{n,RDIFF} = \sqrt{4kTR_{DIFF}} \sqrt{\int_0^{\frac{\pi}{2}f_L} \frac{1}{1+f^2/f_{p,diff}^2} df} \quad (3-368)$$

Using equation $(1-13)$ the result of the above integral is

$$v_{n,RDIFF} = \sqrt{4kTR_{DIFF}f_L} \quad (3-369)$$

The transfer function seen by the differentiator op-amp thermal noise is

$$\frac{\psi_{o,d,T,diff}}{\psi_{T,diff}} = \frac{1+j2\pi f(C_{F2}+C_{DIFF})R_{DIFF}}{1+j2\pi f R_{DIFF}C_{F2}} \quad (3-370)$$

From the transfer function, we can see that there is 1 pole $f_{p,diff}$ and 1 zero

$$f_z = \frac{1}{2\pi R_{DIFF}(C_{F2}+C_{DIFF})} \quad (3-371)$$

$$\psi_{o,d,T,diff} = \frac{\sqrt{1+f^2\left(2\pi R_{DIFF}(C_{F2}+C_{DIFF})\right)^2}}{\sqrt{1+f^2(2\pi R_{DIFF}C_{F2})^2}} \psi_{T,diff} \quad (3-372)$$

The RMS voltage noise

$$v_{n,T,diff} = \sqrt{\int_0^\infty |G_{LPF}(f)|^2 \left|\psi_{o,d,T,diff}\right|^2 df} = \sqrt{\int_0^{\frac{\pi}{2}f_L} \left|\psi_{o,d,T,diff}\right|^2 df} \quad (3-373)$$

$$v_{n,T,diff} = \psi_{T,diff}\sqrt{\int_0^{\frac{\pi}{2}f_L} \frac{1+f^2/f_z^2}{1+f^2/f_{p,diff}^2}df} \qquad (3-374)$$

Using equation $(1-16)$ and noting that $f_{p,diff}=f_L$, the above integral becomes

$$v_{n,T,diff} = \psi_{T,diff}\sqrt{f_L\left(\left(\frac{\pi}{2}-1\right)\frac{f_L^2}{f_z^2}+1\right)} \qquad (3-375)$$

If $\left(\frac{\pi}{2}-1\right)\frac{f_L^2}{f_z^2} \gg 1$

$$v_{n,T,diff} = \frac{f_L}{f_{z,diff}}\psi_{T,diff}\sqrt{\left(\frac{\pi}{2}-1\right)f_L} \qquad (3-376)$$

Substitute $(3-371)$ into $(3-376)$

$$v_{n,T,diff} = (1+2\pi R_{DIFF}C_{DIFF}f_L)\psi_{T,diff}\sqrt{\left(\frac{\pi}{2}-1\right)f_L} \qquad (3-377)$$

The transfer function seen by the differentiator op-amp flicker noise is the same as that seen by the thermal noise. Using equation $(3-370)$ we can write

$$\frac{\psi_{o,d,1/f,diff}}{\psi_{1/f,diff}} = \frac{1+j2\pi f R_{DIFF}(C_{F2}+C_{DIFF})}{1+j2\pi f R_{DIFF}C_{F2}} \qquad (3-378)$$

The noise density is then

$$\left|\psi_{o,d,1/f,diff}\right| = \frac{\sqrt{1+f^2\left(2\pi R_{DIFF}(C_{F2}+C_{DIFF})\right)^2}}{\sqrt{1+f^2(2\pi R_{DIFF}C_{F2})^2}}\frac{FNN_{diff}}{\sqrt{f}} \qquad (3-379)$$

The RMS noise voltage is

$$v_{n,1/f,diff} = \sqrt{\int_{f_0}^{\infty} |G_{LPF}(f)|^2 \left|\psi_{o,d,1/f,diff}\right|^2 df} = \sqrt{\int_{f_0}^{\frac{\pi}{2}f_L} \left|\psi_{o,d,1/f,diff}\right|^2 df} \qquad (3-380)$$

$$v_{n,1/f,diff} = FNN_{diff}\sqrt{\int_{f_0}^{\frac{\pi}{2}f_L} \frac{1+f^2/f_z^2}{1+f^2/f_{p,diff}^2}\frac{1}{f}df} \qquad (3-381)$$

Using equation $(1-19)$ and recalling that $f_{p,diff} = f_L$, the above integral becomes

$$v_{n,1/f,diff} = FNN_{diff}\sqrt{\ln\left(\frac{\pi}{2}\frac{f_L}{f_0}\right) + \frac{1}{2}\left(\frac{f_L^2}{f_z^2}-1\right)\ln\left(\frac{\left(\frac{\pi^2}{4}+1\right)f_L^2}{f_0^2+f_L^2}\right)} \qquad (3-382)$$

If f_0 is chosen to be 1mHz, then $f_L \gg f_0$

$$v_{n,1/f,diff} = FNN_{diff}\sqrt{\ln\left(\frac{\pi}{2}\frac{f_L}{f_0}\right) + \frac{1}{2}\left(\frac{f_L^2}{f_{z,diff}^2}-1\right)\ln\left(\frac{\pi^2}{4}+1\right)} \qquad (3-383)$$

If $\frac{f_L^2}{f_z^2} \gg 1$

$$v_{n,1/f,diff} = FNN_{diff}\sqrt{\ln\left(\frac{\pi}{2}\frac{f_L}{f_0}\right) + \frac{1}{2}\frac{f_L^2}{f_z^2}\ln\left(\frac{\pi^2}{4}+1\right)} \qquad (3-384)$$

If $\frac{1}{2}\frac{f_L^2}{f_z^2}\ln\left(\frac{\pi^2}{4}+1\right) \gg \ln\left(\frac{\pi}{2}\frac{f_L}{f_0}\right)$

$$v_{n,1/f,diff} = \frac{f_L}{f_z}FNN_{diff}\sqrt{\frac{1}{2}\ln\left(\frac{\pi^2}{4}+1\right)} \qquad (3-385)$$

Substitute $(3-371)$ into $(3-385)$

$$v_{n,1/f,diff} = (1+2\pi R_{DIFF}C_{DIFF}f_L)FNN_{diff}\sqrt{\frac{1}{2}\ln\left(\frac{\pi^2}{4}+1\right)} \qquad (3-386)$$

The photocurrent shot noise sees the same transfer function as the photodiode shunt resistance current noise. Thus, using equation $(3-359)$, we can write

$$\frac{\psi_{o,i,\ell s}}{\xi_{\ell s}} = \frac{1}{j2\pi f C_F} \tag{3-387}$$

With the differentiator, the transfer function is

$$\frac{\psi_{o,d,\ell s}}{\xi_{\ell s}} = -\frac{R_{DIFF}C_{DIFF}}{C_F}\frac{1}{1+j2\pi f R_{DIFF}C_{F2}} \tag{3-388}$$

The noise density is then

$$\left|\psi_{o,d,\ell s}\right| = \frac{R_{DIFF}C_{DIFF}}{C_F}\frac{\sqrt{2q\bar{i_p}}}{\sqrt{1+f^2(2\pi R_{DIFF}C_{F2})^2}} \tag{3-389}$$

The RMS voltage noise

$$v_{n,light} = \sqrt{\int_0^\infty |G_{LPF}(f)|^2 \left|\psi_{o,d,\ell s}\right|^2 df} = \sqrt{\int_0^{\frac{\pi}{2}f_L} \left|\psi_{o,d,\ell s}\right|^2 df} \tag{3-390}$$

$$v_{n,light} = \frac{R_{DIFF}C_{DIFF}}{C_F}\sqrt{2q\bar{i_p}}\sqrt{\int_0^{\frac{\pi}{2}f_L} \frac{1}{1+f^2/f_{p,diff}^2} df} \tag{3-391}$$

Using equation $(1-13)$ the result of the above integral is

$$v_{n,light} = \frac{R_{DIFF}C_{DIFF}}{C_F}\sqrt{2q\bar{i_p}f_L} \tag{3-392}$$

The dark noise density is then the quadratic sum of all the inherent noise sources when no light reaches the photodiode. This includes the noise densities in equations $(3-330)$, $(3-337)$, $(3-345)$, $(3-355)$, $(3-361)$, $(3-366)$, $(3-372)$, and $(3-379)$.

$$\left|\psi_{o,dark}\right| = \sqrt{\begin{matrix}\left|\psi_{o,RCFB}\right|^2 + \left|\psi_{o,T,ff}\right|^2 + \left|\psi_{o,1/f,ff}\right|^2 + \left|\psi_{o,s,ff}\right|^2 + \left|\psi_{o,rsh}\right|^2 \\ +\left|\psi_{o,RDIFF}\right|^2 + \left|\psi_{o,T,diff}\right|^2 + \left|\psi_{o,1/f,diff}\right|^2\end{matrix}} \qquad (3-393)$$

The RMS dark noise is then the quadratic some of all the RMS noise voltages observed at the output of the 2nd stage.

$$v_{n,dark} = \sqrt{\begin{matrix}v_{n,RCFB}^2 + v_{n,T,ff}^2 + v_{n,1/f,ff}^2 + v_{n,s,ff}^2 \\ +v_{n,rsh}^2 + v_{n,RDIFF}^2 + v_{n,T,diff}^2 + v_{n,1/f,diff}^2\end{matrix}} \qquad (3-394)$$

Substitute $(3-333)$, $(3-342)$, $(3-352)$, $(3-358)$, $(3-364)$, $(3-369)$, $(3-377)$, and $(3-386)$ into $(3-394)$.

$$v_{n,dark} = \sqrt{\begin{matrix}\left(\frac{R_{DIFF}C_{DIFF}}{C_F}\right)^2 \alpha' f_L + (R_{DIFF}C_{DIFF})^2\left(2\frac{C_{in}}{C_F}+1\right)(2\pi f_L)^2\gamma_{int} \\ +(1+2\pi R_{DIFF}C_{DIFF}f_L)^2\gamma_{diff} + \kappa\end{matrix}} \qquad (3-395)$$

where

$$\alpha' = \xi_{s,ff}^2 + \frac{4kT}{R_{CFB}} + \frac{4kT}{r_{sh}} + 4\pi^2 c_{in}^2 f_L \gamma_{int}$$

$$\gamma_{int} = \psi_{T,ff}^2\left(\frac{\pi}{2}-1\right)f_L + FNN_{ff}^2\frac{1}{2}\ln\left(\frac{\pi^2}{4}+1\right) \qquad (3-396)$$

$$\gamma_{diff} = \psi_{T,diff}^2\left(\frac{\pi}{2}-1\right)f_L + FNN_{diff}^2\frac{1}{2}\ln\left(\frac{\pi^2}{4}+1\right) \qquad (3-397)$$

$$\kappa = 4kTR_{DIFF}f_L + (2\pi R_{DIFF}C_{DIFF})^2\left(\gamma_{int}+\gamma_{diff}\right)f_L^2 \qquad (3-398)$$

If $2\pi R_{DIFF}C_{DIFF}f_L \gg 1$, then equation $(3-395)$ becomes

$$v_{n,dark} = \sqrt{\alpha' f_L \left(\frac{R_{DIFF} C_{DIFF}}{C_F}\right)^2 + \beta f_L \left(\frac{R_{DIFF} C_{DIFF}}{C_F}\right) + \kappa} \qquad (3-399)$$

where

$$\beta = 8\pi^2 c_{in} R_{DIFF} C_{DIFF} \gamma_{int} f_L \qquad (3-400)$$

The total noise is then the quadratic sum of light and dark noise

$$v_{n,total} = \sqrt{v_{n,dark}^2 + v_{n,light}^2}$$

Substituting $(3-399)$ and $(3-392)$ into the expression above gives us the total noise.

$$v_{n,total} = \sqrt{\alpha f_L \left(\frac{R_{DIFF} C_{DIFF}}{C_F}\right)^2 + \beta f_L \left(\frac{R_{DIFF} C_{DIFF}}{C_F}\right) + \kappa} \qquad (3-401)$$

where

$$\alpha = \xi_{s,ff}^2 + \frac{4kT}{R_{CFB}} + \frac{4kT}{r_{sh}} + 2q\bar{i_p} + (2\pi c_{in})^2 f_L \gamma_{int} \qquad (3-402)$$

3.4.2 *Signal-to-Noise Ratio*

The gain of the charge amplifier (integrator and differentiator combined) is

$$G_Q = \frac{R_{DIFF}C_{DIFF}}{C_F} \tag{3-403}$$

The SNR is then the RMS signal current times G_Q over the total RMS noise defined in equation $(3-401)$.

$$SNR = \frac{\frac{R_{DIFF}C_{DIFF}}{C_F}\widetilde{\imath_p}}{\sqrt{\alpha f_L\left(\frac{R_{DIFF}C_{DIFF}}{C_F}\right)^2 + \beta f_L\left(\frac{R_{DIFF}C_{DIFF}}{C_F}\right) + \kappa}} \tag{3-404}$$

Right away we notice many differences between the equation for this topology compared to the ones studied in the previous sections. The coefficient β in this case contains more terms than any of the other topologies studied. Further differences are brought to light when we take the limit of the SNR as the gain goes to infinity.

$$SNR_\infty = \lim_{G_Q\to\infty} SNR = \frac{\widetilde{\imath_p}}{\sqrt{\alpha f_L}} \tag{3-405}$$

Here the coefficient α contains 1 more term than that of the single-resistor topology: the thermal noise from R_{CFB}. Even though R_{CFB} can be made very large when photocurrent is low, this shows that the SNR_∞ of the charge amp will never be as good as that of the single-resistor topology. The value of G_Q at 90% of SNR_∞, can be calculated using the equation below.

$$G_{Q,90} = \frac{81}{38}\left(\frac{\beta}{\alpha} + \sqrt{\frac{\beta^2}{\alpha^2} + \frac{76}{81}\frac{\kappa}{\alpha f_L}}\right) \tag{3-406}$$

After obtaining $G_{Q,90}$, one can choose the differentiator gain $2\pi R_{DIFF}C_{DIFF}$ and use equation $(3-403)$ to calculate C_F. Because the term α contains the DC photocurrent, the value of $G_{Q,90}$ will change with $\overline{\imath_p}$. In order to determine the maximum value of $G_{Q,90}$, we can let the term $\overline{\imath_p}$ go to zero. The result is shown below.

$$\hat{G}_{Q,90} = \lim_{\overline{\imath_p}\to 0} G_{Q,90} = \frac{81}{38}\left(\frac{\beta}{\alpha^*} + \sqrt{\left(\frac{\beta}{\alpha^*}\right)^2 + \frac{76}{81}\frac{\kappa}{\alpha^* f_L}}\right) \qquad (3-407)$$

where

$$\alpha^* = \xi_{s,ff}^2 + \frac{4kT}{R_{CFB}} + \frac{4kT}{r_{sh}} + (2\pi c_{in})^2 f_L \gamma_{int}$$

3.5 Avalanche Photodiode Amplifiers

In this section we will investigate the performance of avalanche photodiodes and the associated transimpedance amplifiers. APDs have been used by some researchers for fluorescence detection [3]. We will see in this section how the internal gain of the APD affects the detection limit.

3.5.1 *Noise Analysis*

The APD and amplifier are shown below in the left panel of Figure 3-10. Here the APD is biased at a high voltage (around 100V) to facilitate avalanche multiplication. In the noise model (right side of the figure), this fixed supply can be modeled as AC ground. The op-amp in this circuit will be modeled as having common-mode and differential-mode input capacitances, c_{cm} and c_{dm} respectively. It will have input-current shot noise ξ_s, thermal noise ψ_T and flicker noise $\psi_{1/f}$. It will be modeled as having infinite gain.

The APD is modeled as having dark current shot noise and photocurrent shot noise. It has junction capacitance c_j. The photodiode junction capacitance and op-amp input capacitance combine in parallel to produce c_{in} which is defined in the previous section in equation $(3-2)$.

For all calculations of RMS noise in this section, we will assume that the TIA is followed by a high-order low-pass filter like the one described in section 1.3.1 which can be approximated by equation $(1-12)$. Thus the upper limit of the integrals will not be ∞ but instead $\frac{\pi}{2} f_L$.

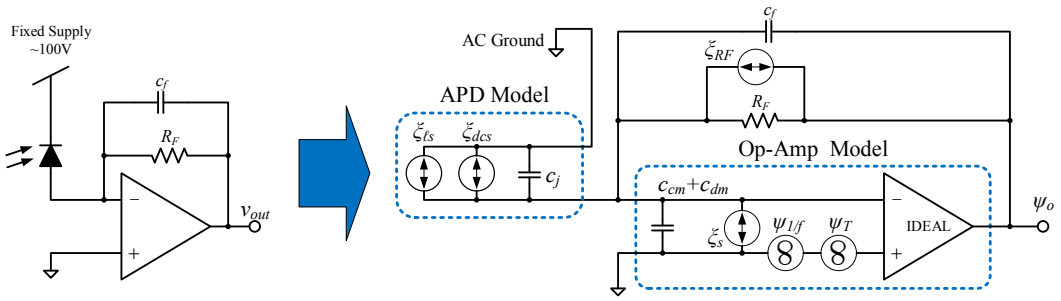

Figure 3-10: Avalanche photodiode circuit (left) and corresponding noise model (right).

For this analysis we will consider each noise source independently and then use superposition to determine the total noise. The thermal noise from the op-amp sees the transfer function shown below

$$\frac{\psi_{o,T}}{\psi_T} = \frac{1 + j2\pi f R_F(c_f + c_{in})}{1 + j2\pi f R_F c_f} \qquad (3-408)$$

Now we can clearly see that there is a pole at

$$f_p = f_L = \frac{1}{2\pi R_F c_f} \qquad (3-409)$$

and a zero at

$$f_z = \frac{1}{2\pi R_F(c_f + c_{in})} \qquad (3-410)$$

Solve f_L for c_f in equation $(3-409)$ and substitute the result into $(3-410)$

$$f_z = \frac{f_L}{1 + 2\pi R_F c_{in} f_L} \qquad (3-411)$$

Take the magnitude of $(3-408)$

$$\left|\psi_{o,T}\right| = \frac{\sqrt{1 + f^2\left(2\pi R_F\left(c_f + c_{in}\right)\right)^2}}{\sqrt{1 + f\left(2\pi R_F c_f\right)^2}}\psi_T \qquad (3-412)$$

Because the transfer function in $(3-408)$ has the form of the filter described in section 1 equation $(1-14)$, we can use equation $(1-16)$.

$$v_{n,T} = \sqrt{\int_0^{\frac{\pi}{2}f_L}\left|\psi_{o,T}\right|^2 df} = \psi_T\sqrt{f_L\left(\left(\frac{\pi}{2}-1\right)\frac{f_L^2}{f_z^2}+1\right)} \qquad (3-413)$$

Substitute $(3-411)$ into $(3-413)$

$$v_{n,T} = \psi_T\sqrt{f_L\left(\left(\frac{\pi}{2}-1\right)(1+2\pi R_F c_{in} f_L)^2+1\right)} \qquad (3-414)$$

If $\left(\frac{\pi}{2}-1\right)(1+2\pi R_F c_{in} f_L)^2 \gg 1$, then

$$v_{n,T} = (1+2\pi R_F c_{in} f_L)\psi_T\sqrt{\left(\frac{\pi}{2}-1\right)f_L} \qquad (3-415)$$

The op-amp flicker noise has the same transfer function as the op-amp thermal noise. Using equation $(3-408)$ we can write

$$\frac{\psi_{o,1/f}}{\psi_{1/f}} = \frac{1 + j2\pi f R_F\left(c_f + c_{in}\right)}{1 + j2\pi f R_F c_f} \qquad (3-416)$$

Take the magnitude of $(3-416)$ to get the noise density.

$$\left|\psi_{o,1/f}\right| = \frac{\sqrt{1 + f^2\left(2\pi R_F\left(c_f + c_{in}\right)\right)^2}}{\sqrt{1 + f^2\left(2\pi R_F c_f\right)^2}}\frac{FNN}{\sqrt{f}} \qquad (3-417)$$

Squaring $(3-417)$, integrating over f, and taking the square root yields the RMS noise voltage. Because the transfer function in $(3-416)$ has the same form as that in $(1-14)$, we can use equation $(1-19)$ as the result of the integration.

$$v_{n,1/f} = \sqrt{\int_0^{\frac{\pi}{2}f_L} \left|\psi_{o,1/f}\right|^2 df} = FNN\sqrt{\ln\left(\frac{\pi}{2}\frac{f_L}{f_0}\right) + \frac{\ln\left(1+\frac{\pi^2}{4}\right)}{2}\left(\frac{f_L^2}{f_z^2}-1\right)} \qquad (3-418)$$

Substitute $(3-411)$ into $(3-418)$ $(3-413)$

$$v_{n,1/f} = FNN\sqrt{\ln\left(\frac{\pi}{2}\frac{f_L}{f_0}\right) + \frac{\ln\left(1+\frac{\pi^2}{4}\right)}{2}((1+2\pi R_F c_{in} f_L)^2 - 1)} \qquad (3-419)$$

If $\left(\frac{\pi}{2}-1\right)(1+2\pi R_F c_{in} f_L)^2 \gg 1$, then

$$v_{n,1/f} = FNN\sqrt{\ln\left(\frac{\pi}{2}\frac{f_L}{f_0}\right) + \frac{\ln\left(1+\frac{\pi^2}{4}\right)}{2}(1+2\pi R_F f_L c_{in})^2} \qquad (3-420)$$

The noise from the op-amp input current and the feedback resistor are the same for the APD amplifier as they are for the single-feedback resistor TIA. The RMS noise voltage associated with the input current shot noise and the feedback resistor thermal noise are defined in equations $(3-33)$ and $(3-28)$ respectively.

The APD's dark current shot noise sees the same transfer function as the op-amp input current shot noise. Using equation $(3-31)$, we can write

$$\frac{\psi_{o,dcs}}{\xi_{dcs}} = \frac{R_F}{1+j2\pi f R_F c_f} \qquad (3-421)$$

The noise density is then the magnitude of the above expression.

$$\left|\psi_{o,dcs}\right| = \frac{R_F\sqrt{2qI_DF}}{\sqrt{1+f^2\left(2\pi R_F c_f\right)^2}} \qquad (3-422)$$

where F is the excess noise factor. The RMS voltage noise at the circuit's output contributed by ξ_{dcs} can be found by taking the square root of the integral of the noise density as shown below. Because the transfer function in $(3-421)$ is the same form as that in $(1-8)$, we can use equation $(1-13)$ as the result of the integral. We then have

$$v_{n,dcs} = \sqrt{\int_0^{\frac{\pi}{2}f_L}\left|\psi_{o,dcs}\right|^2 df} = R_F\sqrt{2qI_DFf_L} \qquad (3-423)$$

Photocurrent shot noise sees the same transfer function as leakage current shot noise. Using equation $(3-421)$

$$\frac{\psi_{o,\ell s}}{\xi_{\ell s}} = \frac{R_F}{1+j2\pi f R_F c_f} \qquad (3-424)$$

The noise density is then

$$\left|\psi_{o,\ell s}\right| = \frac{MR_F\sqrt{2q\bar{\imath_p}F}}{\sqrt{1+f^2\left(2\pi R_F c_f\right)^2}} \qquad (3-425)$$

where M is the APD's avalanche gain and F is its excess noise factor (see section 1.4.5). The RMS voltage noise at the circuit's output contributed by $\xi_{\ell s}$ can be found by taking the square root of the integral of the noise density as shown below. Because the transfer function in $(3-424)$ is the same form as that in $(1-8)$, we can use equation $(1-13)$ as the result of the integral. We then have

$$v_{n,light} = \sqrt{\int_0^{\frac{\pi}{2}f_L}\left|\psi_{o,\ell s}\right|^2 df} = MR_F\sqrt{2q\bar{\imath_p}Ff_L} \qquad (3-426)$$

The total dark noise is then the quadratic sum of all the noise sources inherent to the amplifier. The equation is shown below.

$$v_{n,dark} = \sqrt{v_{n,T}^2 + v_{n,1/f}^2 + v_{n,RF}^2 + v_{n,s}^2 + v_{n,dcs}^2} \qquad (3-427)$$

Substitute equations $(3-415)$, $(3-420)$, $(3-28)$, $(3-33)$, and $(3-423)$ into $(3-427)$. The result is

$$v_{n,dark} = \sqrt{\alpha' f_L R_F^2 + \beta' f_L R_F + \gamma + FNN^2 \ln\left(\frac{\pi}{2}\frac{f_L}{f_0}\right)} \qquad (3-428)$$

where

$$\alpha' = 2qI_D F + \xi_s^2 + (2\pi c_{in})^2 \gamma f_L$$

$$\beta' = 4kT + 4\pi c_{in}\gamma$$

$$\gamma = \psi_T^2\left(\frac{\pi}{2} - 1\right) f_L + FNN^2 \frac{\ln\left(1 + \frac{\pi^2}{4}\right)}{2} \qquad (3-429)$$

The total noise is then the quadratic sum of the light and dark noise voltages.

$$v_{n,total} = \sqrt{v_{n,dark}^2 + v_{n,light}^2}$$

$$v_{n,total} = \sqrt{\alpha f_L R_F^2 + \beta R_F f_L + \kappa_{APD}} \qquad (3-430)$$

$$\alpha = 2q\bar{\imath}_p M^2 F + 2qI_D F + \xi_s^2 + (2\pi c_{in})^2 \gamma f_L \qquad (3-431)$$

$$\beta = 4kT + 4\pi c_{in}\gamma \qquad (3-432)$$

$$\kappa_{APD} = \gamma + FNN^2 \ln\left(\frac{\pi}{2}\frac{f_L}{f_0}\right) \qquad (3-433)$$

3.5.2 *Signal-To-Noise Ratio*

The SNR is the ratio of the RMS output voltage to the total noise given in equation $(3-430)$.

$$SNR = \frac{MR_F\widetilde{\imath_p}}{\sqrt{\alpha f_L R_F^2 + \beta R_F f_L + \kappa_{APD}}} \tag{3-434}$$

Where the terms α, β, and κ_{APD} are defined in equations $(3-431)$, $(3-432)$, $(3-429)$, and $(3-433)$ respectively. Taking the limit of equation $(3-53)$ as R_F approaches infinity gives us the maximum possible SNR for a given op-amp and APD.

$$SNR_\infty = \lim_{R_F\to\infty} SNR = \frac{M\widetilde{\imath_p}}{\sqrt{\alpha f_L}} \tag{3-435}$$

While the SNR_∞ represents the theoretical ceiling, a "practical" target for R_F can be $R_{F,90}$, the feedback resistance corresponding to 90% of SNR_∞. Increasing R_F beyond $R_{F,90}$ would no longer result in significant improvement of SNR. The value of $R_{F,90}$ can be approximated using the following simple formula:

$$R_{F,90} = 4.26\frac{\beta}{\alpha} \tag{3-436}$$

The peak value of $R_{F,90}$ is then found by letting $\overline{\imath_p} \to 0$ in the denominator term α. The result is

$$\hat{R}_{F,90} = \lim_{\overline{\imath_p}\to 0} R_{F,90} = 4.26\frac{\beta}{\alpha^*} \tag{3-437}$$

where

$$\alpha^* = 2qI_D F + \xi_s^2 + (2\pi c_{in})^2 \gamma f_L$$

It is interesting to note that the value of $R_{F,90}$ for APDs is much lower than that for the PIN photodiode transimpedance amplifier. The table in APPENDIX 2 shows this value to be around $1 - 100\text{M}\Omega$. This means that the sensitivity of these amplifiers can be easily increased without the concern of losing bandwidth.

Chapter 4 Assessment of Commercially Available Components for Transimpedance Amplifiers Optimized for low-light Applications

4.1 Photodiodes

4.1.1 *PIN Photodiodes*

There is currently an extremely large selection of photodiodes on the market today. These devices are offered in a range of sizes, performance levels, and compositions. In this section we will present and discuss a survey of the current technology which will aid in determining the best possible for a photodiode amplifier.

In this section we will discuss the range of parameters for some PIN photodiodes. We will be specifically focusing on shunt resistance r_{sh} which determines the noise contribution of the diode, junction capacitance c_j which affects the noise gain and bandwidth, and quantum efficiency η which tells us how good is the diode at converting light into electricity. Figure 4-1 shows plots of data taken from 170 PIN photodiodes that were included in the survey. On the left, we show the relation between r_{sh} and photosensitive area. From this plot, one can clearly see that r_{sh} is inversely proportional to area. The range of values is also important. Here we see r_{sh} ranging anywhere from $\sim 10\text{M}\Omega$ to $\sim 100\text{G}\Omega$. The literature, however, predicts this range to be $\sim 10\text{M} - \sim 1\text{G}\Omega$ [29]. On the right we have data showing the relation of c_j to photosensitive area. Again, as one would expect, the relation between c_j and area is roughly linear. One can observe the range of c_j to be from $\sim 1\text{pF}$ to $\sim 10\text{nF}$. Unlike the shunt resistance, this range agrees with what is reported in the literature [41].

The quantum efficiency is also an important parameter. Our survey has found a variety of photodiodes with quantum efficiency greater than 90%. For the complete survey including manufacturer names and part numbers, please see APPENDIX 1.

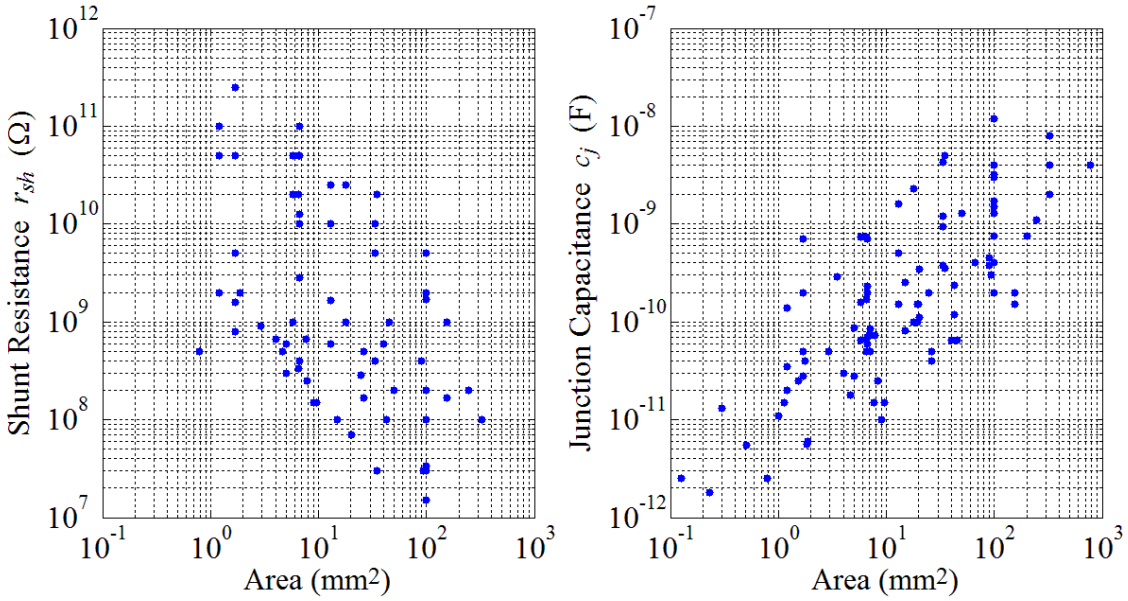

Figure 4-1: Plots of 170 photodiodes included in the survey. The left plot shows the relation between photosensitive area and shunt resistance and the right plot shows the relation between photosensitive area and junction capacitance.

4.1.2 *Avalanche Photodiodes*

Using the noise analysis that we developed in section 3.5, we will show the performance of 44 different APDs manufactured by Hamamatsu Photonics. The left panel of Figure 4-2 shows the effect of dark current I_D on SNR_∞. Indeed, when conducting this survey, the dark noise was always the dominant noise source when used in conjunction with the low-noise OPA140 op-amp. The value of SNR_∞ for each diode was calculated using equation $(3-435)$ with the peak photocurrent assumed to be 1pA (612fA RMS and 500fA average). The red dots are APDs with an avalanche gain M or 100, the black dots have a gain of 50 and the blue dots have a gain of

either 40 or 60 (see table in APPENDIX 2). Surprisingly, the photodiodes with lower avalanche gain M tend to have a higher value of SNR_∞.

The right panel of Figure 4-2 shows the effect of increasing photosensitive area on dark current. As one would expect, the larger diodes have more leakage current and therefore will be noisier. While smaller PIN photodiodes also tend to have better performance, the APDs are typically much smaller by comparison. Notice that the best PIN diodes (highest shunt resistance) in the left panel of Figure 4-1 have area $\sim 1\text{mm}^2$ while the best APDs have area $\sim 100\mu\text{m}^2$. This will make coupling the diode to an imaging system much more difficult and costly.

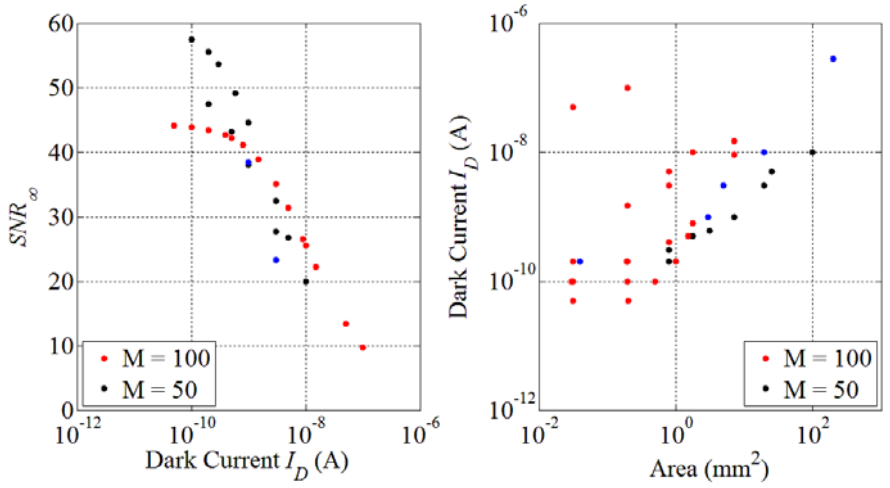

Figure 4-2: Plot of SNR_∞ vs I_D (left) and I_D vs photosensitive area (right) for 44 Hamamatsu APDs. The dots in red have a typical avalanche gain of 100 and the ones in black have a typical gain of 50. The blue dots represent APDs with a gain of either 40 or 60 (see table in APPENDIX 2).

A survey was conducted on APD modules made by Hamamatsu Photonics. The results are shown in Table 4-1. Here we took the information from the datasheet and used it to calculate SNR for each module. The noise performance of each module was given in the form of noise equivalent power (NEP) which was used to calculate the SNR. The formula for the APD noise is shown below.

$$v_{n,apd} = M\, R_F\, NEP\, R(\lambda_p) \sqrt{f_L} \qquad (4-1)$$

The SNR is then calculated using the formula below.

$$SNR = \frac{M R_F \tilde{\imath_p}}{\sqrt{M 2 q \bar{\imath_p} R_F f_L + v_{n,apd}^2}} \qquad (4-2)$$

Here we used $f_L = 300\text{Hz}$, $\tilde{\imath_p} = 612\text{fA}$ and $\bar{\imath_p} = 500\text{fA}$. We have had to drop the excess noise factor F which appears in front of the photocurrent shot noise term because it was not provided in the datasheet.

An interesting anomaly was discovered when investigating the APD modules. While the maximum SNR_∞ for the APDs in the survey was 57.5 for $\hat{\imath_p} = 1\text{pA}$, and many diodes had SNR_∞ around 40 (see table in APPENDIX 2), the highest SNR for the APD modules was only 3.53. One may think that because the value of R_F is low for many of these modules that these devices are built for speed and not sensitivity. However, the value of $R_{F,90}$ for most APDs is around $10\text{M}\Omega$ which is the same value used for the modules with the highest SNR. One may also speculate that it is because the avalanche gain M is lower for the modules with $R_F = 10\text{M}\Omega$, but even if it were increased to $100\text{M}\Omega$ (the typical value calculated for the individual APDs) this would only raise the SNR by about a factor of 3. This begs the question why is the SNR of the modules $\times 10$ lower than that of the APDs?

A possible explanation is that the power supply used to bias the APD may be producing a great deal of noise and thus lowering the SNR. Recall that power supply noise was not included in the analysis of the APD amplifier in section 3.5 due to lack of data. The power supplies typically used for these modules is the switch-mode converter type, which uses a high-frequency square wave as input to a transformer. The harmonics of the square wave may be creating additional noise.

Table 4-1: Table of APD modules from Hamamatsu Photonics. The responsivity at the peak wavelength $R(\lambda_p)$ is specified for gain $M = 1$.

Part #	SNR @ $\widehat{\imath_p} = 1\text{pA}$		M	R_F (Ω)	NEP $(\text{pW}/\sqrt{\text{Hz}})$		Area (mm^2)	$R(\lambda_p)$ (A/W)
	Typ.	Min.			Typ.	Max.		
C10508-01	3.53	1.77	250	10k	0.02	0.04	0.8	0.5
C12702-03	0.24	0.12	30	9.1k	0.30	0.6	0.8	0.5
C12702-04	0.18	0.09	30	3.0k	0.40	0.8	7.1	0.5
C12702-11	0.17	0.08	30	3.9k	0.50	1.0	0.8	0.42
C12702-12	0.08	0.04	30	3.0k	1.00	2.0	7.1	0.42
C12703	0.35	0.18	30	10k	0.20	0.4	1.8	0.5
C12703-01	3.53	1.77	30	10M	0.02	0.04	7.1	0.5
C5658	0.16	-	100	5.5k	0.50	-	0.2	0.45
C5460	0.35	0.18	30	10k	0.20	0.4	1.8	0.5
C5460-01	3.53	1.77	30	10M	0.02	0.04	7.1	0.5

4.2 Operational Amplifiers

As we have shown in section 3.1.1, the op-amp contributes to the total noise of the TIA with its thermal noise, flicker noise and input current shot noise. In this section we will conduct a brief survey of commercially available op-amps and tabulate their relevant parameters.

Figure 4-3 shows plots of 23 different op-amps and their respective noise characteristics. The plot on the left shows each op-amp's current and flicker noise. An inverse proportionality is clearly observable, hence the fit line. The equation of the fit line is shown below.

$$\xi_s = \frac{126}{FNN}$$

The plot on the right side of Figure 4-3 shows the op-amp thermal noise compared to current noise. Notice that the range over which the thermal noise varies is much smaller than that of the flicker noise. There is also no visible correlation between the two parameters.

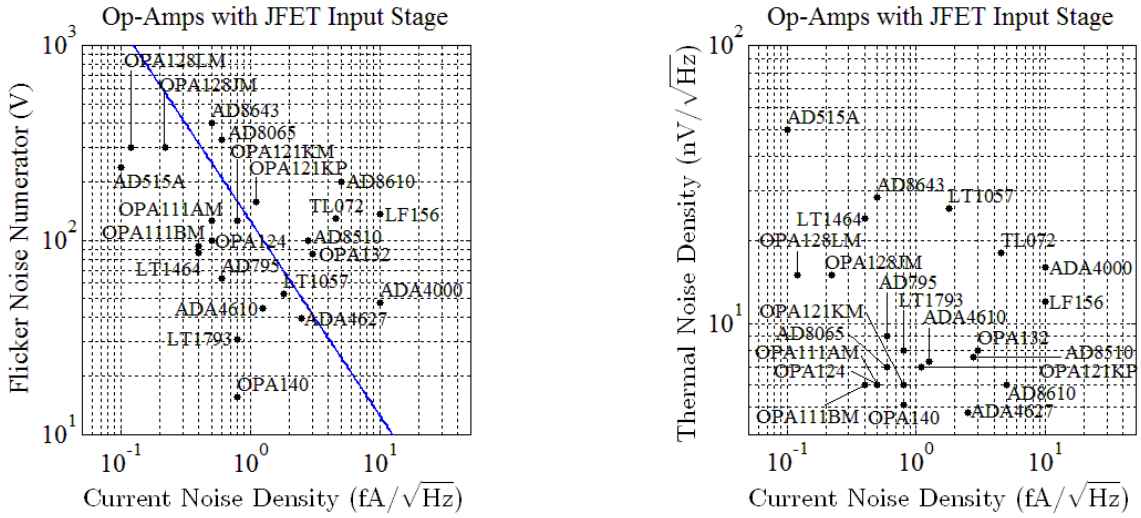

Figure 4-3: Survey of op-amps and their voltage and current noise. Flicker noise and corresponding current noise for op-amps with JFET input stages and fit line (left). Thermal noise and corresponding current noise for op-amps with JFET input stages (right).

A successful physical implementation of a transimpedance amplifier with significantly increased sensitivity is critically dependent on optimal op-amp selection. The analysis of equations $(3-56)$ and $(3-50)$ suggests that in order to maximize the SNR one should minimize both the op-amp current and voltage noise contributions represented by the first and last terms in equation $(3-50)$ respectively. Note that the voltage noise is multiplied by the square of input capacitance c_{in}^2. The main contributor to c_{in} is the junctional capacitance c_j of the photodiode, which can range between 1pF and 1nF. At small c_{in} $(c_{in} < 1\text{pF})$ the contribution of the voltage noise is relatively small and can be ingored. For this range the best

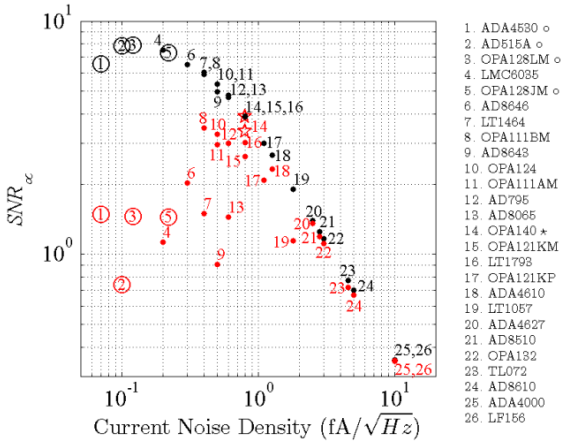

Figure 4-4: Estimated performance of 26 op-amps with the lowest current noise density when used with photodiodes with low and high junctional capacitance. Black and red symbols indicate SNR_∞ of a given op-amp when used with photodiodes with zero and 100pF junctional capacitance, respectively. The smaller numbers indicate op-amps with the lower current noise density. The photodiode shunt resistance is 100GΩ and the bandwidth was 300Hz.

op-amp for our applications should be an electrometer amplifier, which are known for their low current noise density, $\xi_s \sim 0.1\text{fA}/\sqrt{\text{Hz}}$ [26].

However, this is not the case when such op-amps are used in combination with photodiodes having a large surface area and correspondingly large input junctional capacitance c_j. A review of the devices with low current noise density $\left(\leq 10\text{fA}/\sqrt{\text{Hz}}\right)$ show such devices have usually higher thermal and flicker noise voltages. At small c_f and large c_{in} the already high flicker and thermal noise voltages are amplified by the noise-gain-peaking mechanism to become significant [31].

Figure 4-4 shows SNR_∞ for 26 op-amps with low current noise calculated with equations $(3-56)$ and $(3-50)$. Notice that many of the op-amps with lower current noise, the so-called electrometer type (open circles) suffer significantly reduced performance when used with photodiodes with higher junction capacitance (red symbols). The op-amps that show a robust performance and maintain high SNR_∞ are #8, 10-12, and 14- 18. These include the OPA140 (#14, star) which is the one used in our prototype. We also tested the LMC6035 (#4) and the AD8641/AD8643 (#9), which have lower current noise than the OPA140 even though they experience a significant decrease in SNR_∞ with large c_j, they still have good performance with small photodiodes.

Chapter 5 Theoretical Maximum of SNR for TIAs Optimized for Low-Light Detection

5.1 Choosing the Optimal Topology

In this section we will compare all of the topologies discussed in Chapter 3. We will use the SNR equations developed in Chapter 3 and substitute in the optimal parameters uncovered by the component survey in Chapter 4 and the optimal bandwidth determined by the analysis in Chapter 2. We will then select the topology for the application of detecting weak optical signals from tissue.

In Chapter 4, we determined that the OPA140 is one of the best op-amps for our application. We will therefore use the parameters from this op-amp, i.e. ψ_T, FNN, ξ_s, c_{cm}, and c_{dm} for all the simulations in this section unless otherwise noted (see APPENDIX 3 for the specific parameter values).

5.1.1 *T-Bridge Topology vs. Single Feedback-Resistor Topology*

The T-bridge topology (section 3.2) allows one to set the transimpedance gain using a combination of 3 resistors (see equation $(3-59)$). This is especially useful for very high gains $(>100\text{M}\Omega)$ where the standard resistor sizes of the E-12, E-24 and E-96 series are not readily available. It also distributes the resistor parasitics which potentially offers a way to increase the bandwidth of the circuit. However, we will show that there are limitations to this topology which negate these advantages.

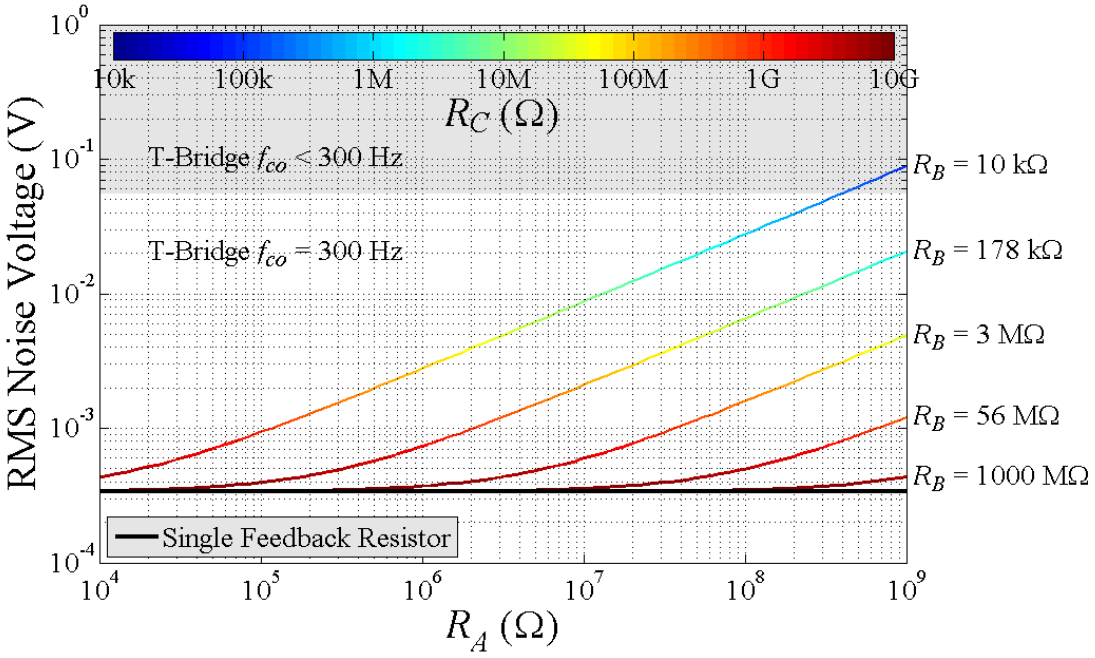

Figure 5-1: Comparison of dark noise of the T-bridge and single feedback-resistor topologies. Both circuits use the OPA140 op-amp and S2386-18K photodiode and have a target bandwidth of 300Hz. The figure shows that the noise performance of the T-bridge will asymptotically approach that of the single-resistor topology.

Figure 5-1 shows a plot of RMS dark noise voltage for the T-bridge using a wide range of resistor values for R_A, R_B, and R_C, compared to the single feedback resistor topology. For this simulation the gain of both circuits has been set to 10GΩ, both used op-amp parameters ψ_T, FNN, ξ_s , c_{cm}, and c_{dm} from the OPA140 datasheet and photodiode parameters $r_{sh} = 100\text{G}\Omega$ and $c_j = 140\text{pF}$ corresponding to the S2386-18K photodiode. The target bandwidth for both circuits was set to 300Hz, the shaded region of the plot shows where the T-bridge could no longer achieve that bandwidth. The resistor were all assumed to have 50fF of parasitic capacitance and the op-amp itself was assumed to have 40fF of parasitic capacitance. As we can see from the plot, the noise performance of the T-bridge will asymptotically approach that of the single-resistor topology.

5.1.2 *AC-Coupled Topologies vs. Single Feedback-Resistor Topology*

Due to the fact that many fluorescent dyes produce large offsets, it may be worthwhile to investigate some AC-coupled TIA topologies. One may think that removing the offset in the first stage will allow that stage to have larger signal gain without clipping and therefore better SNR than a DC-coupled topology. However, in this section we will show that this advantage is always cancelled out by the added noise created by the additional components needed to remove the offset.

The AC-coupled topologies described in section 3.3, i.e. the active current feedback (ACFB) using a resistor circuit (section 3.3.1), the active current feedback using a transconductor circuit (section 3.3.2), and the offset voltage subtraction circuit (section 3.3.3), are compared to the single-resistor DC-coupled circuit described in section 3.1. Analysis carried out in this section shows that there is no significant advantage to AC-coupling. Comparison of equations $(3-194)$, $(3-263)$, $(3-320)$, and $(3-322)$ shows that no matter how the offset is removed the resulting SNR is about the same. The main difference in these equations is the term κ_{INT} which is the feedback integrator noise. While κ_{INT} is the same for the two active-current-feedback topologies, it is different for the offset-voltage-subtraction topology and not present in the equation of the DC-coupled topology. In any case, κ_{INT} can be made very small with proper component selection and careful design.

To illustrate this point further, we created plots of the SNR of the AC-coupled circuits and compared it to that of the single-resistor. The results are shown in Figure 5-2. For this simulation, we plotted equations $(3-194)$, $(3-263)$, $(3-320)$, and $(3-322)$ as a function of peak photocurrent. All circuits used op-amp parameters ψ_T, FNN, ξ_s , c_{cm}, and c_{dm} from the OPA140 datasheet for the forward path and feedback path op-amps and photodiode parameters

$r_{sh} = 100\text{G}\Omega$ and $c_j = 13\text{pF}$. The circuit high-pass and low-pass cutoff frequencies were $f_H = 50\text{mHz}$ and $f_L = 300\text{Hz}$ respectively and the integrator resistors were set to $R_{INT} = 1\text{M}\Omega$. The supply voltage V_{CC} was set to either 1V or 10V and the $\Delta F/F$ of the signal was set to 10% or 100%. As one can see from the figures, there is negligible difference between the SNR of the 4 topologies.

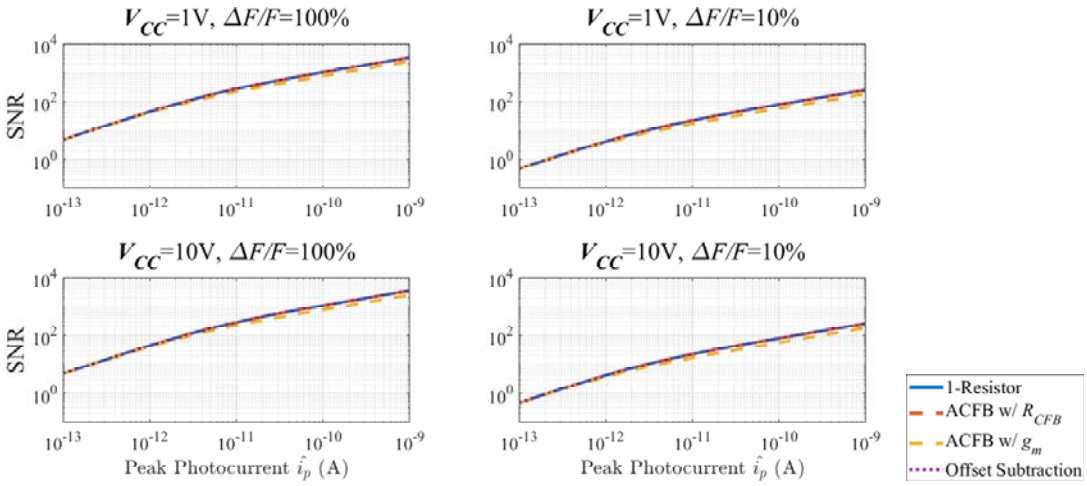

Figure 5-2: Comparison of 3 AC-coupled topologies (active-current feedback (ACFB) with resistor R_{CFB} and transconductor (with conductance g_m) and offset subtraction) with single-resistor DC-coupled topology. Here no limits have been imposed on R_F or R_{CFB}. All circuits used op-amp parameters ψ_T, FNN, ξ_s , c_{cm}, and c_{dm} from the OPA140 datasheet for the forward path and feedback path op-amps and photodiode parameters $r_{sh} = 100\text{G}\Omega$ and $c_j = 13\text{pF}$. The circuit high-pass and low-pass cutoff frequencies were $f_H = 50\text{mHz}$ and $f_L = 300\text{Hz}$ respectively and the integrator resistors were set to $R_{INT} = 1\text{M}\Omega$.

Figure 5-3 shows the same simulation as Figure 5-2 except that practical limits have been imposed on R_F and R_{CFB}, these being $10\text{G}\Omega$ and $100\text{G}\Omega$ respectively. All circuits used op-amp parameters ψ_T, FNN, ξ_s , c_{cm}, and c_{dm} from the OPA140 datasheet for both the forward-path and feedback-path op-amps and photodiode parameters $r_{sh} = 100\text{G}\Omega$ and $c_j = 13\text{pF}$. The circuit high-pass and low-pass cutoff frequencies were $f_H = 50\text{mHz}$ and $f_L = 300\text{Hz}$ respectively (f_H was taken from [14] and f_L was determined using the analysis in Chapter 2) and the integrator resistors were set to $R_{INT} = 1\text{M}\Omega$. The supply voltage V_{CC} was set to either 1V or 10V and the

$\Delta F/F$ of the signal was set to 10% or 100%. Once again, there is negligible difference between the SNR of the 4 topologies.

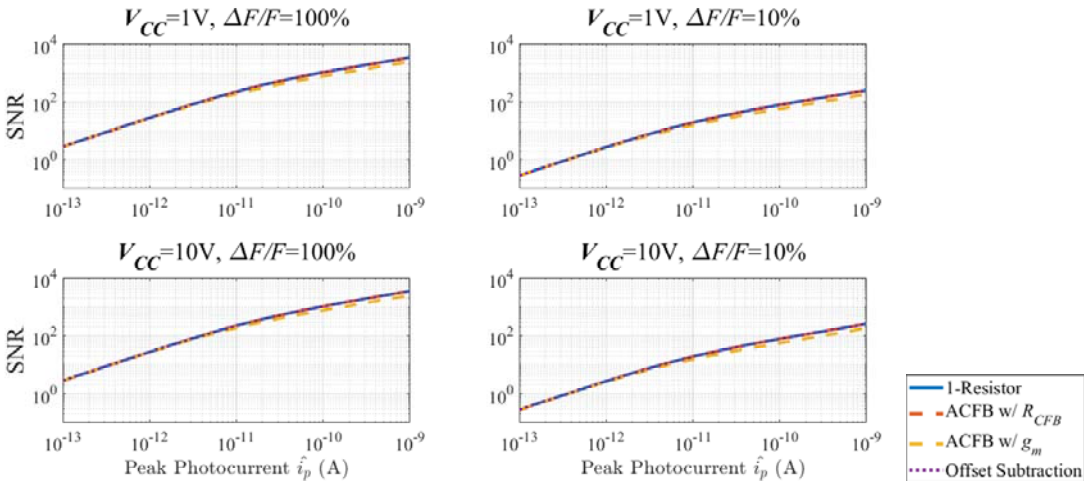

Figure 5-3: Comparison of 3 AC-coupled topologies with single-resistor DC-coupled topology. Here limits have been imposed on R_F which cannot go above 10GΩ and R_{CFB} which cannot go above 100GΩ. All circuits used op-amp parameters ψ_T, FNN, ξ_s , c_{cm}, and c_{dm} from the OPA140 datasheet for the forward path and feedback path op-amps and photodiode parameters $r_{sh} = 100\text{G}\Omega$ and $c_j = 13\text{pF}$. The circuit high-pass and low-pass cutoff frequencies were $f_H = 50\text{mHz}$ and $f_L = 300\text{Hz}$ respectively and the integrator resistors were set to $R_{INT} = 1\text{M}\Omega$.

Thus we conclude that there is no point to AC-coupling for the application of detecting low-intensity optical signals at low bandwidth. We have shown that removing the offset, while allowing for the 1st –stage gain to be increased, does not offer any advantage over a DC-coupled topology. This is because the additional circuit elements required to remove the offset produce additional noise which negates any potential gain. It is worth noting, however, that this result applies to circuits designed to detect biological signals, where the high-pass cutoff of the AC-coupled circuits must be set very low, in this case $f_H = 50\text{mHz}$. For signals with less low-frequency content, the removal of the excess low-frequency noise would certainly offer an advantage. For example, if the signals being detected had been modulated to higher frequency, then AC-coupling would be useful. However, this would put limits on the maximum size of R_F which determines the bandwidth through its parallel combination with parasitic capacitance c_f.

5.1.3 *Charge Amplifier Topology vs. Single-Resistor Topology*

The charge amplifier topology may offer an advantage over the other topologies in this work for 2 reasons: removal of R_F means that the associated resistor thermal noise will no longer be a limiting factor, and the parasitic capacitance c_f is no longer a limiting factor for the bandwidth. In this section we will show that for this application, while the charge amplifier does offer some advantages over the single feedback-resistor topology, they are hardly sufficient to justify the circuit's added complexity.

Figure 5-4 shows the SNR of the charge amplifier and the single feedback-resistor topology (equations $(3-404)$ and $(3-191)$ respectively) vs peak photocurrent. For the simulation in the left panel, we set $R_F = \hat{R}_{F,90} = 80.4\text{G}\Omega$, $C_F = \hat{C}_{F,90} = 36.6\text{pF}$, and $R_{CFB} = 100\text{G}\Omega$ and in the right panel R_F was limited to $10\text{G}\Omega$ while all other parameters remained the same. All circuits used op-amp parameters ψ_T, FNN, ξ_s , c_{cm}, and c_{dm} from the OPA140 datasheet for the forward path and feedback path op-amps except the differentiator which used the parameters from the OPA209 (see APPENDIX 3). The photodiode parameters were $r_{sh} = 100\text{G}\Omega$ and $c_j = 13\text{pF}$. The circuit low-pass cutoff frequencies is $f_L = 300\text{Hz}$ and the $\Delta F/F$ of the signal was set to 10%. As we can see from the figure, if both circuits are set to their maximum gain ($\hat{R}_{F,90}$ and $\hat{C}_{F,90}$) then the charge amplifier has slightly lower SNR than the single-resistor amplifier (left panel). In the right panel we see that once we limit the gain of the single-resistor amplifier to $10\text{G}\Omega$ (the upper limit of what can be achieved in practice while maintaining $f_L = 300\text{Hz}$) we see that the charge amplifier has slightly higher SNR.

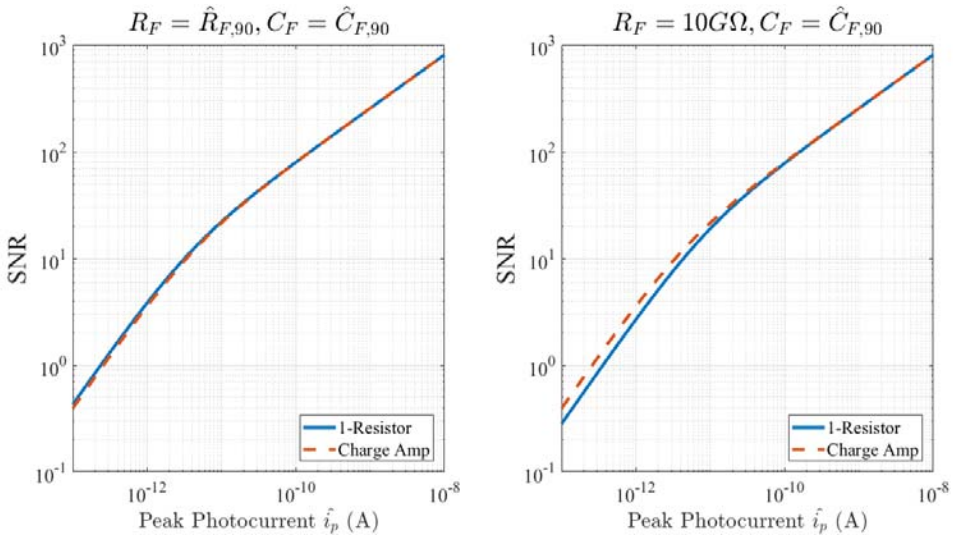

Figure 5-4: Simulations of charge amplifier and single feedback-resistor amplifier. In the left panel, we set $R_F = \hat{R}_{F,90} = 80.4\text{G}\Omega$, $C_F = \hat{C}_{F,90} = 36.6\text{pF}$, and $R_{CFB} = 100\text{G}\Omega$. In the right panel we imposed the practical limit of $10\text{G}\Omega$ on R_F.

Though the charge amplifier can outperform the single-resistor TIA due to the fact that its gain is not limited in the same way by parasitic capacitance, this improvement is likely not enough to justify the added complexity. While the charge amplifier is a good choice for integrated circuit design because it does not require a large linear resistor for R_F (R_{CFB} can be replaced by a MOSFET pseudo resistor), for our application it represents a lot of extra work for a small improvement in performance. This extra work comes in the form of stabilizing the feedback loop that prevents the forward-path integrator from saturating. The charge amplifier is not inherently stable, no matter the choice of op-amps. It therefore falls upon the designer to add an error amplifier to the feedback loop to ensure stability.

5.1.4 *APD TIA Topology vs. Single Feedback-Resistor Topology*

The avalanche photodiode offers the advantage of an internal gain which the PIN photodiode does not have. This allows for higher SNR and lower feedback resistance which makes achieving the desired bandwidth much easier.

Figure 5-5 shows the SNR of the APD amplifier vs that of the single-resistor PIN photodiode amplifier. For this simulation we plotted equations $(3-53)$ and $(3-434)$ as a function of peak photocurrent. We calculated $\hat{R}_{F,90}$ for each topology using equations $(3-58)$ and $(3-437)$. All circuits used op-amp parameters ψ_T, FNN, ξ_s , c_{cm}, and c_{dm} from the OPA140 datasheet and PIN photodiode parameters $r_{sh} = 100\text{G}\Omega$ and $c_j = 13\text{pF}$. The APD is the S12426-02 with $c_j = 0.5\text{pF}$, $I_D = 1\text{nA}$, $F = 3.98$, and $M = 100$ (see APPENDIX 2). The low-pass cutoff frequency was set to 300Hz for both topologies. In the left panel we set $R_F = \hat{R}_{F,90}$ for both topologies. Here we see that the APD offers higher SNR than the PIN by a factor of about 2.5. In the right panel we limit R_F of the PIN photodiode amplifier to $10\text{G}\Omega$, which is near the upper limit of what can be achieved in practice, and the advantage of the APD increases to nearly 4 times higher SNR compared to the PIN. There is no reason to limit R_F in the APD amplifier, because $54.3\text{M}\Omega$ is small enough that there is no concern of not being able to achieve the desired bandwidth.

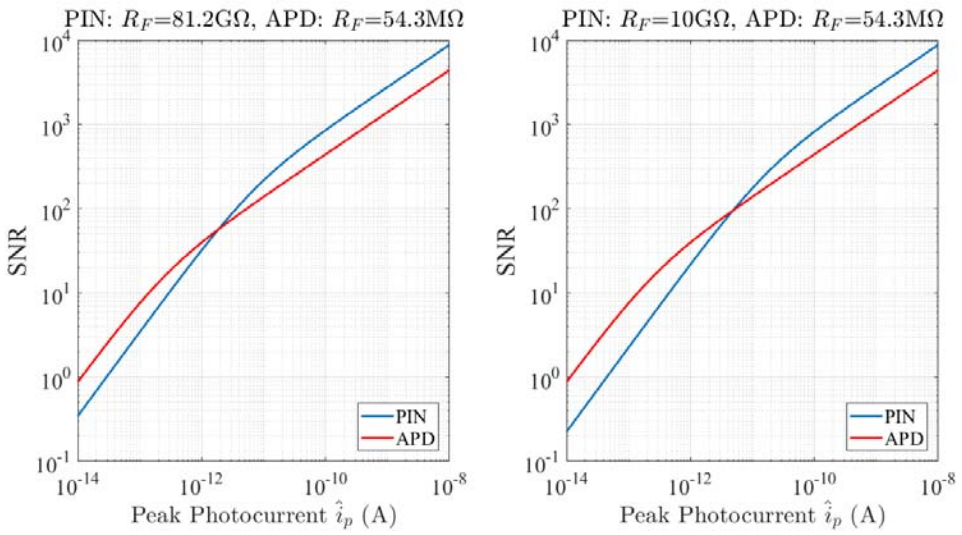

Figure 5-5: Comparison of single-resistor TIA with PIN photodiode to that with an avalanche photodiode. Both circuits used the OPA140 op amp and had a bandwidth of 300Hz.

This analysis clearly shows that the APD has an advantage over the PIN for low photocurrents. However, this model did not account for power-supply coupling from the supply used to bias the APD near its breakdown voltage. This may explain why the commercially available APD modules do not offer an SNR that is higher than that of the PIN photodiode amplifier produced in this work (see section 4.1.2). Not only does this call its performance into question, but the added circuit complexity required to bias the APD and regulate this bias voltage to prevent the device from being destroyed adds a considerable amount of additional circuitry. The cost of APDs is also significantly higher than that of PIN photodiodes. In summation, while the APD may offer some advantages, the single-resistor TIA is a much safer bet.

5.2 Theoretical Limits on Transimpedance Gain

In the previous section we showed that the single-feedback resistor topology is the best choice for detecting low-intensity optical signals. We also referred a number of times to the practical limits of R_F. In this section, we will elaborate on how these limits were determined.

Equation $(3-56)$ is particularly useful for estimating the effect of different characteristics of the photodiode and op-amp on the SNR and for the selection of optimal circuit components. Specifically, from equations $(3-56)$ and $(3-50)$ one can see that for given $\widetilde{\imath_p}$ and f_L, the maximum SNR will be achieved using photodiodes with the highest r_{sh} and op-amps with the lowest current and voltage noise.

Figure 5-6 shows the dependence of SNR on R_F for 2 different peak photocurrents: 1pA and 0.1pA, which are 10^3-10^4 times smaller than those that are commonly recorded [14, 15]. The bandwidth was chosen to be 300Hz, which as we showed in Chapter 2, is sufficient for the majority of biomedical applications. To generate these curves we used a photodiode shunt resistance of $r_{sh}=100\text{G}\Omega$, which is near the upper limit of what current photodiode technology can achieve without thermoelectric cooling (see 3.4). Hamamatsu offers several photodiodes with this shunt resistance such as the S2386 (see APPENDIX 1). The op-amp current noise density ξ_s, thermal noise density ψ_T and flicker noise numerator FNN were taken from the OPA140 datasheet. As we show below this op-amp is optimal for a given class of applications. The input signal was chosen to be a sinusoid with peak photocurrent $\widehat{\imath_p}$, RMS value $\sqrt{6}/4\ \widehat{\imath_p}$ and DC value $\widehat{\imath_p}/2$.

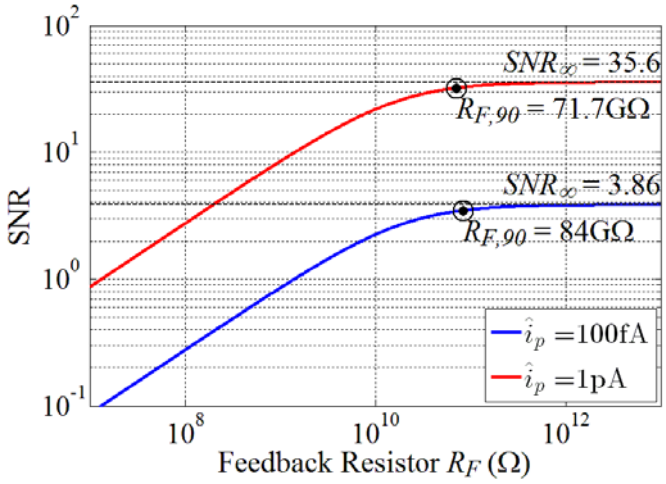

Figure 5-6: Plot of SNR vs R_F for 100fA and 1pA peak photocurrent. The maximum value of the SNR is indicated with a dashed line. Black dots and empty circles show the points where the SNR has reached 90% of the maximum, calcuated using equations (2) and (7) respectively. The RMS signal current is $\widetilde{\imath_p}=\sqrt{6}/4\ \widehat{\imath_p}$ and the DC photocurrent is $\overline{\imath_p}=\widehat{\imath_p}/2$. The op-amp parameters were taken from the OPA140 datasheet and the photodiode parameters are $r_{sh}=100\text{G}\Omega$ and $c_j=13\text{pF}$.

One can see that despite very small photocurrents the theory predicts that at sufficiently high R_F the SNR can be as high as 36 at 1pA and 3.9 at 100fA. This is better than a 10 fold improvement in the SNR as compared to R_F of $10^8\Omega$, which is used in conventional TIAs for biomedical applications.

As can be seen from Figure 5-6 the approximate value of $R_{F,90}$ obtained using $(3-57)$ (empty circles) is not too far off from the exact value obtained using $(3-50)$ (filled circles). For the examples shown in Figure 5-6, $R_{F,90}$ is as high as 71.7 GΩ and 84GΩ for 1pA and 0.1pA, respectively. For very large resistances such as these, the standard resistance values of the commonly used E-12, E-24 and E-96 series are seldom available.

5.3 Theoretical Frequency Response Limits

From the noise analysis carried out in the previous section the target gains should be around $R_{F,90}$, which for photocurrents 1pA and 0.1pA constitute 70-85 GΩ, respectively. The analysis presented below shows, however, that in practice such gains would be difficult to reach due to a bandwidth limitation caused by parasitic capacitance.

The bandwidth of photodiode amplifiers is usually limited by 2 sources: parasitic capacitance (c_f) in parallel with the feedback resistor and the combination of input capacitance (c_{in}) transimpedance gain (R_F), and the op amp's gain-bandwidth product (GBW). The two corresponding poles are shown below [31].

$$f_{p1} = \frac{1}{2\pi R_F c_f} \qquad (5-3)$$

$$f_{p2} = \sqrt{\frac{GBW}{2\pi R_F c_{in}}} \qquad (5-4)$$

The capacitance c_f in $(5-3)$ is the sum of all capacitances between the op-amp's output and inverting input

$$c_f = c_{p,R} + c_{p,oa} + c_{p,s} \qquad (5-5)$$

where $c_{p,R}$ is the parasitic capacitance of the resistor, $c_{p,oa}$ is a parasitic capacitance inherent to the op-amp and its package, and $c_{p,s}$ is the parasitic stray capacitance that may be contributed by the layout. The capacitance $c_{p,oa}$ is itself the sum of the capacitance interal to the op-amp chip c_{pi} and the parasitic capacitance caused by the package containing the chip c_{pp}.

The capacitance c_{in} in $(5-4)$ is the input capacitance, defined as

$$c_{in} = c_{cm} + c_{dm} + c_j \qquad (5-6)$$

where c_{cm} is the op amp's common mode input capacitance, c_{dm} is the op amp's differential mode input capacitance, and c_j is the photodiode's junction capacitance.

To evaluate f_{p1} we assumed that most surface mount resistors have $c_{p,R} \approx 50\text{fF}$ [42, 43]. The $c_{p,oa}$ was assumed to be in the range 5f-150fF. Since there is virtually no data for c_{pi}, the estimate of $c_{p,oa}$ is based on pin-to-pin capacitance c_{pp} of various op-amp packages [44]. Although for most packages the output and inverting input are not on adjacent pins, the pin-to-pin capacitance given for adjacent pins in the datasheet can serve as a worst-case estimate for c_{pp}. Adding $c_{p,oa}$ and $c_{p,R}$ defines the range for $c_f = 55\text{fF} - 150\text{fF}$. Using this range of capacitance along with equation $(5-3)$ determines the range of frequencies for f_{p1}.

To evaluate f_{p2} we assumed the sum of $c_{cm} + c_{dm}$ is typically in the range 1-10pF, c_j is around 10pF for small photodiodes up to 1nF for larger diodes, which puts c_{in}in the range between 10pF and 1nF. The value of GBW was chosen to be 11MHz and A_{ol} was chosen to be

2×10^6 from the OPA140 datasheet. Using these parameters along with equation $(5-4)$ sets the range for f_{p2}.

Whichever of f_{p1} and f_{p2} is lower becomes the low-pass cutoff frequency f_L. Figure 5-7 shows the range of frequencies for f_{p1} (the light grey band) and f_{p2} (the dark grey band) as a function of R_F evaluated for typical circuit characteristics.

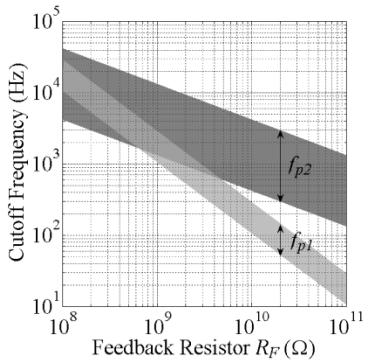

Figure 5-7: The range of pole frequencies for f_{p1} and f_{p2}. The upper and lower limits of f_{p1} are set by $c_f = 55\text{f} - 150\text{fF}$ and the upper and lower limits of f_{p2} are set by $c_{in} = 10\text{p} - 1\text{nF}$ and $GBW = 11\text{MHz}$.

For $R_F > 1\text{G}\Omega$, the f_{p1} pole determined by the feedback capacitance c_f becomes dominant. Thus, the parasitic capacitance in parallel with the feedback resistor sets the limit on gain for a single feedback resistor network. As can be seen from the plot at $R_F = 1\text{G}\Omega$ the predicted range of cutoff frequencies is between 1kHz and 3kHz. At $R_F = 10\text{G}\Omega$ the upper edge of the cutoff frequency band is near 300Hz, which still meets the requirements for the majority of applications (see Chapter 2).

According to the theory, the parasitics-related limitation on the maximal gain should be less pronounced for a T-bridge amplifier topology. A T-bridge network distributes the parasitic capacitance of the resistors. The feedback capacitance in this case is $c_f \approx c_{p,oa} + c_{p,s}$, as opposed to $c_f = c_{p,oa} + c_{p,R} + c_{p,s}$ for the single-resistor amplifier as stated previously. Specifically, at $R_{F,eq} = 10\text{G}\Omega$, one should be able to achieve a 300Hz bandwidth.

However, the higher gain does not necessarily give a T-bridge topology advantage over a single feedback resistance circuit (see the noise analysis in section 3.2.1). Specifically, the estimate obtained using these equations shows that the SNR at the same bandwidth of 300 Hz are 7.9 and

22 for the T-bridge and single-resistor circuits, respectively with $\widehat{\iota_p} = 1\text{pA}$ ($\widetilde{\iota_p} = 612\text{fA}$ and $\overline{\iota_p} = 500\text{fA}$).

Chapter 6 Physical Implementation and Testing of TIA with Maximized Sensitivity

6.1 Reducing Parasitic Capacitance Using Conventional Methods

According to our theoretical analysis it should be possible to increase the gain of a TIA from $100\text{M}\Omega$ to $1\text{G}\Omega - 10\text{G}\Omega$, while satisfying the cutoff-frequency requirements determined by application. However, as shown below achieving this goal appears to be a non-trivial task, which largely depends on one's ability to minimize the parasitic capacitance c_f. We tested 3 different PCB designs. Each comparing ways to minimize c_f, including testing a variety of surface-mount packages with reportedly low pin capacitance c_{pp}, a field-shunting ground trace under R_F, and a T-bridge.

When testing packages, we compared performances of different high-R_F TIAs utilizing op-amps with various pin-to-pin capacitances c_{pp} and package sizes. We tested six op-amps with c_{pp} in the range between 5-100fF.

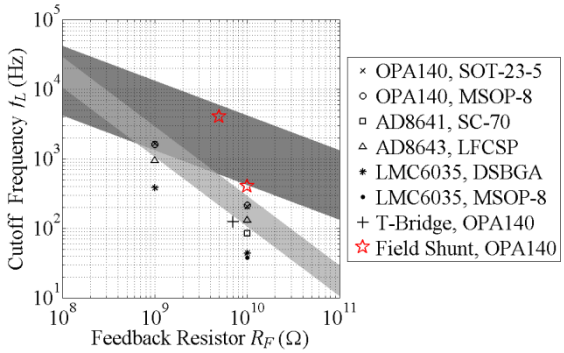

Figure 6-1: Cutoff frequency of different high-R_F TIAs utilizing op-amps with various pin-to-pin capacitances and package sizes. The lower shaded region is bound by $c_f = 55\text{f} - 150\text{fF}$ (see section C for more detail). The stars represent the OPA140 in the SOT-23-5 package with a field-shunting ground trace under the feedback resistor.

The measured bandwidth of varying op-amps and packages at

$R_F = 1, 5,$ and 10GΩ are shown in Figure 6-1. The black symbols correspond to conventional circuit layout with the ground plane cutout under the feedback resistor. The red symbols correspond to layout utilizing a field-shunting ground trace (see the next section). All points obtained for a conventional layout are scattered inside or below the lower f_{p1} band (see section 5.3). The highest cutoff frequencies that were achieved with a conventional layout were close to 2kHz at 1GΩ, and around 200Hz at 10GΩ, which fall within useable bandwidth requirements.

The experimental points falling in the area of overlap between f_{p1} and f_{p2} bands did not manifest a resonance in the frequency response suggesting that f_{p1} indeed is the dominant pole that determines the cutoff frequency f_L.

Notably, the bandwidth obtained with conventional layout, in all but one case was lower than theoretically estimated. Table 6-1 shows the measured values of cutoff frequency f_L and c_f at $R_F = 10\text{G}\Omega$. The op-amps are ordered based on the estimated sum of $c_{pp} + c_{p,R}$, which are major contributors to c_f, the other contributor being $c_{p,s}$ representing the layout-dependent stray parasitic capacitance (see section 5.3). The values of c_{pp} were taken from the package datasheet [44], which we used as an estimate of $c_{p,oa}$. The $c_{p,R}$ was assumed to be around 50fF.

Table 6-1: Cutoff frequency f_L and parasitic capacitance c_f of different implementations of a single feedback resistor TIA at R_F=10GΩ. c_f was calculated from BW using formula (10)

Part #	Package	$c_{pp} + c_{pR}$ (fF)	f_L (Hz)	c_f (fF)	Rank
LMC6035	DSBGA	55	44	362	5
AD8641	SC-70	110	84	189	4
AD8643	LFCSP	120	131	121	3
OPA140	SOT-23-5	-	206	77	2
OPA140	MSOP-8	150	216	74	1
LMC6035	MSOP-8	150	38	419	6

We observed a wide range of f_L from as low as 38Hz (for LMC6035 in MSOP-8 package) to 216Hz (for OPA140 in the same package). However, we did not find any correlation between $c_{pp} + c_{p,R}$ and the actual bandwidth of the circuit. As can be seen from Table 6-1, the circuit utilizing an op-amp with the lowest $c_{pp} + c_{p,R}$ (the first row) rather than having the largest bandwidth has the second lowest bandwidth (rank 5 out of 6 op-amps tested). Similarly, the two

op-amps with the highest $c_{pp} + c_{p,R}$ (see the last two rows) have the highest and the lowest bandwidths (ranks 1 and 6 respectively).

The package type also did not have a consistent effect on the bandwidth for a given op-amp. The use of the OPA140 in the SOT23-5 and the MSOP-8 packages had very little effect on the bandwidth. However, we observed significant differences in bandwidth for the AD8641 and AD8643, which are the same op-amp in two different packages. The op-amp in the LFCSP package had higher bandwidth than the one in the SC70 package. The difference could be attributed to the fact that the AD8641 has bond wires, and so had additional parasitic capacitance.

The experimentally derived values of c_f in three out of six cases (the first two and the last row in Table 6-1) exceeded the sum of $c_{p,R}$ and c_{pp}. This finding may be caused by capacitance added by the op-amp itself c_{pi}, or the presence of so-called stray parasitic capacitance $c_{p,s}$, which according to the literature can be as high as 500fF [31].

6.2 Reducing Parasitic Capacitance Using Field Shunting

We demonstrate that the bandwidths reported in the previous section can be significantly extended by adopting a technique used in high-frequency circuit design, termed field shunting. It involves putting a trace under the resistor connected to ground, which shunts the fringing electric field

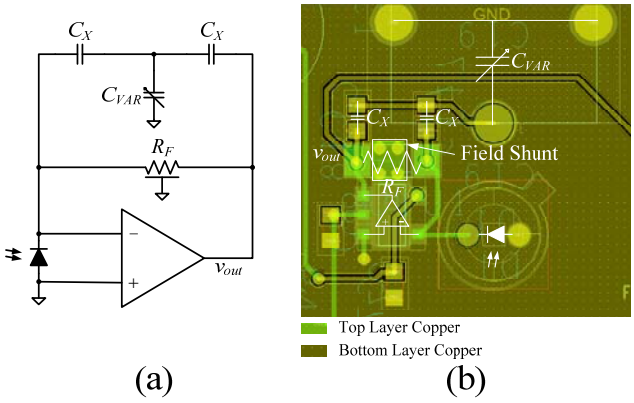

Figure 6-2: Schematic of the modified amplifier design (A) and PCB layout (B). The field shunt is highlighted in white, it is made from top-layer copper and connected to the ground plane with 4 vias.

from around the resistor and thus lowers the feedback capacitance [45].

Figure 6-2a shows the schematic of the modified amplifier design. A line under the feedback resistor represents the field-shunting trace. Since it is difficult to determine exactly what the resulting bandwidth will be, a capacitive T-network is added for tuning the bandwidth with 2-32fF of capacitance. Part B of the figure shows the PCB layout with schematic symbols imposed over the package footprints. The field-shunt is highlighted in white. It is made from top-layer copper and connected to the ground plane with 4 vias. It is placed directly under the feedback resistor ($10\text{G}\Omega \pm 5\%$ in a 1206 package) slightly closer to the output of the amplifier so that any additional stray capacitance will be shifted to the output rather than the inverting input. The values of C_X were chosen at 600fF and the trimmer cap has a range 10p-180pF to add 2-32fF of capacitance. The photodiode SFH229FA with the shunt resistance estimated to be about $35.5\text{G}\Omega$.

The frequency sweeps for this amplifier are shown in Figure 6-3. Part A shows that at $10\text{G}\Omega$ this circuit can achieve bandwidth from 246-405Hz which is well beyond 216Hz limit which was achieved with conventional layout and ground plane removal. Figure 6-3b shows the frequency response for the same circuit with $5\text{G}\Omega$ of gain. Here we see it is possible to achieve bandwidths from 1-4kHz. However, the frequency response has a resonant peak around 1kHz. This causes some overshoot and ringing of the output signal (not shown). The overshoot and ringing can be mitigated by increasing the maximal capacitance of the T-bridge.

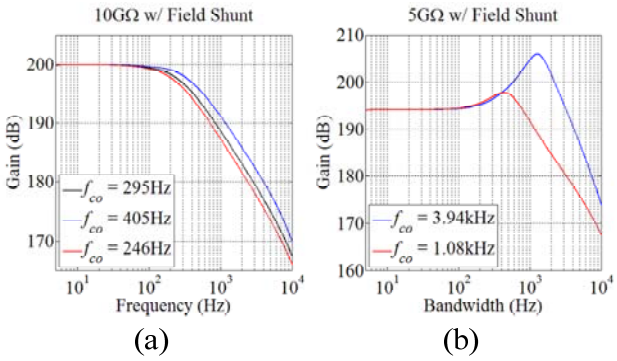

Figure 6-3: Frequency sweeps of amplifiers with field-shunting ground trace and $10\text{G}\Omega$ gain (a) and $5\text{G}\Omega$ gain (b). The bandwidth was adjusted with a capacitive T-network.

6.3 Emulation of Biological Fluorescent Signals

In order to provide the most realistic test for our amplifier, we designed a system to generate a variety of optical signals, including imitations of voltage and calcium transients. A diagram of the system is shown in Figure 6-4. This system uses feedback to linearize the LED (SFH 4058, OSRAM) thus ensuring that the light output stays proportional to the voltage input. There is a switch (not shown) which can vary the output light intensity by 3 orders of magnitude and is used for course adjustment of the light output. The variable attenuator can vary the intensity of the light output over about 1 order of magnitude and is used for fine adjustment. The selector switch allows connection to an external sine wave generator that was used for frequency sweeps to determine the amplifier bandwidth. In the other position, the switch connects the LED driver and feedback circuit to a DAC.

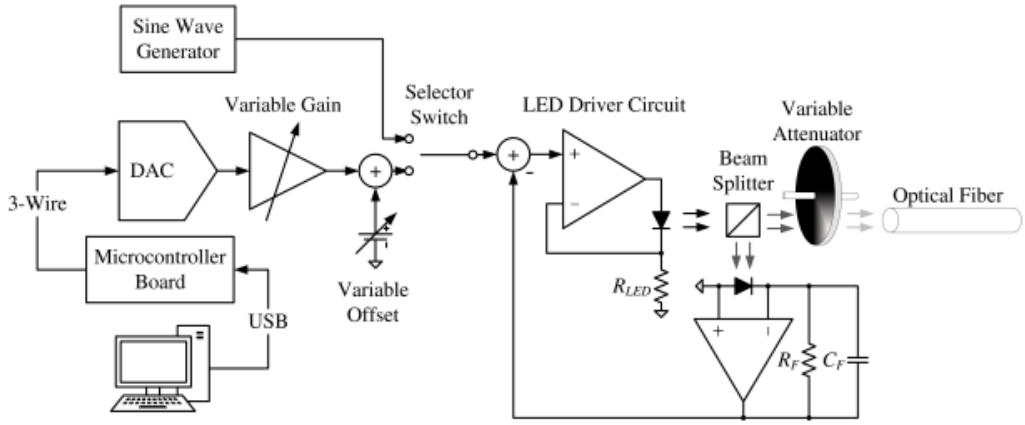

Figure 6-4: Optical action potential generator block diagram.

A computer program controlled by a GUI reads a file containing simulation data, quantizes the data to the selected number of bits (we used 8 for our experiments) and then down-samples and truncates the data to match the specified sampling rate (we used 1kHz) and signal duration respectively. The data is then sent from the computer to the microcontroller via USB. The

microcontroller is programmed in assembly to send the samples to the DAC using a standard 3-wire communication protocol. In order to make it easier to capture the waveform on an oscilloscope, the signal is repeated in a loop.

Next, the signal is amplified (or attenuated) and an offset is added to simulate background fluorescence. Finally the signal was converted from electricity to light where an optical fiber guided it to the amplifier's photodiode.

6.4 Amplifier Response to Realistic Optical Action Potentials

Figure 6-5 compares the 10GΩ amplifier with bandwidth reduced to 300Hz, to a conventional 100MΩ amplifier with a bandwidth of 1.3kHz using a realistic optical signal (action potential of a human Purkinje fiber) generated using our optical signal emulator (see section 6.3). The action potentials came from a computer simulation of a human purkinje fiber. The $\Delta F/F$ was set to 10%, the maximal photocurrent, shown on the right axes, was on the order of 10pA, with a 1pA "voltage-dependent" current. Both recorded signals were well above the oscilloscope noise floor. The high-gain TIA produces a much cleaner recording which is consistent with the noise measurements reported in the previous section. The effect was achieved by a combination of increased gain (factor of 8 improvement) and eliminating excess bandwidth (factor of 1.9 improvement).

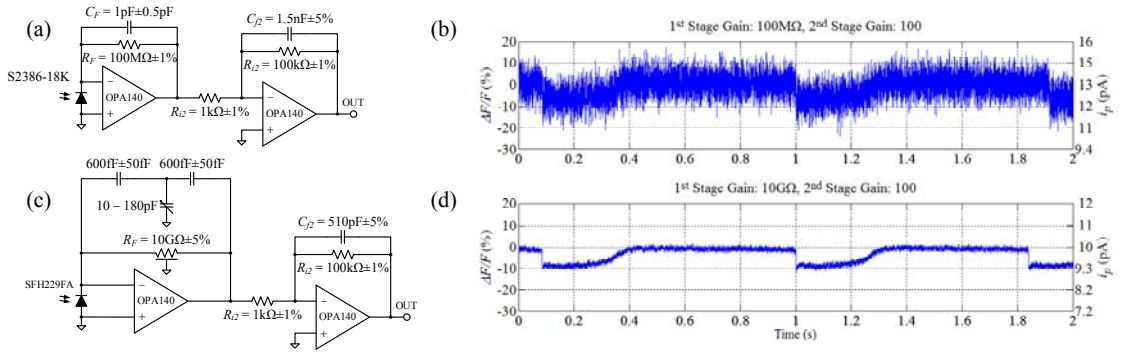

Figure 6-5: Schematic of circuit analogous to the typical TIA (a), the response of the amplifier in (a) to an artificial OAP (b), the optimized TIA (c) and its response to the same signal (d). The signal was generated by an optical action potential emulator (see section 6.3), the data for which came from a simulation of a human purkinje fiber. The $\Delta F/F$ was set to 10% and the maximal photocurrent was on the order of 10pA, with a 1pA "voltage-dependent" current.

Chapter 7 Discussion and Conclusions

Since the introduction of voltage-sensitive and Ca_i^{2+}-sensitive fluorescent dyes there have been a number of reports on the design of photodiode-based recording systems [2, 3, 15, 46, 8, 18, 11, 6]. The most common systems utilized a multi-stage amplifier, with a $100\text{M}\Omega$ transimpedance amplifier (TIA) as the first stage [7, 2, 18, 11, 8, 18, 6]. Yet, it remained unclear if there is any room for improvement, and if there was, then how much? The goal of this study was to answer this question. Specifically, the main focus was on the selection and optimization of the transimpedance amplifier topology specialized for detecting voltage and calcium transients in low-light biological applications.

A distinct feature of our approach is that it is not purely empirical, but is based on a thorough theoretical analysis of the SNR and the bandwidth of the circuit as a function of the op-amp, photodiode, and the feedback resistor characteristics. Our analysis shows that current technology allows for significant improvements of the circuit performance at low photocurrents. We demonstrated the feasibility of increasing the transimpedance gain from the conventional $100\text{M}\Omega$ to $10\text{G}\Omega$ while still meeting the minimal bandwidth requirement. At low photocurrents $i_p < 10^{-11}\text{A}$ such an increase allows improvement of the SNR by a factor of 10 compared to commonly used systems with a $100\text{M}\Omega$ gains [7, 2, 18, 11, 8, 18, 6].

Another novel aspect of our work is the use of mathematical modeling to quantify bandwidth requirements for specific applications. Lowering the bandwidth as much as the application allows represents an important resource for increasing the SNR. The conventional bandwidth range utilized in TIAs for biomedical applications is between 300Hz and 2kHz [15, 7, 2, 11, 3]. However, until recently there were no studies that would explore the signal distortion that occurs

in this range. Our study fills this gap by providing the information which is necessary for optimal selection of the bandwidth.

Our linear distortion analysis suggests that in many applications the bandwidth can be significantly reduced. For example we demonstrate that for recording Ca_i^{2+} transients the cutoff frequency can be safely reduced to 100Hz. This alone would increase the SNR by a factor of three compared to the SNR of an amplifier with a 1kHz bandwidth. On top of this improvement one can also maximize the gain of the first stage bringing it up to 10, which will provide an additional $\times 10$ boost in SNR. Compared to conventional $100\text{M}\Omega$ amplifier with a 1kHz cutoff, the overall improvement would be as high as $\times 30$.

It is worth noting that a 100Hz bandwidth would be sufficient for many voltage measurements as well. Indeed the majority of optical recording are used to evaluate the action potential duration APD mapping or conduction velocity mapping (activation mapping) [5]. As can be seen from our analysis reduction of bandwidth to 100Hz result in reasonably small errors (around 1 %). Thus, an amplifier with a 100Hz bandwidth (with the exception of cases where the accurate measurements of the action potential upstroke are required) can be used for simultaneous voltage and Ca_i^{2+} recordings as well.

While increasing the transimpedance gain produces the best results in low bandwidth applications (100Hz - 300Hz), it can lead to significant improvements in broader bandwidth applications (1-2kHz) as well [2, 3]. Our analysis suggests that in low light applications a $2-3\text{G}\Omega$ TIA with field shunting and conventional photodiodes should have about 5 times higher SNR compared to both conventional $100\text{M}\Omega$ and more recent avalanche photodiodes based systems [3] (see section 3.5).

A recently reported alternative approach for detecting fluorescence in low-light biological applications is the use of avalanche photodiodes known for their high light sensitivity [3]. It

utilizes the module C5460-01 (Hamamatsu) which integrates an avalanche photodiode, amplifier and power supply. However, the study does not report the noise characteristics of the system, which makes it difficult to compare this approach with the earlier designs and our high-gain amplifier performance.

To make such a comparison we used the noise equivalent power (NEP), responsivity $R(\lambda)$, feedback resistance R_F and avalanche gain M given in the C5460-01 datasheet, along with the bandwidth reported in [3] (2kHz). These parameters are sufficient to calculate the total noise contribution of the avalanche photodiode $v_{n,pd}$ in V using a modified form of the equation in [28].

We can now plug the result into $(4-1)(3-44)$ which gives the total dark noise of the circuit and then use $(4-2)$ to get the SNR. Such calculation gives the SNR of an avalanche diode-based system at 2pA to be 0.19. Compared to the standard $100\text{M}\Omega$-gain amplifier with the same bandwidth, this system offers 30% improvement. However, the avalanche diode based system does not outperform amplifier proposed in this work. Using the equations in section 3.1.3 we can calculate that a PIN photodiode with $5\text{G}\Omega$ of gain and the same bandwidth gives an SNR of 1, which is roughly a factor of 5 better than the C5460-01.

Can an increase in gain above $10\text{G}\Omega$ result in further improvement in SNR at low photocurrents? The noise analysis suggests that at the current technology level SNR approaches saturation at about $70\text{G}\Omega$ (see section 5.2), which could provide some additional factor of 1.5 (note that near saturation the SNR is no longer $\propto \sqrt{R_F}$). However, in practice the additional improvement would be difficult to achieve. The main limiting factor at high gains is the feedback parasitic capacitance which lowers the bandwidth below the required range. Success in further increasing SNR will largely depend on one's ability to mitigate the effect of the parasitics.

The major difficulty in dealing with parasitic capacitance is that at high gains it is extremely sensitive to the circuit layout. In our experiments, the total feedback capacitance significantly exceeded the sum of the parasitic capacitances of the feedback resistor and the op-amp. The additional capacitance can be attributed to a combination of the op-amp's internal capacitance $c_{p,oa}$ and the so-called stray capacitance, which according to the literature can be as high as 500fF [31] and which is very difficult to control. The standard measures for reducing the parasitic capacitance, such as removal of the ground plane around the op-amp and the feedback resistor were only able to reduce c_f to around 74fF-419fF. This is much higher than one would expect from the amplifier specs.

One of the standard approaches to expanding the bandwidth at a given feedback resistance is using a T-bridge. Using the T-bridge reduces the feedback parasitic capacitance by distributing it between 3 different resistors. Our analysis shows, however, that at equal gains the SNR of a T-bridge circuit is always lower than that of the single resistor circuit. Moreover, our experiments with a T-bridge TIAs suggest the actual bandwidth of a T-bridge amplifier, as compared to a single resistor circuit with the equivalent gain is not significantly wider due to the stray capacitance. This makes the T-bridge topology less attractive than a single resistor circuit for low-light applications where maximizing the SNR is critical.

We found that the most efficient way of dealing with parasitic capacitance is the field shunting method adopted from high-frequency circuit design techniques [45]. The use of field shunting enabled the reduction of the total feedback capacitance to an extent that the minimum bandwidth specification could easily be met. Specifically, with the field shunting method, we were able to consistently achieve the bandwidths 400Hz at $10\text{G}\Omega$ and close to 5KHz at $5\text{G}\Omega$ (see Figure 6-3), which allowed us to stay within the frequency range usually utilized in biological applications. Using this approach it seems quite realistic to increase the gain to $50\text{G}\Omega$ while still preserving a useful bandwidth $\geq 100\text{Hz}$. Compared to a $10\text{G}\Omega$, 300Hz system this would

increase the SNR by an additional factor of 2.5, which is probably as far as one can get with the existing technology.

Notably, for the discussed range of applications the use of high-end electrometer op-amps known for their low current noise would not likely result in a significant improvement of the SNR. The significant reduction in current noise in electrometer op-amps comes at a price, which is increased voltage noise. Our analysis shows that the noise gain mechanism [31] negates the advantages of this type of amplifiers for the discussed applications, in particular when the photodiodes with large surface area and high c_{in} are being used (see section 4.2).

One of the main mechanisms of improvement for amplifiers operating below the shot noise limit is the reduction of the dark noise contribution. At higher photocurrents the contribution of the dark noise becomes less prominent than the photocurrent shot noise. To illustrate this, we compare 2 TIAs with the same op-amp, photodiode, and bandwidth but with 2 different gains. Our estimates show that at $i_p > 10^{-9}\text{A}$ using a $10\text{G}\Omega$ gain is only 1.5 times better than over conventional TIAs with $100\text{M}\Omega$ gain (see Figure 7-1).

It is interesting that one of the earliest attempts at photodiode amplifiers optimized for detecting biological fluorescence [15] utilized a rather high gain ($5 - 6\text{G}\Omega$). However, this system was never widely adopted. Moreover, later designed amplifiers for similar applications [6, 8, 18] used the more common $100\text{M}\Omega$ gain.

This is not coincidental. The system was used to detect the signals from SCG neurons stained with voltage-sensitive dye RH423.Voltage-dependent changes in fluorescence in neurons stained with this dye usually constitute a very small portion of the total fluorescence $\Delta F/F$ is ~1%. To boost the signal the researchers had to work in the range of photocurrents $i_p \sim 10^{-9}\text{A} - 10^{-10}\text{A}$

where the advantage a high –gain amplifier over the conventional amplifiers is less prominent (see Figure 7-1).

We anticipate that the applications that will mostly benefit from our findings are the optical recordings from single cells and monolayers of cardiac myocytes and neural cells [46, 15], where increasing of the light intensity as a way of increasing the SNR is not always possible because of phototoxic effects. Our findings would also apply to optrodes [4] as well as in optogenetics applications, in which the ability to monitor electrical and Ca_i^{2+} activity at reduced light intensity is important. The maximal improvements should be expected in detection of Ca_i^{2+} signals, which have much less background signal than voltage-sensitive fluorescent signals and thus should have much higher SNR at the same photocurrents.

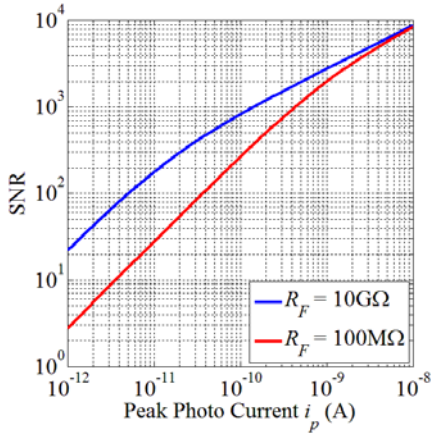

Figure 7-1: Effect of photocurrent on SNR for the same TIA with $R_F = 10\text{G}\Omega$ and $R_F = 100\text{M}\Omega$ gain and 300Hz bandwidth.

Part 2 Characterizing Light Transport in Biological Tissue

Chapter 8 Background and Significance

8.1 Interpretation of Voltage- and Calcium-Dependent Fluorescence Signals in Biological Systems. The Role of Light Transportation in Shaping Voltage and Calcium Transients

The interpretation of optical mapping data often requires a detailed model of light scattering in tissue [47]. Some models are derived analytically by solving the radiative transfer equation. Others are generated from computer simulations that treat the direction of photon travel as a random variable, these are called monte carlo simulations. In the following sections we will discuss the mathematical foundations of both types of models and how the model parameters can be obtained through experimentation.

In section 8.2 we will discuss the mathematics of light-scattering models, including the physical meaning of the model parameters.

In Chapter 9 we will discuss the experiments we conducted in tissue phantoms and cardiac tissue. The interest towards investigating light transport in cardiac tissue has been triggered by the development of fluorescent imaging techniques, known as optical mapping,

utilizing voltage-sensitive and Ca_i^{2+}-sensitive fluorescent probes. These optical methods are increasingly utilized for monitoring the propagation of electrical impulses and intracellular Ca_i^{2+}-transients in the heart, which play an important role in electro-mechanical coupling [48, 1, 14]. The optical recordings are usually taken in epifluorescence mode, where significant contributions from sub-surface layers are present. Quantitative interpretation of such signals as well as the development of three-dimensional tomographic imaging techniques requires detailed knowledge of light transport in the surface layers of the myocardial wall. However, experimental data providing such information are scarce, which was the main motivation for this work.

In this study, we use a thin custom-made fiber optic probe to investigate the forward directed flux (FDF) with a 10μm resolution. The experiments are carried out in pig myocardial wall, homogenized pig myocardial tissue as well as in lipid-based tissue phantoms. In the vicinity of the illuminated surface we observed a rapid decay of the light intensity with a spatial constant in the range of one hundred microns, suggesting that we were likely detecting a phenomenon linked to the decay of ballistic photons. This effect was observed in the intact myocardial wall, homogenized cardiac tissue and intralipid-based tissue phantoms.

To determine the factors affecting the rate of the fast exponent we simulated measurements of FDF using Monte Carlo (MC) simulations. The FDF was evaluated in the physiological range of absorption and scattering coefficients, variable anisotropy parameter *g*, and different numerical apertures of the probe. Based on the MC model we obtained a simple empirical formula linking the rate of the fast exponent to the scattering coefficient, the anisotropy parameter, and the numerical aperture. The predictions of the formula were tested experimentally in phantoms.

Potential applications of optical fiber-based FDF measurements for the evaluation of optical parameters in turbid media are discussed as a crude alternative to collimated transmittance measurements [49, 50] or reflectance-mode confocal microscopy and OCT [51, 52, 53, 54], requiring rather sophisticated equipment.

8.2 Mathematical Foundations of Light Transport Models

8.2.1 *Specific Intensity (or Spectral Radiance)*

Differential radiant energy in the frequency interval $(\nu, \nu + d\nu)$ transported across the surface *ds* and in the element of solid angle $d\Omega$ during time interval *dt* [55, p. 1]

$$dE_\nu = I_\nu \left(\widehat{\mathbf{\Omega}} \bullet d\mathbf{s}\right) d\nu \, d\Omega \, dt = I_\nu \cos(\theta) \, d\nu \, ds \, d\Omega \, dt \qquad (8-1)$$

Where I_ν is the specific intensity (or just intensity) in $\frac{\mathrm{W}}{\mathrm{m^2 \cdot sr \cdot Hz}}$ or $\frac{\mathrm{erg}}{\mathrm{s \cdot m^2 \cdot sr \cdot Hz}}$, θ is the angle between the beam of radiation and the outward normal of *d***s**, $d\nu$ is the width of the frequency interval being considered, ds is the area over which the energy is transported, $d\Omega$ is the area of the differential solid angle element, dt is the time interval, and $\widehat{\mathbf{\Omega}}$ is a unit vector that points along the direction of the radiation. The construction here defines also a ***pencil of radiation*** [56, p. 1] and is shown in Figure 8-1.

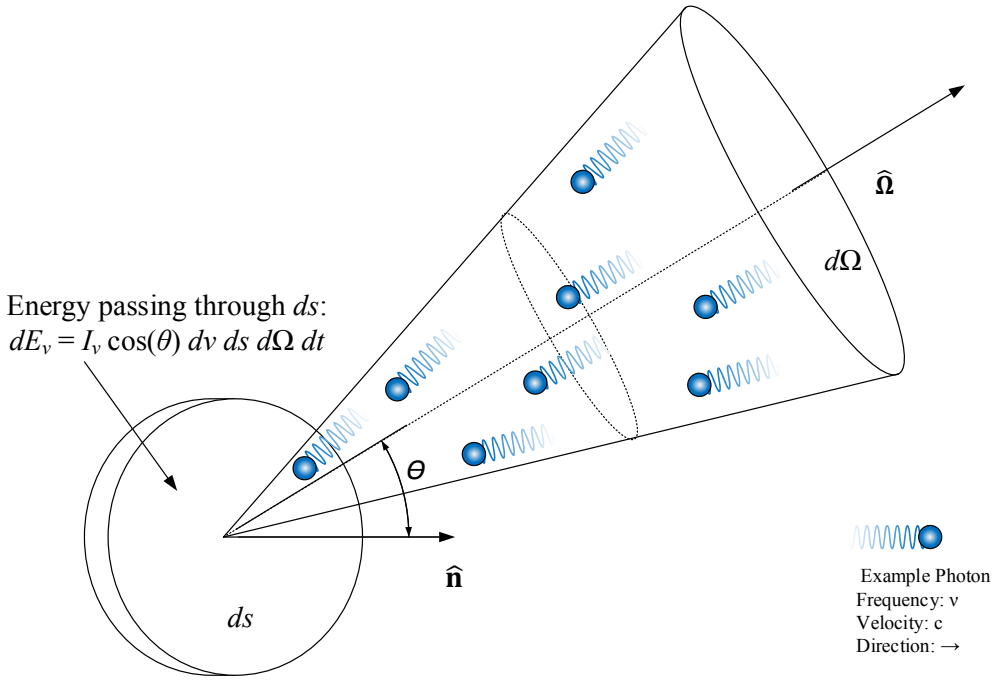

Figure 8-1: Pencil of radiation.

If I_ν is integrated over all frequencies, it is called the integrated intensity and is given by [55, p. 2]

$$I = \int_0^\infty I_\nu \, dv \qquad (8-2)$$

8.2.2 *Energy Density*

Energy density is related to specific intensity by the equation shown below [57, p. 3]

$$\Phi_\nu(r,t) = \frac{1}{c}\int_{4\cdot\pi} I_\nu(r,t)\, d\Omega \qquad (8-3)$$

Note that the factor of $1/c$ is multiplied with equation $(8-3)$ will yield the correct units for energy density. The units of I_ν are $\mathrm{erg}/(\mathrm{s\ cm^2\ Hz\ sr})$, hence multiplying by $1/c$ gives us units of

$$\frac{I_\nu}{c} \Longrightarrow \frac{\frac{\text{erg}}{\text{s cm}^2\ \text{Hz sr}}}{\text{cm/s}} = \frac{\text{erg}}{\text{cm}^3\ \text{Hz sr}}$$

Then integrating over the solid angle will yield units of

$$\frac{\text{erg}}{\text{cm}^3\ \text{Hz}}$$

Thus we have the energy density for photons with frequency ν to $\nu + d\nu$.

8.2.3 *Net Flux*

The flux F_ν is the amount of radiant energy transferred across a unit area in unit time in unit frequency interval $\left(\text{erg}/(\text{cm}^2\ \text{s Hz})\right)$ [55, pp. 2-3]. It is found by integrating the intensity over all solid angles

$$d\nu\ ds\ dt \int_{4\cdot\pi} I_\nu\ \cos(\theta)\ d\Omega$$

or

$$F_\nu = \int_{4\cdot\pi} I_\nu\ \left(\hat{\mathbf{\Omega}} \bullet \hat{\mathbf{n}}\right) d\Omega = \int_{4\cdot\pi} I_\nu\ \cos(\theta)\ d\Omega \qquad (8-4)$$

Integrating over all solid angles for the structure shown in Figure 8-1 gives us the total amount of energy that falls upon a differential surface element per second for a given frequency range. Flux can also be described as a vector

$$\mathbf{F}(\mathbf{r}, t) = \int_{4\cdot\pi} \hat{\mathbf{\Omega}}\, I_\nu\, d\Omega \qquad (8-5)$$

8.2.4 *Extinction Coefficient: True Absorption and Scattering*

A pencil (beam) of radiation of intensity I_ν is attenuated while passing through matter of thickness $d\ell$ and its intensity becomes $I_\nu + dI_\nu$, where [55, p. 9]

$$dI_\nu = -I_\nu \, \mu_t \, d\ell \tag{8-6}$$

where μ_t is called the ***mass extinction coefficient***, the ***mass absorption coefficient***, or the ***total attenuation coefficient***. μ_t comprises two important processes: (1) true absorption and (2) scattering. Therefore we can write [55, p. 9]

$$\mu_t = \mu_a + \mu_s \tag{8-7}$$

where μ_a and μ_s are the ***absorption*** and ***scattering coefficients*** respectively and have units mm^{-1} or cm^{-1}. Energy removed from a pencil of radiation can be defined as

$$dE_{\nu,sink} = -(\mu_a + \mu_s) \, I_\nu\left(\mathbf{r}, \widehat{\mathbf{\Omega}}, t\right) d\ell \, ds \, d\Omega \, d\nu \, dt \tag{8-8}$$

Equation $(8-8)$ has units of erg or J, as it represents the specific amount of energy lost in a differential volume that the beam passes through. The units of an energy sink/source would have units joules (or erg) per unit volume per unit time. Hence we would drop the terms $d\ell$, ds, and dt.

$$E_{sink} = -\int_{4\cdot\pi}\int_0^\infty (\mu_a + \mu_s) \, I_\nu\left(\mathbf{r}, \widehat{\mathbf{\Omega}}, t\right) d\nu \, d\Omega \tag{8-9}$$

Both scattering and absorption cause energy to be removed from a beam traveling through a material [55, pp. 9-10]. For the individual photons in the beam, a scattering event may change their direction and energy (inelastic scattering) or just their direction (elastic scattering). Below is a brief summary of the types of scattering a photon may experience.

- Elastic Scattering (kinetic energy of particles is conserved, direction is changed but not wavelength)
    - Thomson Scattering – Photon interacts with electrons
    - Rayleigh Scattering – A photon penetrates into a medium composed of particles whose sizes are much smaller than the wavelength of the incident photon.
- Inelastic Scattering (kinetic energy is lost or gained, the wavelength and direction change)
    - Raman Scattering – The incident photon interacts with matter and the frequency of the photon is shifted toward red or blue.
    - Stokes Scattering – Part of the energy of the photon is transferred to the interacting matter, causing a shift toward red
    - Anti-Stokes Raman Scattering – Internal energy of the matter the photon collides with is transferred to that photon causing a shift toward blue.
    - Compton Scattering – When a high-energy photon collides with a free electron and loses energy.
    - Inverse Compton Scattering – When an electron with relativistic energy collides with an infrared or visible photon, the electron gives energy to the photon.

The drawing in Figure 8-2 shows how energy can be lost from a pencil of radiation. Note that energy removed from the beam by scattering is not necessarily lost to the radiation field. As shown in Figure 8-2, a photon can be removed from the beam without losing energy. In fact, some of the energy lost from the incident pencil may appear in other directions as ***scattered radiation*** [56, p. 5]. $1/\mu_t$ gives the photon ***mean free path*** or ***mfp*** which is the distance over which a photon travels before it is removed from the pencil of the beam of radiation [55, p. 10].

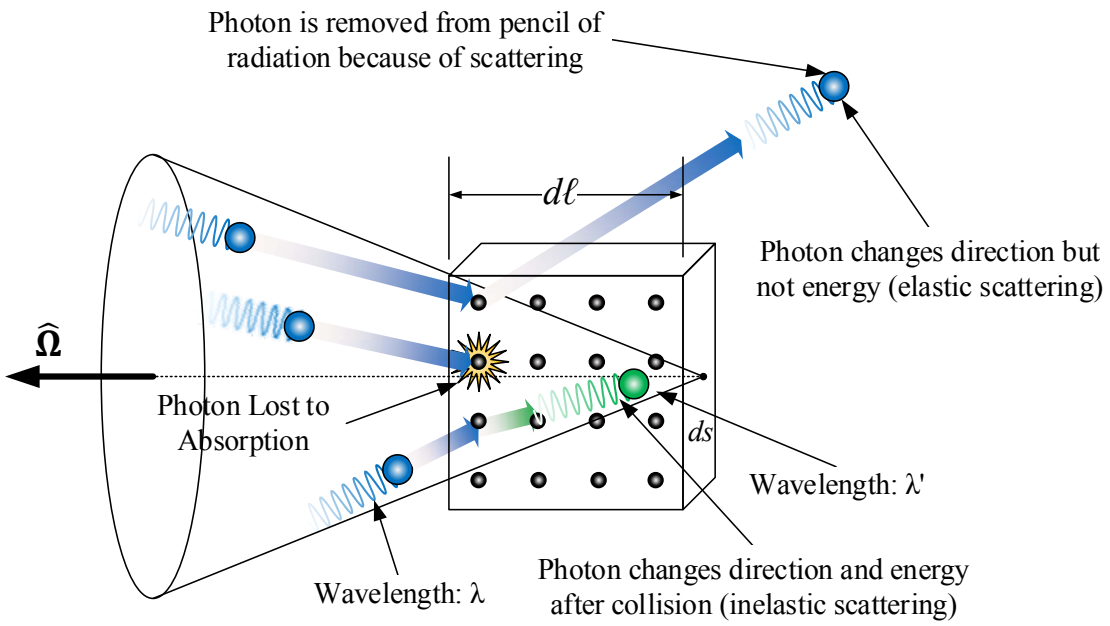

Figure 8-2: Examples of energy being removed from a pencil of radiation.

8.2.5 *Emission Coefficient*

Let an element of mass with a volume element dV emit an amount of energy $dE_{\nu,source}$ into an element of solid angle $d\Omega$ centered around $\hat{\mathbf{\Omega}}$ in the frequency interval ν to $\nu + d\nu$ time interval t to $t + dt$. Then [55, pp. 10-11]

$$dE_{\nu,source} = j_\nu \, dV \, d\Omega \, d\nu \, dt \qquad (8-10)$$

where j_ν is called the ***macroscopic emission coefficient*** or ***emissivity*** and has units of $\left(\frac{\text{erg}}{\text{cm}^3\cdot\text{sr}\cdot\text{Hz}\cdot\text{s}}\right)$. As mentioned earlier, the energy sink/source must have units of Joules (or erg) per unit volume per unit time. Hence, we can modify equation $(8-10)$ to get

$$E_{source} = \int_{4\cdot\pi}\int_0^\infty j_\nu \, d\nu \, d\Omega \qquad (8-11)$$

Emission is the combination of the reverse of physical processes that cause true absorption. One such process is ***fluorescence***, where a photon is absorbed by an atom and is excited from bound state *p* to another bound state *r*, decays to an intermediate bound state *q* and then to the original state *p*. The energy of the absorbed photon is re-emitted in two photons each of different energy [55, p. 11]. When local thermal equilibrium (LTE) exists [55, p. 11]

$$j_\nu^a(LTE) = \mu_a \, B_\nu(T) \qquad (8-12)$$

where $B_\nu(T)$ is the Planck function

$$B_\nu(T) = \frac{2h\nu^3}{c^2} \frac{1}{e^{\frac{h\cdot\nu}{k\cdot T}} - 1} \qquad (8-13)$$

The equation for j_ν^a called the ***Kirchhoff-Planck Relation*** basically says that a certain percentage of the energy absorbed by the medium will be emitted as photons of a longer wavelength.

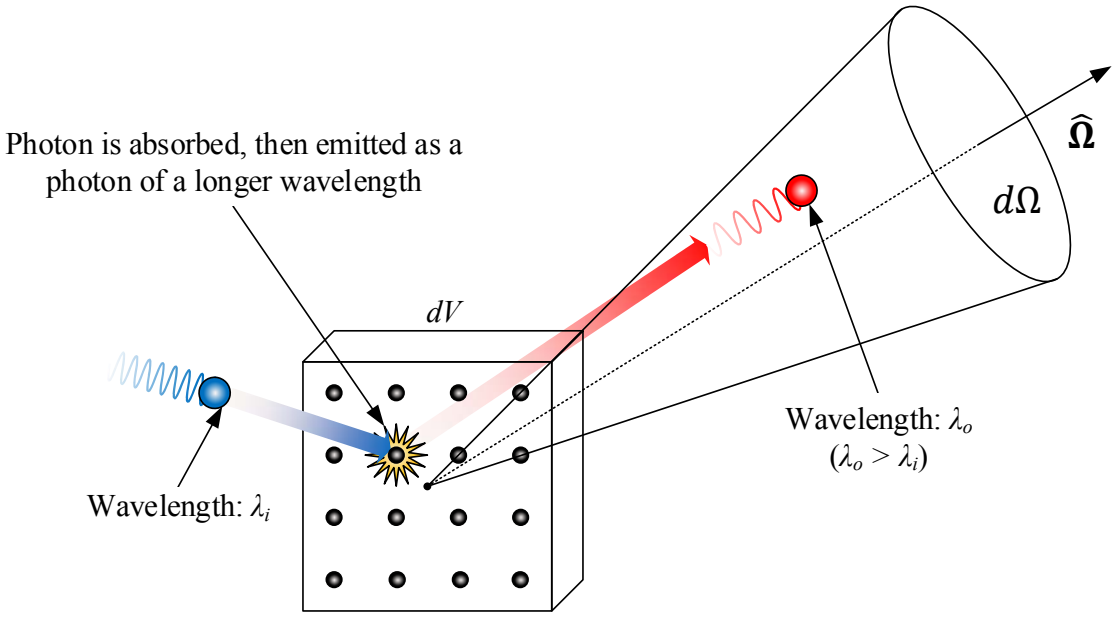

Figure 8-3: Absorption and fluorescence. A photon of wavelength λ_i is absorbed causing the release of a photon of wavelength λ_o, where $\lambda_o > \lambda_i$, which enters a pencil of radiation.

Emission of radiation can also be from scattered photons. One can write [55, p. 11]

$$j_\nu^s(\mathbf{r},\hat{\mathbf{\Omega}}) = \int_{4\cdot\pi}\int_0^\infty \left[\int_{4\cdot\pi}\int_0^\infty \mu_s(\mathbf{r},t)\, f(\nu,\hat{\mathbf{\Omega}}\,;\,\nu',\hat{\mathbf{\Omega}}'\,;\,\mathbf{r},t)\, I_\nu(\mathbf{r},\hat{\mathbf{\Omega}}',t)\, d\nu' d\Omega'\right] d\nu\, d\Omega \quad (8-14)$$

Which represents the amount of energy added to a pencil of radiation because of scattering. More commonly, we will used the simplified version of $(8-14)$ where it is assumed that all photons added to pencil after scattering had experienced an elastic collision where no energy was lost and therefore the frequency did not change. It is also assumed that the scattering coefficient does not change with position or time. Equation $(8-14)$ then becomes

$$j_\nu^s(\mathbf{r},\hat{\mathbf{\Omega}}) = \int_{4\cdot\pi}\int_0^\infty \left[\mu_s \int_{4\cdot\pi} f(\hat{\mathbf{\Omega}},\hat{\mathbf{\Omega}}',\mathbf{r},t) I_\nu(\mathbf{r},\hat{\mathbf{\Omega}}',t)\, d\Omega'\right] d\nu\; d\Omega \quad (8-15)$$

The angular distribution of light intensity scattered by a particle at a given wavelength is called the ***phase function***, or the ***scattering phase function*** and is here symbolized as *f*; it is the scattered intensity at a particular angle θ relative to the incident beam and normalized by the integral of the scattered intensities at all angles [58, p. 693]

$$f(\nu,\hat{\mathbf{\Omega}};\,\nu',\hat{\mathbf{\Omega}}';\mathbf{r},t) = \frac{I_\nu(\mathbf{r},\hat{\mathbf{\Omega}},t)}{\int_{4\cdot\pi} I_\nu(\mathbf{r},\hat{\mathbf{\Omega}},t)\, d\Omega}$$

In other words, it is the probability that a photon traveling in direction $\hat{\mathbf{\Omega}}'$ is scattered into direction $\hat{\mathbf{\Omega}}$ [57, p. 4]. The phase function f is normalized in such a way that [57, p. 4]

$$\int_{4\cdot\pi} f(\nu,\hat{\mathbf{\Omega}};\,\nu',\hat{\mathbf{\Omega}}';\mathbf{r},t)\, d\Omega' = 1$$

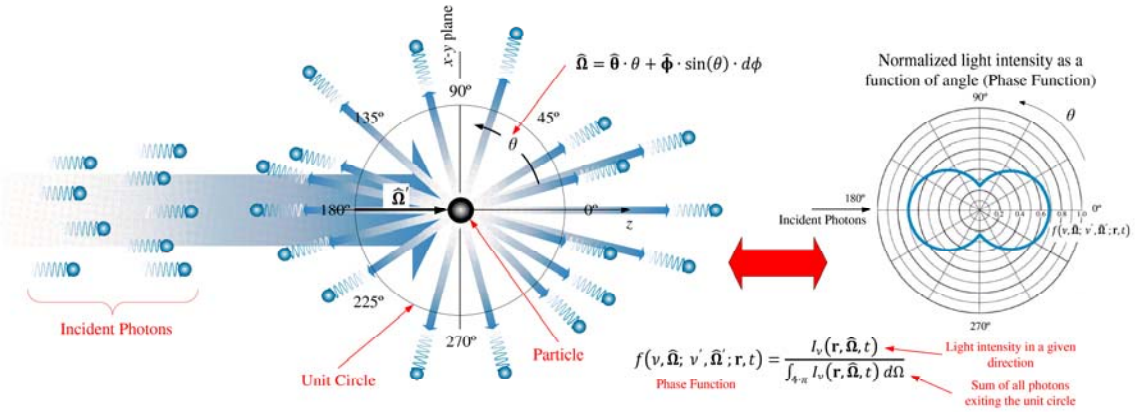

Figure 8-4: Incident photons being scattered by a particle (left) and plot of phase function (right).

Note that the assumption of a spherical particle allows removal of the azimuthal ϕ dependence of f [58, p. 693].

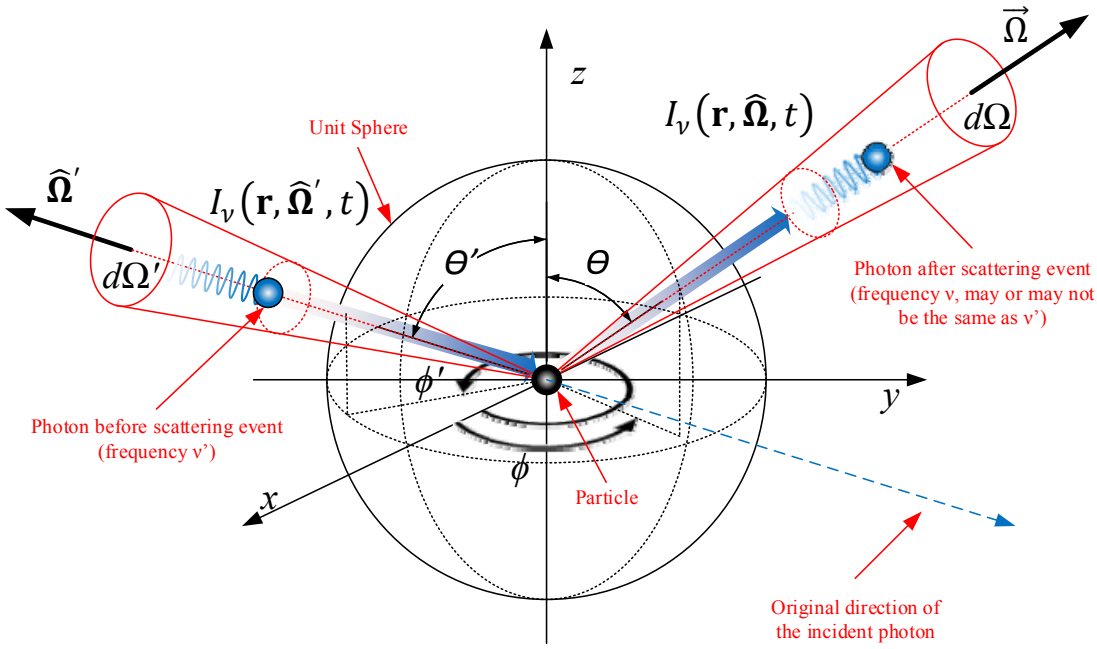

Figure 8-5: A photon is added to the pencil of radiation due to a scattering event.

The phase function works well for modeling single scattering events or even thin slices of turbid media where there are relatively few scattering events. In thicker slices of turbid media,

where a great many scattering events occur, the angular dependence of light intensity becomes an averaged version of the phase function. For example, if the scattering elements are oriented randomly, then the azimuthal dependence of the phase function is averaged and can no longer be observed. Over the course of many scattering events, nearly all visible traces of the phase function disappear. Thus the an average parameter called the ***anisotropy of scatter*** $g = \langle \cos(\theta) \rangle$ (expected value of $\cos(\theta)$) is used to characterize tissue scattering in terms of the relative forward versus backward direction of scatter [59, p. R38].

Figure 8-6A shows the Henyey-Greenstein phase function for several values of g. The function itself is shown below.

$$f(\theta) = \frac{1}{4\pi} \frac{(1 - g^2)}{(1 + g^2 - 2g\cos(\theta))^{3/2}} \qquad (8-16)$$

Notice that the above function is not a function of ϕ and thus has azimuthal symmetry. From the plots of $f(\theta)$ we can see that $g = 0$ represents an isotropic medium where scattering at any angle is equally likely while as g increases the scattering is directed more and more forward. In Figure 8-6B, the upper panel shows the angular distribution of scattered light at different depths, 0.01mm, 0.1mm and 1mm, simulated using monte carlo code [60, 61]. The parameters used in the simulation were $\mu_a = 0.1\text{mm}^{-1}$, $\mu_s = 10\text{mm}^{-1}$, and $g = 0.95$. In the bottom panel of the same figure, we the Henyey-Greenstein function for $g = 0.95$. With these figures we can see that at about 0.01mm from the surface (after relatively few scattering events) that the angular distribution of scattered light has a shape much like the phase function. The deeper we go into the medium, the more distorted the angular distribution becomes until at 1mm it looks nothing like the phase function. Thus we have demonstrated the averaging effect described in the previous paragraph and justified the use of g in place of the phase function for high-scattering environments.

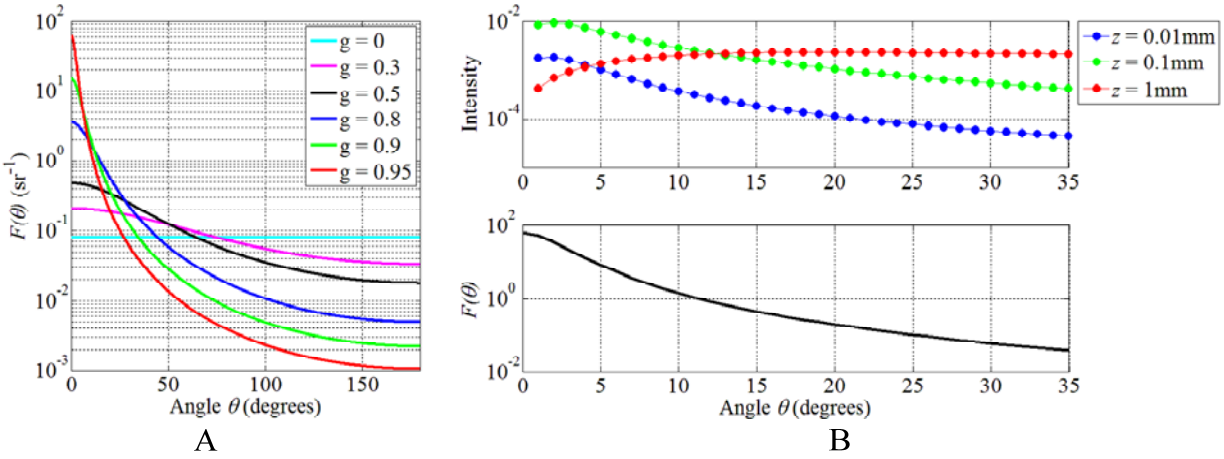

Figure 8-6: Henyey-Greenstein phase function for 6 different values of g as a function of angle (A) and distribution of intensity as a function of angle (top) taken from monte carlo simulations with parameters $\mu_a = 0.1\text{mm}^{-1}$, $\mu_s = 10\text{mm}^{-1}$, and $g = 0.95$ at depths 0.01mm, 0.1mm and 1mm (B, Top) and the Henyey-Greenstein function for $g = 0.95$ (B, Bottom).

8.2.6 *General Derivation of the Radiative Transfer Equation*

Begin with the continuity equation

$$\frac{\partial \Phi}{\partial t} + \nabla \cdot \mathbf{F} = \sigma \qquad (8-17)$$

Where Φ is the photon density (amount of photons per unit volume), $\mathbf{F}$ is the flux (amount of photons per unit area per unit time) and σ is the generation of photons per unit volume per unit time and represents internal sources and sinks. The term $\nabla \cdot \mathbf{F}$ in equation $(8-17)$ can be visualized as shown in the figure below. The figure shows a differential element with surfaces through which photons may pass. For simplicity, we will consider the change in flux only along the x-direction. From the figure we can see that the term $\nabla \cdot \mathbf{F}$ represents the difference between photons leaving a volume and photons entering a volume divided by the distance over which the change took place.

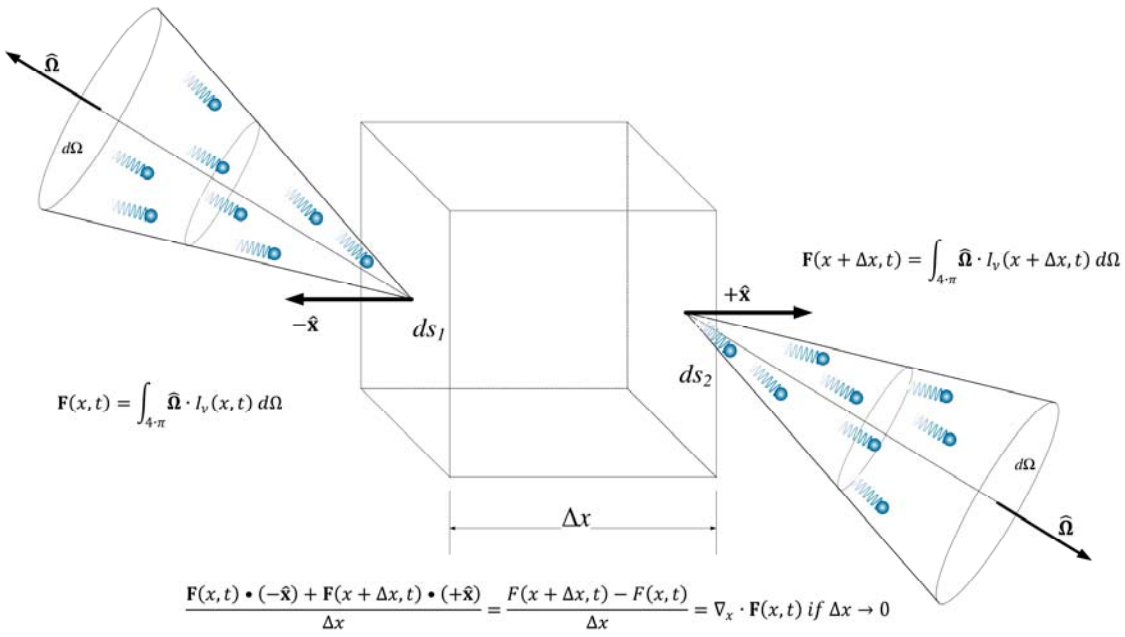

Figure 8-7: Simplified diagram of the divergence of photon flux in a differential volume.

We assume that radiation with intensity $I_\nu(\mathbf{r}, \hat{\boldsymbol{\Omega}}, t)$ in the frequency interval $d\nu$, passes in time *dt* through an element of length *ds* and cross section $d\sigma$ normal to the direction of the ray $\hat{\boldsymbol{\Omega}}$ into the solid angle $d\Omega$ [55, p. 29]. In to equation $(8-17)$ we substitute equations $(8-3)$, $(8-5)$, $(8-11)$, and $(8-15)$, which yields

$$\underbrace{\frac{1}{c}\frac{d}{dt}\int_{4\cdot\pi}\int_{\nu} I_\nu(\mathbf{r},\hat{\boldsymbol{\Omega}},t)\, d\nu\, d\Omega}_{\substack{Change\ in\ photon\ density \\ in\ dV\ with\ time}} + \underbrace{\nabla\cdot\underbrace{\int_{4\cdot\pi}\int_{\nu} \hat{\boldsymbol{\Omega}}\, I_\nu(\mathbf{r},\hat{\boldsymbol{\Omega}},t)\, d\nu\, d\Omega}_{\mathbf{F}(\mathbf{r},t)}}_{Photons\ leaving\ dV - Photons\ Entering\ dV}$$

$$= \left.\begin{aligned} &\underbrace{\int_{4\cdot\pi}\int_0^\infty \left[\mu_s \int_{4\cdot\pi} f(\hat{\boldsymbol{\Omega}}, \hat{\boldsymbol{\Omega}}', \mathbf{r}, t)\, I_\nu(\mathbf{r},\hat{\boldsymbol{\Omega}}',t)\, d\Omega'\right] d\nu\ d\Omega}_{Photons\ added\ to\ the\ pencil\ after\ scattering} \\ &- \underbrace{\int_{4\cdot\pi}\int_0^\infty (\mu_a+\mu_s)\, I_\nu(\mathbf{r},\hat{\boldsymbol{\Omega}},t)\, d\nu\, d\Omega}_{\substack{Photons\ lost\ due\ to \\ absorption\ and \\ scattering}} + \underbrace{\int_{4\cdot\pi}\int_0^\infty j_\nu\, d\nu\, d\Omega}_{\substack{Photons\ gained\ due \\ to\ fluorescence}} \end{aligned}\right\} sinks/sources \quad (8-18)$$

If we assume that $(8-18)$ is satisfied in the strong sense, that is the left-hand side of the integrand is equal to the right-hand side of the integrand, we get [57, p. 8]

$$\frac{1}{c}\frac{d}{dt}I_\nu(\mathbf{r},\widehat{\mathbf{\Omega}},t)+\nabla\cdot\left[\widehat{\mathbf{\Omega}}\,I_\nu(\mathbf{r},\widehat{\mathbf{\Omega}},t)\right]$$

$$=\mu_s\int_{4\cdot\pi}f(\widehat{\mathbf{\Omega}},\widehat{\mathbf{\Omega}}',\mathbf{r},t)\,I_\nu(\mathbf{r},\widehat{\mathbf{\Omega}}',t)\,d\Omega'-(\mu_a+\mu_s)\,I_\nu(\mathbf{r},\widehat{\mathbf{\Omega}},t)+j_\nu^a(\mathbf{r},\widehat{\mathbf{\Omega}},t)\qquad(8-19)$$

The term $\nabla\cdot\left[\widehat{\mathbf{\Omega}}\,I_\nu(\mathbf{r},\widehat{\mathbf{\Omega}},t)\right]$ is often replaced with $\widehat{\mathbf{\Omega}}\cdot\nabla I_\nu(\mathbf{r},\widehat{\mathbf{\Omega}},t)$. We can easily show that these two forms are equivalent. First we have

$$\nabla\cdot\left[\widehat{\mathbf{\Omega}}\cdot I_\nu(\mathbf{r},\widehat{\mathbf{\Omega}},t)\right]=\nabla\cdot\left(\hat{\mathbf{x}}\,\Omega_x\,I_\nu(\mathbf{r},\widehat{\mathbf{\Omega}},t)+\hat{\mathbf{y}}\,\Omega_y\,I_\nu(\mathbf{r},\widehat{\mathbf{\Omega}},t)+\hat{\mathbf{z}}\,\Omega_z\,I_\nu(\mathbf{r},\widehat{\mathbf{\Omega}},t)\right)$$

$$=\Omega_x\frac{\partial}{\partial x}I_\nu(\mathbf{r},\widehat{\mathbf{\Omega}},t)+\Omega_y\frac{\partial}{\partial y}I_\nu(\mathbf{r},\widehat{\mathbf{\Omega}},t)+\Omega_z\frac{\partial}{\partial z}I_\nu(\mathbf{r},\widehat{\mathbf{\Omega}},t)\qquad(8-20)$$

Then we can expand the form $\widehat{\mathbf{\Omega}}\cdot\nabla I_\nu(\mathbf{r},\widehat{\mathbf{\Omega}},t)$ to get

$$\widehat{\mathbf{\Omega}}\cdot\nabla I_\nu(\mathbf{r},\widehat{\mathbf{\Omega}},t)=\left(\hat{\mathbf{x}}\,\Omega_x+\hat{\mathbf{y}}\,\Omega_y+\hat{\mathbf{z}}\,\Omega_z\right)\cdot\left(\hat{\mathbf{x}}\frac{\partial}{\partial x}I_\nu(\mathbf{r},\widehat{\mathbf{\Omega}},t)+\hat{\mathbf{y}}\frac{\partial}{\partial y}I_\nu(\mathbf{r},\widehat{\mathbf{\Omega}},t)+\hat{\mathbf{z}}\frac{\partial}{\partial z}I_\nu(\mathbf{r},\widehat{\mathbf{\Omega}},t)\right)$$

$$=\Omega_x\frac{\partial}{\partial x}I_\nu(\mathbf{r},\widehat{\mathbf{\Omega}},t)+\Omega_y\frac{\partial}{\partial y}I_\nu(\mathbf{r},\widehat{\mathbf{\Omega}},t)+\Omega_z\frac{\partial}{\partial z}I_\nu(\mathbf{r},\widehat{\mathbf{\Omega}},t)\qquad(8-21)$$

It can clearly be seen that $(8-20)$ and $(8-21)$ are identical. We can then write

$$\frac{1}{c}\cdot\frac{d}{dt}I_\nu(\mathbf{r},\widehat{\mathbf{\Omega}},t)+\widehat{\mathbf{\Omega}}\cdot\nabla I_\nu(\mathbf{r},\widehat{\mathbf{\Omega}},t)$$

$$=\mu_s\cdot\int_{4\cdot\pi}f(\widehat{\mathbf{\Omega}},\widehat{\mathbf{\Omega}}',\mathbf{r},t)\cdot I_\nu(\mathbf{r},\widehat{\mathbf{\Omega}}',t)\,d\Omega'-(\mu_a+\mu_s)\cdot I_\nu(\mathbf{r},\widehat{\mathbf{\Omega}},t)+j_\nu^a(\mathbf{r},\widehat{\mathbf{\Omega}},t)\qquad(8-22)$$

8.3 Practical Methods for Determining Light Transport Model Parameters in Tissues and Other Turbid Media

As we have shown in the previous sections, the main light-scattering model parameters are the absorption coefficient μ_a, the scattering coefficient μ_s, and the anisotropy of scatter g. Over the years many methods have been devised to extract these parameters. However, we can group them into 5 categories: collimated transmittance, sampled fluence, diffuse transmittance, diffuse reflectance, and time-resolved. In the next few sub sections we will describe each and then provide examples of how they can be used together or separately to extract model parameters.

8.3.1 *Collimated Transmittance*

Collimated transmittance is an old but effective method of separating ballistic from diffuse photons, typically for the purpose of determining the total attenuation coefficient $\mu_t = \mu_s + \mu_a$. It is based on the principle that the decay of ballistic photons in a turbid media is described by the equation below [62, 50, 63].

$$I(z) = I_0 e^{-z/\mu_t} \qquad (8-23)$$

where z is the depth within the medium, I_0 is the initial intensity and $I(z)$ is the intensity at depth z.

An example setup for measuring collimated transmittance is shown in Figure 8-8. Here we see that a narrow, collimated beam enters the sample where the light becomes scattered. The light that escapes the sample then passes through an aperture some distance away thus eliminating

all or at least most diffuse photons. The distance L and the size of the aperture near the detector determine the effectiveness of the system at eliminating diffuse photons. The maximum angle at which a scattered photon may reach the detector is

$$\alpha = \tan^{-1}\left(\frac{r_A}{L}\right) \qquad (8-24)$$

where r_A is the radius of the aperture near the detector. In some cases a third aperture may be used to narrow the angle at which photons leaving the sample may travel and still reach the detector. The minimum allowable angle is related to the medium under study. For example, with high values of g where scattering is primarily directed forward, there will be a great number of photons which may undergo a few collisions but still moving relatively straight. These are the so-called snake photons and can be very difficult to separate from ballistic photons. Collimated transmittance can be coupled with other methods, i.e. one used to determine μ_a, so that μ_s can be determined, or if $\mu_s \gg \mu_a$ which is often the case with tissue, it can be used on its own to estimate μ_s.

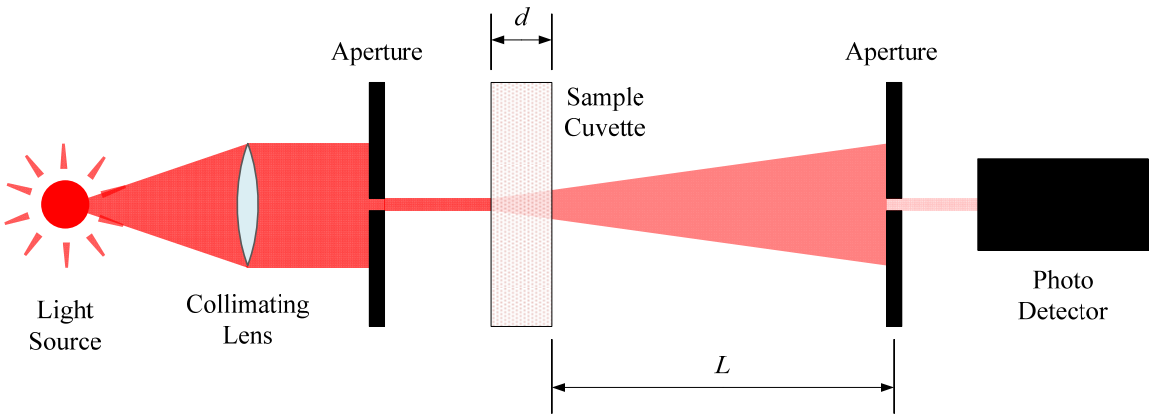

Figure 8-8: Example setup for measuring collimated transmittance.

8.3.2 *Sampling of Fluence Rate*

The added absorber method is a common application of sampled fluence rate. This method relies entirely on the diffusion approximation, where measurements of forward-directed flux can be considered proportional to measurements of fluence. The procedure consists of first measuring on-axis transmission in a scattering medium, then adding an absorber with a known absorption coefficient and repeating the measurement [64].

The absorber used is typically black ink, which is known to produce almost no scatter, and the scattering agent is typically intralipid (IL). Most importantly, it has been shown that ink and intralipid do not interact with each other in solution. In addition, while ink has very little scatter intralipid has very little absorbance, allowing μ_a and μ_s' to be adjusted independently [65]. Using the diffusion approximation, the spatial constants with and without the absorber are defined as

$$\delta_2 = \frac{1}{\sqrt{3\mu_a(\mu_a + \mu_s')}} \qquad (8-25)$$

and

$$\delta_{2,a} = \frac{1}{\sqrt{3(\mu_a(1-C_{ink}) + \Delta\mu_a)\big(\mu_a(1-C_{ink}) + \Delta\mu_a + \mu_s'(1-C_{ink})\big)}} \qquad (8-26)$$

respectively. Here C_{ink} is the concentration of ink and $\Delta\mu_a$ is the absorbance of the ink. In practice, I have found it rather difficult to work with undiluted ink. In its natural state, the absorbance is so high that one is forced to work with very small quantities. This is further complicated by the fact that the ink tends to stick to the sides of the pipettes used to measure out these small quantities. Hence, a solution of ink and water was mixed, calibrated, and used as the absorber. Using the ink and water solution adds a significant amount of water along with the ink.

Hence the values of μ_a and μ_s' must be adjusted to account for the dilution. That is the reason for the factor $(1 - C_{ink})$ that appears in equation $(8 - 26)$. Solving equations $(8 - 25)$ and $(8 - 26)$ yields

$$(3(1 - C_{ink})\Delta\mu_a)\mu_a^2 + \left(3\Delta\mu_a^2 + \frac{(1 - C_{ink})^2}{\delta_2^2} - \frac{1}{\delta_{2,a}^2}\right)\mu_a + \frac{\Delta\mu_a(1 - C_{ink})}{\delta_2^2} = 0 \qquad (8 - 27)$$

and

$$\mu_s' = \frac{1}{3\mu_a\delta^2} - \mu_a \qquad (8 - 28)$$

8.3.3 *Diffuse Transmittance*

A measurement of diffuse transmittance involves collecting light transmitted through a sample with an integrating sphere. An example setup is shown in Figure 8-9. Results from this measurement can be interpreted using the Kubelka-Munk (KM) model [66, 67]. This model divides the diffuse flux into 2 groups: the flux traveling forward (same direction as incident light) and the flux traveling backward. Solving the differential equations for a slab geometry and a diffuse source of illumination yields

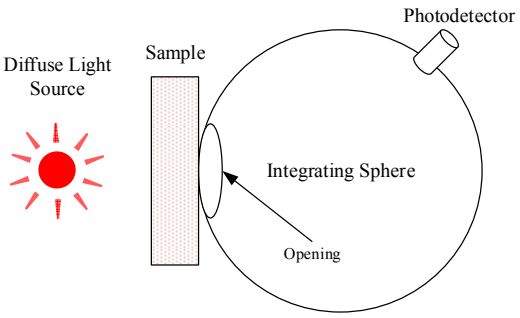

Figure 8-9: Experimental setup for collecting diffuse transmittance through a turbid medium.

$$A_{KM} = 2\mu_a \qquad (8 - 29)$$

$$S_{KM} = \frac{3}{4}(\mu_a + \mu_s') - \mu_a = \frac{3}{4}\mu_s' - \frac{1}{4}\mu_a \qquad (8 - 30)$$

where S_{KM} (m^{-1}) denotes backscattering and A_{KM} (m^{-1}) denotes absorption. We can determine the values of A_{KM} and S_{KM} through a measurement of diffuse transmittance with total diffuse reflectance R_d (see next section). The equations are shown below.

$$S_{KM} = \frac{1}{bd}\mathrm{Ln}\left(\frac{1 - R_d(a-b)}{T_d}\right) \tag{8-31}$$

$$A_{KM} = S_{KM}(a-1) \tag{8-32}$$

where d is the thickness of the slab and

$$a = \frac{1 + R_d^2 - T_d^2}{2R_d} \tag{8-33}$$

$$b = \sqrt{a^2 - 1} \tag{8-34}$$

The diffuse transmittance, along with other measurements, has also been used to determine the light scattering model parameters using different mathematics and/or computer simulations. For example, a multiple-polynomial regression method based on monte carlo simulations was used to extract optical parameters from T_d, R_d, and collimated transmittance measurements in heart tissue [49].

8.3.4 *Diffuse Reflectance*

When light is incident on the surface of a turbid medium it stands to reason that some of it will enter the medium and some will be reflected back. If the light source is collimated and the light is incident parallel to the surface normal of the medium, then light is reflected due to collision with particles within the medium and not, for the most part, refractive index mismatch. The light reflected back is termed diffuse reflectance.

Diffuse reflectance has gained a great deal of popularity due to its non-invasive nature. There are 2 main types of diffuse reflectance measurements: Total diffuse reflectance R_d and spatially-resolved diffuse reflectance $R(\rho)$. Figure 8-10 shows and example experimental setup for measuring total diffuse reflectance (panel A) and spatially-resolved diffuse reflectance (panel B).

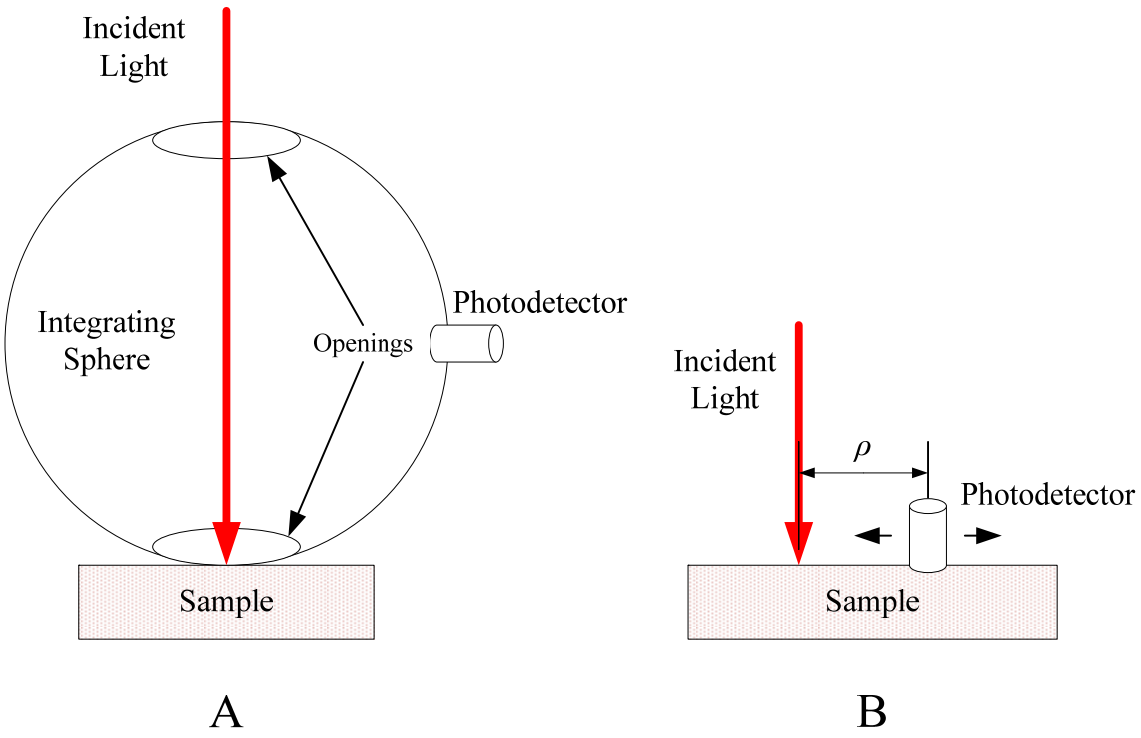

Figure 8-10: Example experimental setups for measuring diffuse reflectance. Panel A shows an integrating sphere collecting light reflected from the sample which is proportional to total reflectance R_d. Panel B shows a system for measuring spatially-resolved diffuse reflectance $R(\rho)$. Here we show a single movable detector a distance ρ from the incident beam, though alternatively multiple fixed photodetectors could be used.

Experimentally, $R(\rho)$ can be used by itself to extract the parameters of the medium as was done in [68]. However it is more commonly used with other measurements. For example, measurements of R_d can be combined with collimated transmittance [63, 49] or diffuse transmittance (see previous section). There are also examples in literature of combining $R(\rho)$ with time-resolved measurements [69, 70]. It is also possible to use both R_d and $R(\rho)$ together to

get the optical parameters of a medium. In [71] expression for $R(\rho)$ and R_d are derived from the diffusion approximation of the RTE. They are

$$R(\rho) = \frac{z_0}{2\pi}\exp\left\{\frac{-\mu_{eff}\sqrt{z_0^2+\rho^2}}{z_0^2+\rho^2}\left(\mu_{eff}+\frac{1}{\sqrt{\rho^2+z_0^2}}\right)\right\} \qquad (8-35)$$

and

$$R_d = \frac{a'}{1+2k(1-a')+\left(1+\frac{2k}{3}\right)\sqrt{3(1-a')}} \qquad (8-36)$$

where z_0, the depth at which all incident photons are assumed to be isotropically scattered, is

$$z_0 = \frac{1}{\mu_s'} \qquad (8-37)$$

a', the scattering albedo, is

$$a' = \frac{\mu_s'}{\mu_a+\mu_s'} \qquad (8-38)$$

and k is

$$k = \frac{1+R}{1-R} \qquad (8-39)$$

where R is related to the index of refraction by the empirically derived equation [72]

$$R = -1.44n^{-2} + 0.71n^{-1} + 0.668 + 0.0636n \qquad (8-40)$$

Using the above equations together it is possible to extract μ_a and μ_s' from a turbid medium.

8.3.5 *Time-Resolved Measurements*

When light first enters a medium, it exhibits some time-dependent behavior. The methods described previously ignore this because they are only concerned with steady-state measurements, but there are ways of extracting meaningful information from these transient phenomena. Because the transient effects of light traveling through a medium are typically very brief, the light source must be modulated at high frequency. The modulating signal is typically either short pulses or a sinusoid.

When a light source is pulsed at high frequency, one can observe the effect that the turbid medium has on the shape of the pulse. Figure 8-11 shows a simplified setup for observing time-dependent behavior of pulsed light diffusing through a turbid medium. The light enters through the surface of the medium, and travels to the detector a distance ρ from the point of entry. The oscilloscopes show the initial impulse of light and the delayed and dispersed collected light seen by the detector on the surface of the medium. In this example, the light collected is diffuse because ballistic photons cannot reach the detector in the position shown.

In reality, the setup must be more complex because it is generally not possible to observe these time-domain effects on a traditional oscilloscope. A real implementation of this setup could use a time-to-amplitude converter (TAC) to capture the optical signal [70]. The TAC is basically an integrator designed to operate at high speeds and is commonly used to capture phenomena that occur ~100ps. The output of the TAC would of course need to be differentiated to yield the true optical signal.

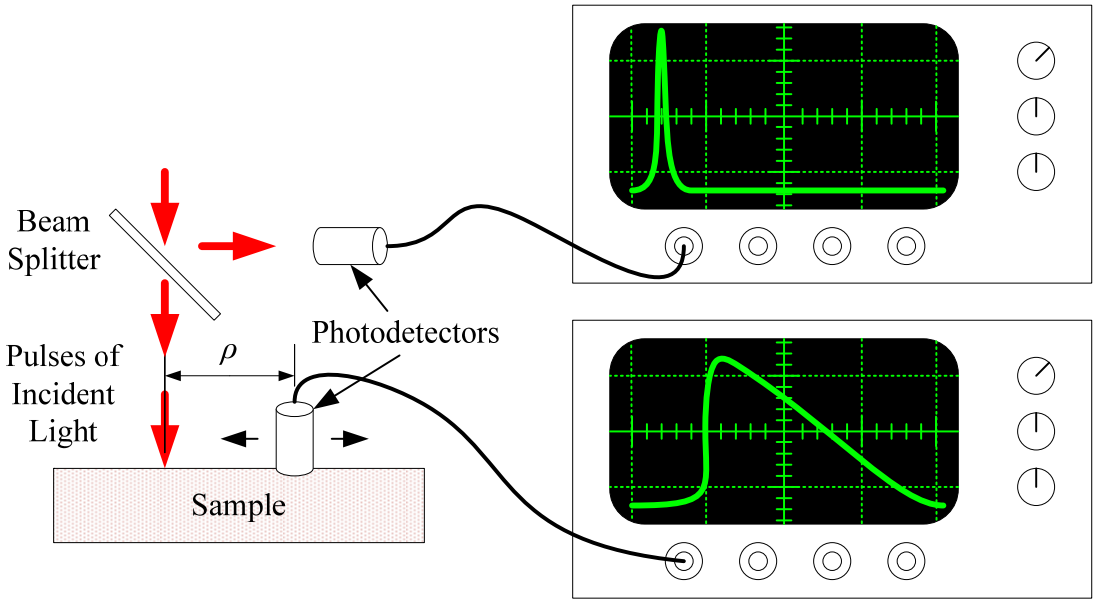

Figure 8-11: Example setup for extracting optical parameters from a turbid medium by observing the time-dependent effects on a pulse of light.

As mentioned previously, this method can be used to collect diffuse light. If this is the case, then the detected signal can be modeled using a time-dependent version of the diffusion approximation [70] as shown below.

$$\frac{n}{c}\frac{\partial}{\partial t}\phi(\rho,t) - D\nabla^2\phi(\rho,t) + \mu_a\phi(\rho,t) = S(\rho,t) \qquad (8-41)$$

Assuming that a depth z_0 light is isotropically scattered (see equation $(8-37)$), we can solve equation $(8-41)$ for an isotropic point source $S(\rho,t) = \delta(0,0)$ located at depth z_0 and assuming $\phi(\rho,t) = 0$ at the medium surface. The result is

$$R(\rho,t) = (4\pi Dc/n)^{3/2} z_0 t^{-5/2} e^{-\mu_a ct/n} e^{-\frac{\rho^2+z_0^2}{4Dct/n}} \qquad (8-42)$$

where D is the diffusion coefficient and n is the refractive index of the medium. The equation is not valid before time $t_0 = \rho_0 \frac{n}{c}$ because no photons will have reached the

observation point ρ_0. In [70] the diffuse light escaping from the medium was detected. The rising edge and tail of the pulse were ignored and equation $(8-42)$ was fit to the data to extract μ_a and μ_s'.

When the light source is sinusiodally modulated instead of pulsed, then the parameters of interest are the amplitude and phase change of the detected waveform. The setup is basically the same as that shown in Figure 8-11. Once again the goal is detect diffuse light exiting the surface of the medium some distance ρ from the source. This method was used in [73] where measurements of amplitude and phase delay were taken at several distances from the source.

Chapter 9 Determining Light-Scattering and Absorption Parameters from Forward-Directed Flux Measurements in Cardiac Tissue

In this section we will describe in detail how this method is used to characterize turbid media in terms of μ_a and μ_s', and then suggest a modification that can be used in certain cases to get the remaining light scattering model parameters μ_s and g.

9.1 Experimental Setup

A schematic of the experimental setup for forward-directed flux measurements is shown in Figure 9-1. The sample was illuminated from underneath with a broad, collimated beam of light. The fiber-optic probe was placed over the sample and gradually advanced via a micromanipulator to measure the forward-directed flux $\psi(z)$.

The apparatus consisted of an aluminum stand (not shown) with a sample tray, the three-axis micromanipulator with attached fiber-optic probe, and the illumination system. The stand was painted flat black so as not to reflect light. The micromanipulator, bolted to the top of the stand, allowed the probe to move along *x*, *y*, and *z* axes as well as to rotate up to 90^o around the horizontal axis. The fine-adjustment allows the probe to be advanced into the sample in steps as small as 10 microns.

The light sources (Shanghai Dream Lasers) were a 660nm, 600mW laser (model SDL-LM-660-600T) and a 532nm, 1000mW laser (model SDL-532-1000T). To remove

the non-uniformity in the 660nm laser's beam profile, the beam was focused with a 45mm DCX lens (F=250mm) onto a holographic diffuser plate. The outgoing beam was collimated using an 83mm diameter DCX lens with F=173mm (Anchor Optics AX74813), and reflected upward by a 108mm x 145mm x 3mm mirror (Anchor Optics AX27536) to illuminate the tissue sample.

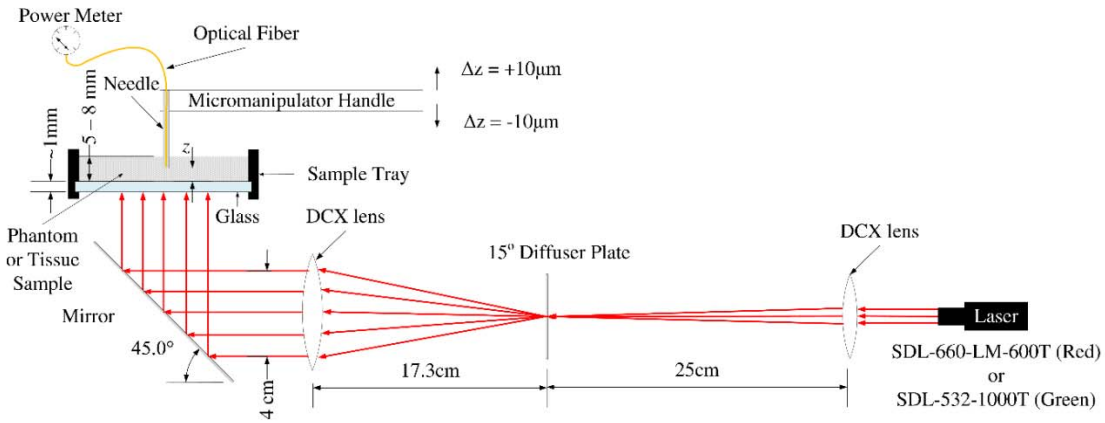

Figure 9-1: Schematic of the experimental setup used for light attenuation measurments (side view).

9.1.1 *Manufacturing and Characterization of the Optical Probes*

The optical fibers were threaded through a needle mounted on a 1ml syringe and secured with super glue. A 25 gauge needle was used for the 200μm fibers. To pass the fiber through the shaft of the needle, the jacket and coating were removed. We then applied Norland Optical Adhesive 81 (NOA81) from Thorlabs, which protected the fiber from chipping and secured it within the needle. The fiber and needle were both cleaned prior to application of the adhesive; then a small amount of NOA81 was poured into the needle and cured with a UV light source. Care was taken to ensure that the tip of the

probe was covered with a protective layer of adhesive. The tip was then sanded flat using 5 micron, 0.3 micron and then 0.05 micron lapping film (Digi-Key). The probe was continuously inspected under a microscope to ensure flatness and that the layer of NOA81 had been sufficiently polished to remove any imperfections. The fiber was attached to an optical sensor S120C (or an S150C for measurements at lower intensity) connected to a PM100D optical power meter, all from Thorlabs.

The angular sensitivity of the probes was measured by rotating the optrode with respect to the light beam as shown in Figure 9-2a. To approximate the change in refractive index at the probe/tissue interface, the tip of the probe was immersed in a petri dish containing normal saline (0.9% w/v NaCl). Figure 9-2b shows the relative light intensity as a function of angle, for all probes measured at 532nm and 660nm.

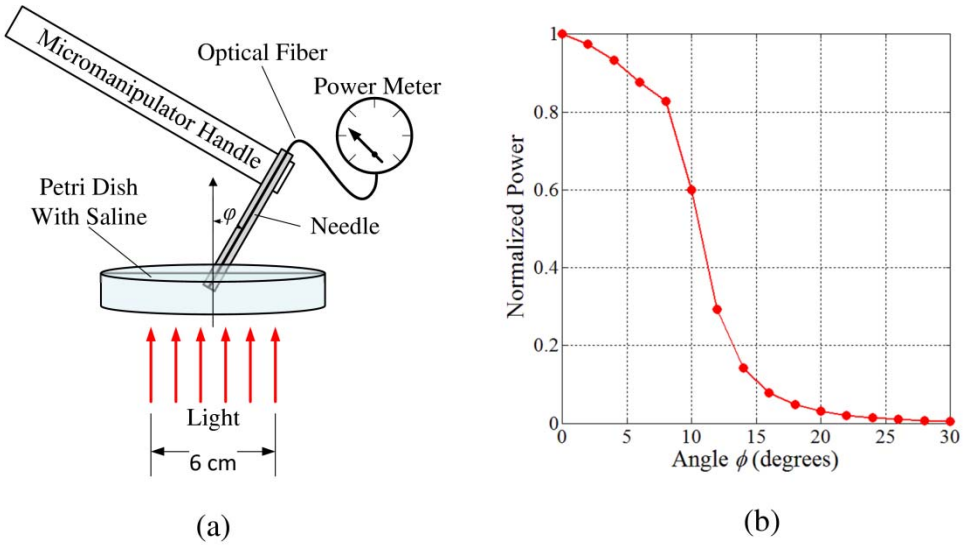

Figure 9-2: Measurement of the angular sensitivity of the probe. (a) Schematic of the experimental setup. (b) Angular sensitivity of the 25 guage needle optical probes at 660nm.

9.2 Methods for Measuring Forward-Directed Flux

Measuring the forward directed flux required calibrating the position of the probe, such that the micromanipulator would read 0 when the tip of the needle was touching the glass. Next the probe was raised and the sample (heart tissue, homogenized heart tissue, or phantom) was placed under the probe. The needle was then advanced in small steps into the sample, starting on the surface and continuing until the probe tip touched the glass bottom ($z = 0$). To keep the change in intensity more uniform over the entire thickness of the medium, the step size (Δz) varied with z, so that the change in power between steps did not exceed 10%. The initial value of Δz was chosen between $100\mu m - 200\mu m$. When change in power between steps exceeded 10% the step size was cut in half. As a result , Δz was reduced to 50μm, 20μm, and 10μm at depths of $z = 1mm$, 200μm, and 100μm respectively.

9.2.1 *Tissue Samples*

All tissue experiments were performed in accordance with National Institutes of Health guidelines in the use of laboratory animals and approved by the SUNY Upstate Medical University Animal Care and Use Committee. Female Yorkshire pigs (26-32 kg) undergoing 48 hour sepsis studies were anesthetized using a continuous infusion of ketamine/xylazine. Our choice of the specimens was determined in part by the availability of freshly harvested hearts from another study, which enabled us to achieve our objectives without sacrificing additional animals. Upon completion of the study, pigs were euthanized and the hearts removed. The right ventricle was dissected from each

heart and laid flat on a piece of glass. The epicardial side faced the light source and the endocardial side faced the fiber-optic probe. A small incision was made in the endocardial side with a scalpel at the fiber-optic probe insertion site to prevent a dimple from forming on the surface as the flat-tipped and comparatively large-diameter needle went in.

In some of the experiments the measurements of forward directed flux were carried out in homogenized tissue. The heart ventricles were separated from the valves, veins, arteries, atria, auricle, and fat. The isolated muscle tissues were then homogenized into a fine paste by the Omni Macro ES digital programmable homogenizer by Omni International.

9.2.2 *Phantoms*

We used a mixture of India Ink as the absorber with Intralipid 20% emulsion (Sigma Aldrich) as the scattering media. The experiments were conducted for intralipid (IL) concentration of 8% being close to the scattering properties of cardiac tissue at 660 nm; see discussion below.

For our experiments, we used a solution of India Ink and water as an absorber, and characterized its absorption using a the DU730 spectrophotometer by Beckman Coulter, as was done in [71]. The result is shown in Figure 9-3A, which depicts the absorption coefficient as a function of ink concentration. Notice that $\Delta\mu_a$ is a linear function of concentration, the same as in [65]. The equation of the fit line for 660nm light is

$$\Delta\mu_a = 0.007\, C_{ink} \qquad (9-1)$$

and for 532nm light is

$$\Delta\mu_a = 0.009\, C_{ink} \qquad (9-2)$$

For the scattering agent, we used intralipid (Sigma Aldrich). For each concentration of intralipid (IL) used 2 measurements of sampled flux were taken: one with ink solution and one without. Solving equations $(8-27)$and $(8-28)$ gives us μ_a and μ_s' of the intralipid. This process was repeated for both red light (660nm) and green light (532nm). The results is shown in Figure 9-3B. As predicted in [65], μ_s' is a linear function of intralipid concentration.

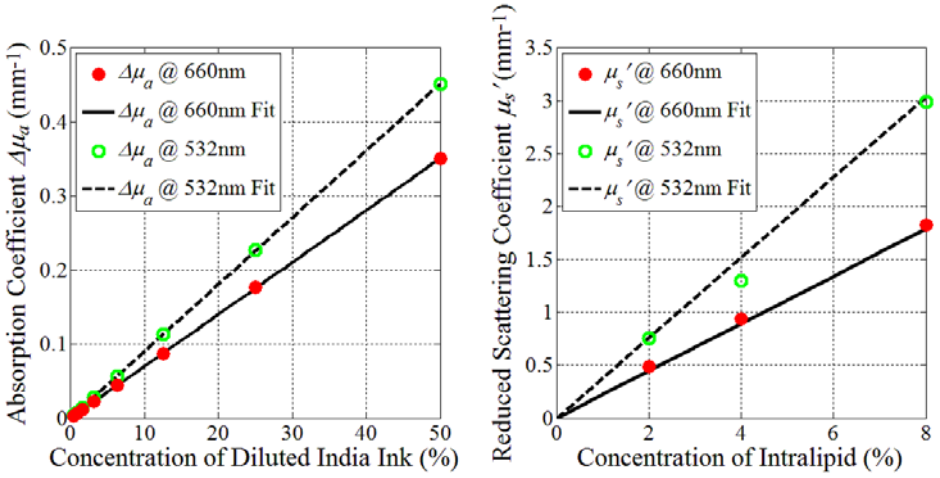

A **B**

Figure 9-3: Absorption and Scattering vs. concentration. Plots of the absorption of the ink and water solution used for added absorber experiments (A) and reduced scattering coefficient of intralipid (B).

Now that we have characterized our scatter, we can choose an intralipid concentration of 8% for our experiments because it has a μ_s' that is closest to heart tissue (see discussion below).

9.3 Monte Carlo Light-Transport Simulations

To simulate measurements of forward-directed flux at different depths, $\psi(z)$, using optical fibers of varying numerical aperture (*i.e.*, varying maximum acceptance angle, θ, where $NA = n\sin(\theta)$ and n = index of refraction of the tissue), we performed Monte Carlo (MC) simulations using the open-source software packages MCML [60] and CONV [61].

Using MCML, we obtained the tissue response to an infinitely narrow light beam. The 'total transmittance' MCML routine was modified to allow simulation of the forward-directed flux at any given depth z inside the tissue. This was achieved by allowing user-defined placement of the z-plane where total transmittance was calculated, which in the original routine was fixed at the tissue's rear surface. The output of the modified program produced the forward directed flux $\psi(z, r, \alpha)$ as function of the distance, r, from the beam axis, and the angle of photon incidence α, with respect to a line normal to a given z-plane (grid spacing, $\Delta\alpha = 1°$; $\alpha = 0°$ to $90°$) .

The function $\psi(z, r, \alpha)$ was then convolved using the CONV package to simulate broad field illumination. We simulated a circular, flat incident beam of radius $R = 1.5$ cm with total incident energy of 1.0 Joule. The probe was located in the center of the beam ($r = 0$). Increasing R above the set value did not affect the convolution results. This suggests that the condition of uniform broad field illumination was satisfied. To obtain responses for probes with different numerical apertures, the function $\psi(z, r = 0, \alpha)$ was convolved with the function representing the angular sensitivity of the respective probe.

The following parameters were used as inputs to the program: 1) the photon absorption coefficient, μ_a; 2) the photon scattering coefficient, μ_s; 3) the scattering anisotropy factor, g; 4) the refractive index of both the tissue ($n_{tissue} = 1.4$) and surrounding ambient air medium ($n_{air} = 1.0$); and, 5) the thickness of the tissue, d. We used a single value for the absorption coefficient, $\mu_a = 0.1$ mm^{-1}, but three different values for the scattering coefficient, μ_s : 5.0 mm^{-1}, 10.0 mm^{-1} and 20.0 mm^{-1}. We explored how the forward-directed flux, $\psi(z)$, as function of depth (z = 0 to 5 mm), was affected by the anisotropy coefficient, g (from 0.10 to 0.99) and fiber optic probe maximum acceptance angle, α (from 1° to 36°). The tissue thickness, d, was set at a value of 5.0 mm. For each MCML simulation, a total of 100,000,000 photon packets were launched.

9.4 Forward-Directed Flux Measurements in Heart Tissue

Representative samples of forward flux measurements in intact pig right ventricular wall at 660nm and 532nm are shown in Figure 9-4a. The normalized FDF is plotted on a log scale. The data points for 530nm lie well below of those for 660nm, which reflects the higher rate of attenuation of green light as compared to red light. However, both curves have an important similarity. Each has a steeper slope at smaller z and a lower one at larger z suggesting that the curves represent a sum of two decaying exponents.

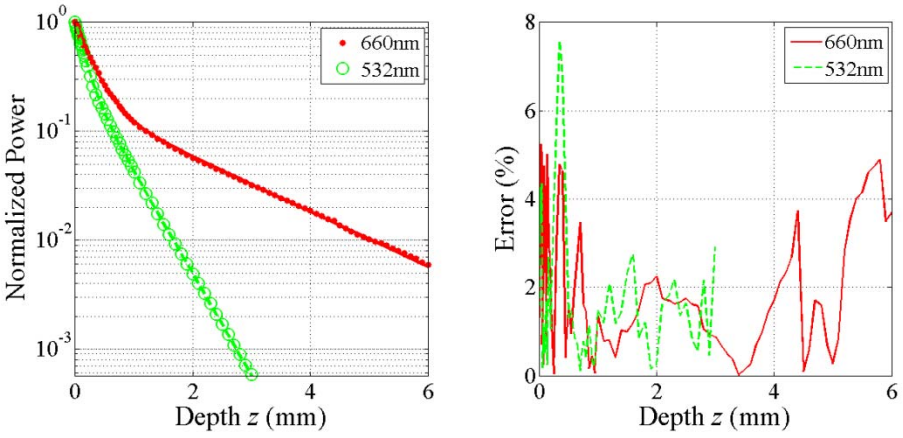

(a) **(b)**

Figure 9-4: (a) Forward-directed flux plots at 660nm (red) and 532 nm (green) in pig right ventricular wall. Red and green solid lines show the respective two-exponent fits. (b) Relative error of the fits

Confirmation that the data in Figure 9-4a, is indeed in accordance with the sum of two-exponential decay functions as presented in equation $(9-3)$, is obtained by using the FIT

function of MATLAB.

$$\psi(z) = k_1 e^{-z/\delta_1} + k_2 e^{-z/\delta_2} \quad . \qquad (9-3)$$

Note that for normalized data $k_1 + k_2 = 1$. The weighting of each point was set to the inverse of its value. Such weighting enabled accurate fitting of the smaller-valued points of the slow exponent which otherwise would not be given the same consideration as the larger values of the fast exponent. Figure 9-4b shows the error of the two-exponent fit of the data shown in Figure 9-4a. One can see that the maximum error is below 8% and the average error is about 1.5%, which supports the two-exponent function hypothesis.

Similar measurements were carried out in different locations, in five different hearts. The recording sites were chosen primarily across the apical section of the right ventricle, which lacks fat patches and large blood vessels. An example of the measurement sites we chose is shown in Figure 9-5, which depicts the endocardial and epicardial surfaces of the right ventricle in one of the hearts and all of the measurement sites. The number of measurements conducted on each heart was 20 (10 with red light and 10 with green).

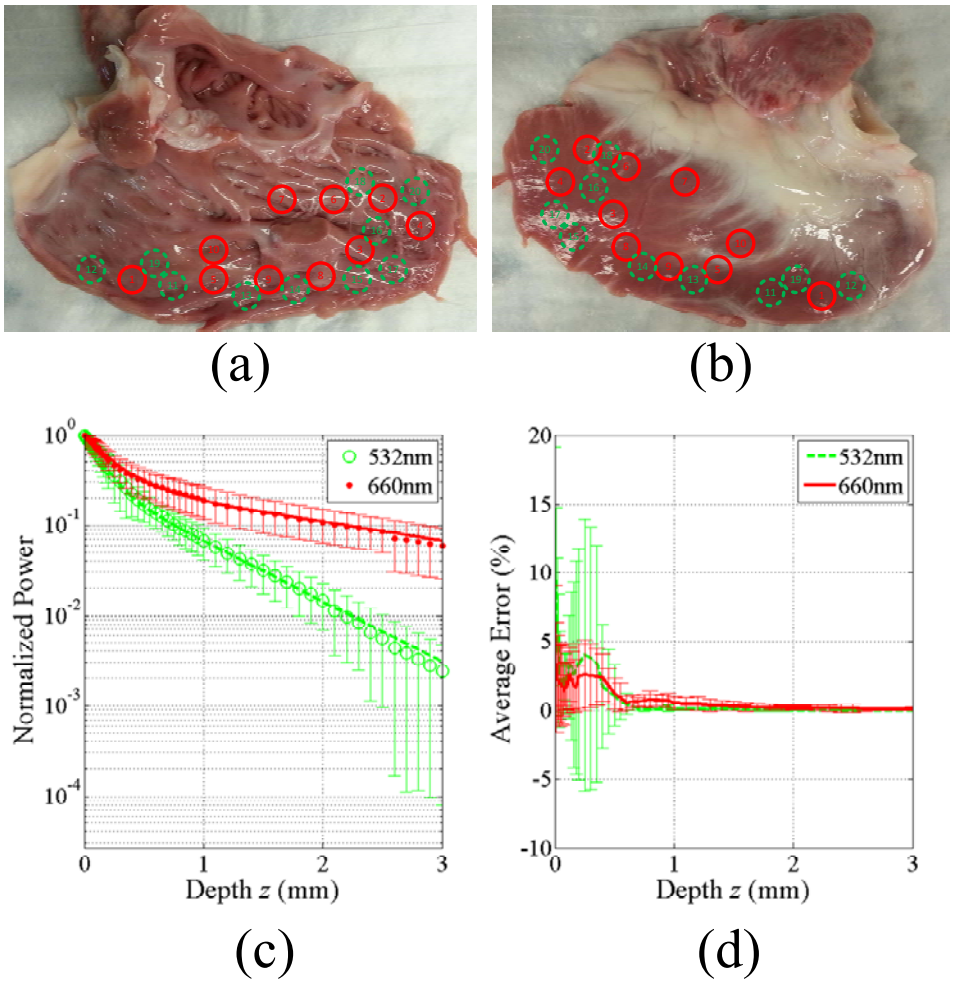

Figure 9-5: Picture of endocardial (a) and epicardial (b) sides of pig right ventricular wall in one of the hearts. The red-solid circles represent measurement sites for 660nm light and the green-dashed circles represent measurement sites for 532nm light. (c) Plot of average forward-directed flux data across all recording sites for 660nm and 532nm light. (d) Averaged fit error.

Figure 9-5 shows the averaged forward-directed flux data and fit curves in one of the preparations. It is notable that while the scatter of the light intensity at any given depth is quite significant, the accuracy of the individual fits (see Figure 9-5d) remains relatively high. This reflects the fact that while the optical properties of the tissue vary from one location to another, $\psi(z)$ remains a two-exponential function. The average fit parameters k_1, δ_1, and δ_2 for different hearts and their standard deviations for 532nm and 660nm light are shown in Table 9-1 for 5 hearts each with 10 measurements for red and green light, for a total of 100 measurements.

Table 9-1: Optical characteristics of pig ventricular myocardium at 660nm and 532nm. Five hearts were examined and 10 measurements for red and green each were taken for a total of 100 measurements.

Wavelength (nm)	k_1	δ_1 (mm)	δ_2 (mm)
660	0.76 ± 0.05	0.24 ± 0.05	2.1 ± 0.45
530	0.71 ± 0.08	0.13 ± 0.02	0.58 ± 0.13

Due to signal normalization to $\psi(0)$, the parameter k_2 is calculated as: $k_2 = 1 - k_1$. The attenuation length for ballistic photons δ_1 at 530nm is almost two times smaller than at 660nm (0.13±0.02mm vs 0.24±0.05mm). The difference is even greater for δ_2 (0.58±0.13mm vs 2.1±0.45mm). The observed differences are the manifestation of reduced light absorption and scattering at longer wavelengths.

The interpretation of the long spatial constant is rather straightforward. It represents a spatial decay of fluence rate in the diffuse regime, with δ_2 being the attenuation length commonly symbolized as δ in the literature. Indeed, our numerical values of δ_2 are within the range of values reported in the literature for cardiac tissue [74,

49, 68, 75]. The origin of the fast exponent is less obvious. The numerical value of δ_1^{-1} between 5-8 mm^{-1} is not too far off from the values reported for the scattering coefficient in biological tissues suggesting that it may represent the decay of ballistic photons in the tissue. It may also reflect a heterogeneity of the optical properties of the myocardial surface layer, or both.

To assess the potential contribution of myocardial heterogeneity on $\psi(z)$ we carried out the following experiment. After measuring $\psi(z)$ in intact heart tissue, the tissue was homogenized and the experiments were repeated. Figure 9-6 compares $\psi(z)$ before and after homogenization. If the first exponent was the result of optical heterogeneity, after homogenization we would have observed a significant reduction, or the complete disappearance, of the fast exponent. However, this was not the case.

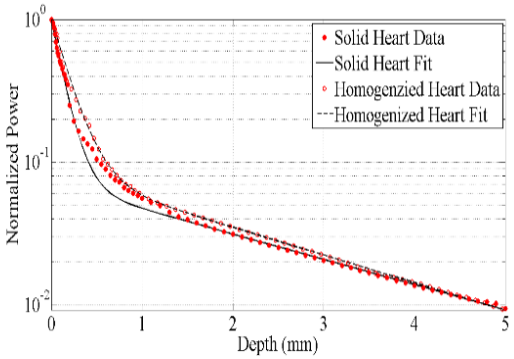

Figure 9-6: Comparison of $\psi(z)$ measured in the same heart, once as intact tissue and once after being homogenized, illuminated with 660nm light. The data was collected with the optrode made from the 25G needle and the FG200LCC optical fiber (0.22NA).

One can see that, after homogenization, the first exponent is largely preserved, which suggests that it is not the result of tissue heterogeneity. The average values of δ_1 and δ_2 obtained in intact and homogenized tissues (N = 100 and 5 respectively) at 660 nm are compared in Table 9-2. The differences are insignificant, suggesting that the process of homogenization does not affect the decay constants.

Table 9-2: Optical characteristics of intact and homogenized pig ventricular myocardium at 660nm.

Tissue	$\boldsymbol{\delta_1}$ **(mm)**	$\boldsymbol{\delta_2}$ **(mm)**
Intact	0.24 ± 0.05	2.1 ± 0.45
Homogenized	0.25 ± 0.10	2.1 ± 0.28

9.5 Monte Carlo Simulation Results

To determine a potential link between the fast exponent and the rate of decay of ballistic photons, we carried out MC simulations of forward directed flux measurements reproducing our experimental protocol Figure 9-7.

Figure 9-7a shows simulated $\psi(z)$ for two probes with different numerical apertures. One had a NA=0.22, matching the probe used in our experiments, while the second probe had a much smaller numerical aperture (NA=0.024) and consequently should accept much fewer diffuse photons. The parameters (see figure legend) were chosen to be close to those reported in the literature for pig myocardium [68]. As in the tissue experiments, both plots could be well approximated with the sum of two exponents (see fit error plots in Figure 9-7b).

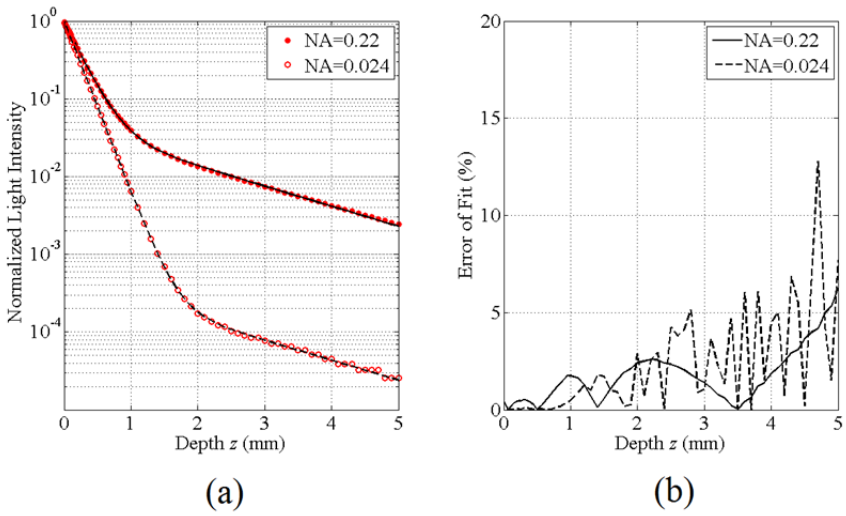

Figure 9-7: MC simulations of the FDF, $\psi(z)$, for fiber optic probes with large (NA=0.22) and small (NA=0.024) numerical apertures (a). The error of curve fit is shown on the right. (μ_s=5 mm^{-1}, μ_a=0.1 mm^{-1}, g=0.80) (b).

The slope of the slow exponent δ_2 is nearly identical in both cases (for NA=0.024 and for NA= 0.22). As expected, δ_2 corresponds to attenuation length reflecting the decay of diffuse photons:

$$\delta_2 = [3\mu_a\,(\mu_a + \mu_s{}')]^{-\frac{1}{2}} \qquad (9-4)$$

where μ_a and $\mu_s{}'$are the absorption and reduced scattering coefficients, respectively. Note that for equation $(9-4)$ to be valid $\mu_s' \gg \mu_a$ which is satisfied in our case.

We compared the δ_2 predicted by Eq. $(9-4)$ with the respective value obtained from fitting the $\psi(z)$. The value of $\mu_s{}'$ was calculated using the following equation

$$\mu_s' = \mu_s(1-g) \qquad (9-5)$$

where μ_s and g are the scattering coefficient and anisotropy, respectively. The difference between the predicted and the "experimental" values of δ_2 was within 3%.

The slopes of the fast exponents were also similar. Despite a 10-fold difference in the numerical aperture (NA=0.22 and NA=0.024), the values of δ_1 were respectively, 0.24 and 0.20. The only significant difference between the two cases was in the distribution of the weights between the fast and the slow exponents, which could be anticipated. Indeed, the weight of the slow exponent k_2 obtained using the probe with larger numerical aperture should be greater, because it accepts a larger portion of diffuse photons.

Notably, the shorter δ_1 obtained from the fit was very close to the rate of decay of ballistic photons $\delta_b = 0.196$ for given values of μ_a (0.1mm^{-1}) and μ_s (5 mm^{-1}):

$$\delta_b = (\mu_a + \mu_s)^{-1}. \qquad (9-6)$$

This result suggests that for a given set of optical characteristics the decay rate is not significantly influenced by diffuse photons despite relatively large numerical apertures of the probe. This was unexpected considering that the NA for measuring δ_b are usually 10^{-3} smaller than NA used in our experiments.

To determine how well this observation holds at different parameters, we carried out a series of MC simulations varying the scattering coefficient μ_s, the anisotropy coefficient, g, and the numerical aperture of the probe NA. The absorption coefficient was held constant at $\mu_a = 0.1\ \text{mm}^{-1}$ for all simulations, which is close to the upper limit reported in the literature for this parameter [74, 49]. The values of μ_s were varied in the range between $5\ \text{mm}^{-1}$ and $20\ \text{mm}^{-1}$ which are close to the lower and the upper values reported in the literature, respectively [68, 74]. Note that in all simulations $\mu_a << \mu_s$.

The simulation results are shown in Figure 9-8. Panel (a) shows the dependence of δ_1^{-1} on g at 3 different values of μ_s for a probe with NA=0.22 which we used in our experiments. Panel (b) shows the same data after normalization by μ_s. Panel (c) shows the effect of NA on δ_1^{-1} at different g for $\mu_s = 10\text{mm}^{-1}$.

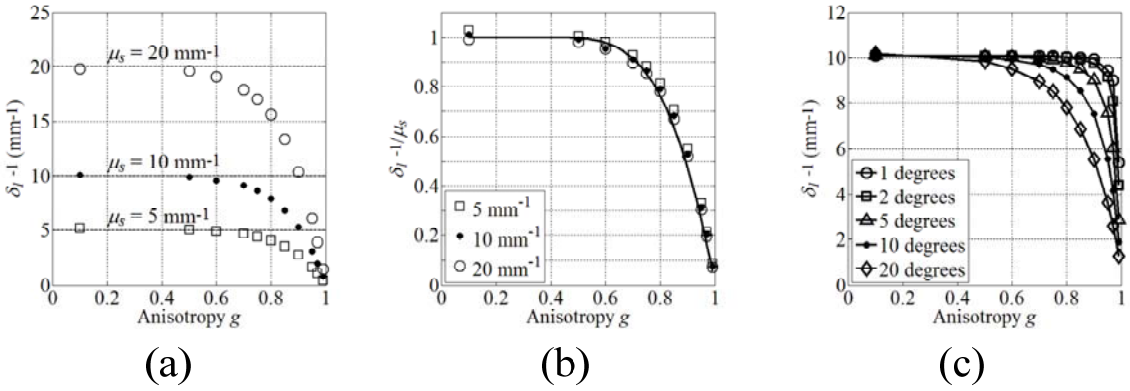

Figure 9-8: Data from the MC simulations. (a) The dependence of δ_1^{-1} on anisotropy g for $\mu_s = 5\text{mm}^{-1}$, 10mm^{-1}, and 20mm^{-1}. (b) The data from panel A replotted with δ_1^{-1} normalized by dividing by μ_s. (c) The dependence of δ_1^{-1} on anisotropy g for five different values of the optical probe maximum acceptance angle α (here, μ_s=10 mm^{-1}). In panels A and B, the numerical aperture of the probe was NA=0.22 ($\alpha \approx 10°$).The absorption coefficient was μ_a=0.1 mm^{-1} for all plots.

Our findings can be summarized as follows:

1. δ_1^{-1} is proportional to μ_s for all values of g tested. Indeed, Figure 9-8b shows that after normalization by μ_s the data points from the three sets in panel (a) fall on top of each other for all values of g.
2. At smaller values of g, $\delta_1^{-1} \approx \mu_s$. The range of g where this holds (the plateau region in Figure 9-8a and Figure 9-8b) is rather wide and becomes even wider as the NA of the probe becomes smaller (see Figure 9-8c). For g<0.7 and a probe with NA=0.22 the difference between $\delta_1^{-1}$and μ_s is less 10%.

3. The dependence of $\delta_1{}^{-1}$ on μ_s, g, and the optical probe's maximum acceptance angle, θ', (in radians) can be fitted using the following simple empirical formula:

$$\delta_1{}^{-1} = \mu_s \left[1 - \exp\left(\frac{g-1}{\theta' g}\right)\right] \qquad (9-7)$$

The accuracy of the fit can be appreciated from Figure 9-8, panel (b), which shows plots of Eq. $(9-7)$ for $\delta_1{}^{-1}/\mu_s$ versus the anisotropy coefficient g, superimposed on the normalized MC simulation data. Please note that all the above is valid for $\mu_s \gg \mu_a$, the condition which is usually satisfied in the cardiac and other biological tissues.

9.6 Using Forward Directed Flux measurements for estimating μ_s, μ'_s,and μ_a in Cardiac Tissue

In cardiac tissues, the reported values of g fall in the range between 0.78 [68] and 0.96 [74]. In pig myocardium, at 700nm it is reported to be around g=0.91 [49]. Using this value of g as well as the experimentally derived values of δ_1 and δ_2 we estimated the key optical parameters of the tissue such as μ_s, μ'_s,and μ_a and compared them with the respective values reported in the literature. The value of μ_s was obtained from formula $(9-7)$ by substituting the numerical value of g and the average value of δ_1 obtained in our experiments. Then we calculated the reduced scattering coefficient μ'_s, from Eq. $(9-5)$ using the earlier derived value of μ_s. Finally, we plugged μ'_s into Eq. $(9-4)$ and solved for μ_a. The respective results are shown in Table 9-3.

Table 9-3: Optical parameters of pig myocardial tissue At 660 nm

	μ_s	μ'_s	μ_a
Estimated	9.6	0.87	0.08
From Swartling et al. 2003	10.4	0.94	0.094

One can see that our estimates of all three parameters are consistent with the data reported in the literature obtained using completely different techniques. The difference between the values of μ_s, and μ'_s estimated from δ_1 and those reported in the literature is about 8% which is rather small and can be the result of myocardial heterogeneity. The differences in μ_a are larger (≈15%), yet still in the range of scatter of the experimentally derived values of δ_2 (see Table 9-1).

9.7 Using Forward-Directed Flux Measurements for Estimating μ'_s, μ_a, g, and μ_s in Intralipid-Based Tissue Phantoms

As we will show below, the values of μ'_s, μ_a, g, and μ_s can be obtained from forward directed flux even without prior knowledge of g. All we need is to repeat the measurements of $\psi(z)$ after adding a known amount of absorber. By comparing the changes in δ_2 after adding an absorber one can determine the values of μ'_s and the absorption coefficient μ_a. The method is known in the literature as the added absorber method [64]. Indeed, adding an absorber with a known absorption coefficient $\Delta\mu_a$ changes the attenuation length δ_2 to a new value $\delta_{2\Delta}$which can be expressed using the following formula:

$$\delta_{2\Delta} = [3(\mu_a + \Delta\mu_a)(\mu_a + \Delta\mu_a + \mu_s{}')]^{-\frac{1}{2}} \qquad (9-8)$$

Solving Eqs. $(9-4)$ and $(9-8)$ together yields the values of μ_a and μ_s'. Subsequently, one can solve Eq. $(9-5)$ and Eq. $(9-7)$ together to derive g, and μ_s. To illustrate the feasibility of this approach we carried out experiments in intralipid-based tissue phantoms.

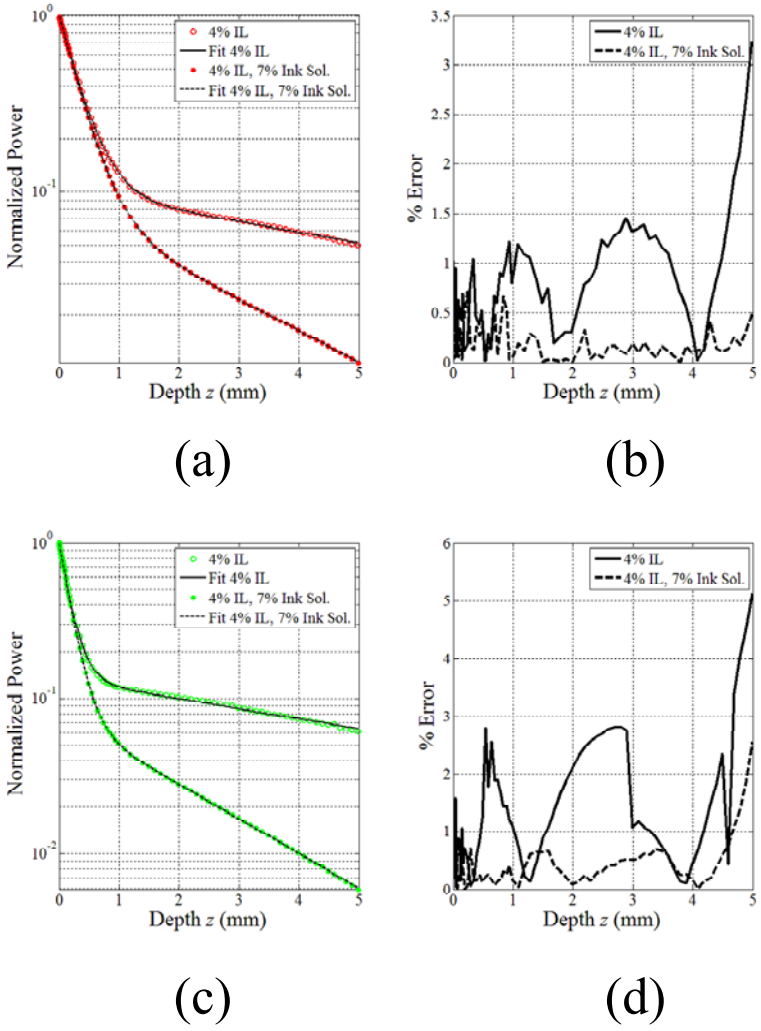

Figure 9-9: Forward-directed flux measurements in phantoms at 660 and 532nm. The data was collected with the optrode made from the 25G needle and the FG200LCC optical fiber (0.22NA).

Figure 9-9 shows sample plots of $\psi(z)$ in 4% intralipid phantom with and without absorber (India Ink) at 660 nm (panel A) and 532 nm (panel C). The data fit average error was within 1%-2% (panels b and d). The addition of absorber has a negligible effect on δ_1 because $\Delta\mu_a$ is very small. In contrast the values of δ_2 undergoes a significant change, which is roughly proportional to the square root of μ_a (see Eq. $(9-8)$)

Table 9-4 shows the values of $\delta_1, \delta_2,$ as well as estimated values of $\mu'_s,\ \mu_a,\ g,$ and μ_s for different phantoms at 660 nm and 532 nm. Notably, the values of g obtained in our experiments are within 8% of the values reported in the literature (0.64 for red and 0.73 for green) for this particular type of intralipid [63] as well as reproducing the increase in g caused by the reduction of the illumination wavelength from 660 nm to 532 nm. To compare our values of μ_s with those reported in the literature we also estimated values of μ_s for 20% emulsion intralipid under the assumption that μ_s is proportional to intralipid concentration. Using the scattering coefficient for undiluted intralipid given in the literature ($\mu_s = 70\text{mm}^{-1}$ for red light and 123mm^{-1} for green light), we can expect $\mu_s = 5.6\text{mm}^{-1}$ for red light and $\mu_s = 9.84\text{mm}^{-1}$ for green light at 8% concentration. The estimated values are close to the measured values in Table 9-4.

Table 9-4: Optical characteristics of intralipid phantoms at 660nm and 532nm derived from the forward directed flux measurements.

λ (nm)	Concentrations	δ_1 (mm)	δ_2 (mm)	μ_a (mm^{-1})	μ_s' (mm^{-1})	μ_s (mm^{-1})	g
660	8% IL	0.17	5.30	0.006	1.83	5.91	0.69
	8% IL, 7% Ink	0.18	1.79	0.055		5.62	0.67
532	8% IL	0.10	5.85	0.003	2.99	11.5	0.74
	8% IL, 7% Ink	0.10	1.33	0.066		11.5	0.74

9.8 A Simplified Method for Extracting μ_a, μ_s, and g for Media with Low Anisotropy

The following method was developed before the above method. It could be considered an early prototype of the method described above. This approach involves approximating the fast exponent as δ_b from equation $(9-6)$. We can see from figure Figure 9-8, that this approach will only work for small values of g, roughly less than 0.70 for a probe with numerical aperture of 0.22.

In Figure 9-9, notice the exponent with the short spatial constant near the surface of the medium. If this is assumed to be approximately the total attenuation coefficient μ_t, we can modify our added absorber experiment to get μ_s and g. The fast exponent can then be estimated to

$$\delta_1 = \frac{1}{\mu_s + \mu_a} \qquad (9-9)$$

and

$$\delta_{1,a} = \frac{1}{(\mu_s + \mu_a)(1 - C_{ink}) + \Delta\mu_a} \qquad (9-10)$$

for media without and with absorber, respectively. Either of the above equations can be used to get the parameter μ_s. The value of g can then be calculated using the well-known relation $\mu_s' = (1-g)\mu_s$.

Table 9-5: Optical characteristics of intralipid phantoms at 660nm

Concentrations	δ_1 (mm)	δ_2 (mm)	μ_a (mm^{-1})	μ_s (mm^{-1})	g	μ_s' (mm^{-1})
2% IL	0.65	12.02	0.005	1.61	0.70	0.49
2% IL, 7% Ink	0.63	3.39	0.054	1.54	0.69	
4% IL	0.32	7.23	0.007	3.15	0.70	0.94
4% IL, 7% Ink	0.31	2.45	0.056	3.14	0.70	
8% IL	0.17	5.30	0.006	5.91	0.69	1.83
8% IL, 7% Ink	0.18	1.79	0.055	5.62	0.67	

Our calculated values of g and μ_s were in good agreement with those determined by Michels et al. [63]. In particular, our experimental values for $g = 0.69 \pm 1.5\%$ were close to their experimental value ($g = 0.64$). By using the value $\mu_s = 70\text{mm}^{-1}$ for undiluted intralipid illuminated by 660nm light, we can adjust for the concentration of intralipid that we used in our experiments. This yields $\mu_s = 1.4\text{mm}^{-1}$ for 2%, $\mu_s = 2.8\text{mm}^{-1}$ for 4%, and $\mu_s = 5.6\text{mm}^{-1}$ for 8% intralipid concentration. This shows that our calculated values of μ_s varied less than 15% from the values of μ_s determined from Michels et al. [63].

Table 9-6: Optical characteristics of intralipid phantoms at 532 nm

Concentrations	δ_1 (mm)	δ_2 (mm)	μ_a (mm^{-1})	μ_s (mm^{-1})	g	μ_s' (mm^{-1})
2% IL	0.40	6.53	0.010	2.49	0.70	0.755
2% IL, 7% Ink	0.38	2.44	0.073	2.57	0.71	
4% IL	0.17	6.78	0.006	5.77	0.77	1.30
4% IL, 7% Ink	0.18	1.96	0.069	5.39	0.76	
8% IL	0.10	5.85	0.003	10.2	0.71	2.99
8% IL, 7% Ink	0.10	1.33	0.066	9.73	0.69	

The predicted value of g for 532 nm ($g = 0.72 \pm 3\%$) is larger than that of 660 nm, which is in good agreement with the value of g = 0.73 reported by Michels et al. at 532 nm [63]. We can compare our results to the reported value of $\mu_s = 123\text{mm}^{-1}$ for undiluted intralipid and 532nm light by adjusting for the concentration used in our experiments. The value of μ_s as predicted by [63] is then 2.46mm^{-1} for 2%, 4.92mm^{-1} for 4%, and 9.84mm^{-1} for 8% IL. With the exception of the 4% IL experiment, the measured μ_s was within less than 5% of the value determined by Michels et al [63]. These experiments show that even with only the approximation given by (4-29), we can still obtain reasonably accurate results.

Chapter 10 An Algorithm for Solving the Radiative Transfer Equation

The goal of this chapter is to determine the photon distribution along a single path through a medium which is uniformly illuminated on one side as shown in Figure 10-1. To do so, we will solve the radiative transfer equation (RTE) numerically in 1-D.

10.1 Solving the RTE Numerically

Key Assumptions:

- The light at a given depth z is uniformly distributed throughout the medium for all distances r.
- Backscattered light is negligible and can be ignored. This means the algorithm will have higher accuracy with higher values of g.
- Only light from adjacent scattering events effects the photon density along the z-axis.

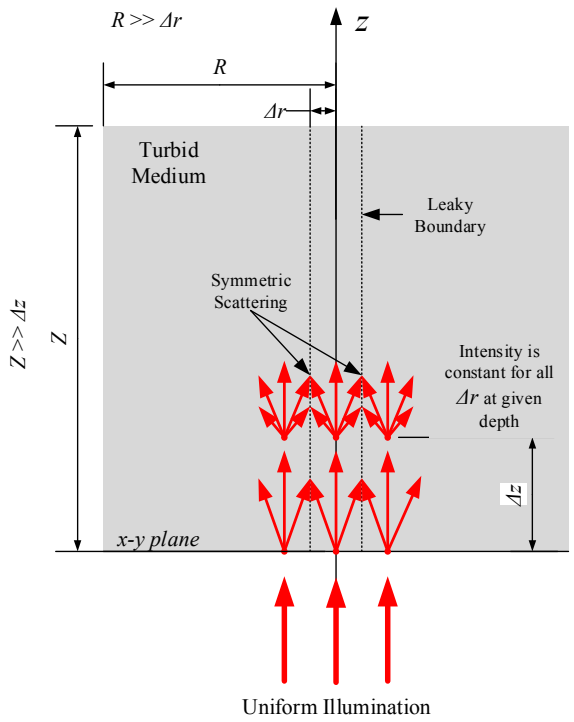

Figure 10-1: Diagram of photon scattering in medium

- Flux only changes along the z-direction, anything that exits along the r-direction is assumed to re-enter the differential element through the leaky boundary as shown in the figure. Thus the net flux along the r-direction is always null.
- The light intensity just outside the medium is the same as the light intensity just inside the medium, i.e. $I_v(z = 0^-) = I_v(z = 0^+)$. Thus the boundary condition is the continuity type.

Begin with radiative transfer equation [55]

$$\frac{1}{c}\frac{d}{dt}I_v(\mathbf{r},\hat{\mathbf{\Omega}},t) + \hat{\mathbf{\Omega}}\cdot\nabla I_v(\mathbf{r},\hat{\mathbf{\Omega}},t)$$

$$= \mu_s\int_{4\cdot\pi} f(\hat{\mathbf{\Omega}},\hat{\mathbf{\Omega}}',\mathbf{r},t)\, I_v(\mathbf{r},\hat{\mathbf{\Omega}}',t)\, d\Omega' - (\mu_a+\mu_s)\, I_v(\mathbf{r},\hat{\mathbf{\Omega}},t) + j_v^a(\mathbf{r},\hat{\mathbf{\Omega}},t) \qquad (10-1)$$

Assuming steady-state operation the time dependent term goes to 0.

$$\frac{1}{c}\frac{d}{dt}I_v(\mathbf{r},\hat{\mathbf{\Omega}},t) = 0$$

If we are only concerned with transmittance and there is no fluorescence, then the fluorescence term goes to 0.

$$j_v^a(\mathbf{r},\hat{\mathbf{\Omega}},t) = 0$$

These simplifications reduce equation $(10-1)$ to

$$\hat{\mathbf{\Omega}}\cdot\nabla I_v(\mathbf{r},\hat{\mathbf{\Omega}}) = \mu_s\int_{4\cdot\pi} f(\hat{\mathbf{\Omega}},\hat{\mathbf{\Omega}}',\mathbf{r})\, I_v(\mathbf{r},\hat{\mathbf{\Omega}}')\, d\Omega' - (\mu_a+\mu_s)\, I_v(\mathbf{r},\hat{\mathbf{\Omega}}) \qquad (10-2)$$

Assuming azimuthal and radial symmetry for I_v, the above equation then becomes

$$\widehat{\boldsymbol{\Omega}} \cdot \nabla I_v(z,\theta) = \mu_s \int_{4\cdot\pi} f\left(\widehat{\boldsymbol{\Omega}}, \widehat{\boldsymbol{\Omega}}', \mathbf{r}\right) I_v(z,\theta')\, d\Omega' - (\mu_a + \mu_s)\, I_v(z,\theta) \qquad (10-3)$$

For spherical coordinates, the integral becomes

$$\mu_s \int_0^{2\pi} \int_0^{\pi} f\left(\widehat{\boldsymbol{\Omega}}, \widehat{\boldsymbol{\Omega}}', \mathbf{r}\right) I_v(z,\theta')\ \sin(\theta')\, d\theta' d\phi' \qquad (10-4)$$

For the phase function $f\left(\widehat{\boldsymbol{\Omega}}, \widehat{\boldsymbol{\Omega}}', \mathbf{r}\right)$ we will use the Henyey-Greenstein function, which is defined below [76]. Note that the phase function is the same at any point in space within the medium, so the **r** term will be dropped.

$$f(\theta) = \frac{1}{4\pi} \frac{1-g^2}{(1+g^2-2g\cos(\theta))^{3/2}} \qquad (10-5)$$

The function $f(\theta)$ can be plotted in 3-D as shown below in Figure 10-2. Note that for the form of the equation shown above, the incident photons are assumed to be traveling at an angle $\theta' = 0°$.

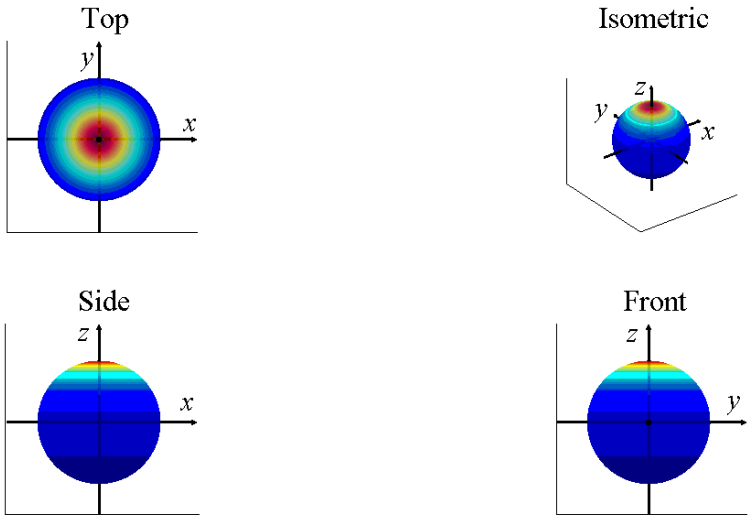

Figure 10-2: Orthogonal and isometric views of the Henyey-Greenstein phase function for $g = 0.50$ plotted on the surface of a unit sphere. Here the incident photons enter at $\theta' = 0°$.

The phase function is defined as the scattered intensity at a particular angle θ relative to the incident beam and normalized by the integral of the scattered intensities at all angles [58, p. 693]. Therefore, if the incident photon is not traveling at an angle $\theta' = 0°$, then function must be rotated in 3 dimensional space. We can modify the original phase function in equation $(10-5)$ to account for non-zero θ'. The result is shown below.

$$f(\theta, \phi, \theta', \phi') = \frac{1}{4\pi} \frac{1 - g^2}{\left(1 + g^2 - 2g(\cos(\theta)\cos(\theta') + \cos(\phi - \phi')\sin(\theta)\sin(\theta'))\right)^{3/2}} \quad (10-6)$$

It is important to note, that θ in equation $(10-6)$ is an absolute measure of the zenith angle relative to the z-axis and not relative to the direction of the incident photons. This is done to simplify the algorithm presented later on. Figure 10-3 shows an example of the phase function plotted on the surface of a sphere for photons incident at $\theta' = 45°$ and $\phi' = 0°$.

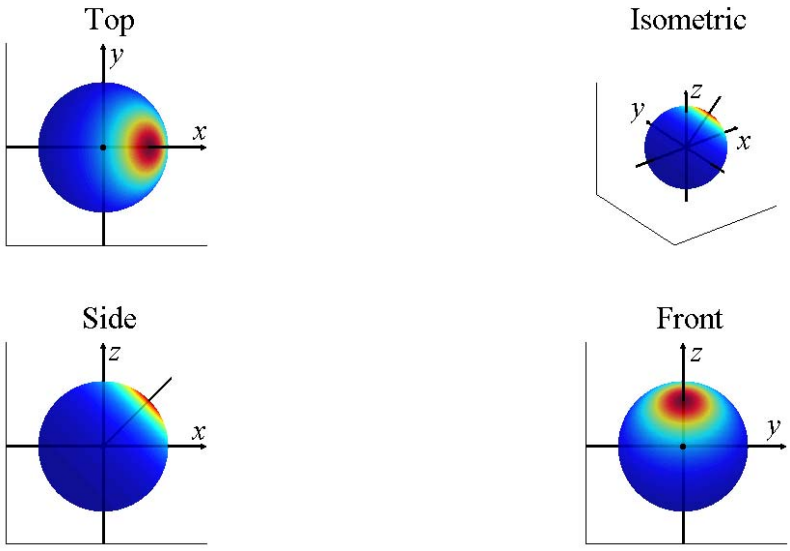

Figure 10-3: Orthogonal and isometric views of the Henyey-Greenstein phase function for $g = 0.50$ plotted on the surface of a unit sphere. Here the incident photons enter at $\theta' = 45°$ and $\phi' = 0°$.

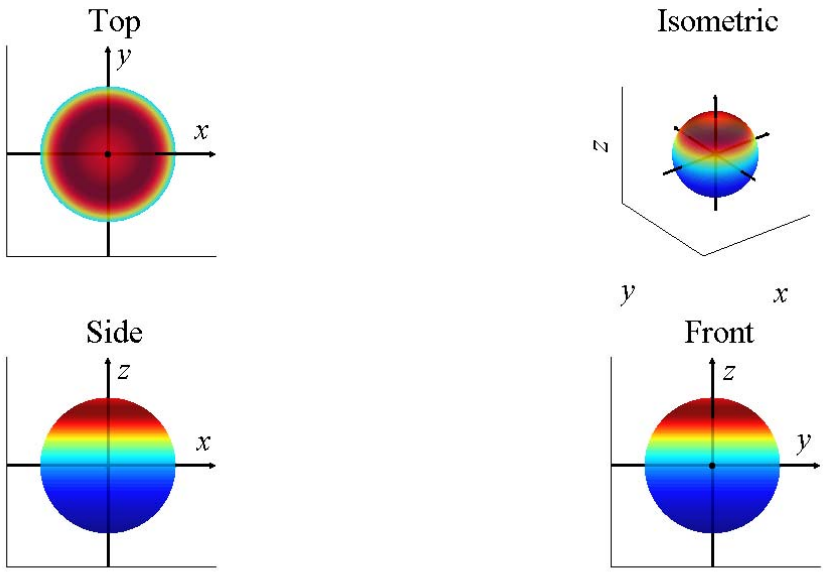

Figure 10-4: Orthogonal and isometric views of the Henyey-Greenstein phase function for $g = 0.50$ plotted on the surface of a unit sphere. Here the incident photons enter at $\theta' = 45°$ and all angles of ϕ'.

Following the assumption that for a given θ' the amount of incident photons is the same for all ϕ', we can also make the assumption that for a given θ, all the amount of scattered photons is the same for all ϕ. This can be seen graphically in Figure 10-4. We can therefore integrate over ϕ' and ϕ' leaving us with scattered light that is a function of θ and θ'. The expression for integrating over the azimuthal angles is shown below.

$$dE_{ss}(\theta, \theta') = \mu_s \int_0^{2\pi} \int_0^{2\pi} f(\theta, \phi, \theta', \phi') d\phi \, d\phi' \qquad (10-7)$$

Unfortunately, the phase function in $(10-6)$ cannot be integrated analytically. We will therefore have to compute the integral in $(10-7)$ using numerical integration. Begin by discretizing the phase function

$$f[i_\theta, i_\phi, i_{\theta'}, i_{\phi'}] = f\left((i_\theta + 0.5)\Delta\theta, (i_\phi + 0.5)\Delta\phi, (i_{\theta'} + 0.5)\Delta\theta', (i_{\phi'} + 0.5)\Delta\phi'\right)$$

where $i_\theta = 0 \rightarrow N_\theta - 1$, $i_\phi = 0 \rightarrow N_\phi - 1$, and $i_{\theta'} = 0 \rightarrow N_{\theta'} - 1$. The numerical integration then takes the form shown below.

$$f[i_\theta, i_{\theta'}] = \frac{1}{2\pi} \sum_{i_{\phi'}=0}^{N_{\phi'}-1} \sum_{i_\phi=0}^{N_\phi-1} f\left[i_\theta, i_\phi, i_{\theta'}, i_{\phi'}\right] \Delta\phi \, \Delta\phi' \;, \forall \, i_\theta, i_{\theta'} \qquad (10-8)$$

Using the same procedure, we can discretize the solid angle as well

$$\Delta\Omega\left[i_\theta, i_\phi\right] = \left(\frac{\pi}{180^\circ}\Delta\phi\right) 2\sin\left((i_\theta + 0.5)\Delta\theta\right)\sin(\Delta\theta/2)\,;$$

Discretize the integral

$$dE_{ss}[i_\theta, i_{\theta'}] = \mu_s \sum_{i_{\theta'}=0}^{N_{\theta'}-1} f[i_\theta, i_{\theta'}] \sin\left((i_{\theta'} + 0.5)\Delta\theta'\right)\sin(\Delta\theta'/2)\, I_\nu[i_z, i_{\theta'}]$$

Discretize the rest of the radiative transfer equation $(10-1)$

$$\frac{I_\nu[i_z + 1, i_\theta] - I_\nu[i_z, i_\theta]}{\Delta z} = dE_{ss}\left[i_\theta, i_\phi\right] - (\mu_a + \mu_s) I_\nu[i_z, i_\theta]$$

Solve for $I_\nu[i_z + 1, i_\theta]$

$$I_\nu[i_z + 1, i_\theta] = \Delta z dE_{ss}\left[i_\theta, i_\phi\right] - (\mu_a + \mu_s)\Delta z I_\nu[i_z, i_\theta] + I_\nu[i_z, i_\theta]$$

Pseudo Code:

// Initialize Constants: Total depth Z, differential path length Δz, differential angle $\Delta\theta$

$N_Z = Z/dz;$ // Number of steps along depth Z

$N_\theta = 180^\circ/\Delta\theta;$ // Number of zenith angle divisions

$N_\phi = 360°/\Delta\phi;$ // Number of azimuthal angle divisions

$N_{\theta'} = N_\theta;$ // Number of zenith angles for incident photons

$N_{\phi'} = N_\phi;$ // Number of azimuthal angles for incident photons

// Initialize input intensity

for $i_{\theta'} = 0 \rightarrow N_{\theta'} - 1$

// Set the initial values of I_ν to the angular distribution of the input light source

$I_\nu[0, i_{\theta'}] = I_\nu(0, \Delta\theta * i_{\theta'});$ // Discretize continuous function of intensity $I_\nu(\theta)$

end

// Discretize phase function

for $i_{\theta'} = 0 \rightarrow N_{\theta'} - 1$

for $i_{\phi'} = 0 \rightarrow N_{\phi'} - 1$

for $i_\theta = 0 \rightarrow N_\theta - 1$

for $i_\phi = 0 \rightarrow N_\phi - 1$

// Discretize phase function

$f[i_\theta, i_\phi, i_{\theta'}, i_{\phi'}] = f\left((i_\theta + 0.5)\Delta\theta, (i_\phi + 0.5)\Delta\phi, (i_{\theta'} + 0.5)\Delta\theta', (i_{\phi'} + 0.5)\Delta\phi'\right);$

end

end

end

end

// Integrate over ϕ and ϕ'

$$f[i_\theta, i_{\theta'}] = \frac{1}{2\pi} \sum_{i_{\phi'}=0}^{N_{\phi'}-1} \sum_{i_\phi=0}^{N_\phi-1} f[i_\theta, i_\phi, i_{\theta'}, i_{\phi'}]\, \Delta\phi\, \Delta\phi'$$

// Solve the RTE

for $i_z = 0 \rightarrow N_Z - 1$

// Compute distribution of scattered light

// Each incident ray at angle θ' produces a distribution of scattered light over all angles θ and ϕ

for $i_{\theta'} = 0 \rightarrow N_\theta - 1$ // for each $\widehat{\boldsymbol{\Omega}}'$ (or θ') of incident photons

for $i_\theta = 0 \rightarrow N_\theta - 1$

$dE_{ss}[i_{\theta'}, i_\theta] = \mu_s * f[i_\theta, i_{\theta'}] * I_v[i_z, i_{\theta'}] * \sin\big((i_{\theta'} + 0.5)\Delta\theta'\big)\sin(\Delta\theta'/2)$;

end

end

// For each discrete angle $\theta[i_\theta]$ calculate the intensity I_v at the next step

for $i_\theta = 0 \rightarrow N_\theta - 1$

// The summation integrates over θ' for each value of θ

$$I_v[i_z + 1, i_\theta] = \Delta z \sum_{i_{\theta'}=0}^{N_\theta - 1} dE_{ss}[i_{\theta'}, i_\theta] - (\mu_a + \mu_s)\Delta z I_v[i_z, i_\theta] + I_v[i_z, i_\theta];$$

end

end

10.2 Simulation Results

The comparison between the radiative transfer equation solver and the Monte Carlo simulation yielded a close match for the parameter δ_1. Figure 10-5 shows a plot of δ_1 vs the anisotropy parameter g, the scattering coefficient was set to $\mu_s = 5\text{mm}^{-1}$, 10mm^{-1}, and 20mm^{-1}. The absorption coefficient was set to $\mu_a = 0.1\text{mm}^{-1}$ and the acceptance angle of the probe was set to $10°$ for all simulations. The spatial resolution Δz and the angle resolution $\Delta\theta$ for each RTE simulation are shown in Table 10-1 along with the corresponding values of μ_s and g. The Monte Carlo simulation data presented here

are the same presented in [77]. Here we can see a good match between δ_1 obtained using the RTE and that using the MC simulations. The error is highest at low values of g, likely because the approximation used to solve the RTE work best when light is scattered in the forward direction.

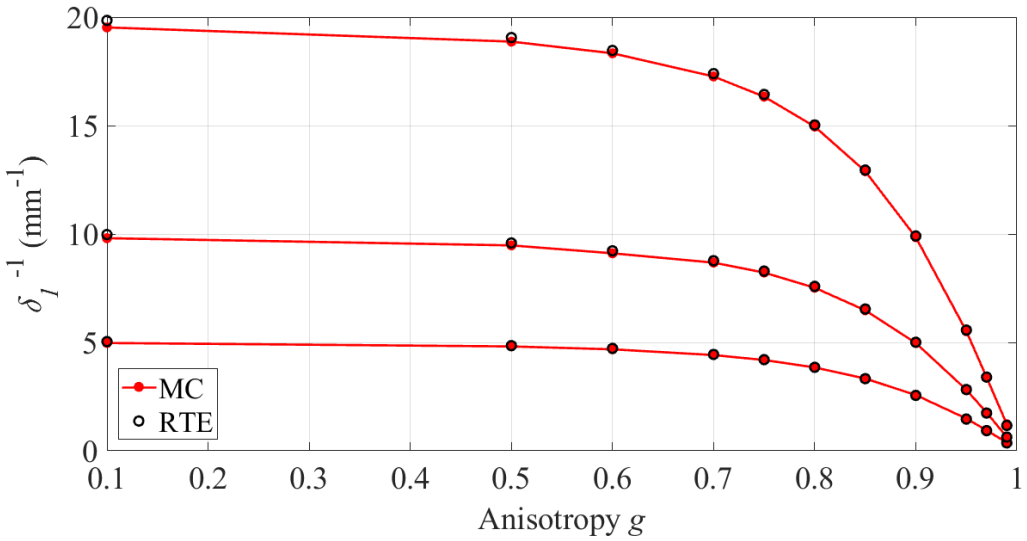

Figure 10-5: Plot of δ_1^{-1} vs g for Monte Carlo simulations and RTE simulations with $\mu_s = 5\text{mm}^{-1}$, 10mm^{-1}, and 20mm^{-1}. The absorption coefficient was set to $\mu_a = 0.1\text{mm}^{-1}$ and the acceptance angle was set to 10° for all simulations.

Table 10-1: Parameters used in RTE model for comparison with Monte Carlo

μ_s (mm^{-1})	g	Δz (μm)	$\Delta\theta$ (°)	μ_s (mm^{-1})	g	Δz (μm)	$\Delta\theta$ (°)
5	0.10	0.2	0.5	10	0.10	0.1	0.5
	0.50	0.4	0.5		0.50	0.1	0.5
	0.60	0.2	0.5		0.60	0.1	0.5
	0.70	2.0	0.5		0.70	1.0	0.5
	0.75	2.0	0.5		0.75	1.0	0.5
	0.80	2.0	0.5		0.80	1.0	0.5
	0.85	2.0	0.1		0.85	1.0	0.5
	0.90	2.0	0.1		0.90	1.0	0.5
	0.95	2.0	0.1		0.95	1.0	0.5
	0.97	2.0	0.1		0.97	1.0	0.5
	0.99	2.0	0.1		0.99	1.0	0.1
μ_s (mm^{-1})	g	Δz (μm)	$\Delta\theta$ (°)				
20	0.10	0.1	0.5				
	0.50	0.1	0.5				
	0.60	0.1	0.5				
	0.70	0.5	0.5				
	0.75	0.5	0.5				
	0.80	0.5	0.5				
	0.85	0.5	0.5				
	0.90	0.5	0.5				
	0.95	0.5	0.5				
	0.97	0.5	0.5				
	0.10	0.1	0.5				

Figure 10-6 shows samples of the RTE and MC simulations for selected μ_s and g values, the acceptance angle was chosen to be $10°$. This series of plots shows that while the fit near the surface is quite accurate ($z < 1\text{mm}$), further from the surface the curves begin to diverge. We also see that for higher values of g, the deviation is less, and the RTE and MC simulations produce similar data.

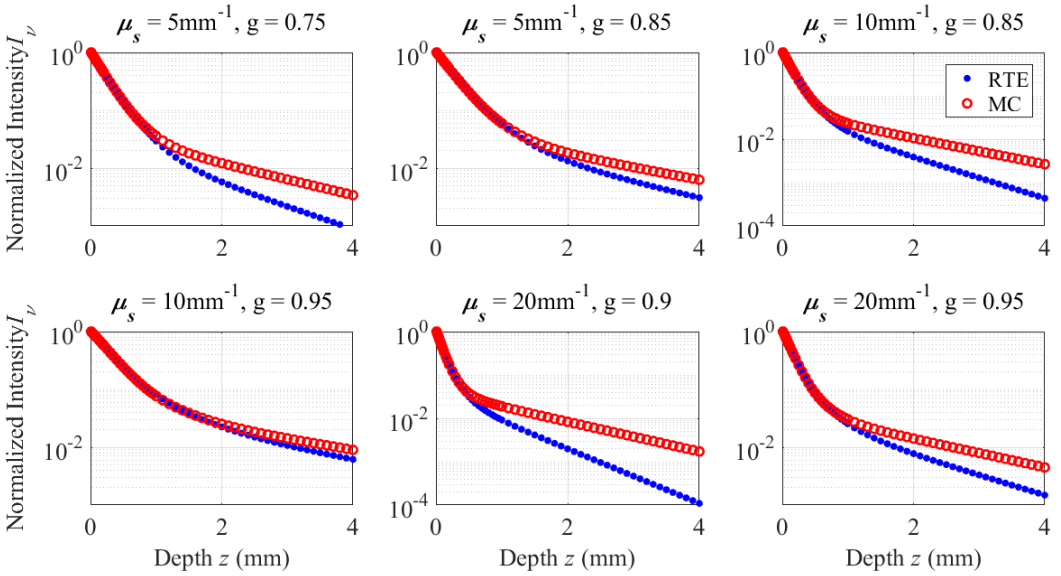

Figure 10-6: Sample plots of forward-directed flux for MC and RTE simulations. The curves are for the parameter listed at the top of each figure and acceptance angle 10°. The spatial and angular resolution for each can be found in Table 10-1.

Figure 10-7 shows the normalized intensity as a function of zenith angle at selected depths in the medium for both the MC and RTE simulations. For both simulations $\mu_a = 0.1\text{mm}^{-1}$, $\mu_s = 10\text{mm}^{-1}$, and $g = 0.90$. Here we see that the numerical solution of the RTE is in close agreement with the MC simulations.

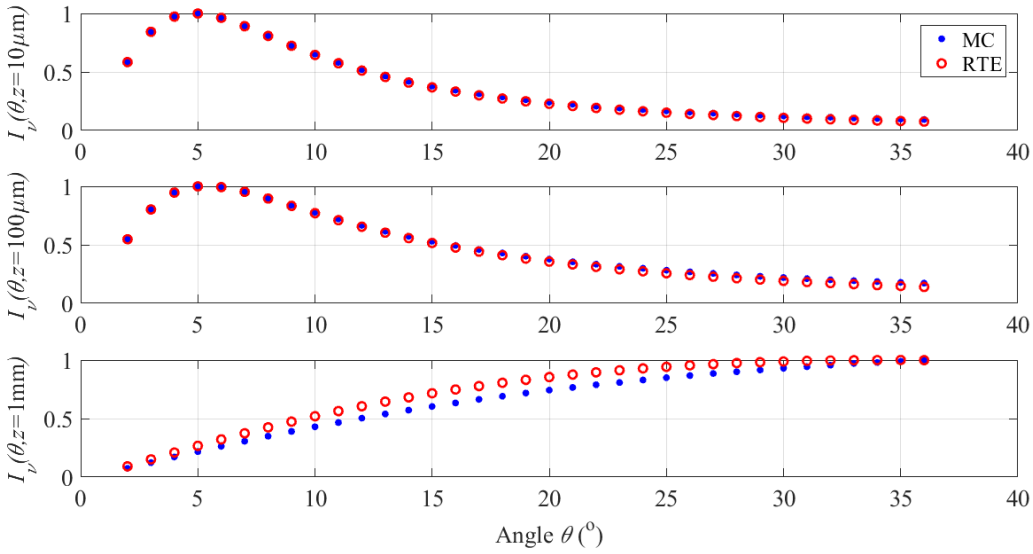

Figure 10-7: Plot of normalized intensity vs zenith angle at depths $z = 10\mu m$, $100\mu m$, and 1mm for RTE and MC simulations. The parameters chosen for this simulation were $\mu_s = 10 mm^{-1}$ and $g = 0.90$.

These preliminary results show that it is possible to solve the RTE for the case of forward-directed flux measurements with a simple algorithm. This means that the fast spatial constant δ_1 can be determined quickly and accurately without need to modify Monte Carlo code.

Chapter 11 Discussion and Conclusions

In this study, we use a thin custom made fiber optic probe to investigate the forward directed flux (FDF) with a 10μm resolution in pig myocardial wall. The measurements were carried out at 660 nm and 532 nm which represent the most common range of the excitation and emission wavelengths of fluorescent voltage-sensitive and Ca_i^{2+}-sensitive probes used in cardiac electrophysiology [78, 2]. We show that the FDF can be described as the sum of two exponents with distinctly different decay rates. In the vicinity of the illuminated surface we observed a rapid decay of the light intensity with the decay constant δ_1 in the range 100 - 200 microns for green and red light respectively. The slower exponent δ_2 had a decay constant 5-10 times longer. A similar effect was observed in homogenized cardiac tissue and intralipid-based tissue phantoms.

A similar two exponential decay was previously observed in collimated transmission experiments [50]. In these experiments the fast exponent represents the decay of ballistic photons. However, this interpretation does not fully apply to our experimental data. There are the following two major differences between collimated transmittance and our experiments: a) in our experiments the probe is inside and not outside the specimen; b) the numerical aperture of the optical fiber in our experiments was about two orders of magnitude larger than the numerical aperture typically used in collimated transmittance experiments. Thus, it would be reasonable to expect that in our experiments δ_1 is affected by the gradient of diffuse photons near the surface.

It is notable that previous measurements of forward-directed flux did not report the fast exponent [78, 64] and describe only the slow exponent. The decay constant of the

slow exponent δ_2 is typically referred to in the literature as the "attenuation length" [75, 78]. The value of δ_2 measured in our cardiac tissue experiments is comparable to the attenuation lengths reported in the literature [74, 78, 79] at similar wavelengths. Considering that δ_1 is on the order of 100μm, the fast exponent can be easily missed, unless the probe is advanced at very small increments near the surface. In our experiments, the increments of *z* near the surface were as low as 10μm, which enabled us to reconstruct the fast exponent.

To determine the factors affecting the rate of the fast exponent we reproduced our experiments using Monte Carlo (MC) simulations. The FDF was evaluated in the physiological range of absorption and scattering coefficients, variable anisotropy parameter *g*, and different numerical apertures of the probe.

One of the unexpected findings was that despite the relatively large numerical aperture of the probe and the existence of a gradient of diffuse photons near the illuminated surface, as long as *g* was not too large, the decay constant δ_1 still determined the rate of decay of the ballistic photons. The MC simulations show that in turbid media with $g < 0.7$ the value δ_1^{-1} yields a quite accurate (error less than 10%) estimate of μ_s. Thus, simple FDF measurements using a fiber-optic probe provide an alternative to the more sophisticated methods that are usually used to assess the scattering coefficient. Specifically, such an approach would be useful for estimating μ_s in lipid-based phantoms which are characterized with relatively low anisotropy parameter [63].

It is interesting that the dependence of the rate of the fast exponent on the scattering coefficient, the anisotropy parameter *g*, and the numerical aperture of the probe can be linked by a simple empirical formula without any adjustable parameters. The

formula predicts MC simulation results in a broad range of parameters. It works particularly well at $NA \leq 0.22$. We started observing deviations only at NA > 0.34. We tested the predictions of the formula in the cardiac tissue and in well characterized intralipid-based tissue phantoms. The tests results were in agreement with the data reported in the literature.

Our findings pave the way to an alternative method for determining major optical parameters in turbid media based exclusively on forward-directed flux measurements. The new approach allows the utilization of the same simple experimental setup for measuring all key optical parameters including anisotropy *g.* Previously, however, measurements of μ_s and g required completely different experimental setups than those used for measurements of μ_a and μ_s'. The simplicity of the experimental approach described here as well as the ability to utilize the same setup for all measurements can make it a viable alternative to existing methods. While the feasibility of the new approach was tested only in intralipid-based tissue phantoms. It would be reasonable to assume that it would work in homogenized tissues as well. Indeed, our data suggest that the values of δ_1 and δ_2 in the homogenized tissues are not significantly different from the respective values in the intact tissue (see Table 9-2).

The results of our work sheds a new light on light transport in the vicinity of the myocardial surface. This can be particularly useful for the interpretation of the optical recordings of cardiac excitation obtained using voltage-sensitive dyes, known as optical mapping, as well as for the development of 3D tomographic approaches [80]. One of the potential applications of our findings is obtaining an accurate description of voltage

distribution in the vicinity of the myocardial surface during strong defibrillation shocks. According to theoretical models the transmembrane voltage should fall off rapidly with depth [79], which makes the detailed knowledge of light transport near the illuminated surface critically important for accurate description of this phenomenon. Our study adds a potentially useful tool to the arsenal of existing methods which could help to fill this gap.

APPENDIX 1. Survey of Commercially Available Photodiodes

Part #	Manufacturer	NEP		Q.E.	c_j		r_{sh} (MΩ)
		Value ($\mathrm{pW}/\sqrt{\mathrm{Hz}}$)	V_R (V)		Value (pF)	V_R (V)	
SD200-11-21-241	Advanced Photonics	0.086	5	0.76	345	0	70
SD172-11-31-221	Advanced Photonics	0.200	5	0.76	82	0	-
SD445-11-21-305	Advanced Photonics	0.15	5	0.76	1490	0	15
PDB-C107	Advanced Photonics	0.3	0	0.85	100	10	1,000
PDB-C109	Advanced Photonics	0.5	0	0.85	120	10	100
PDB-C110	Advanced Photonics	0.3	0	0.85	300	10	30
PDB-C134	Advanced Photonics	0.18	100	0.76	6	10	2,000
PDB-C139	Advanced Photonics	0.02	10	0.76	18	10	500
PDB-C142	Advanced Photonics	0.02	10	0.76	18	10	500
PDB-C152SM	Advanced Photonics	0.15	10	0.72	2.5	5	500
PDB-C156	Advanced Photonics	0.044	10	0.76	10	10	150
PDB-C158	Advanced Photonics	0.044	10	0.76	15	10	150
PDB-C158F	Advanced Photonics	0.024	10	0.70	15	10	150

Part #	Manufacturer	NEP		Q.E.	c_j		r_{sh} (MΩ)
		Value ($\mathbf{pW/\sqrt{Hz}}$)	V_R (V)		Value (pF)	V_R (V)	
PDB-C160SM	Advanced Photonics	0.041	10	0.88	72	0	250
PDB-C171SM	Advanced Photonics	0.04	10	0.94	25	3	-
SD057-11-21-011	Advanced Photonics	0.028	5	0.76	28	0	800
SD057-14-21-011	Advanced Photonics	0.010	5	0.76	28	0	1,600
S1087	Hamamatsu	-	-	0.66	200	0	250,000
S1087-01	Hamamatsu	-	-	0.75	200	0	250,000
S1133	Hamamatsu	-	-	0.66	700	0	100,000
S1133-01	Hamamatsu	-	-	0.75	700	0	100,000
S1133-14	Hamamatsu	-	-	0.69	200	0	50,000
S1223	Hamamatsu	0.0094	20	0.78	70	0.1	2,857
S1223-01	Hamamatsu	0.0130	20	0.78	150	0.1	1,667
S1226-18BQ	Hamamatsu	0.0016	-	0.62	35	0	50,000
S1226-18BK	Hamamatsu	0.0016	-	0.62	35	0	50,000
S1226-5BQ	Hamamatsu	0.0025	-	0.62	160	0	20,000
S1226-5BK	Hamamatsu	0.0025	-	0.62	160	0	20,000
S1226-44BQ	Hamamatsu	0.0036	-	0.62	500	0	10,000
S1226-44BK	Hamamatsu	0.0036	-	0.62	500	0	10,000
S1226-8BQ	Hamamatsu	0.0050	-	0.62	1200	0	5,000
S1226-8BK	Hamamatsu	0.0050	-	0.62	1200	0	5,000
S1227-16BQ	Hamamatsu	0.0025	-	0.62	170	0	20,000
S1227-16BR	Hamamatsu	0.0021	-	0.74	170	0	20,000
S1227-33BQ	Hamamatsu	0.0025	-	0.62	160	0	20,000

Part #	Manufacturer	NEP		Q.E.	c_j		r_{sh} (MΩ)
		Value ($\mathbf{pW/\sqrt{Hz}}$)	V_R (V)		Value (pF)	V_R (V)	
S1227-33BR	Hamamatsu	0.0021	-	0.74	160	0	20,000
S1227-66BQ	Hamamatsu	0.0050	-	0.62	950	0	5,000
S1227-66BR	Hamamatsu	0.0042	-	0.74	950	0	5,000
S1227-1010BQ	Hamamatsu	0.0080	-	0.62	3000	0	2,000
S1227-1010BR	Hamamatsu	0.0067	-	0.74	3000	0	2,000
S1227-16BQ	Hamamatsu	0.0025	-	0.62	170	0	20,000
S1227-16BR	Hamamatsu	0.0021	-	0.74	170	0	20,000
S1227-33BQ	Hamamatsu	0.0025	-	0.62	160	0	20,000
S1227-33BR	Hamamatsu	0.0021	-	0.74	160	0	20,000
S1227-66BQ	Hamamatsu	0.0050	-	0.62	950	0	5,000
S1227-66BR	Hamamatsu	0.0042	-	0.74	950	0	5,000
S1227-1010BQ	Hamamatsu	0.0080	-	0.62	3000	0	2,000
S1227-1010BR	Hamamatsu	0.0067	-	0.74	3000	0	2,000
S1336-18BQ	Hamamatsu	0.0057	-	0.65	20	0	2,000
S1336-18BK	Hamamatsu	0.0057	-	0.65	20	0	2,000
S1336-5BQ	Hamamatsu	0.0081	-	0.65	65	0	1,000
S1336-5BK	Hamamatsu	0.0081	-	0.65	65	0	1,000
S1336-44BQ	Hamamatsu	0.0100	-	0.65	150	0	600
S1336-44BK	Hamamatsu	0.0100	-	0.65	150	0	600
S1336-8BQ	Hamamatsu	0.0130	-	0.65	380	0	400
S1336-8BK	Hamamatsu	0.0130	-	0.65	380	0	400
S1337-16BQ	Hamamatsu	0.01	-	0.65	65	0	600
S1337-16BR	Hamamatsu	0.0084	-	0.80	65	0	600

Part #	Manufacturer	NEP		Q.E.	c_j		r_{sh} (MΩ)
		Value ($\mathbf{pW/\sqrt{Hz}}$)	V_R (V)		Value (pF)	V_R (V)	
S1337-33BQ	Hamamatsu	0.0081	-	0.65	65	0	1,000
S1337-33BR	Hamamatsu	0.0065	-	0.80	65	0	1,000
S1337-66BQ	Hamamatsu	0.013	-	0.65	380	0	400
S1337-66BR	Hamamatsu	0.01	-	0.80	380	0	400
S1337-1010BQ	Hamamatsu	0.018	-	0.65	1100	0	200
S1337-1010BR	Hamamatsu	0.015	-	0.80	1100	0	200
S1337-21	Hamamatsu	0.025	-	0.67	4000	0	100
S1787-04	Hamamatsu	-	-	0.66	700	0	100,000
S1787-08	Hamamatsu	-	-	0.75	700	0	100,000
S1787-12	Hamamatsu	-	-	0.67	200	0	10,000
S2281	Hamamatsu	0.018	0	0.65	1300	0	200
S2281-01	Hamamatsu	0.0086	0	0.62	3200	0	1,700
S2281-04	Hamamatsu	0.018	0	0.65	1300	0	200
S2386-18K	Hamamatsu	0.00068	0	0.78	140	0	100,000
S2386-18L	Hamamatsu	0.00068	0	0.78	140	0	100,000
S2386-5K	Hamamatsu	0.00096	0	0.78	730	0	50,000
S2386-44K	Hamamatsu	0.0014	0	0.78	1600	0	25,000
S2386-45K	Hamamatsu	0.0014	0	0.78	2300	0	25,000
S2386-8K	Hamamatsu	0.0021	0	0.78	4300	0	10,000
S2387-16R	Hamamatsu	0.00099	0	0.75	730	0	50,000
S2387-33R	Hamamatsu	0.00099	0	0.75	730	0	50,000
S2387-66R	Hamamatsu	0.0022	0	0.75	4300	0	10,000
S2387-1010R	Hamamatsu	0.0031	0	0.75	12000	0	5,000

Part #	Manufacturer	NEP		Q.E.	c_j		r_{sh} (MΩ)
		Value ($pW/\sqrt{Hz}$)	V_R (V)		Value (pF)	V_R (V)	
S2387-130R	Hamamatsu	0.0016	0	0.75	5000	0	20,000
S2506-02	Hamamatsu	0.0100	10	0.72	15	12	667
S2506-04	Hamamatsu	0.0100	10	0.72	15	12	667
S6775	Hamamatsu	0.0180	12	0.90	40	10	167
S6775-01	Hamamatsu	0.0190	12	0.88	40	10	167
S6967	Hamamatsu	0.0200	12	0.90	50	10	500
S2551	Hamamatsu	0.039	0	0.81	350	0	30
S2592-03	Hamamatsu	0.0081	0	0.65	65	0	1,000
S3477-03	Hamamatsu	0.0081	0	0.65	65	0	1,000
S2592-04	Hamamatsu	0.013	0	0.65	380	0	400
S3477-04	Hamamatsu	0.013	0	0.65	380	0	400
S2744-08	Hamamatsu	0.047	70	0.85	750	0.1	-
S2744-09	Hamamatsu	0.047	70	0.85	750	0.1	-
S3588-08	Hamamatsu	0.047	70	0.85	450	0.1	-
S3588-09	Hamamatsu	0.047	70	0.85	450	0.1	-
S5627-01	Hamamatsu	-	-	0.69	700	0	5,000
S6931-01	Hamamatsu	-	-	0.83	200	0	50,000
S4797-01	Hamamatsu	-	-	0.69	50	0	50,000
S2833-01	Hamamatsu	-	-	0.75	700	0	100,000
S4011-06DS	Hamamatsu	-	-	0.75	200	0	250,000
S3071	Hamamatsu	0.021	24	0.81	150	0.1	-
S3072	Hamamatsu	0.016	24	0.81	50	0.1	-
S3399	Hamamatsu	0.0094	10	0.89	85	0.1	-
S3883	Hamamatsu	0.0067	20	0.89	40	0.1	-

Part #	Manufacturer	NEP		Q.E.	c_j		r_{sh} (MΩ)
		Value ($\mathbf{pW/\sqrt{Hz}}$)	V_R (V)		Value (pF)	V_R (V)	
S3204-08	Hamamatsu	0.066	70	0.85	2000	0.1	-
S3204-09	Hamamatsu	0.066	70	0.85	2000	0.1	-
S3584-08	Hamamatsu	0.086	70	0.85	4000	0.1	-
S3584-09	Hamamatsu	0.086	70	0.85	4000	0.1	-
S3590-08	Hamamatsu	0.038	70	0.85	200	0.1	-
S3590-09	Hamamatsu	0.038	70	0.85	200	0.1	-
S3590-18	Hamamatsu	0.076	70	0.84	400	0.1	-
S3590-19	Hamamatsu	0.076	70	0.75	400	0.1	-
S3759	Hamamatsu	-	-	0.44	100	0.1	0.25
S3994-01	Hamamatsu	-	-	0.84	200	0.1	33.3
S4707-01	Hamamatsu	-	-	0.78	60	0.1	400.0
S5106	Hamamatsu	0.016	10	0.93	200	0.1	-
S5107	Hamamatsu	0.024	10	0.93	750	0.1	-
S7509	Hamamatsu	0.017	10	0.93	150	0.1	-
S7510	Hamamatsu	0.025	10	0.93	400	0.1	-
S5821	Hamamatsu	0.0067	10	0.78	15	0.1	-
S5821-01	Hamamatsu	0.0067	10	0.78	15	0.1	-
S5821-02	Hamamatsu	0.0067	10	0.78	15	0.1	-
S5821-03	Hamamatsu	0.0067	10	0.78	15	0.1	-
S5971	Hamamatsu	0.0074	10	0.88	15	0.1	-
S5972	Hamamatsu	0.0031	10	0.88	5.5	0.1	-
S5973	Hamamatsu	0.0011	3.3	0.85	2.5	0.1	-
S5973-01	Hamamatsu	0.0011	3.3	0.85	2.5	0.1	-

Part #	Manufacturer	NEP		Q.E.	c_j		r_{sh} (MΩ)
		Value ($pW/\sqrt{Hz}$)	V_R (V)		Value (pF)	V_R (V)	
S5973-02	Hamamatsu	0.0019	3.3	0.65	2.5	0.1	-
S6036	Hamamatsu	-	-	0.72	50	0.1	400.0
S6036-01	Hamamatsu	-	-	0.72	50	0.1	400.0
S6801	Hamamatsu	-	-	0.92	150	0.1	166.7
S6801-01	Hamamatsu	-	-	0.80	150	0.1	166.7
S6968	Hamamatsu	-	-	0.92	200	0.1	1,000.0
S6968-01	Hamamatsu	-	-	0.80	200	0.1	1,000.0
S7478	Hamamatsu	-	-	0.93	200	0.1	286
S7686	Hamamatsu	-	-	0.86	200	0	100,000
S8193	Hamamatsu	-	-	0.86	950	0	5,000
S8265	Hamamatsu	-	-	0.69	230	0	12,500
S8385	Hamamatsu	0.01	-	0.72	30	0.1	667
S8385-04	Hamamatsu	0.01	-	0.72	30	0.1	667
S8729	Hamamatsu	0.011	-	0.90	50	0.1	333
S8729-04	Hamamatsu	0.012	-	0.88	50	0.1	333
S8729-10	Hamamatsu	0.011	-	0.90	50	0.1	333
S8552	Hamamatsu	-	-	0.39	4000	0	100
S8553	Hamamatsu	-	-	0.39	8000	0	100

APPENDIX 2. Survey of Commercially Available Avalanche Photodiodes

Part #	SNR_∞		$R_{F,90}$ (MΩ)		M	F	η (e^-/phot.)	Dark Current (nA)		c_j (pF)
	Typ.	Min.	Max.	Typ.				Typ.	Max.	
S12426-02	43.8	40.4	10.6	9.00	100	3.98	0.70	0.1	1.0	0.5
S12426-05	43.4	37.4	10.4	7.72	100	3.98	0.70	0.2	2.0	1.1
S12023-02	44.0	42.2	10.7	9.82	100	3.98	0.75	0.05	0.5	1
S12023-05	43.8	40.4	10.6	9.00	100	3.98	0.75	0.1	1.0	2
S12051	43.8	40.4	10.6	9.00	100	3.98	0.75	0.1	1.0	2
S12086	43.8	40.4	10.6	9.00	100	3.98	0.75	0.1	1.0	2
S12023-10	43.4	37.4	10.4	7.72	100	3.98	0.75	0.2	2.0	6
S12023-10A	43.4	37.4	10.4	7.72	100	3.98	0.75	0.2	2.0	6
S3884	42.2	31.3	9.82	5.40	100	3.98	0.75	0.5	5.0	10
S2384	38.3	18.7	22.5	5.34	60	3.42	0.75	1.0	10	40
S2385	23.3	8.2	18.7	2.31	40	3.02	0.75	3.0	30	95
S12053-02	47.4	22.8	49.6	11.5	50	2.99	0.80	0.2	5.0	2
S12053-05	47.4	22.8	49.6	11.5	50	2.99	0.80	0.2	5.0	5
S12053-10	47.4	22.8	49.6	11.5	50	2.99	0.80	0.2	5.0	15
S9075	43.2	14.2	41.1	4.43	50	2.99	0.80	0.5	15	30
S5344	38.1	10.2	32.0	2.30	50	2.99	0.80	1.0	30	120
S5345	27.7	5.7	16.9	0.71	50	2.99	0.80	3.0	100	320
S12060-02	44.0	42.2	10.7	9.82	100	3.98	0.75	0.05	0.50	1.5
S12060-05	43.8	40.4	10.6	9.00	100	3.98	0.75	0.1	1	2.5
S12060-10	43.4	37.4	10.4	7.72	100	3.98	0.75	0.2	2	6
S6045-04	42.2	31.3	9.82	5.40	100	3.98	0.75	0.5	5	12
S6045-05	38.3	18.7	22.5	5.34	60	3.42	0.75	1	10	50
S6045-06	23.3	8.2	18.7	2.31	40	3.02	0.75	3	30	120
S8664-02K	57.5	44.5	72.8	43.7	50	2.19	0.70	0.1	1	0.8
S8664-05K	55.4	40.3	67.8	35.8	50	2.19	0.70	0.2	1.5	1.6
S8664-10K	53.6	32.4	63.4	23.1	50	2.19	0.70	0.3	3	4
S8664-20K	49.1	24.8	53.1	13.6	50	2.19	0.70	0.6	6	11
S8664-30K	44.5	16.6	43.7	6.05	50	2.19	0.70	1	15	22
S8664-50K	32.4	11.1	23.1	2.71	50	2.19	0.70	3	35	55
S8664-55	26.7	9.3	15.7	1.92	50	2.19	0.70	5	50	80
S8664-1010	19.9	6.6	8.74	0.97	50	2.19	0.70	10	100	270
S8890-02	43.4	37.4	10.4	7.72	100	3.98	0.92	0.2	2	0.20
S8890-05	38.8	22.1	8.31	2.70	100	3.98	0.92	1.5	15	0.50
S8890-10	31.3	13.3	5.40	0.98	100	3.98	0.92	5	50	1.50
S8890-15	25.6	9.66	3.60	0.51	100	3.98	0.92	10	100	2.50
S8890-30	22.1	7.95	2.70	0.35	100	3.98	0.92	15	150	8.00
S10341-02	13.3	4.41	0.98	0.11	100	3.98	0.75	50	500	1
S10341-05	9.66	3.12	0.51	0.05	100	3.98	0.75	100	1000	2
S11519-10	35.0	16.7	6.75	1.54	100	3.98	0.65	3	30	2
S11519-30	26.5	10.2	3.86	0.57	100	3.98	0.65	9	90	12
S12092-02	43.8	40.4	10.6	9.00	100	3.98	0.5	0.1	1	0.4
S12092-05	43.4	37.4	10.4	7.72	100	3.98	0.5	0.2	2	0.7
S9251-10	42.6	33.0	10.0	6.00	100	3.98	0.5	0.4	4	1.9
S9251-15	41.1	27.5	9.31	4.16	100	3.98	0.5	0.8	8	3.6

APPENDIX 3. Survey of Commercially Available Operational Amplifiers

Part #	Thermal Noise ψ_T (nV/√Hz)	FNN (nV/√Hz)	Current Noise ξ_s (fA/√Hz)	CM Input Impedance (Ω‖pF)	DM Input Impedance (Ω‖pF)	Open-Loop Gain A_{ol}	GBW (MHz)
ADA4000-1	16	47.4	10	10^{12} ‖ 5.5	10^{10} ‖ 4	316,228	5
ADA4177	8.0	13	200	10^{11} ‖ 1	$4x10^{6}$ ‖ 1	-	-
ADA4530-1	14.0	250	0.07	10^{14} ‖ 8	-	31,622,777	2
ADA4610	7.3	44.4	1.26	10^{13} ‖ 4.8	10^{13} ‖ 3.1	223,872	15.4
ADA4627	4.8	39.7	2.5	10^{12} ‖ 7	10^{12} ‖ 8	1,000,000	19
ADA4637	4.8	39.7	2.5	10^{12} ‖ 7	10^{12} ‖ 8	1,000,000	19
ADA4817	4.0	632	2.5	500G ‖ 1.3	? ‖ 0.1	1,778	200
AD515AJ	50	237	0.10	10^{15} ‖ 0.8	10^{13} ‖ 1.6	40,000	1
AD515AK	50	237	0.10	10^{15} ‖ 0.8	10^{13} ‖ 1.6	100,000	1
AD515AL	50	237	0.10	10^{15} ‖ 0.8	10^{13} ‖ 1.6	50,000	1
AD795	9.0	63.2	0.6	10^{14} ‖ 2.2	10^{12} ‖ 2	1,000,000	1.6
AD8065	7.0	326	0.6	10^{12} ‖ 2.1	10^{12} ‖ 4.5	501,187	145
AD8066	7.0	326	0.6	10^{12} ‖ 2.1	10^{12} ‖ 4.5	501,187	115
AD823	13.0	113	1.0	10^{13} ‖ 1.3	10^{13} ‖ 0.6	450,000	19
AD8510	7.6	100.0	2.8	? ‖ 11.5	? ‖ 12.5	196,000	8
AD8512	7.6	100.0	2.8	? ‖ 11.5	? ‖ 12.5	196,000	8
AD8513	7.6	100.0	2.8	? ‖ 11.5	? ‖ 12.5	196,000	8
AD8610	6	200	5.0	? ‖ 15	? ‖ 8	180,000	25
AD8620	6	200	5.0	? ‖ 15	? ‖ 8	180,000	25
AD8622	11	16.7	150.0	10^{12} ‖ 3	-	7,079,458	0.560
AD8624	11	20	220	10^{12} ‖ 3	-	7,079,458	0.560
AD8625	17.5	-	0.4	-	-	-	-
AD8626	17.5	-	0.4	-	-	-	-
AD8627	17.5	-	0.4	-	-	-	-
AD8641	28.5	401	0.5	? ‖ 3.0	? ‖ 4.5	290,000	3.5
AD8642	28.5	401	0.5	? ‖ 3.0	? ‖ 4.5	290,000	3.5
AD8643	28.5	401	0.5	? ‖ 3.0	? ‖ 4.5	290,000	3.5
AD8646	6	221	0.3	? ‖ 7.8	? ‖ 2.5	125,893	24.0
AD8647	6	221	0.3	? ‖ 7.8	? ‖ 2.5	125,893	24.0
AD8648	6	221	0.3	? ‖ 7.8	? ‖ 2.5	125,893	24.0
AD8655	3	86.4	1.0	? ‖ 16.5	-	316,228	28.0
AD8656	3	86.4	1.0	? ‖ 16.5	-	316,228	28.0
AD8691	6.5	150	0.25	10^{12} ‖ 5	-	-	-
AD8692	6.5	150	0.25	10^{12} ‖ 5	-	-	-
AD8694	6.5	150	0.25	10^{12} ‖ 5	-	-	-
LF156	12	137	10	10^{12} ‖ 3	10^{12} ‖ 3	200,000	5
LM6211	5.5	100	10	10^{13} ‖ 5.5	-	-	-
LMC6001	22	276	0.13	>1T	>1T	1,400,000	1
LMC6035	27	304	0.2	> 10^{13} ‖ 1		2,000,000	1.4

Part #	Thermal Noise ψ_T (nV/√Hz)	FNN (nV/√Hz)	Current Noise ξ_s (fA/√Hz)	CM Input Impedance (Ω‖pF)	DM Input Impedance (Ω‖pF)	Open-Loop Gain A_{ol}	GBW (MHz)
LMC662	22	285	0.20	$> 10^{12}$	-	2,000,000	1.4
LMC8101	36	269	1.5	10^{10} ‖ 10	-	-	
LMV341-N	40	780	1.0	-	-	446,684	1
LMV342-N	40	780	1.0	-	-	446,684	1
LMV344-N	40	780	1.0	-	-	446,684	1
LPV521	265	648	100.0	-	-	1,778,279	0.0061
LT1057	26	52.6	1.8	$400x10^9$ ‖ 4	$400x10^9$ ‖ 4	300,000	5.0
LT1058	26	52.6	1.8	$400x10^9$ ‖ 4	$400x10^9$ ‖ 4	300,000	5.0
LT1464	24	85.7	0.4	10^{12} ‖ 3	10^{12} ‖ 3	1,000,000	1
LT1793	6	31	0.8	10^{13} ‖ 1.5	10^{14} ‖ 1.5	3,000,000	3.1
OP482	36	142	10	-	-	20,000	4
OPA111AM	6	125	0.5	10^{14} ‖ 3	10^{13} ‖ 1	1,778,279	2
OPA111BM	6	93	0.4	10^{14} ‖ 3	10^{13} ‖ 1	1,778,279	2
OPA111SM	6	125	0.5	10^{14} ‖ 3	10^{13} ‖ 1	1,778,279	2
OPA121KM	6	125	0.8	10^{14} ‖ 3	10^{13} ‖ 1	1,000,000	2
OPA121KP	7	157	1.1	10^{14} ‖ 3	10^{13} ‖ 1	501,187	2
OPA121KU	7	157	1.1	10^{14} ‖ 3	10^{13} ‖ 1	501,187	2
OPA124	6	99.8	0.5	10^{14} ‖ 3	10^{13} ‖ 1	1,778,279	2
OPA128JM	15	300	0.22	10^{15} ‖ 2	10^{13} ‖ 1	2,511,886	1
OPA128KM	15	300	0.16	10^{15} ‖ 2	10^{13} ‖ 1	2,511,886	1
OPA128LM	15	300	0.12	10^{15} ‖ 2	10^{13} ‖ 1	2,511,886	1
OPA128SM	15	300	0.16	10^{15} ‖ 2	10^{13} ‖ 1	2,511,886	1
OPA132	8	85	3.0	10^{13} ‖ 6	10^{13} ‖ 2	1,000,000	8
OPA1602	2.5	15	2200	10^9 ‖ 2.5	-	-	-
OPA140	5.1	15.7	0.8	10^{13} ‖ 7.0	10^{13} ‖ 10	1,995,262	11
OPA141	6.5	18	0.8	10^{13} ‖ 6	-	-	-
OPA209	2.2	8	17.89	10^9 ‖ 2	-	-	-
OPA376	7.5	55	2.00	10^{14} ‖ 13	? ‖ 6.5	5,011,872	5.5
OPA659	8.9	632	-	10^{12} ‖ 2.5	-	-	-
OPA827	3.8	20	0.98	10^{13} ‖ 9	-	-	-
TC75S63TU	7.5	85.4	0.57	-	-	-	-
TL072	18	130	4.56	1T	1T	200,000	3
TSX920	12.9	671	-	10^{12} ‖ 8	-	-	-

REFERENCES

[1] M. Canepari, D. Zecevic and O. Bernus, Membrane Potential Imaging in the Nervous System and Heart, 2 ed., vol. 859, New York: Springer, 2015.

[2] V. Fast and R. Ideker, "Simultaneous Optical Mapping of Transmembrane Potential and Intracellular Calcium in Myocyte Cultures," *Journal of Cardiovascular Electrophysiology,* vol. 11, no. 5, pp. 547-556, May 2000.

[3] F. Jousset and S. Rohr, "Optical Recording of Calcium Currents During Impulse Conduction in Cardiac Tissues," *Neurophotonics,* vol. 2, no. 2, pp. 021011-1 - 021011-9, April 2015.

[4] W. Kong, A. Pollard and V. Fast, "A New Optrode Design for Intramural Optical Recording," *IEEE Transactions on Biomedical Engineering,* vol. 58, no. 11, 2011.

[5] W. Bian and L. Tung, "Structure-Related Initiation of Reentry by Rapid Pacing in Monolayers of Cardiac Cells," *Circulation Research,* vol. 98, no. 4, pp. e29-e38, 3 March 2006.

[6] R. Enoki, M. Namiki, Y. Kudo and H. Miyakawa, "Optical Monitoring of Synaptic Summation Along the Dendrites of CA1 Pyramidal Neurons," *Neuroscience,* vol. 113, no. 4, pp. 1003-1014, 2002.

[7] E. Entcheva, S. Lu, R. Troppman, V. Sharma and L. Tung, "Contact Fluorescence Imaging of Reentry in Monolayers of Cultured Neonatal Rat Ventricular Myocytes," *Journal of Cardiovascular Electrophysiology,* vol. 11, no. 6, pp. 665-676, June 2000.

[8] K. Fukunishi, N. Murai and H. Uno, "Dynamic Characteristics of the Auditory Cortex of Guinea Pigs Observed with Multichannel Optical Recording," *Biological Cybernetics,* vol. 67, no. 6, pp. 501-509, 1992.

[9] N. Hama, S. Ito and A. Hirota, "Optical Imaging of the Propogation Patterns of Neural Responses in the Rat Sensory Cortex: Comparison Under Two Different Anesthetic Conditions," *Neuroscience,* vol. 284, pp. 125-133, 22 January 2015.

[10] S. A. Park, S.-R. Lee, L. Tung and D. T. Yue, "Optical Mapping of Optogenetically Shaped Cardiac Action Potentials," *Scientific Reports,* vol. 4, no. 6125, pp. 1-10, August 2014.

[11] S. Rohr and J. Kucera, "Optical Recording System Based on a Fiber Optic Image Conduit: Assessment of Microscopic Activation Patterns in Cardiac Tissue," *Biophysical Journal,* vol. 75, no. 2, pp. 1062-1065, August 1998.

[12] M. Shrivastav, M. B. Ghai, A. Singal and P. A. Iaizzo, "The Design and Use of an Optical Mapping System for the Intracardiac Electrical Signaling," *Indian Pacing and Electrophysiology Journal,* vol. 12, no. 4, pp. 138-151, 2012.

[13] J. A. Scull, L. C. McSpadden, H. D. Himel IV, N. Badie and N. Bursac, "Single-Detector Simultaneous Optical Mapping of Vm and [Ca2+]i in Cardiac Monolayers," *Annals of Biomedical Engineering,* vol. 40, no. 5, pp. 1006-1017, May 2012.

[14] S. Dhein, F. Mohr and M. Delmar, Practical Methods in Cardiovascular Research, New York: Springer Link, 2005.

[15] C. Chien and J. Pine, "An Apparatus for Recording Synaptic Potentials from Neuronal Cultures Using Voltage-Sensitive Fluorescent Dyes," *Journal of Neuroscience Methods,* vol. 38, no. 2-3, pp. 93-105, 1991.

[16] A. Matiukas, B. Mitrea, M. Qin, A. Pertsov, A. Shvedko, M. Warren, A. Zaitsev, J. Wuskell, M. Wei, J. Watras and L. Loew, "Near-Infrared Voltage-Sensitive Fluorescent Dyes Optimized for Optical Mapping in Blood-Perfused Myocardium," *Heart Rhythm Society,* vol. 4, no. 11, pp. 1441-1451, November 2007.

[17] Y. Qian, W. Clusin and S. Lin, "Spatial Heterogeneity of Calcium Transient Alternans During the Early Phase of Myocardial Ischemia in the Blood-Perfused Rabbit Heart," *Circulation,* vol. 104, no. 17, pp. 2082-2087, October 2001.

[18] A. Hirota, K. Sato, Y. Momose-Sato, T. Sakai and K. Kamino, "A new simultaneous 1020-site optical recording system," *Journal of Neuroscience Methods,* vol. 56, no. 2, pp. 187-194, 1995.

[19] H. Kawaguchi, R. Tokioka, N. Murai and K. Fukunishi, "Multichannel optical recording of neuronal network activity and synaptic potentiation in dissociated cultures from rat hippocampus," *Neuroscience Letters,* vol. 205, no. 3, pp. 177-180, 1 March 1996.

[20] C. Du, G. A. MacGowan, D. L. Farkas and A. P. Koretsky, "Calcium Measurements in Perfused Mouse Heart: Quantitating Fluorescence and Absorbance of Rhod-2 by Application of Photon Migration Theory," *Biophysical Journal,* vol. 80, no. 1, pp. 549-561, January 2001.

[21] S. B. Knisley, "Mapping Intacellular Calcium in Rabbit Hearts With Fluo 3," in *IEEE 17th Annual Conference*, Montreal, 1995.

[22] Hamamatsu Photonics K.K. Editorial Comittee, Photomultiplier Tubes Basics and Applications, 3a ed., W. T. W. Inc., Ed., Hamamatsu Photonics K.K. Electron Tubes Division, 2007.

[23] R. Baker, CMOS Circuit Design, Layout and Simulation, 3 ed., Hoboken, New Jersey: John Wiley & Sons Inc., 2010.

[24] R. Mancini, Op Amps for Everyone, 2 ed., New York: Elsevier, 2003.

[25] Texas Instruments, *SLVA043B.*

[26] Analog Devices, "Tutorial MT-047 Op Amp Noise".

[27] National Instruments, *041.*

[28] Excelitas Technologies, "Applications Notes".

[29] OSI Optoelectronics, "Photodiode Characteristics and Applications".

[30] Hamamatsu Photonics, "Opto-Semiconductor Handbook".

[31] J. Graeme, Photodiode Amplifiers Op Amp Solution, Boston: McGraw-Hill, 1996.

[32] Excelitas Technologies, "Avalanche Photodiode: A User Guide".

[33] S. Flyct and C. Marmonier, Photomultiplier Tubes Principles & Applications, Brive, 2002.

[34] G. C. Holst, CCD Arrays Cameras and Displays, 2nd ed., Winter Park; Bellingham, Florida; Washington: JCD Publishing; SPIE Optical Engineering Press, 1998, p. 378.

[35] B. G. Mitrea, B. J. Caldwell and A. M. Pertsov, "Imaging Excitation Inside the Myocardial Wall," *Biomedical Optics Express,* vol. 2, no. 3, pp. 620-633, 16 February 2011.

[36] Photometrics, *Keep the Noise Down! Low Noise: An Integral Part of High-Performance CCD (HCCD) Camera Systems,* 2010.

[37] B. Salzberg, P. Kosterin, M. Muschol, A. Obaid, S. Rumyantsev, Y. Bilenko and M. Shur, "An Ultra-Stable Non-Coherent Light Source for Optical Measurements in Neuroscience and Cell Physiology," *Journal of Neuroscience Methods,* vol. 141, no. 1, pp. 165-169, January 2005.

[38] P. Lee, K. Wang, C. E. Woods, P. Yan, P. Kohl, P. Ewart, L. M. Loew, D. A. Terrar and C. Bollesndorf, "Cardiac Electrophysiological Imaging Systems Scalable for High-Throughput Drug Testing," *Pflugers Arch.,* vol. 464, no. 6, pp. 645-656, December 2012.

[39] E. Entcheva, Y. Kostov, E. Tchernev and L. Tung, "Fluorescence Imaging of Electrical Activity in Cardiac Cells Using an All-Solid-State System," *IEEE Transactions on Biomedical Engineering,* vol. 51, no. 2, pp. 333-341, February 2004.

[40] P. Stewart, O. V. Aslanidi, D. Noble, P. J. Noble, M. R. Boyett and H. Zhang, "Mathematical Models of the Electrical Action Potential of Purkinje Fibre Cells," *Philosophical Transactions of the Royal Society A,* vol. 367, no. 1896, pp. 2225-2255, 13 June 2009.

[41] L. Orozco, "Optimizing Precision Photodiode Sensor Circuit Design," Norwood, MA, 2014.

[42] J. Bellemen, "Shunt Capacitance of 1206 SMD Resistors," December 2010. [Online]. Available: http://jeroen.web.cern.ch/jeroen/resistor/shuntC.html.

[43] Vishay, "Frequency Response of Thin Film Chip Resistors," 2009.

[44] Texas Instruments, "Electrical Performance of Packages," 2004.

[45] G. Briseboise, "Op Amp Provides Femptoamp Bias Current with 4GHz Gain Bandwidth Product, Shines New Light on Photonics Applications," *LT Journal of Analog Innovation,* vol. 25, no. 2, pp. 1-7, July 2015.

[46] E. Entcheva, S. Lu, R. Troppman, V. Sharma and L. Tung, "Contact Fluorescence Imaging of Reentry in Monolayers of Cultured Neonatal Rat Ventricular Myocytes," *Journal of Cardiovascular Electrophysiology,* vol. 11, no. 6, pp. 665-676, June 2000.

[47] V. D. Khait, O. Bernus, S. F. Mironov and A. M. Pertsov, "Method for the Three-Dimensional Localization of Intramyocardial Excitation Centers Using Optical Imaging," *Journal of Biomedical Optics,* vol. 11, no. 3, pp. 034007-1 - 034007-12, May 2006.

[48] D. Rosenbaum and J. Jalife, Optical Mapping of Cardiac Excitation and Arrhythmias, New York, New York: Wiley, 2001.

[49] J. Swartling, S. Palsson, P. Platonov, S. Olsson and S. Andersson-Engels, "Changes in Tissue Optical Properties Due to Radio-Frequency Ablation of Myocardium," *Medical and Biological Engineering & Computing,* vol. 41, no. 4, pp. 403-409, 2003.

[50] A. Yaroshevsky, Z. Glasser, E. Granot and S. Sternklar, "The Transition from the Ballistic to the Diffusive Regime in a Turbid Medium," *Optics Letters,* vol. 36, no. 8, p. 1395, 2011.

[51] D. Gareau, G. Merlino, C. Corless, M. Kulesz-Martin and S. Jacques, "Noninvasive Imaging of Melanoma with Reflectance Mode Confocal Scanning Laser Microscopy in a Murine Model," *Journal of Investigative Dermatology,* vol. 127, no. 9, pp. 2184-2190, 2007.

[52] S. Jacques, R. Samatham, N. Choudhury, Y. Fu and D. Levitz, "Measuring Tissue Optical Properties in vivo Using Reflectance-Mode Confocal Microscopy and OCT," *Biomedical Applications of Light Scattering II,* vol. 6864, no. 1, p. 68650B, 2008.

[53] T. Collier, D. Arifler, A. Malpica, M. Follen and R. Richards-Kortum, "Determination of

Epithelial Tissue Scattering Using Confocal Microscopy," *Journal of Selected Topics in Quantum Electronics,* vol. 9, no. 2, pp. 307-313, 2003.

[54] T. Collier, M. Follen, A. Malpica and R. Richards-Kortum, "Sources of Scattering in Cervical Tissue: Determination of the Scattering Coefficient by Confocal Microscopy," *Applied Optics,* vol. 44, no. 11, pp. 2072-2081, 2005.

[55] A. Peraiah, An Introduction to Radiative Transfer: Methods and Applications in Astrophysics, 1st ed., Cambridge: Cambridge University Press, 2001.

[56] S. Chandrasekhar, Radiative Transfer, 1st ed., New York, New York: Dover Publications, 1960.

[57] T. Khan and A. Thomas, "On Derivation of the Radiative Transfer Equation and its Spherical Harmonics Approximation for Scattering Media with Spatially Varying Refractive Indices," Clemson, 2016.

[58] J. Seinfeld and S. Pandis, Atmospheric Chemistry and Physics: From Air Pollution to Climate Change, 2nd ed., Hoboken, New Jersey: John Wiley & Sons, 2006.

[59] S. L. Jacques, "Optical Properties of Biological Tissues: A Review," *Physics in Medicine and Biology,* vol. 58, no. 11, pp. R37-R61, 10 May 2013.

[60] L. Wang, S. Jacques and L. Zheng, "MCML- Monte Carlo Modeling of Light Transport in Multilayered Tissues," *Computer Methods and Programs in Biomedicine,* vol. 47, no. 2, pp. 131-146, 1995.

[61] L. Wang, S. L. Jacques and L. Zheng, "CONV - Convolution for Responses to a Finite Diameter Photon Beam Incident on Multi-Layered Tissues," *Computer Methods and Programs in Biomedicine,* vol. 54, no. 3, pp. 141-150, 1997.

[62] C. J. M. Moes, M. J. C. van Gamert, W. M. Star, M. J. P. A and S. A. Prahl, "Measurements and Calculations of the Energy Fluence Rate in a Scattering and Absorbing Phantom at 633nm," *Applied Optics,* vol. 28, no. 12, pp. 2292-2296, 15 June 1989.

[63] R. Michels, F. Foschum and A. Kienle, "Optical Properties of Fat Emulsions," *Optics Express,* vol. 16, no. 8, pp. 5907-5925, 2008.

[64] B. Wilson, M. Patterson and D. Burns, "Effect of Photosensitizer Concentration in Tissue on the Penetration Depth of Photoactivating Light," *Lasers in Medical Science,* vol. 1, no. 4, pp. 235-244, 1986.

[65] R. Cubeddu, A. Pifferi, P. Taroni, A. Torricelli and G. Valentini, "A Solid Tissue Phantom for Photon Migration Studies," *Physics in Medicine and Biology,* vol. 42, no. 10, pp. 1971-

1979, October 1997.

[66] M. J. C. van Gemert, A. J. Welch, W. M. Star, M. Motamedi and W.-F. Cheong, "Tissue optics for a slab geometry in the diffusion approximation," *Lasers in Medical Science,* vol. 2, no. 4, pp. 295-302, December 1987.

[67] R. Splinter, W.-F. Cheong, M. J. C. van Gemert and A. J. Welch, "In Vitro Optical Properties of Human and Canine Brain and Urinary Bladder Tissues at 633 nm," *Lasers in Surgery and Medicine,* vol. 9, no. 1, pp. 37-41, October 1989.

[68] R. Srinivasan and M. Singh, "Development of Biological Tissue-Equivalent Phantoms for Optical Imaging," *Indian Journal of Experimental Biology,* vol. 40, no. 5, pp. 531-535, 2002.

[69] I. Tachtsidis, L. Gao, T. Leung, M. Kohl-Bareis, C. Cooper and C. Elwell, "A Hybrid Multi-Distance Phase and Broadband Spatially Resolved Spectrometer and Alogorithm for Resolving Absolute Concentrations of Chromophores in the Near-Infrared Light Spectrum," *Advances in Experimental Medicine and Biology,* vol. 662, pp. 169-176, 24 October 2009.

[70] R. Cubeddu, M. Musolino, A. Pifferi, P. Taroni and G. Valentini, "Time-Resolved Reflectance: A Systematic Study for Application to the Optical Characterization of Tissues," *Journal of Quantum Electronics,* vol. 30, no. 10, pp. 2421-2430, October 1994.

[71] M. S. Patterson, E. Schwartz and B. C. Wilson, "Quantitative Reflectance Spectrophotometery for the Noninvasive Measurement of Photosensitizer Concentration in Tissue During Photodynamic Therapy," in *Photodynamic Therapy: Mechanisms*, Los Angeles, 1989.

[72] R. A. J. Groenhuis, H. A. Ferwerda and J. J. Ten Bosch, "Scattering and absorption of turbid materials determined from reflection measurements. 1: Theory," *Applied Optics,* vol. 22, no. 16, pp. 2456-2462, 15 August 1983.

[73] D. Hueber, M. Franceshini, H. Ma, Q. Zhang, J. Ballesteros, S. Fantini, D. Wallace, V. Ntziachristos and B. Chance, "Non-Invasive and Quantitative Near-Infrared Haemoglobin Spectrometry in the Piglet Brain During Hypoxic Stress, Using a Frequency-Domain Multi-Distance Instrument," *Physics in Medicine and Biology,* vol. 46, no. 1, pp. 41-62, January 2000.

[74] L. Ding, S. Splinter and S. Knisley, "Quantifying Spatial Localization of Optical Mapping Using Monte Carlo Simulations," *IEEE Transactions on Biomedical Engineering,* vol. 48, no. 10, pp. 1098-1107, 2001.

[75] R. Walton, C. Xavier, I. Tachtsidis and O. Bernus, "Experimental Validation of Alternating Transillumination for Imaging Intramural Wave Propagation," *Conf Proc IEEE Eng Med Biol Soc,* vol. 2011, pp. 1676-1679, 2011.

[76] B. Mitrea, M. Wellner and A. Pertsov, "Monitoring Intramyocardial Reentry Using Alternating Transillumination," in *IEEE Eng. Med. Biol. Soc.*, 2009.

[77] M. Bishop, B. Rodriguez, F. Qu, I. Efimov, D. Gavaghan and N. Trayanova, "The Role of Photon Scattering in Optical Signal Distortion During Arrhythmia and Defibrillation," *Biophysical Journal,* vol. 93, no. 10, pp. 3714-3726, 2007.

[78] E. M. C. Hillman, O. Bernus, E. Pease, M. B. Bouchard and A. Pertsov, "Depth-resolved optical imaging of transmural electrical propagation in perfused heart," *Optics Express,* vol. 15, no. 26, pp. 17827-17841, 13 December 2007.

[79] W. T. Baxter, S. F. Mironov, A. V. Zaitsev, J. Jalife' and A. M. Pertsov, "Visualizing Excitation Waves inside Cardiac Muscle Using Transillumination," *Biophysical Journal,* vol. 80, no. 1, pp. 516-530, January 2001.

[80] K. Wang, P. Lee, G. R. Mirams, P. Sarathchandra, T. K. Borg, D. J. Gavaghan, P. Kohl and C. Bollensdorff, "Cardiac tissue slices: preparation, handling, and successful optical mapping," *American Journal of Physiology Heart and Circulatory Physiology,* vol. 308, no. 9, pp. H1112-H1125, 1 May 2015.

[81] M. G. Klein, A. Lacampagne and M. F. Schneider, "Voltage dependence of the pattern and frequency of discrete Ca2+ release events after brief repriming in frog skeletal muscle," *Proceedings of the National Academy of Sciences,* vol. 94, no. 20, pp. 11061-11066, 30 September 1997.

[82] R. Arora, S. Verheule, L. Scott, A. Navarrete, V. Katari, E. Wilson, D. Vaz and J. E. Olgin, "Arrhythmogenic Substrate of the Pulmonary Veins Assessed by High-Resolution Optical Mapping," *Circulation,* vol. 107, no. 13, pp. 1816-1821, 8 April 2003.

[83] W. Boesmans, M. M. Hao and P. V. Berghe, "Optical Tools to Investigate Cellular Activity in the Intestinal Wall," *Journal of Neurogastroenterology and Motility,* vol. 21, no. 3, pp. 337-351, 3 July 2015.

[84] Y. Ma, M. A. Shaik, S. H. Kim, M. G. Kozberg, D. N. Thibodeaux, H. T. Zhao, H. Yu and E. M. C. Hillman, "Wide-field optical mapping of neural activity and brain haemodynamics: considerations and novel approaches," *Philosophical Transactions of the Royal Society B: Biological Sciences,* vol. 371, no. 1705, 29 August 2016.

[85] T. Berger, A. Borgdorff, S. Crochet, F. B. Neubauer, S. Lefort, B. Fauvet, I. Ferezou, A. Carleton, H.-R. Lüscher and C. C. H. Petersen, "Combined Voltage and Calcium Epifluorescence Imaging In Vitro and In Vivo Reveals Subthreshold and Suprathreshold Dynamics of Mouse Barrel Cortex," *Journal of Neurophysiology,* vol. 97, no. 5, pp. 3751-37-62, 1 May 2007.